# NIR sensitive organic dyes for tandem solar cells and transparent photodiodes

THÈSE N$^O$ 6595 (2015)

PRÉSENTÉE LE 29 MAI 2015
À LA FACULTÉ DES SCIENCES ET TECHNIQUES DE L'INGÉNIEUR
SMX - ENSEIGNEMENT
PROGRAMME DOCTORAL EN PHOTONIQUE

## ÉCOLE POLYTECHNIQUE FÉDÉRALE DE LAUSANNE

POUR L'OBTENTION DU GRADE DE DOCTEUR ÈS SCIENCES

PAR

## Hui ZHANG

acceptée sur proposition du jury:

Prof. O. Martin, président du jury
Prof. F. Nüesch, Dr R. Hany, directeurs de thèse
Prof. W. Brütting, rapporteur
Prof. R. A. J. Janssen, rapporteur
Prof. J.-E. Moser, rapporteur

*(EPFL*
ÉCOLE POLYTECHNIQUE
FÉDÉRALE DE LAUSANNE

Suisse
2015

献给我最亲爱的家人和爱人

*Dedicated to My Beloved Family and Jia Hu*

感谢他们无私的爱和支持！

*For Their Endless Love and Support!*

# Acknowledgements

Firstly I would like to express my sincere thanks to my dear supervisor Prof. Frank Nüesch who offered me such a chance to pursue my dream. His instructive advice and optimistic attitude on science has guided and encouraged me through all the stages of my study. It is my great honor to be a member of his group, and I have had a very wonderful experience at EMPA in the past three and an half years.

I am also very grateful to my co-supervisor Dr. Roland Hany for his illuminating instruction and daily caring. Without him this thesis wouldn't go through successfully, he has always been supporting with big patience and helping me out of difficulties on whatever problems I have on the project and some personal issues.

Special thanks to Dr. Gaëtan Wicht, who passed in the spring of 2013, for his very kind introduction at the beginning of my doctoral study. I will miss him forever.

For those who contributed to my thesis, I appreciate them very much for their knowledge and valuable discussions. Particularly Christina Gretener and Yaroslav Romanyuk for MoO3 substrate preparation, Jean-Nicolas Tisserant for nice TEM images, Matthias Nagel for CV measurement, Fernando A. Castro, Rowena Crockett and Alina Zoladek-Lemanczyk for Raman spectra, Okan Deniz and Carlos Sanchez-Sanchez for UPS measurements, Jakob Heier for fluorescence measurements, Andreas Borgschulte for XPS measurements, Gaëtan Wicht and Sandra Jenatsch for optical modeling, Andreas C. Gerecke for ESI-HRMS experiments, Jelissa De Jonghe for transient photocurrent experiments, Anna C. Véron and Thomas Geiger for the synthesis of cyanine dyes, Roland Steim for the discussion on photodetector, Björn Niesen, Stephan Bücheler and Fan Fu for IPCE measurements, Erwin Hack for ellipsometry measurements, Isabella Gartmann, Beatrice Fischer and Katerina Andric for ordering of the chemicals and organizing everything.

I am extremely thankful to all my colleagues who are and were in the laboratory for functional polymers for such a wonderful working atmosphere, especially the young colleagues, Jean-Nicolas Tisserant, Jose Enrico Quinsaat, Anna C. Véron, Lei Wang, Sandra Jenatsch, Nicolas Leclaire, Mohammed Makha, Yee Song Ko, Simon Dünki, Etienne Berner, Oswaldo Neto and Chuyao Peng *et al.* for the coffee breaks, fondue, raclette and drinking. It has been a great pleasure to work with these outstanding scientists.

Prof. Hua Wu and his wife are greatly appreciated for their regular gathering on every Chinese traditional festival, which makes me feel at home. I want to thank Yuebin Liu and Lin

# Abstract

Due to advantages such as mechanical flexibility, light weight and the prospect to use low-cost roll-to-roll manufacturing processes, organic semiconductors have been widely investigated in many application areas as alternatives for their inorganic counterpart. In organic semiconductors, the rather weak Van der Waals interactions holding together the molecular building blocks result in narrow absorption bands which endow organic electronics with important advantages for the development of smart functionalities. Transparent organic electronics (TOEs), for example, incorporate devices through which visible light is transmitted. Among other semiconducting devices, it is actually possible to construct sensors and photovoltaic devices that solely use ultraviolet (UV) and near infrared (NIR) light to produce electrical energy or signal. TOEs have been proposed for easy integration with other electronic devices. Among the different molecular materials, cyanine dyes stand out by sharp, intense absorption bands exhibiting the highest molar extinction coefficients. The absorption peak can be easily shifted into the NIR wavelength region by increasing the length of the conjugated polymethine chain. For example, NIR light absorbing heptamethine cyanine dyes (Cy7) are promising candidates as transparent and colorless photoactive film materials.

In this thesis work, highly efficient TOE devices such as transparent solar cells and transparent photodetectors using NIR absorbing cyanine dyes as photosensitive materials have been successfully fabricated. To optimize these multilayer devices, various cyanine dyes were investigated, device architecture and interfaces were engineered. Optical simulations of the stacked thin film structures allowed understanding and tuning device performance. Moreover, organic solar cells which are transparent in the visible range have been integrated into tandem and triple junction solar cells. Low bandgap materials that absorb NIR light were combined with cyanine cells which absorb visible light, thereby more sunlight could be harvested and power conversion efficiency was dramatically enhanced in such tandem solar cells. The photo-stability investigation of cyanine solar cells showed that cyanine dyes were photostable when illuminated in the absence of oxygen and water vapor. We found that the initial degradation of cyanine dye devices during operation was due to the photo-polymerization of the widely used electron acceptor material fullerene $C_{60}$ and photo-chromism of the hole extraction interfacial layer molybdenum oxide ($MoO_3$).

**Keywords**: organic photovoltaics, photodetectors, transparent, tandem solar cells, stability, cyanine dye, power conversion efficiency

# Résumé

Grâce à leur flexibilité mécanique, leur poids léger ainsi que la possibilité de fabrication par des processus dits de rouleau à rouleau, les semiconductors organiques offrent de nombreux avantages dans des applications jadis réservées aux semiconducteurs inorganiques. Dans les semiconducteurs organiques, les constituants moléculaires sont reliés entre eux par les forces de Van der Waals plutôt faibles, ce qui mène à des bandes électroniques étroites. Par ce fait, il est possible d'obtenir des spectres d'absorption étroits qui engendrent de nouvelles fonctionnalités. L'électronique organique transparente (EOT) constitue un exemple ou les dispositifs sont transparents à la lumière visible. Parmi d'autres dispositifs semiconducteurs, ceci permet de construire des cellules photovoltaïques et des senseurs qui absorbent uniquement la lumière ultraviolette et infrarouge en la convertissant en signal ou énergie électrique. L'EOT s'apprête également en tant qu'élément d'intégration parmi d'autres disipositifs électroniques.

Parmi les différents matériaux moléculaires, les cyanines sont des colorants qui se distinguent par une bande d'absorption étroite et intense montrant les coefficients d'extinction molaire les plus élevés. Le maximum de la bande d'absorption peut être facilement déplacé dans l'infrarouge proche en augmentant la longueur de la chaine polymethine. Les cyanines heptamethines (Cy7), par exemple, sont des candidats prometteurs pour fabriquer des films photoactifs transparents et non-colorés.

Dans le présent travail de thèse, des dispositifs OET à base de Cy7 tels que des cellules photovoltaïques transparentes et des photodétecteurs absorbant uniquement dans l'infrarouge proche ont été fabriqués avec succès. Afin d'optimiser ces dispositifs multicouches, plusieurs colorants cyanines, l'architécture des dispositifs ainsi que les interfaces ont été investigués. La simulation optique des structures à films minces ont permis d'analyser et de contrôler la performance des dispositifs. De plus, les cellules solaires transparentes dans le domaine visible, ont été intégrées dans des cellules tandem et à triple jonction. En combinant le matériau cyanine à faible bande interdite avec d'autres cyanines absorbant la lumière visible, le rendement énergétique a été grandement amélioré. L'étude de stabilité de cellules solaires à base de cyanines a démontré la photostabilité de ces matériaux en absence d'oxygène et de vapeur d'eau. Il a été mis en évidence que la dégradation initiale de ces dispositifs sous irradiation est due à la photopolymérisation de l'accepteur omniprésent $C_{60}$ ainsi qu'au photochromisme de la couche d'injection de trous à base d'oxyde de molybdène ($MoO_3$).

# Contents

# List of Figures

# List of Tables

# Chapter I. Introduction and state of the art

## 1. Motivation

One of the main goals of this thesis is to further explore the suitability of cyanine dyes as organic semiconductors in thin film devices. A particular focus is given to heptamethine cyanine dyes absorbing near infrared light and their use in transparent solar cells and photodiodes as well as in multijunction solar cells. Further emphasis is also given to the exploration of degradation mechanisms of cyanine solar cells.

Different NIR light absorbing dyes are used as electron donor materials combined with suitable transparent counter acceptors to fabricate organic photosensitive diodes such as organic solar cells or organic photodetectors. Physical and optical characterizations guide the optimization in order to achieve highly transparent and efficient devices. For the fabrication of transparent and color free optoelectronic devices, the ideal photoactive layer materials for both the electron donor and electron acceptor have a strong absorption in the UV and NIR spectral range but do not absorb visible light. Due to their outstanding photophysical properties, cyanine dyes prove to be ideal candidates as colorless photoactive layer materials. These dyes are characterized by sharp, intense absorption bands with very high molar extinction coefficients reaching $3 \times 10^5$ L·mol$^{-1}$cm$^{-1}$, and the absorption peaks can be tuned into the NIR wavelength region by increasing the length of the conjugated polymethine chain, such as in heptamethine cyanine (Cy7) dyes.

Tandem devices will be the "Holy Grail". The devices fabricated in this thesis by using heptamethine dyes as low band-gap materials to absorb near infrared light and combining them with cells which absorb visible light, for example trimethine cyanine dyes (Cy3) and pentamethine cyanine (Cy5) dyes, thereby harvesting more sunlight and improving power conversion efficiency. The study of the long term stability of organic solar cells using cyanine dyes is an important objective of this thesis. This study shall provide crucial information on the suitability of cyanine solid films in optoelectronic devices.

## 2. Opportunities and challenges

As industrial development and population in the world is growing fast, energy consumption and supply is humanity's most serious problem for the next 50 years. Most of global concerns have been focused on the development and applications of renewable and sustainable energy technologies which are based on affordable, inexhaustible and environmentally safe resources

to replace the traditional fossil fuels in power generation, transporting and heating. Some clean energy sources in terms of sunlight, wind, water, geothermal and biomass have been realized in the last decades and will continue to be invested in the transition to a cleaner and more secure energy future.

## 2.1 Solar energy

Solar energy is the most abundant source of renewable power from nature and has the potential to meet almost all of mankind's energy needs. At the surface of the Sun, the power of solar radiation is $\sim 6.33 \times 10^7$ W/m$^2$, the yearly average radiation intensity falling on the surface of the planet is $\sim 1360$ W/m$^2$. When extrapolated to half the surface of our planet, this amount goes up to a gigantic energy input of $1560 \times 10^{15}$ kWh/year, which is about twice as much as will ever be obtained from all of the other non-renewable resources on earth such as coal, oil and natural gas. Put in other words, the yearly solar irradiation meets existing global energy needs 10000 times over [1].

### 2.1.1 Solar technologies

Solar technologies are ways used to directly or indirectly harvest the solar energy and make it useable for mankind. Some technologies have been exploited by human beings since a very long time ago in the field of architecture, agriculture and transportation. According to the ways how sunlight is converted and used, the solar technologies can be classified in different types:

- solar thermal collectors that collect heat by absorbing sunlight for heating or water warming
- solar heaters that use solar energy to distill water, make biologically-contaminated water safe to drink or to cook food
- solar reactors that convert solar energy into storable and transportable fuels through photo induced chemical or thermal reactions
- solar cells that convert sunlight into electricity using the photovoltaic effect

### 2.1.2 Solar cells

Only a long time after the first discovery of photovoltaic effect by Alexandre Edmond Becquerel in 1839 [2], solar cells have started to attract the attention of the scientific community, a major achievement being the demonstration of an efficient crystalline silicon solar cell by D.

D. M. Chapin, C. S. Fuller and G. L. Pearson in 1954 [3]. It is only during the last decades, that photovoltaic technology has experienced a massive industrial development. Up to now, many types of solar cells have been invented, produced and commercialized. It is common to classify these different approaches into three categories.

*2.1.2.1 Photovoltaic technology generations*

***First generation***: silicon wafer solar cells, which are made of different crystalline silicon wafers such as mono-crystal silicon (mc-Si), poly-crystal silicon (pc-Si) and ribbon and sheer defined film growth silicon (ribbon/sheet c-Si). The thicknesses of the silicon layers are typically ~200 micrometers. These technologies have been developed for more than 50 years and are the most mature technologies dominating the present market with a share of 80% [1]. Even though silicon is the second most abundant element on earth, the expensive processing cost for crystallizing silicon limits the cost reduction potential.

***Second generation***: thin film solar cells, which are made by depositing thin layers of photosensitive materials such as polycrystalline Cu (In, Ga) Se$_2$ (CIGS), CdTe, amorphous silicon (a-Si) and related materials on back substrates. Because these materials show high absorption coefficients, active layer thicknesses in the order of ~2 micrometers are needed to absorb enough solar light. The back substrates can be chosen between low-cost rigid glasses and flexible plastic films. This opens more application areas for thin film technologies.

***Third generation***: these are the emerging technologies based on some new concepts, for example; dye sensitized solar cells (DSSC), quantum dot solar cells (QDSC), perovskite cells, ultra-low-cost inorganic solar cells and organic photovoltaics (OPVs). Due to the potential of flexibility, light weight and cost-effectiveness, these concepts have attracted more and more attention in the last decade. However, some challenges are still existing related to the problem of low performance and stability.

*2.1.2.2 Photovoltaic efficiency*

The cell efficiencies including the best research cells [4] and market modules [1, 5] for all types of devices are listed in Table 1-1.

Table 1- 1 Best efficiencies of research solar cells and modules

| | *mc-S* | *pc-Si* | *a-Si* | *CIGS* | *CdTe* | *DSSC* | *QDSC* | *Perovskite* | *OPV* |
|---|---|---|---|---|---|---|---|---|---|
| Research cells | 25% | 20.4% | 13.4% | 21.7% | 21.0% | 11.9% | 9.2% | 20.1% | 11.1% |
| Modules | 14-20% | 13-15% | 4-7% | 12-14% | 11-12% | 5-8% | | 8-13% | 5-7% |

## 2.2 Opportunities for OPVs

Most of commercially available solar cells are made from refined, highly purified silicon crystals. The high cost of these inorganic silicon solar cells and their complex production processes have generated considerable interest in developing alternative photovoltaic technologies. As one of the alternatives, OPVs have attracted much research interest as is demonstrated by the tremendous increase in the number of scientific publications over the last decade. OPVs have been suggested to be used in many application areas including low-power consumer electronics such as mobile phone rechargers, lighting applications and self-powered displays, outdoor recreational applications and built-in photovoltaics.

### 2.2.1 Advantages of OPVs

Due to high absorption coefficients, organic materials with layer thicknesses in the range of ~100 nm can absorb enough sunlight for power generation. In addition, since device fabrication utilizes low temperature processes, flexible plastic substrates can be used for OPVs to be made lightweight and flexible.

The energy generation cost is the most critical aspect of a given PV technology. It largely determines the market demand and penetration. Levelised electricity cost (*LEC*) is a standard basis for comparing different electricity generation cost, and is defined as the ratio of total electrical energy production cost to total electrical energy output. The introduction of high throughput mass production via roll-to-roll (R2R) technology using solution processable OPVs is crucial for reducing the fabrication cost. Assuming a 1kWp system containing OPV modules with 7% efficiency and a lifetime of 5 years, the *LEC* is estimated between 0.19 and 0.5 €/KWh [6]. By using commercial scale OPV specific costs as the basis, as calculated by C. J. Mulligan *et al*. [7], lower *LEC* of 0.20 $/kWh or 0.13 $/kWh can be achieved for OPV efficiencies and lifetimes of 3% and three years, respectively, or 5% and five years, respectively. These prices are competitive with traditional silicon wafer and thin film modules whose *LEC*s are in the range of 0.16–0.29 $/kWh [7] even if the efficiencies of OPV devices up to now are quite low. The OPV systems will become economically viable and sustainable if the efficiency and lifetime can be further enhanced.

### 2.2.2 Status of OPVs

As a relatively new technology, OPV does not match the performance of established solar technologies in terms of efficiency and lifetime. However, performance has risen rapidly in

the recent years. Heliatek and Mitsubishi Chemical Corp have announced OPV power conversion efficiency of 12% [8] and 11.1% [9] without revealing the employed organic materials. In the academic community, record efficiencies of 10.8 % [10] for single junction devices, 10.6% [11] for tandem devices and 11.5 % [12] for triple junction devices have been reported respectively. The sizes of all lab-scale devices are small, therefore efforts have also been put into the upscaling of OPV devices. Toshiba company has announced a large OPV module with area of 20×20 cm$^2$ and a power conversion efficiency up to 6.8% [5].

In addition to the pursuit of high device efficiency, solar cells have also been intensively investigated for their potential in unique applications. Narrow absorption spectra in organic semiconductors are fundamentally different from the very broad absorption bands of their inorganic counterparts. Therefore, OPVs are considered to have important advantages for the development of truly transparent solar cells (TSCs). TSCs have been proposed for large scale applications such as power-generating windows which provide sun shading at the same time, building integrated photovoltaics, integrated PV chargers for portable electronics and as low band-gap materials in tandem solar cells [13].

### 2.2.3 Transparent devices

Previous efforts to construct transparent solar cells have been focused on using thin active layers with absorption in the visible wavelength range combined with non-reflecting conductors. This has allowed for the fabrication of semitransparent cells since not all of the incoming light is absorbed by the active layer. However, these cells are limited by either a low transmittance or a low efficiency because of the tradeoff between harvesting photons and transparency.

*2.2.3.1 Fabrication of transparent solar cells*

To make a highly transparent and efficient solar cell, the absorption of active layers should be tuned to the UV [14] or NIR spectral region [13] as shown in Figure 1-1. Besides finding the right visible transparent photoactive materials, all the other components have to be equally transparent, especially electrodes, which should not only be transparent in the desired wavelength region but also highly conductive and easy to process. Transparent conductors have been widely investigated due to the multitudes of applications for solar energy utilization, for instance a single layer of PEODT: PSS or PEDOT:PSS with Ag grid [15], indium tin oxide (ITO) [16, 17], a single graphene layer [18] and dielectric / metal / dielectric (DMD) structures of $MoO_3/Ag/MoO_3$ [19], $WoO_3/Ag/WoO_3$ [20], $BCP/Ag/MoO_3$ [21] and $MoO_3/Ag/V_2O_5$ [22].
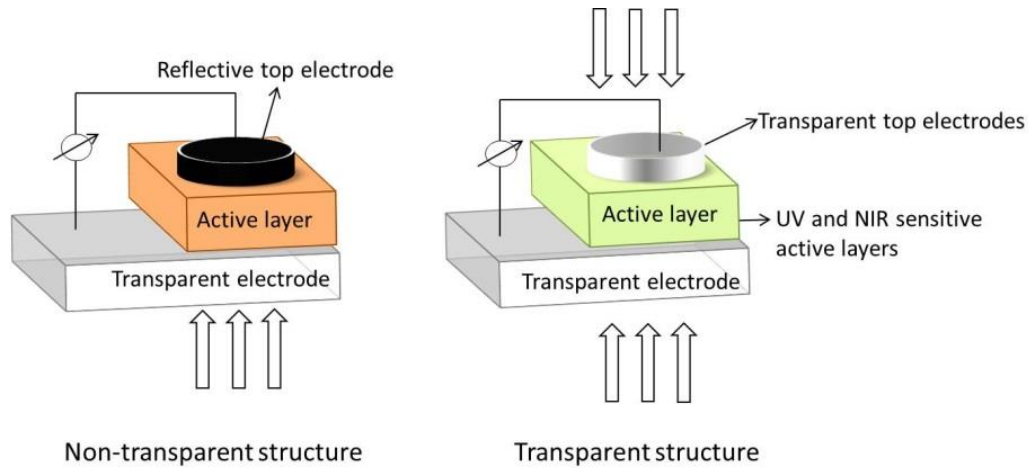
Figure 1- 1 Comparison of transparent and non-transparent OPVs

*2.2.3.2 Characterizations of transparent devices*

In many applications, for example, the integration of transparent devices with other electronic devices, power generating windows used in automobiles and architectural installation, optical properties of the transparent devices in terms of transparency, color appearance and color rendering are typically required. These parameters need to be balanced which is a demanding task.

***Average visible transmittance (AVT)***: AVT is the mean value of the experimentally measured transmittance spectrum $T(\lambda)$ in the visible light wavelength region $[\lambda_1, \lambda_2]$.

$$AVT = \frac{\int_{\lambda_1}^{\lambda_2} I_{sun}(\lambda) \times T(\lambda) d\lambda}{\int_{\lambda_1}^{\lambda_2} I_{sun}(\lambda) d\lambda} \times 100\%$$

***Human eye perception of transmittance (HPT)***: Human eye perception of brightness is spectrally dependent. Therefore the radiometric measurement of light intensity does not reflect the intensity perceived by the human eye, which causes differences between *HPT* and *AVT*. The *HPT* of a transparent device can be calculated by using the eye sensitivity function $\bar{y}(\lambda)$ to normalize the measured transmittance spectrum $T(\lambda)$ in the visible light region [23].

$$HPT = \frac{\int_{\lambda_1}^{\lambda_2} I_{sun}(\lambda) \times \bar{y}(\lambda) \times T(\lambda) d\lambda}{\int_{\lambda_1}^{\lambda_2} I_{sun}(\lambda) \times T(\lambda) d\lambda} \times 100\%$$

***Color appearances***: Color is a psychophysical interaction of human photoreceptor cells in the retina and the spectra of light reflected, transmitted or emitted from an object. As defined in the chromaticity diagram, colors can be represented numerically by their coordinates. The human eye contains three types of photoreceptor cells with different spectral sensitivities.

Color matching functions $\bar{x}(\lambda)$, $\bar{y}(\lambda)$ and $\bar{z}(\lambda)$, are the numerical description of the chromatic response of the averaged human eye as defined by international commission on illumination (CIE 1931). Given an object with reflected light spectrum $S(\lambda)$, its normalized color coordinates can be calculated as $(x, y)$:

$$x = \frac{\int_{\lambda_1}^{\lambda_2} S(\lambda) \times \bar{x}(\lambda) d\lambda}{\int_{\lambda_1}^{\lambda_2} S(\lambda) \times \bar{x}(\lambda) d\lambda + \int_{\lambda_1}^{\lambda_2} S(\lambda) \times \bar{y}(\lambda) d\lambda + \int_{\lambda_1}^{\lambda_2} S(\lambda) \times \bar{z}(\lambda) d\lambda}$$

$$y = \frac{\int_{\lambda_1}^{\lambda_2} S(\lambda) \times \bar{y}(\lambda) d\lambda}{\int_{\lambda_1}^{\lambda_2} S(\lambda) \times \bar{x}(\lambda) d\lambda + \int_{\lambda_1}^{\lambda_2} S(\lambda) \times \bar{y}(\lambda) d\lambda + \int_{\lambda_1}^{\lambda_2} S(\lambda) \times \bar{z}(\lambda) d\lambda}$$

This allows the corresponding color of this object to be identified in the CIE 1931 Chromaticity diagram. For analysing the colored or transparent organic devices, the folding of the transmittance spectra $T(\lambda)$ of the designed devices with the AM1.5 sunlight spectrum $I(\lambda)$ can be used as investigated light spectra to quantify the color coordinates of the devices, where $S(\lambda)=I(\lambda)T(\lambda)$.

***Color rendering index (CRI)***: Color is not an intrinsic property of an object and depends on illumination condition. The human color perception system is able to distinguish those deviations caused by varying light source conditions. A good indoor light source should ensure that the perception of colors of objects does not deviate from the colors under sunlight illumination. When transparent devices are integrated in automobile windshields or household glass panes, the rendering property of the transmitted light through the windows is of interest. *CRI* defines how well colors under these light conditions are rendered. It is usually analysed by the test sample method, comparing the color differences of 8 defined standard testing samples [24] under reference light condition and testing light condition [25]. The testing light sources are the folding of the measured devices' transmittance spectra with standard AM1.5 sunlight spectrum. The reference light is chosen to be either a blackbody irradiator if correlated color temperatures (*CCT*) of the testing light sources are smaller than 5000 K or some other CIE standard illuminants if *CCT* > 5000 K. The *CCT* can be estimated by using McCamy's approximation algorithm [26]. Only if the distance of the CIE 1965 UCS color coordinates of the testing light sources to the blackbody locus lies within 0.0054, the *CCT* is meaningful. However, in many cases the distance is slightly out of the recommended range. Nevertheless this procedure is still followed because no other method can be used to analyse the *CRI* [25, 27]. Special *CRI* represents deviations of each standard testing color between testing light and reference light condition. General *CRI* is the mean value of the eight special *CRI*s. By defini-

tion, the *CRI* can range from 0 to 100 where a higher value represents a better color rendering capacity.

## 2.3 Challenges for OPVs

The efficiency of OPVs has doubled in the last decade from 5% to over 10%. Two main factors that still limit the commercialization of OPVs are the problems of long-term stability and mass production.

### 2.3.1 Stability

Mechanisms of the degradation in OPVs are diverse, complicated and only poorly understood so far. Many factors can induce cell degradation, such as the penetration of water or oxygen into the devices, heat-induced chemical reactions or photo-decomposition of active layers. The degradation phenomena can occur at various parts of the devices, in each layer or at each interface between any two layers.

#### 2.3.1.1 Water and oxygen induced degradation

OPV devices degrade much faster when exposed to ambient environment when stored in a glove box in the absence of water and oxygen. This is particularly true under light illumination. The reason for this significant degradation has been attributed to the penetration of water and oxygen into the devices which can induce exciton quenching, oxidation of organic active materials and inorganic oxides or lead to the corrosion of metal electrodes.

As have been found that the main entrances for the penetration of water and oxygen into devices are microscopic pinholes and grains in thermally evaporated metal electrodes [28]. Low work function electrodes such as Al and Ca are highly reactive. They are easy to be oxidized in the presence of water and oxygen. The formed metal oxides and hydroxides especially at the organic/metal interfaces are electrically insulating and act as charge transport barriers. The latter are detrimental for charge collection and can cause reduction in the fill factor [29]. High work function metals such as Ag and Au can be used to avoid this problem because they are less reactive and refractory against the degradation induced by water and oxygen.

As has been demonstrated by F. C. Krebs *et al.* [30] water and oxygen diffuse continuously throughout all active layers in the devices down to the bottom electrode. When oxygen molecules penetrate into the light absorbing organic material, energy transfer between the organic semiconductor and oxygen can produce reactive oxygen singlet species that destructively react with the semiconductor. Also, electron transfer to oxygen forming the superoxide anion

can compete with the desired electron transfer reaction from donor to acceptor leading to a significant reduction in quantum efficiency and further irreversible reaction of the oxygen radical. Some useful relationship between the active materials' photo-oxidation and the devices' operation time has been found by K. Norrman *et al.* [31] and M. Hermenau *et al.* [32]. Therefore, lowering the frontier orbitals of the active materials to reduce electron transfer to oxygen would in principal enhance the environmental stability of OPV devices.

The bottom transparent electrodes usually made of ITO are also not stable against water and oxygen. As investigated by F.C. Krebs *et al*. [30], the $In^+$ ions can diffuse throughout all device layers. These phenomena have already been documented in organic light emitting devices, being strongly related to OPVs in this respect.

In order to reduce the penetration of water and oxygen, some air stable active materials [33] and buffer layers are introduced in the devices, but these are not sufficient to prevent the degradation [34]. It is obvious that in real applications the OPV devices need to be well encapsulated. The water and oxygen transmission rate should be kept below $10^{-3}$ g m$^{-2}$ day$^{-1}$ and $10^{-3}$ cm$^3$ m$^{-2}$ day$^{-1}$, respectively, for OPV devices to survive several years [34]. Some methods have been investigated, for example, another layer of glass [35] is glued, metal oxides (such as $Al_2O_3$ [36, 37]) are thermal deposited, nanocomposite solutions are spin coated [38] or flexible plastic barriers (such as PET [39] and PEN [40]) are laminated on top of the devices. A good encapsulation simultaneously enhances the mechanical stability and filters some harmful UV light. Whatever type of barrier is being used, it is very important that the barrier substrate is flexible enough for R2R manufacturing and retains its barrier property after the manufacturing process.

### 2.3.1.2 Photo-induced degradation

Double bonds in conjugated organic semiconductors undergo many photochemical reactions. By absorbing light, the molecules are excited to excited states whose chemical and physical properties differ greatly from the original states. These excited species can fall apart or combine with each other and hence induce decomposition or polymerization reactions. The reaction rate is dependent on the oxygen concentration, light intensity, temperature, humidity of the environment and optical properties of the organic molecules.

For example, the most often used electron donors in the early stage, poly-phenylenevinylene (PPV) type polymers showed rapid loss of the ether functions and double bonds [41] under UV light irradiation. As summarized by Manceau *et al*. [42] long side chains, exocyclic double bonds, cleavable bonds and moieties containing a quaternary site in the main backbones of

organic semiconductors resulted in poorly stable materials. The elimination of these chains can significantly improve their photochemical stability, for example, when the long hexyl side chains were removed from poly [3-hexylthiophene] (P3HT) to form polythiophene (PT), the degradation rate was decreased by one order of magnitude [43].

The most efficient acceptors, fullerene $C_{60}$ and derivatives thereof are also not stable under light illumination. When the $C_{60}$ molecules are excited from the ground state to the excited singlet state by photons, they can either return to the ground state by radiative recombination with low quantum yields of around ~0.07% [44] or decay through very fast intersystem crossing in 1 ps [45] to the triplet state with nearly 100% efficiency. Triplet state excitons are relatively long-lived with lifetimes up to ~50 ms [46] and can either return to the ground state or react with another neighboring photo-excited triplet state $C_{60}$ molecule [47] other than ground state $C_{60}$ monomer [48, 49] in a 2+2 cyclo-addition reaction. The degradation of solar cells using fullerene as acceptors has been recently correlated to the photochemical reactions of $C_{60}$, more details will be discussed in Chapter V.

As studied by S. Scholz *et al.* [50], photochemical reactions were also observed in some frequently used electron conductive materials like bathocuproine (BCP), 4,7-diphenyl-1,10-phenanthroline (BPhen) and tris(8-hydroxyquinolinato)-aluminum ($Alq_3$) under UV light irradiation. However, some other materials in terms of N,N,N',N'-Tetrakis (4-methoxyphenyl) benzidine (MeO-TPD) as we used in cyanine photodetectors in Chapter III and 2,2',7,7'-Tetrakis (N,N-diphenylamino)-9,9-spirobifluorene (Spiro-TAD) as widely used in perovskite cells have shown very good photo stability due to their high vibrational degrees of freedom [50].

As has been found, some hole or electron transporting oxides such as $MoO_3$ [51], $WO_3$ [52] and $TiO_2$ [53] suffer from pronounced photochemical reactions. Due to the presence of oxygen vacancy defects, these oxides tend to be n-type doped wide bandgap semiconductors which can be excited by high energy UV light. The photo-excitation changes the optical absoption of oxide films and turns the oxides from transparent to colored materials, which is the so-called photo-chromic effect [51]. The colored films can act as light filters and cause a reduction in photocurrents when used in OPV devices. The influence of the photochromism of the frequently used $MoO_3$ on the stability of OPVs will be disscussed in Chapter V.

### 2.3.1.3 Heat induced degradation

In solar cells, interface nanostructures of any two adjacent layers are critically important parameters for exciton generation and dissociation [54, 55]. Particularly in bulk heterojunction

solar cells, the phases of donors and acceptors should form a bicontinuous network to achieve high performance. Any morphology changes at the interface will cause variations in the performance and influence the stability of the solar cells. As far as solution processed solar cells are concerned, glass transition temperatures of commonly used organic semiconductors are low and their morphological structures are thermally dynamic. Solar cells can be heated up to 80°C when exposed to the full sun, this is high enough to induce rearrangement of active molecules and cause morphology changes.

In order to enhance the thermal stability of the morphology and consequently the stability of device performance, some methods based on chemical modifications of the molecular structures have been suggested. Some reactive side chains such as azide [56], alkyl halide [57] are added on the backbone of molecules which can react with other counterpart materials and form chemically bonded donor-acceptor structures, the interfaces between donors and acceptors are well controlled. Or some cleavable side chains such as carboxylic acid groups, which can increase the solubility of the materials and be removed by heating after the film formation, can be grafted on the molecules. The glass transition temperature of the solid films can be increased such that the films are mechanically rigid against thermal dynamics. Both concepts have been proven to be good solutions to enhance the morphological stability and long term stability of organic solar cells.

### 2.3.1.4 Investigation of OPV degradation

To study the long term durability of OPV devices, degradation processes need to be accelerated at reasonable rates. Parameters that affect the lifetime of OPVs such as temperature, light intensity, atmospheric conditions can be varied to accelerate the processes.

As studied by O. Haillant *et al*. [58], the degradation rates show temperature dependence and follow the Arrhenius equation,

$$k = A \cdot exp(-\frac{E_a}{RT})$$

Where $E_a$ is the activation energy for the process and $R$ is the gas constant. The acceleration factor *AF* can then be expressed by considering different temperatures ($T_1$, $T_2$) and light intensities ($I_1$, $I_2$):

$$AF = (\frac{I_1}{I_2}) \cdot exp\left[\frac{E_a}{R}(\frac{1}{T_2} - \frac{1}{T_1})\right]$$

Using this equation, the acceleration factor can be calculated and the lifetime at another temperature or light intensity can be predicted.

The atmospheric condition including oxygen concentration and humidity is also important for studying the factors causing degradation. For regular P3HT: PCBM solar cells, the device showed a significantly different degradation rate when exposed to vacuum, nitrogen or oxygen environment [59] as well as different relative humidity [60].

Since degradation mechanisms of OPV devices are complex, different lifetimes for similar devices have been reported from lab to lab and are not comparative. Some standard procedures to measure the lifetime have been established recently [61], where the light source, temperature, humidity and environmental conditions for the study of degradation are well defined.

### 2.3.2 Upscaling

OPV devices reported in the literatures generally have small active device area ($< 1$ cm$^2$). In real applications, the devices need to be up scaled and connected in series and parallel to form OPV modules. R2R processes are the fastest technologies used to fabricate homogenous thin films in traditional industries, and they can be adapted with different coating and printing methods for large scale OPV fabrication.

OPV devices are composed of multiple layers with different functionalities, for example, organic active layers used to absorb light and metal electrodes used to collect charges. Technologies required for the deposition of each layer are different. Spin coating of organic materials and high vacuum deposition of metal electrodes are the most frequently used technologies for the fabrication of lab-scale devices. Those methods are not suitable to be integrated in high speed R2R processes, because a large fraction of materials are wasted during the deposition process and the generation of high vacuum is time consuming. Some other technologies for the film preparation, which are compatible with R2R procedures, are required.

*2.3.2.1 Thin film deposition methods*

Many thin film preparation methods in the market such as slot-die coating, blade coating, spray coating, screen printing, inkjet printing, gravure printing and others, can be implemented in R2R processes. Working principles of these deposition methods are demonstrated in Figure 1-2.
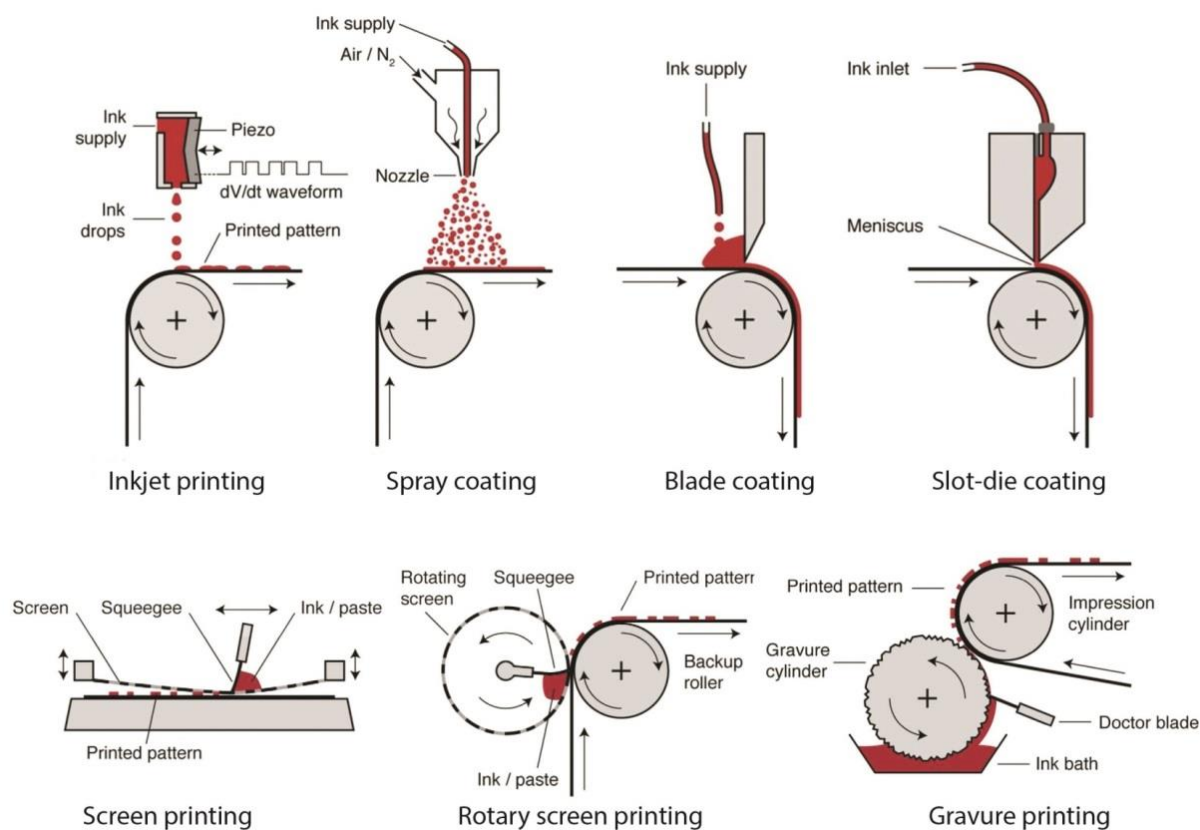
Figure 1- 2 Schematic illustration of inkjet printing, spray coating, blade coating, slot-die coating, screen printing and gravure printing adapted from [62]

The choice among different depositing methods is depending on the requirements of solution viscosity, substrate's surface energy, layer uniformity and thickness, possibility also pattern-ing and throughput speed. Properties and requirements of these technologies [62] are listed in the following Table 1-2.

Table 1- 2 Properties, requirements and challenges of different coating and printing methods

| Methods | Pattern | Viscosity mP·S | Speed m/min | Thickness accuracy | Challenges |
|---------|---------|----------------|-------------|--------------------|------------|
| Slot-die coating | Stripes | <10000 | 0.1-200 | Very good | Deweting on some substrates |
| Blade coating | Not possible | <1000 | 0.1-200 | Good | Deweting on some substrates |
| Spray coating | Low resolution | <40 | | Low | Contamination of equipment |
| Screen printing | Well defined | 50-50000 | Rotary >100 Flat <35 | Moderate | Screens are hard to clean |
| Inkjet printing | High resolution | <40 | <75 | Good | Complex, hard to optimize |
| Gravure printing | Well defined | 15-500 | 900 | Good | Long time needed to engrave gravure |

*2.3.2.2 Transparent electrodes and flexible substrates*

In addition, solution processable transparent electrodes and flexible substrates are the other key factors for the application of R2R in OPV mass productions.

***Transparent electrodes***: ITO is currently used as transparent top electrode in OPVs, which is deposited in vacuum. The high cost and limited supply of indium together with the requirement of costly deposition methods will increase the price of OPV production. Alternatives to replace ITO substrates have been developed, to be compatible with R2R manufacturing processes. These electrodes should be solution processable, flexible, conductive and transparent. Some progresses have been made by the introduction of metal nanowires [63, 64, 65], carbon nanotubes [66], graphene [67], metal grids [68], modified PEDOT:PSS [69] and DMD structure layers [19, 20, 21, 22].

***Flexible substrates***: Substrates for R2R processes should be flexible, and as barrier substrates they should be able to prevent the penetration of water and oxygen into the devices, high resistant against any chemicals used during processing and withstand thermal and mechanical loads. Two main substrates such as stainless steel and plastic foils made of polymers such as polyethylene terephthalate (PET) and polyethylene naphthalate (PEN) *etc*. [70] are developed and their properties are listed in Table 1-3.

Table 1- 3 Comparison of metal foil substrates with plastic foils

| *Flexible substrates* | *Properties* |
|---|---|
| Metal foils | Advantages: high process temperature capability, excellent barrier properties against water and oxygen, high resistance to corrosion |
| | Disadvantages: non-transparent, rough surface, conductive |
| Plastic foils | Advantages: highly transparent, cheap, R2R compatible |
| | Disadvantages: limited process temperature capability, water and oxygen permeable, low mechanical stability |

# 3. NIR absorbing organic semiconductors

## 3.1 Organic semiconductors

Organic semiconductors are composed of conjugated systems with alternatively connected single and double bonds. A conjugated system has a region of overlapping $\pi$-orbitals with delocalized electrons bridging the inter-adjacent single bonds. Delocalized electrons are free to

move and capable of receiving energy from an applied field, they are typically contained within bonding levels that are shared by several neighboring atoms and can be found in conjugated systems and meso-ionic compounds. The electrical conductivity of the organic semiconductors is arising from the presence of delocalized electrons and the possibility to hop from one delocalized molecule or molecular assembly to another.

In the photovoltaic process, electrons need to be promoted from the highest occupied molecular orbitals (HOMO) to the lowest unoccupied molecular orbitals (LUMO) by gaining energy from absorbing either phonons or photons. The bandgap energy of a semiconductor is the specific minimum amount of energy required for the transition. It is an intrinsic property of a semiconductor and differs with different materials. Semiconducting molecules with bandgaps lower than 1.5 eV are typically considered as low-bandgap semiconductors.

## 3.2 NIR absorbing organic semiconductors

NIR absorbing organic materials are low bandgap materials. The development of NIR absorbing materials is driven by the diverse and extensive applications in a number of technological sectors, for example, they can be used as heat filters to absorb NIR light, photosensitizers for photodynamic therapy, tags for bio-imaging and donors in OPVs.

By integrating the photon flux of standard one sun AM1.5G spectrum as shown in Figure 1-3, 5%, 23% and 31% of the solar photons are in the UV (300-450 nm), visible (450-670nm, defined for photopic responses >5% peak sensitivity) and NIR (670-1000 nm)  region, respectively. In order for photovoltaic devices to capture more solar energy over the whole solar spectral range, low bandgap materials are usually used as donor materials in the devices to extend the absorption range into the NIR light region.
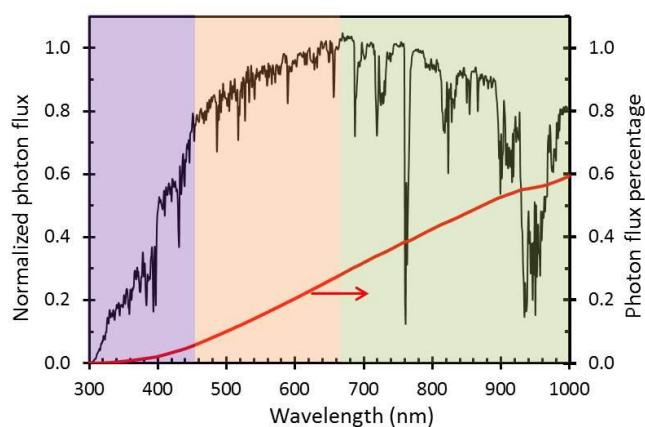


Figure 1- 3 Normalized photon flux of AM1.5G spectrum and integrated photon flux percentage

**3.2.1 Tuning the bandgap**

In particular, tuning HOMO-LUMO level positions and thereby the bandgap energy of materials is of great importance for obtaining organic semiconductors that absorb light in the NIR region. In order to reduce the bandgaps, π-electrons must be effectively delocalized along the conjugated backbones. Various approaches can be carried out to achieve low bandgap molecules, for instance the synthesis of donor-acceptor (D-A) systems, exploiting substituent effects or by extending the π-conjugation length.

*3.2.1.1 Donor-Acceptor systems*

Alternation of electron donor and acceptor units in the conjugated molecular backbone is one of the design criteria to obtain low bandgap semiconductors. In D-A systems, the hybridization between donor and acceptor moieties raise HOMO levels of donors to higher positions and lower LUMO levels of acceptors to lower positions. Intramolecular charge transfer from the higher HOMO level to the lower LUMO level leads to a reduction in binding energy [71]. This can be represented by the appearance of a resonace structure in alternative D-A systems: D-A and $D^+ \leftrightarrow A^-$ [72] can improve double bond character between the repeating units and result in a suppression of the Peierls distortion and hence reduce the bandgap [73].

*3.2.1.2 Substituent effects*

The bandgaps of organic semiconductors can be tuned by replacing some atoms or groups with other specific substituents. The introduction of electron donating groups or electron withdrawing groups in the conjugated backbone reduces the bandgap by raising the energetic position of the HOMO or lowering the energetic position of the LUMO, respectively. For example, using electron-withdrawing element fluorine to replace hydrogen in thienothiophene and benzodithiophene units, LUMO levels of the molecules were lowered approximately by 0.1 eV per fluorine [74]. Side chains of alkyl groups were substituted by more electron-donating alkoxy groups and the HOMO energy levels of the molecules were raised by 0.1 eV [75].

*3.2.1.3 Conjugation length*

It has been found in conjugated systems, that the bandgap varies with the number of repeating units in the backbone [76]. Prolonging π-conjugation length can reduce the bandgap of semiconductors, but when torsions in the molecular backbones start to disturb the conjugation, the bandgap starts to increase. Tuning the conjugation length, which is widely used in cyanine

dyes, is an easy and effective way to modify the electronic properties of the organic semiconductors.

### 3.2.1.4 Other effects

Besides the strategies mentioned above, several other factors can influence energetic properties of the conjugated molecules: space effects play important roles in changing the interactions of electronic orbitals of donors and acceptors. Additional large aromatic or heteroaromatic rings fused to backbones can enhance delocalization degree of π-electrons in the conjugated compounds and result in a reduction of the bandgap. Some heavier atoms can be introduced in the molecular structures to lower the bandgaps due to polar effects. Taking copper phthalocyanine dyes as example, replacing the central copper atoms by heavier Tin atoms leads to a reduction of the bandgap by 0.5 eV [77]. Furthermore, organic semiconductors are found to have a narrower bandgap in solid state as compared to the solvated molecules in solution due to the well-ordered structures and strong intermolecular interactions.

### 3.2.2 NIR absorbing small molecules

Compared with polymer semiconductors, small molecular semiconductors combine easy tunability of the absorption to a specific wavelength region and reproducible properties from batch to batch with well-defined chemical structures and high purity. Some small molecules such as phthalocyanines, porphyrins, squaraines and cyanines have been shown with good absorption in the NIR region. In this section, properties and applications of these dyes will be demonstrated and discussed.
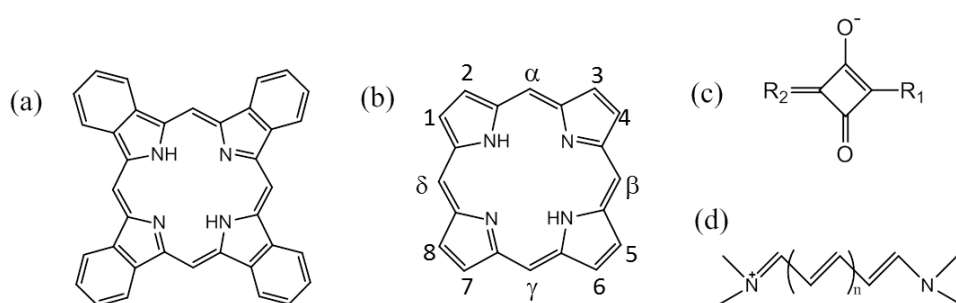


Figure 1- 4 Molecular structures of (a) phthalocyanine, (b) porphyrin, (c) squaraine and (d) cyanine

### 3.2.2.1 Phthalocyanines and porphyrins

Phthalocyanines and porphyrins are cyclic macromolecules, four isoindole or pyrrole units, respectively, linked to form a 16-membered fused backbone ring by alternating carbon and ni-

trogen atoms. The molecular center consists of two hydrogen atoms which are likely replaced by some covalent metals inwardly projecting nitrogen atoms. The absorption peaks of unsubstituted porphyrins and phthalocyanines are at around 450 nm and 620 nm, respectively [78, 79]. Their optical properties can be tailored by using different center atoms. It has been found that the heavier the substituted elements are, the more the absorption peaks shift toward the NIR region.

Many phthalocyanine derivatives, for example, CuPc [80, 81], SnPc [77, 82], TiOPc [83], ClInPc [83], ClAlPc [84] and so on, have been previously shown to have excellent absorptivity in the NIR region and good overall photoelectrical activities. The other type of phthalocyanine derivatives, naphthalocyanines show extremely high absorption coefficients in the wavelength region of 1000 nm [85]. Compared with porphyrins, phthalocyanines exhibit broader absorption spectral range, higher charge mobility and longer exciton diffusion length due to their highly planar molecular structure that packs more closely, resulting in an increased crystallinity and thereby allowing for much stronger intramolecular electronic interactions. Together with these advantages, phthalocyanines are widely investigated in the field of OPVs, DSSC, transistors and sensors [86].

Four meso and eight β positions on the porphyrin ring are reactive and can be functionalized to tune the optical properties [87]. Introducing conjugated D-A systems in porphyrin small molecules can facilitate the intramolecular charge transportation, and the modified materials are prospective dyes showing very strong and broad absorptions in the NIR region [88]. The dimerization of metallated porphyrins can extend the absorption peaks further to wavelengths >1500 nm [89]. Inspired by the efficient energy transfer in naturally occurring photosynthetic reaction centers, NIR absorbing porphyrin dyes are excellent candidates to promote the efficiency if suitable structural modifications and procedures are applied.

### 3.2.2.2 Squaraine dyes

Squaraine dyes belong to the class of polymethine dyes and are characterized by their unique aromatic four membered ring systems. They show similar intense and sharp absorption or emission in the visible-near infrared region as do cyanine compounds, with the difference of being electrically neutral [90]. Squaraines are synthesized by reactions of two electron rich precursors with squaric acids. By using equivalent or different precursors, symmetric [91, 92] and non-symmetric dyes can be synthesized, respectively [93]. Most of squaraine dyes are encumbered by nucleophilic attack of the central four membered ring, which is highly electron deficient. Their optical and physical properties can be tuned by attaching different side chains

[94]. The most notable feature of squaraine dyes is their solubility in low polarity solvents and good phase separation with fullerene derivatives allowing the formation of bulk heterojunctions [95]. Self-assembly of squaraine molecules into stable nanocrystalline structures by thermal annealing results in relatively high charge carrier mobility and extended exciton diffusion length. These factors are beneficial in solar cells for charge separation and transport [96, 97].

*3.2.2.3 Others*

Some other small molecules and derivatives such as thiadiazoles [98], benzothiadiazole [99], and D-A systems by incorporating the latter groups or thiophene, pyrole among others also show good NIR absorbing properties.

## 3.3 Cyanine dyes

Cyanine dyes belong to the family of polymethine dyes. Two nitrogen centers are bonded together by alternating single and double bond conjugated chains with an odd number of methine groups and an even number of π-electrons. Due to the delocalization of the positive charge on one nitrogen atom, the chromophores are positively charged and accompanied by negatively charged counter ions. Cyanine dyes were originally synthesized and used as sensitizer in photographic emulsions to improve the sensitivity of silver halide grains one century ago. Recently, cyanine dyes have been intensively investigated in other application areas such as fluorescent labels, optical data storage and optoelectronic devices [100, 101].

### 3.3.1 Types of cyanine dyes

According to different nitrogen centers, cyanine dyes are classified into three types: streptocyanines, hemicyanines and closed chain cyanines.

In this work, we classified cyanine dyes according to the number of carbon atoms in the conjugated polymethine chains, for example, trimethine cyanine (Cy3) dyes, pentamethine cyanine (Cy5) dyes and heptamethine cyanine (Cy7) dyes.

When using different counter ions, cyanine dyes are indicated accordingly for example Cy-I, Cy-Cl, Cy-PF$_6$, Cy-ClO$_4$. It has been noted that the optical and electrical properties of cyanine chromophores are independent on the type of counter ion [102], but the influence of counter ions on the solubility and crystallinity cannot be neglected. Furthermore, if the counterions are redox active such as I⁻, exciton quenching readily occurs in the solid state.

### 3.3.2 Cyanine dye properties

Cyanine dyes are known for their unique properties such as high extinction coefficients and tunable maximum absorption peak, ionic effects and self-aggregation properties.

### *3.3.2.1 Optical properties*

Cyanine dyes are characterized by sharp absorption spectra and high absorption coefficients with maximum values in the order of $10^5$ L mol$^{-1}$ cm$^{-1}$. When forming solid films, this translates into absorption coefficients of up to $10^5$ cm$^{-1}$. The bandgaps of the cyanine dyes are tunable by changing the number of double bonds between nitrogen atoms in the conjugated backbones, their absorption peaks are red shifted by ~100 nm by adding one vinylene unit [103]. For example, bandgaps of Cy3 dyes, Cy5 dyes and Cy7 dyes are ~1.8 eV [104], ~1.4 eV [105] and ~1.2 eV, respectively [106].

### *3.3.2.2 Ionic effects*

The associated cationic cyanine molecules and counter ions can be separated in polar solvents and in the solid state. Mobile ions can diffuse or drift in an external electrical field to move within the cyanine layer or to adjacent non-ionic layers. This displacement establishes an internal electric field by the non-equilibrium ion distribution, which can facilitate charge transport processes in organic electronic devices and tune the photovoltaic characteristics [105, 107]. These ionic effects can be applied in some research fields, e.g. homojunction photovoltaic cells and light emitting electrochemical cells [108], where a single layer of ionic semiconductors is sandwiched between two electrodes. Upon applying an external bias voltage, anions separate from the cations and are driven to the anode side leaving an accumulation of cations at the cathode side. Thereby, regions close to the electrodes are then n-type or p-type doped, and p-n or p-i-n heterojunctions can be built. The formed heterojunction structures allow for charge separation occurring in one single layer. The simplified fabrication procedure of such device architecture is of great interest.

### *3.3.2.3 Self-aggregation*

Due to strong intermolecular van der Waals attractive forces between molecules, cyanine dyes easily self-assemble and form two types of aggregates: H-aggregates (H for hypsochromic) and bathochromic J-aggregates (J for Jelley [109]) by stacking parallel molecules plane-to-plane with a slipping angle of more than 32° (H-aggregation) or less than 32° (J-aggregation), respectively. High quality J-aggregates show an extremely narrow red shifted absorption peak.

Aggregation behavior of cyanine dyes have been widely investigated since their application as spectral sensitizers in the field of photography. Many technologies including different substrate surfaces [110, 111], matrices, and solvents were introduced to induce the formation of well-organized cyanine dye aggregates and to control the aggregate size, growth speed, reproducibility and durability.

### 3.3.3 NIR absorbing cyanine dyes

NIR absorbing cyanine dyes are achieved by increasing the number of vinylene units in polymethine chains to seven. Cy7 dyes show intensive and sharp absorptions in the NIR light region. Their absorption maxima can be fine-tuned by different substituent moieties. As studied by Q. Li *et al.* [112], the strength of the bathochromic shift induced by the substituents on the indolenium group is as follows: benzo- > methoxyl > $NO_2$- > methyl > chloro-.

As is well known, cyanine dyes suffer from some problems of photodegradation in the presence of oxygen [113, 114] due to the formation of both oxygen singlet species and superoxide anions [115]. It was found that the photofading effects increased with the increase of the central methine chain length. NIR light absorbing Cy7 dyes are less stable as compared with Cy3 and Cy5 dyes since the long conjugated chains are easier to be attacked by oxygen molecules. It is worthwhile to design cyanine dyes with good photostability. As studied by J. Li *et al.* [115] the photostability of cyanine dyes was enhanced significantly when cyclic units were introduced into the polymethine chains. And the introduction of some electron donating substituents on the nitrogen atoms or indoleninium fragments is favorable to obtain greater resistance against photobleaching [116].

Heptamethine cyanine dyes have recently been investigated in different types of organic electronic devices such as OPVs [106], DSSC [117] as well as tandem solar cells to provide organic semiconductors absorption in the NIR region which will be discussed in Chapter IV. As colorless photoactive materials absorbing in the NIR region, Cy7 dyes are promising candidates to produce transparent OPVs [106] and transparent photodetectors [118], more details will be found in Chapter II and Chapter III, respectively.

# 4. Organic tandem solar cells

## 4.1 Heterojunction

Unlike inorganic semiconductors where free charges are formed directly after light excitation, when organic semiconductors absorb photons with energy larger than their optical bandgaps,

electrons are excited from the HOMO level to the LUMO level. The excited electrons are still in the Columbic potential of the localized positively charged holes and form so called excitons, electron-hole pairs with binding energy above 0.1 eV. These bonded excitons have to overcome the binding energy in order to dissociate into free electrons and holes. So a driving force greater than the binding energy is required to dissociate excitons in organic semiconductors. The realization of a heterojunction structure, which incorporates an interface between an electron donating semiconductor and an electron accepting semiconductor can provide an efficient way for exciton dissociation if the respective electronic orbital energies of donor and acceptor have a large enough offset. The first solar cells based on heterojunctions were reported by C. W. Tang in 1986 with power conversion efficiency ~1% [119]. This was much more efficient than the homojunction organic solar cells which showed typical efficiencies less than 0.01% due to the insufficient separation efficiency of highly bonded holes and electrons [120].

### 4.1.1 Working principle of a donor/acceptor heterojunction

The efficiency of a heterojunction device is determined by following four critical steps as shown in Figure 1-5: light absorption, exciton diffusion, exciton dissociation and charge collection. The typical time scales for each step are taken from [121] and shown in the brackets.
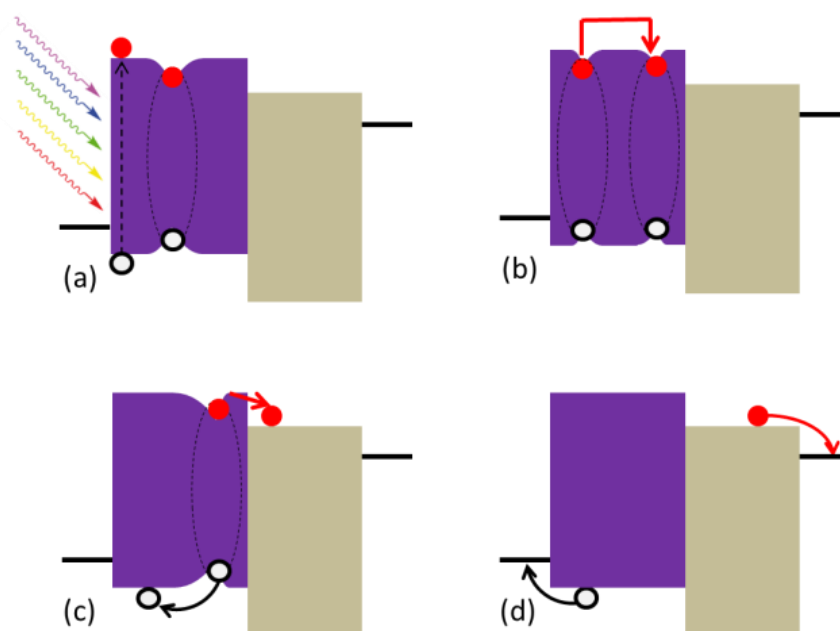


Figure 1- 5 Working principle of heterojunction devices with (a) light absorption and exciton formation, (b) exciton diffusion, (c) exciton separation and (d) charge transport and collection.

**Light absorption and exciton formation (~$10^{-15}$)**: This step takes place very fast, and its efficiency is dependent on active layers' absorption coefficients and thicknesses.

**Exciton diffusion (<$10^{-9}$ s)**: Photo-excited electrons can either decay by radiative or non-radiative recombination to the ground state or diffuse to the heterojunction interfaces where exciton dissociation can occur. During this competing process, the so called exciton diffusion length, the distance that an exciton can travel within its lifetime, determines the efficiency of this step. To achieve exciton diffusion to the hetero-interface, the layer thickness should be kept within the range of the exciton diffusion length which is typically around 5-50 nm for organic materials.

**Exciton dissociation (~$10^{-14}$ s)**: When an exciton reaches a donor/acceptor interface, the energy difference between the LUMO levels of donor and acceptor can provide the driving force for the dissociation of the exciton into a free electron and hole. The same is true if the energy offset between the HOMO levels is large enough (e.g. photocurrent contribution from $C_{60}$). The efficiency of this step can reach nearly 100% at optimal conditions. However, the question about how the excitons are dissociated at the interface is still under debate [122,123].

**Charge transport and collection (~ $10^{-6}$ s)**: Once separated, charges have to be transported through the organic layers and collected at respective electrodes. The recombination of holes and electrons is the main loss mechanism during this transporting process. The charge collection efficiency is dependent on the morphology of the heterojunctions. Donor and acceptor phase should be kept bicontinuous, otherwise the charges would be trapped in the active layers or reach the wrong contacts and lead to low collection efficiency. In addition, energy barriers between the organic layers and electrodes should be minimized to facilitate charge extraction.

## 4.2 Single junction OPVs

A Single junction OPV is composed of a donor/acceptor heterojunction structure and two electrodes with different work functions for electron and hole collection. Typically, a film of transparent metal oxide (ITO, FTO *etc*.) acts as front electrode and a film of reflective metal (Au, Ag, Al *etc*.) acts as back electrode.

### 4.2.1 Device architectures

According to different types of donor-acceptor interface structures, OPV devices can be fabricated in planar bilayer, bulk or ordered heterojunction structures as depicted in Figure 1-6.
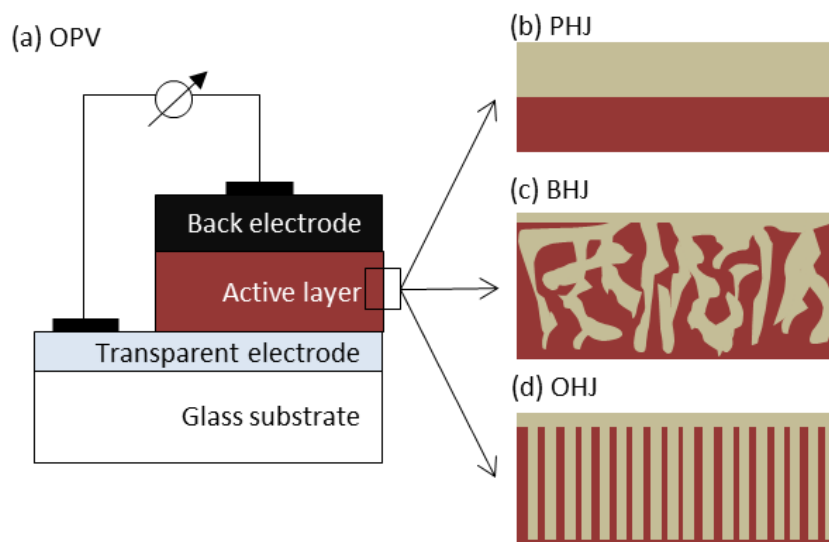
Figure 1- 6 Architectures of (a) organic solar cells with (b) PHJ, (c) BHJ and (d) OHJ

### 4.2.1.1 Planar heterojunctions

Planar heterojunction (PHJ) is the simplest architecture where an organic donor layer and an organic acceptor layer are sandwiched between two conducting electrodes. The advantages of these simple bilayer devices are morphology stable and the reduced charge recombination, once the exciton separated at the interface, free electrons and holes have less chance to meet and recombine with each other. However, the photo-generated excitons have to diffuse from the place where excitons are generated through the acceptor layer or donor layer to the interface region where charge separation occurs. Layer thicknesses should be kept within the range of the exciton diffusion length for efficient exciton separation, but the small thicknesses limit light absorption efficiency. A compromise must be reached for an efficient OPV device.

### 4.2.1.2 Bulk heterojunctions

This shortcoming of PHJs can be addressed by the interpenetrating bulk heterojunction (BHJ) morphology. In a BHJ, a blend of electron donor and acceptor materials is cast as a mixture, which then phase-separates. In this way, the donor/acceptor interfaces are located randomly everywhere in the bulk, making it easy for an exciton to reach a nearby interface and be dissociated into free charges. However, phase separation of BHJs should be well controlled on the nanoscale and both phases should be continuous, otherwise charges would be trapped inside the device and cannot be extracted.

*4.2.1.3 Ordered heterojunctions*

Ordered heterojunctions (OHJs) are then introduced to overcome the phase separation problem of BHJs. A well-ordered template with a highly aligned nanostructure is fabricated through nanoimprinting, and the other layer is spin coated on the top [124]. OHJs minimize the variability associated with BHJs and maximize the interface area compared with PHJs. OHJs are generally hybrids of structured inorganic materials and solution process organic semiconductors. OHJs suffer similar thickness limitations because the size of the pore must be in the range of exciton diffusion length. And technologies for the fabrication of highly ordered molds are another difficulty.

## 4.2.2 Parameters limiting the efficiency of single junction OPVs

Organic semiconductors are known for their low charge carrier mobility and short exciton diffusion length and energy barriers at organic/ inorganic interfaces. All these drawbacks limit the power conversion efficiency in OPVs [125].

*4.2.2.1 Charge carrier mobility*

The charge mobility in organic films are typically in the range of $10^{-6}$ - $10^{-1}$ cm$^2$/V.s [126, 127, 128, 129]. Low mobility means that charge transport and collection efficiency is low. In order to enhance the charge collection efficiencies, the thicknesses of active layers have to be minimized. Increasing active layer thickness will increase the internal resistance and result in reductions of $V_{OC}$ and fill factor [130]. Factors that affect charge carrier mobility include molecular packing, disorder, presence of impurities, temperature, electric field, charge-carrier density, molecular size/weight and pressure. Methods commonly used to measure charge carrier mobility in organic materials are space-charge-limited-current (SCLC), organic field effect transistors (OFET), time-of-flight (TOF) and charge extraction by linearly increasing voltage (CELIV) and are reviewed in different publications [126, 131].

Increasing charge mobility in the organic films does not always improve the efficiency of the devices, because this would not only enhance charge extraction but also speed up the rate of charge recombination. The balance between charge extraction and recombination leads to a distinct optimum in the carrier mobility with regard to the efficiencies of organic solar cells. The best device efficiencies are achieved using materials with mobility in the range of $10^{-6}$ - $10^{-4}$ m$^2$/V.s [132] and the ratio of the electron to hole mobility is around 1:0.3 [133].

*4.2.2.2 Energy barrier at organic/metal electrode interfaces*

The energy barriers at anode/donor interfaces for hole extraction and cathode/acceptor interfaces for electron extraction in OPV devices lead to an increase of the series resistance and an decrease of $V_{OC}$. Ohmic contacts are required to overcome these drawbacks, which can be achieved by modifying electrical properties at the interfaces. The best strategy as has been proven is to employ buffer layers with aligned band for the transport of majority carriers and without alignment for minority carriers. In addition, buffer layers can act as optical spacers to improve light management and enhance the optical absorption efficiency. Many functional materials have been successfully employed in OPVs as buffer layers, for example, anode buffer layers such as PEDOT:PSS, TPD [134], graphene oxide (GO) [135], $MoO_3$ [136] and $WO_3$ [137] *etc*. and cathode buffer layers [138] such as $Alq_3$, BCP, $TiO_2$, ZnO *etc*.
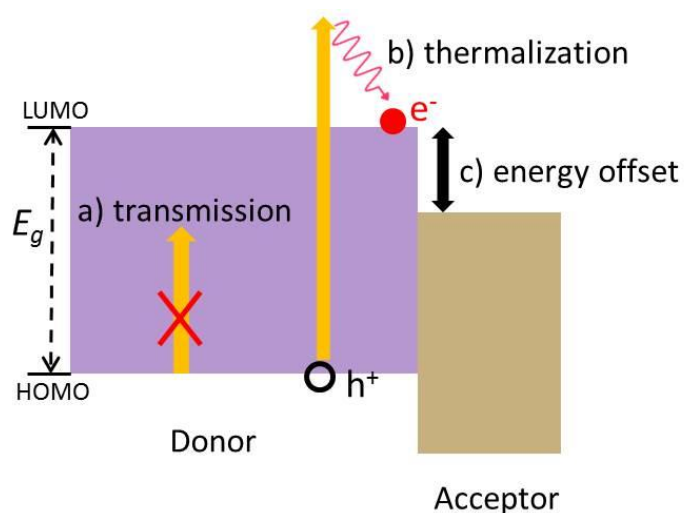


Figure 1- 7 Energy loss mechanisms in single junction OPVs

## 4.3 Tandem solar cells

In the last decade, efforts have been focused on pushing the OPV efficiencies by enhancing light management, improving interfacial design, optimizing the balance of charge carrier mobility and better morphology control [139, 140, 141, 142]. The efficiencies of single junction OPV cells have been repeatedly reported in excess of 9% for polymers (10.8% [10], 9.2% [143]) and small molecules (9.02% [144], 9.3% [145], 9.95% [146]).

However, some losses are unavoidable in single junction devices. By assuming an ideal case where the only recombination mechanism of electron-hole pairs is radiative, and highly ideal materials are used and all avoidable losses are switched off, as calculated by Shockley and Queisser (SQ) [147], maximum efficiency for single junction solar cells is around 33% for an

active material's bandgap $E_g$ of ~1.3 eV. 18% is lost through transmission of photons with energy smaller than $E_g$, and 47% is lost through thermalization of energetic charges generated by photons with energy larger than $E_g$ that decay to lower energies close to the band edge, and others are lost due to the blackbody radiation and exciton recombination. These losses are more pronounced in OPVs as shown in Figure 1-7. Due to the spectral and sharp optical absorption properties of organic semiconductors, both photons with energy smaller than the minimum optical gap $E_{g,min}$ and larger than the maximum optical gap $E_{g,max}$ cannot be absorbed by the active materials. The energy offset required for exciton dissociation in organic heterojunction devices causes additional loss [148, 149, 150]. Taking the energy offset (0.3 eV), external quantum efficiency (65%) and fill factor (65%) into account, as derived by Scharber *et al.* [151], the highest achievable energy conversion efficiencies of OPVs are around 10%.

In order to overcome the drawback of single junction solar cells and harvest more solar energy, multi-junction solar cell connected by single cells with complementary absorption spectra in series or parallel is a well proven concept to reduce thermalization and transmission losses. Stacked multiple active layers allow absorption over a wider range of the solar spectrum and enhance power conversion efficiency as compared with single junction solar cells. In addition, photons emitted by radiative recombination from large band gap subcells can still be captured by the neighboring low band gap subcells.

Tandem solar cells have the potential to surpass the SQ limit of single junction solar cells. In inorganic PVs, the maximum efficiencies for tandem and triple junction solar cells are 42% and 49%, respectively, comparing with 33% maximum efficiency for single junction devices when exposed to 1 sun irradiation [152]. In OPVs, the estimations are more complex. In optimistic assumptions by assuming $EQE$=90% and $FF$=70% [153] or $EQE$=75% and $FF$=75% [154], efficiencies around 23~24% can be achieved for tandem OPVs. In an empirical case, by assuming $EQE$=65% and $FF$=65%, maximum efficiencies of 15% are predictable [155], 30% efficiency increases are obtained compared with the best single OPVs under the same assumptions [156]. For triple junction devices, by assuming $EQE$=75% and $FF$=75%, at optimal configurations, the maximum efficiency of 22.7% is achievable [157]. To date, tandem and triple junction OPVs with efficiency exceeding 10% [10.6% [158], 10.1% [159]] and 11% [11.5% [160]], respectively, have been reported.

## 4.3.1 Tandem device structures and working principle

To build the multijunction devices, subcells can be electrically connected either in series (monolithically integrated tandem) or in parallel (mechanically stacked tandem). The simplified configurations are shown in Figure 1-8.
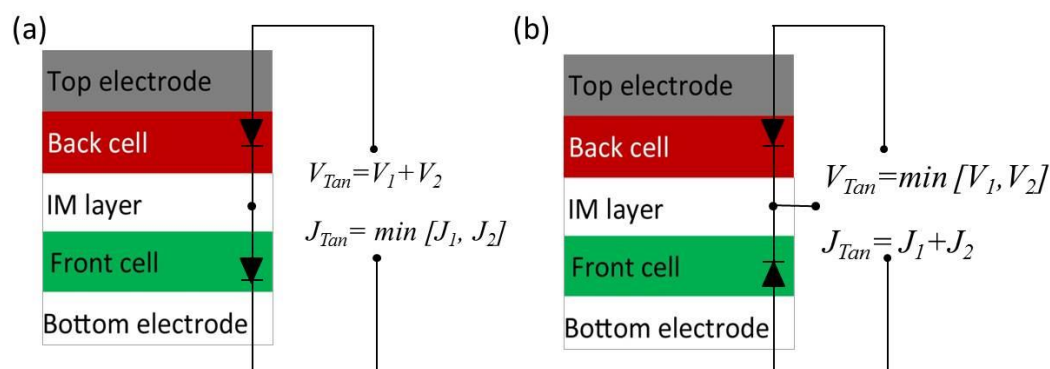


Figure 1- 8 Architectures of series (a) and parallel (b) connected tandem cell

### 4.3.1.1 Monolithic integration

In monolithically integrated tandem solar cells, the two subcells are connected in series and result in two terminals for connection to external circuit as shown in Figure 1-8 (a). The cathode of the bottom cell is electrically connected with the anode of the top cell through an intermediate (IM) layer where electrons and holes accumulate and recombine. When operated under short circuit condition, the excess of charge carriers from the subcell with more photo-generated current will negatively charge the other subcell inducing an increase of the photocurrent from the limiting device, the steady state is reached when the flowing current from two subcells are equal. This means that in order to have an efficient tandem cell both of the subcells should have matched current. When operated under open circuit condition, assuming ohmic contact formed between the subcells and no energy loss during charge recombination, the $V_{OC}$ of the tandem device is the sum of the $V_{OC}$s of individual subcells.

### 4.3.1.2 Stacked devices

In mechanically stacked tandem solar cells, a middle transparent electrode acts as the third terminal connecting the subcells in parallel as shown in Figure 1-8 (b). Each subcell can be contacted and measured separately, and the stacked devices do not require current matching. According to the Kirchhoff's circuit laws, the output current is the sum of the currents of individual subcells and the output $V_{OC}$ is equal to the smaller one.

The choice between the series and parallel configurations is dependent on the differences of *J-V* characteristics of individual subcells. If the differences are more significant on $V_{OC}$, series tandem cells are performing better than parallel tandem cells. Otherwise, if $J_{SC}$ differences are more pronounced, parallel connections work principally better than series connections [161]. In OPVs, the photocurrents are easier to tune by varying the thicknesses of active layers and reach current matching. In addition, the requirement of highly transparent electrodes makes the stacked devices more problematic than monolithic devices, so the monolithic integrated tandem solar cells have obtained much more attentions than stacked devices.

*4.3.1.3 Intermediate layers*

To achieve highly performing monolithic tandem solar cells, the design and choice of intermediate interlayers play an important role. As shown in Figure 1-9, the intermediate layers should firstly collect electrons and holes from neighboring subcells and secondly act as recombination centers for the collected charges.
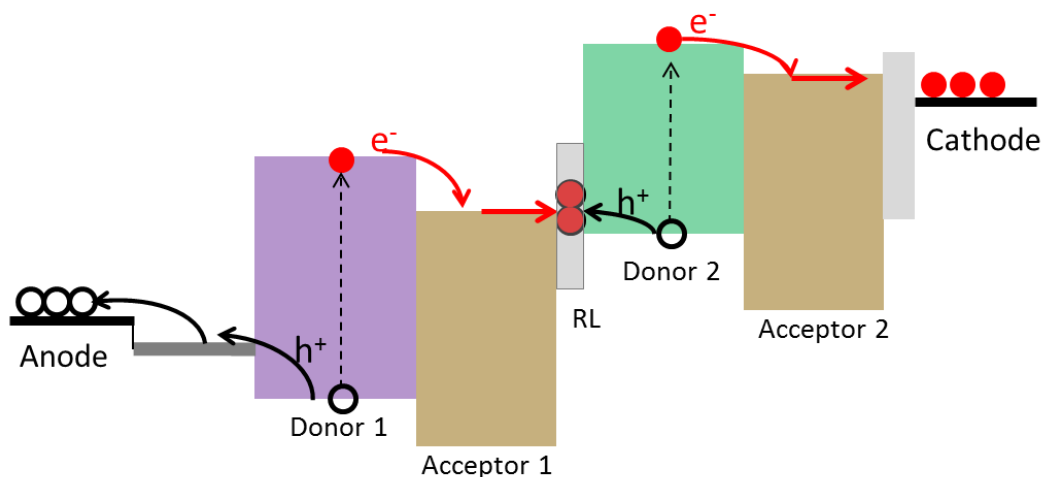


Figure 1- 9 Working principle of recombination layer in tandem solar cells

The interlayers typically consist of one electron transport layer and one hole transport layer, the materials and the structures of interlayer are reviewed in the literature [162]. Some requirements for the interlayers are listed below. [163, 164, 165]

- the interlayers should be thick and robust enough to separate two subcells to prevent formation of inverted diode behavior  and protect bottom active layers against the damage from spin coating the top active layers from solution;
- the interlayers should be highly transparent to avoid optical losses;

- the interlayers should present no energy barrier for charge collection and recombination from the two subcells;

- the conductivity of the interlayers should be suitable, neither too low to increase the series resistance nor too high to increase the effective area and overestimate the efficiency (this is only an issue in small laboratory cells);

- the optical spacer effect of interlayers should be considered, the maximum intensity of transmitted light through bottom subcells can be tuned by varying the thickness of interlayers to match with the absorption spectra of top cells [166, 167].

## 4.3.2 Optimization and characterization of tandem solar cells

*4.3.2.1 Optical modelling for current matching*

To reduce energy loss in tandem cells, currents from each subcell should be matched [168, 169]. The configurations of the multi-junction solar cells are very complex owing to the large number of stacked layers in such devices, and the optimization of their performance is hard to be done experimentally by varying active layer thicknesses. Optical modeling is an invaluable tool to calculate the photocurrents in each subcell and optimize the active layer thicknesses and subcell sequences.

The model established by Pettersson *et al.* [170], which is based on transfer matrix methods, has been successfully used in single junction OPVs [171] and can be extended in tandem solar cells [168, 172]. Similarly to single junction solar cells, the electrical field distributions $E_i(x)$ at the position *x* in a layer *i* are calculated and the number of excited states $Q_i(x)$ is proportional to the square of the electric field:

$$Q_i(x) = \frac{1}{2} c \epsilon_0 n_i \frac{4\pi k_i}{\lambda} |E_i(x)|^2$$

Where *c* is the speed of light, $\epsilon_0$ is the permittivity of free space, $n_i$ is the reflection coefficient, $k_i$ is the extinction coefficient and $\lambda$ is the wavelength. The optical indexes of all layers as function of wavelength and the thicknesses of each individual layer can be measured by the spectroscopic ellipsometry by measuring the change of light polarization upon reflection or transmission and then fitting the measurement to a model.

By assuming that every generated exciton converts to an electron, which means that the internal quantum efficiency (*IQE*) is equal to 1, the maximum achievable current density $J_{SC,\,max}$ can be calculated by integrating the number of excited states over the full wavelength region. Comparing $J_{SC,\,max}$ to the experimentally measured $J_{SC,\,exp}$, the average *IQE* can be obtained

from the ratio of $J_{SC,\,exp}/J_{SC,\,max}$. A series of corresponding single junction solar cells with different active layer thicknesses can be fabricated to determine the *IQE* values. Then the determined average *IQE* values can be combined in the optical model to predict the achievable $J_{SC}$ of the tandem cells [173]. By assuming that the $V_{OC}$ is sum of $V_{OC}$s of each subcell and taking a reasonable fill factor value, efficiencies of the tandem solar cells can be predicted. This method was used in our cyanine multijunction solar cells in Chapter IV.

### 4.3.2.2 IPCE measurements

To accurately measure the performance of tandem OPVs, the *EQE* spectra must be folded with the standard AM 1.5G solar spectrum to calculate $J_{SC}$ [174]. Also the *EQE* of each subcell is a critical measurement for well understanding the working mechanism and determining the limiting subcells in tandem solar cells. However, the *EQE* measurement of tandem devices is quite challenging, especially for two terminal tandem devices because the subcells cannot be measured separately. Unlike in single junction OPVs, the photo-generated charges can be extracted from tandem devices only if both subcells are simultaneously excited. In order to measure the *EQE* of the investigated subcell, a selectively strong light bias must be applied to the other subcell, such that the investigated subcell limits the current over the whole wavelength region. While in the *EQE* measurements, the current limiting device is always operated in reverse bias due to the light biased subcell which works under open circuit condition, this will lead to an overestimation of $J_{SC}$ of the investigated subcell. An additional positive electrical bias should be applied to the tandem device to compensate for this effect and avoid overestimation of performance. The magnitudes of optical bias and electrical bias to be applied on the device during the *EQE* measurements must be well defined.

For the optical bias, the selected light should be in the wavelength region which is not or only slightly absorbed by the investigating cell, and the light intensity should be high enough to make sure that the amount of charges generated from the biased cell higher than the charges from the investigated cell at any scanned wavelength region. In OPVs, the photo generated currents are dependent on the light intensity. However, the intensity of probe light used in the *EQE* measurements is usually lower than the 1 sun condition, so the measured *EQE* should be corrected to standard AM1.5G sunlight illumination condition according to the light dependence properties of the corresponding single cell. In some cases, the bias light is absorbed by both subcells but primarily by the biased subcell, therefore, the light intensity can be tuned to generate 1 sun condition for the investigated cell, no corrections need to be done afterwards [175].

For the electrical bias, the determination of the magnitudes of the applied voltage is more complicated. Simply, the electrical bias can be approximately applied in the same magnitude with the $V_{OC}$ of the optically biased subcell. However, as studied by Gilot *et al.* [175], the real bias voltage can deviate significantly from the $V_{OC}$. The precise way to determine the correct electrical bias should use *J-V* characteristics of each subcell under the illumination conditions that are representative for the subcells in the tandem. The positive bias voltage, to be applied on the tandem cell to ensure short-circuit conditions for the investigated subcell, is the absolute value of the voltage of the data points shown in both the *J-V* curves of the two subcells with equal $J_{SC}$s and voltages opposite. And also the modulated probe light induced photovoltage should be taken into account to modify the electrical bias voltage and make sure the current limiting device is working under short circuit condition.

### 4.3.3 Factors limiting tandem cells

Compared with single junction cells, subcells used in tandem solar cells suffer from some losses. For example, for the front subcell, absorption is reduced because there is no reflective back contact and for the back subcell some light is filtered out by the front cell [176]. The state of the art for the efficiency increase in tandem solar cells is the reduced photocurrents can be compensated by the increase of $V_{OC}$. However, multijunction devices do not always improve the efficiency over the corresponding single devices [155]. In order to achieve high performing tandem cells, besides parameters necessary to achieve high performing single junction solar cells, some other requirements to construct efficient tandem devices are discussed below.

*4.3.3.1 Layer sequences*

Layer sequences are a critically important parameter determining the maximum efficiencies of tandem solar cells. Theoretically, efficient tandem devices put the wide band gap subcells in the front and small band gap subcells in the back to avoid the thermerlization loss. However, in some thin layer solar cells, the devices with reversed layer sequences are performing better than the regular devices due to the specific absorption profiles and interference effects [176, 177].

As simulated by G. Dennler *et al.* [155], the efficiencies can be dramatically improved by stacking subcells whose performance are limited by low $J_{SC}$s due to the small active layer thicknesses and poor optical electric field distributions [178]. By stacking these single cells into a multi-junction cell, the optical distributions can be optimized by spacer effects and in-

terference effects from the subcells and interlayers. The optical absorption of each subcell and the performance of the stacked devices can be significantly enhanced compared with the corresponding single cells [169].

*4.3.3.2 Band gap combinations*

An appropriate band gap combination is another key parameter to determine the efficiency of tandem solar cell. In order to effectively capture photons from the sun, materials with complementary absorptions over the whole solar spectrum should be chosen as donors in tandem devices [179, 180] and the absorption overlap between these materials should be minimized [155]. Unlike in inorganic multijunction solar cells, the optimal band gap combinations in organic multijunction cells can widely differ depending on minimum energy offsets and optical absorption bandwidths, for example, (1.7 eV, 1.1 eV) [157] and (1.6 eV, 1.3 eV) [155] for tandem cells, and (2.0 eV, 1.5 eV, 1.1 eV) [157] for triple junction cells, respectively. In other cases, the efficiency can be enhanced by stacking the same subcells because the light is not fully absorbed in one single cell, for example, W. Li *et al.* [181] fabricated 1+2 triple junction cells using a wide bandgap subcell as bottom cell and the same photoactive layer with different thicknesses as middle and back subcell, the efficiencies increased from 8.9% for tandem to 9.64% for triple junction cells. Therefore, the optimization of tandem OPVs should be done case-by-case. A case study for the optimization of cyanine multijunction solar cells will be discussed in Chapter IV.

# 5. Organic Photodetectors

Based on the concept of organic heterojunctions, many organic electronic devices with different functionalities can be produced. One example are photodetectors, which are light sensors used to convert a light signal into an electrical signal.

## 5.1 Operational mechanism

A commonly used photodetector is a photodiode. The device structure is very similar to solar cells but optimized for working under reverse bias condition with low dark current and fast response speed. According to the type of output signal, photodetectors can be classified as photo-conductive mode and photo-voltaic mode.

***Photo-conductive mode***: the diode is an electrical insulator when operated under reverse bias condition in the dark. Once a light signal is detected, free charges are generated by incident photons and can flow through the device, and then the diode becomes conductive. The

amount of photogenerated charges is dependent on the incident light intensity, and the electrical conductivity of the diode varies as a function of the intensity of light signal. Because the charges are simultaneously driven by the reverse bias and the built-in electric field, photodetectors can respond to the light signal very fast. However, the drawback of this operation mode is that the applied bias injects charges from electrodes to the device and increases the noise current.

***Photo-voltaic mode*:** When operated in an open circuit condition, photogenerated electrons in the diode are accumulated at the cathode side and holes are accumulated at the anode side, an internal electric field is established due to the energy difference between these accumulated positive and negative charges. The magnitude of the voltage is dependent on the amount of charges and hence the incoming light intensity. In this mode, the dark current is kept at a minimum because no external bias is applied. The shortcoming of this mode is the limited response time.

## 5.2 Applications

The technology of light detection is used very often in our daily life, it can be directly used or integrated with other devices to invent some new applications such as: environmental monitoring for security and safety, position sensors in industrial automatic systems, sensors used to automatically control doors in the buildings or public transportation, light detection in biomedical applications, optical communications *etc*.

Photodetectors have to be sensitive in some given spectral regions depending on applications. Organic semiconductors have broadened the application in many areas due to their tunable spectral sensitivity. Organic photodetectors (OPDs) can be made panchromatic or selectively sensitive in some specific wavelength regions, such as UV, VIS and NIR light detectors. Particularly, medical and industrial sensors often have the requirement to operate in the NIR region only as the NIR light penetrates deeper into the tissues and benefit for being invisible and inducing less interference, OPDs are attractive as filter-free solid state alternatives. And also, OPDs can be made transparent by using NIR light absorbing dyes. The transparent OPDs can be easily monolithically integrated with other optical electronic devices to form integrated systems with smart functionalities, more details will be described in Chapter III.

## 5.3 Important properties of photodetectors

### 5.3.1 Response time

The response time of a detector is the time required to respond to an incoming light signal or changes in light intensity. It is a key parameter to determine the performance of the photodetector. The response time is determined by the time required for the charge generation at the interface, charge diffusion to reach the electrode, and RC time constant.

In OPDs, the charge generation is typically very fast in the time scale of $10^{-9}$ s. The main limitations for fast response are the low charge mobility, trap states in disordered organic semiconductors and the *RC* time. To enhance the response speed, external electrical bias is normally applied to the device [182] and the size of the photodetector is kept small to minimize the *RC* time constant. In some other cases, methods such as increasing the temperature [183] and enhancing organic vertical carrier mobility [184] have been used to overcome the drawback of low carrier mobility. Decreasing the active layer thicknesses is another choice to enhance the response time, but pin holes and the reduction in quantum efficiency are hardly avoided in ultrathin film devices.

### 5.3.2 Spectral responsivity

Spectral responsivity *R* is related to the efficiency of light detection as a function of the wavelength, and is defined as the magnitude of the electrical signal output from a photodetector in response to a particular light power,

$$R = \frac{J_{ph}}{I_{light}} = \eta_{QE} \frac{\lambda q}{hc}$$

Where, $J_{ph}$ is the photocurrent and $I_{light}$ is the incident light intensity, $\eta_{QE}$ is quantum efficiency, $\lambda$ is the wavelength, *h* is Planck's constant, *c* is the speed of light in vacuum, *R* is in units of mA W$^{-1}$. *R* increases with applied reverse bias due to the improved charge collection efficiency in the photodiode. The responsivity should be constant or at least well defined within some wavelength range. In some cases, it can also be important to have zero response in some other wavelength range, for example, transparent detectors are non-sensitive to visible light.

### 5.3.3 Noise current

As a major contribution of detection limit, the dark current plays a key role in determining the overall performance of a photodetector. It should be minimized in order to improve the power

consumption and the effectiveness of photocurrent readout process. Therefore, its origins have to be understood in order to effectively reduce the dark current. Two factors have been identified as major contributions of the dark current [185, 186].

### 5.3.3.1 Shot noise

The term of shot noise is derived from fluctuations in the stream of electrons in a vacuum tube, and its magnitude is expressed as:

$$I_{sn} = \sqrt{2qI_{DC}\,\Delta f}$$

Where, $q$ is the absolute value of the elementary charge, $I_{DC}$ is the average DC diode current, $\Delta f$ is the electrical bandwidth in Hz. Shot noise is referred to as reverse bias leakage current. It can be minimized by keeping leakage current small. Photodetectors are normally operated under biased condition, their high leakage currents have been attributed to the charge injection from electrodes. Suitable engineering of the electrode/active layer interfaces is generally accepted as an efficient way to suppress charge injection phenomena, some hole blocking layers (HBL) [187, 188] and electron blocking layers (EBL) [189, 190] have been incorporated into photodiodes and dark currents can be reduced to the range of nA/cm$^2$ [189, 191, 192, 193]. For example, a wide bandgap of MeO-TPD layer with high LUMO level was used as EBL in cyanine photodetectors as will be shown in Chapter III. In order to choose suitable blocking layers, following requirements should be satisfied,

- the LUMO level of EBL should be high enough and the HOMO level of HBL should be low enough to create a Schottky barrier for the effective suppression of misdirected charge extraction and electron injection;
- the charge mobility should be high and the HOMO level of EBL and LUMO level of HBL should be positioned between the energy levels of the active materials and the Femi level of the respective electrodes, charge collection efficiency is not significantly hindered;
- Materials should not absorb light to be sensed and should not influence the absorption of the active layers.

### 5.3.3.2 Johnson Noise

Johnson noise is also called thermal noise, which is generated by the thermal agitation of the electrons inside the photodetector and occurs regardless of any applied voltage. The shunt resistance in a photodetector has a Johnson noise associated with it. The magnitude of the Johnson noise $I_{jn}$ is defined as,

$$I_{jn} = \sqrt{\frac{4k_B T \, \Delta f}{R_{sh}}}$$

Where, $k_B$ is Boltzmann constant, $T$ is the absolute temperature in degrees Kelvin and $R_{sh}$ is the shunt resistance of the photodiode. This type of noise is the dominant current noise in unbiased operation mode.

In organic photodetectors, the main source of $I_{jn}$ is the carrier generation at the donor/acceptor interface via heat induced ground state charge transfer, and the generated carrier concentration ($n_i$) is dependent on the activation energy ($E_a$) of the semiconductor [186],

$$n_i \propto e^{-\frac{E_a}{2kT}}$$

This effect is non negligible and can hardly be avoided especially for NIR light sensitive low band gap semiconductors. In bulk heterojunction devices, the interpenetrating networks between the donor and acceptor inherently increase the interface area for charge recombination and consequently increase $I_{jn}$. Using planar heterojunctions instead of bulk heterojunctions [193] is therefore a promising way to reduce the cross section of donor and acceptor pairs. Increasing active layer thicknesses is another method to decrease dark current by increasing the shunt resistance, but it causes a parasitic reduction in carrier collection efficiency [192]. A compromise must be reached to obtain a maximum ratio of photo current to dark current.

### 5.3.3.3 Total noise

The total noise current generated in a photodetector is determined by

$$I_{tn} = \sqrt{I_{sn}^2 + I_{jn}^2}$$

In most of cases, photodetectors are operated under biased condition, the shot noise dominates the total noise current and the Johnson noise can be neglected.

### 5.3.3.4 Noise equivalent power

Noise equivalent power (*NEP*) is the power of incident optical signal required to generate a photocurrent equal to the noise current of the photodetector at a specified wavelength region within a specific bandwidth. It is defined as:

$$NEP = \frac{I_{tn}}{R}$$

The unit of *NEP* is Watts/ $Hz^{1/2}$. Since the power to current conversion of a diode depends on the wavelength, the *NEP* is always quoted at a particular wavelength.

### 5.3.4 Detectivity

The specific detectivity $D^*$ is defined as

$$D^* = \frac{\sqrt{A\,\Delta f}}{I_d}R$$

Where, $A$ is the effective area of the detector in cm$^2$, $R$ is the responsivity and $I_d$ is the noise current in ampere, $D^*$ is in unit of cm Hz$^{\frac{1}{2}}$ W$^{-1}$ or Jones for memory of the Robert Clark Jones [194]. With the assumption that under reverse bias the shot noise from the dark current is the dominant contribution to the overall electronic noise of the device, the $D^*$ can be expressed as,

$$D^* = \frac{R}{\sqrt{2qJ_d}}$$

Where, $J_d$ is the dark current density, $D^*$ produces a figure of merit and indicates the ability to detect levels of radiant power.

## References

[1] Solar generation 6, EPIA, 2011.

[2] R. Williams, Becquerel photovoltaic effect in binary compounds, J. Chem. Phys. 1960, 32 (5), 1505-1514.

[3] D. M. Chapin, C. S. Fuller, G. L. Person, a new silicon p-n junction photocell for converting solar radiation into electrical power, 1954, 25, 676-677

[4] http://www.nrel.gov/ncpv/images/efficiency_chart.jpg, 2015.2.25

[5] http://pvinnovation.ca/status-organic-photovoltaics/ , 2015.2.25

[6] B. Azzopardi, C. J. M. Emmott, A. Urbina, F. C. Krebs, J. Mutale, J. Nelson, economic assessment of solar electricity production from organic based photovoltaic modules in a domestic environment, Energy Environ. Sci., 2011, 4, 3741-3753.

[7] C. J. Mulligan, C. Bilen, X. Zhou, W. J. Belcher, P. C. Dastoor, levelised cost of electricity for organic photovoltaics, Sol. Energy Mater. Sol. Cells, 2015, 133, 26-31.

[8] http://www.heliatek.com/wp-content/uploads/2013/01/130116_PR_Heliatek_achieves_record_cell_effiency_for_OPV.pdf, 2015.2.25

[9] T. Nozawa, "Mitsubishi Chemical Claims Efficiency Record for Organic Thin Film PV Cell," 1 Jun 2012.

[10] Y. Liu, J. Zhao, Z. Li, C. Mu, W. Ma, H. Hu, K. Jiang, H. Lin, A. Ade, H. Yan, aggregation and morphology control enables multiple cases of high efficiency polymer solar cells, Nat. Commun., 2014, 5, 5293.

[11] J. You, L. Dou, K. Yoshimura, T. Kato, K. Ohya, T. Moriarty, K. Emery, C. C. Chen, J. Gao, G. Li, Y. Yang, a polymer tandem solar cell with 10.6% power conversion efficiency, Nat. Commun., 2013, 4, 1446.

[12] C. C. Chen, W. H. Chang, K. Yoshimura, K. Ohya, J. You, J. Gao, Z. Hong, Y. Yang, an efficient triple-junction polymer solar cell having a power conversion efficiency exceeding 11%, Adv. Mater., 2014, 26, 5670-5677.

[13] R. R. Lunt, theoretical limits for visibly transparent photovoltaics, Appl. Phys. Lett., 2012, 101, 043902.

[14] M. Wielopoiski, K. Linton, M. Marszalek, M. Gulcur, M. R. Bryce and J. E. Moser, harvesting UV photons for solar energy conversion applications, Phys. Chem. Chem. Phys., 2014, 16, 2090-2099.

[15] Y. Zhou, H. Cheun, S. Choi, C. Fuentes-Hernandez, B. Kippelen, optimization of a polymer top electrode for inverted semitransparent organic solar cells, Org. Electron., 2011, 12 (5), 827-831.

[16] H. Schmidt, H. Flügge, T. Winkler, T. Bülow, T. Riedl, W. Kowalsky, efficient semitransparent inverted organic solar cells with indium tin oxide top electrode, Appl. Phys. Lett., 2009, 94 (24), 243302..

[17] J. Huang, G. Li, Y. Yang, a semi-transparent plastic solar cell fabricated by a lamination process, Adv. Mater., 2008, 20(3), 415-419.

[18] Z. Liu, J. Li, Z. H. Sun, G. Tai, S. P. Lau, F. Yan, the application of highly doped single-layer graphene as the top electrodes of semitransparent organic solar cells, ACS Nano, 2012, 6(1), 810-818.

[19] C. Tao, G. Xie, C. Liu, X. Zhang, W. Dong, F. Meng, X. Kong, L. Shen, S. Ruan, W. Chen, semitransparent inverted polymer solar cells with MoO3/Ag/MoO3 as transparent electrode, Appl. Phys. Lett., 2009, 95(5), 053303.

[20] C. Tao, G. Xie, F. Meng, S. Ruan, W. Chen, tailoring spatial distribution of the optical field intensity in semitransparent inverted organic solar cells, J. Phys. Chem. C, 2011, 115 (25), 12611-12615.

[21] G. H. Jung, K. Hong, W. J. Dong, S. Kim, J. L. Lee, BCP/Ag/MoO3 transparent cathodes for organic photovoltaics, Adv. Energy Mater., 2011, 1(6), 1023-1028.

[22] L. Shen, S. Ruan, W. Guo, F. Meng, W. Chen, semitransparent inverted polymer solar cells using MoO3/Ag/V2O5 as transparent anodes. Sol. Energy Mater. Sol. Cells, 2012, 97, 59-63.

[23] T. Ameri, G. Dennler, C. Waldauf, H. Azimi, A. Seemann, K. Forberich, J. Hauch, M. Scharber, K. Hingerl, C. J. Brabec, fabrication, optical modeling, and color characterization of semitransparent bulk heterojunction organic solar cells in an inverted structure, Adv. Func. Mater., 2010, 20, 1592-1598.

[24] Commission international de I'Eclairage international, 1995, ISBN 3900734577.

[25] A. Colsmann, A. Puetz, A. Bauer, J. Hanisch, E. Ahlswede, U. Lemmer, efficient semitransparent organic solar cells with good transparency color perception and rendering properties, Adv. Energy Mater., 2011, 1, 599-603.

[26] Schanda, J. (2007) CIE Colorimetry, in Colorimetry: Understanding the CIE System (ed J. Schanda), John Wiley & Sons, Inc., Hoboken, NJ, USA. doi: 10.1002/9780470175637.ch3.

[27] J. Czolk, A. Puetz, D. Kutsarov, M. Reinhard, U. Lemmer, A. Colsmann, inverted semitransparent polymer solar cells with transparency color rendering indices approaching 100, Adv. Energy Mater., 2013, 3, 386-390.

[28] M. Jørgensen, K. Norrman, F. C. Krebs, stability/degradation of polymer solar cells, Sol. Energy Mater. Sol. Cells, 2008, 92, 686-714.

[29] M. Glatthaar, M. Riede, N. Keegan, K. Sylvester-Hvid, B. Zimmermann, M. Niggemann, A. Hinsch, A. Gompert, Efficiency limiting factors of organic bulk heterojunction solar cells identified by electrical impedance spectroscopy, Sol. Energy Mater. Sol. Cells, 2007, 91, 390-393.

[30] F. C. Krebs, K. Norrman, analysis of the failure mechanism for a stable organic photovoltaic during 10000 h of testing, Prog. Photovolt: Res. Appl., 2007, 15, 697–712.

[31] K. Norrman, M. V. Madsen, S. A. Gevorgyan, F. C. Krebs, degradation patterns in water and oxygen of an inverted polymer solar cell, J. Am. Chem. Soc., 2010, 132, 16883-16892.

[32] M. Hermenau, M. Riede, K. Leo, S. A. Gevorgyan, F. C. Krebs, K. Norrman, water and oxygen induced degradation of small molecule organic solar cells, Sol. Energy Mater. Sol. Cells, 2011, 95, 1268-1277.

[33] F.C. Krebs, design and applications of polymer solar cells with lifetimes longer than 10000 hours, Proc. SPIE, 2005, 5938, 59380Y.

[34] M. Jørgensen, K. Norrman, S. A. Gevorgyan, T. Tromholt, B. Andreasen, F. C. Krebs, stability of polymer solar cells, Adv. Mater., 2012, 24, 580-612.

[35] F. C. Krebs, encapsulation of polymer photovoltaic prototypes, Sol. Energy Mater. Sol. Cells, 2006, 90, 3633-3643.

[36] S. Sarkar, J. H. Culp, J. T. Whyland, M. Garvan, V. Misra, encapsulation of organic solar cells with ultrathin barrier layers deposited by ozone-based atomic layer deposition, Org. Electron., 2010, 11, 1896-1900.

[37] W. J. Potscavage, S. Yoo, B. Domercq, B. Kippelen, encapsulation of pentacene/C60 organic solar cells with Al2O3 deposited by atomic layer deposition, Appl. Phys. Lett., 2007, 90, 253511.

[38] H. J. Lee, H. P. Kim, H. M. Kim, J. H. Youn, D. H. Nam, Y. G. Lee, J. G. Lee, A. R. M. Yusoff, J. Jang, solution processed encapsulation for organic photovoltaics, Sol. Energy Mater. Sol. Cells, 2013, 111, 97-101.

[39] F. C. Krebs, J. Alstrup, H. Spanggaard, K. Larsen, E. Kold, production of large-area polymer solar cells by industrial silk screen printing, lifetime considerations and lamination with polyethyleneterephthalate, Sol. Energy Mater. Sol. Cells, 2004, 83, 293-300.

[40] G. Dennler, C. Lungenschmied, H. Neugebauer, N. S. Sariciftci, M. Latréche, G. Czeremuszkin, M. R. Wertheimer, a new encapsulation solution for flexible organic solar cells, Thin Solid Films, 2006, 511–512, 349-353.

[41] S. Chambon, A. Rivaton, J. L. Gardette, M. Firon, L. Lutsen, Aging of a donor conjugated polymer: Photochemical studies of the degradation of poly[2-methoxy-5-(3',7'-dimethyloctyloxy)-1,4-phenylenevinylene], J. Polym. Sci. A Poly. Chem., 2007, 45(2), 317-331.

[42] M. Manceau, E. Bundgaard, J. E. Carlé, O. Hagemann, M. Helgesen, R. Søndergaard, M. Jørgensen and F. C. Krebs, photochemical stability of pi-conjugated polymers for polymer solar cells: a rule of thumb, J. Mater. Chem., 2011, 21, 4132-4141.

[43] T. Tromholt, M. V. Madsen, J. E. Carlé, M. Helgesen. F. C. Krebs, photochemical stability of conjugated polymers, electron acceptors and blends for polymer solar cells resolved in terms of film thickness and absorbance. J. Mater. Chem., 2012, 22, 7592-7601.

[44] P. A. Lane, L. S. Swanson, Q-X. Ni, J. Shinar, J. P. Engel, T. J. Barton, L. Jones, dynamics of photoexcited states in C60: An optically detected magnetic resonance, ESR, and light-induced ESR study, Phys. Rev. Lett., 1992, 68, 887.

[45] S. Iwai, A. Nakamura, femtosecond spectroscopic studies of the initial formation process of self-trapped excitons in KI, J. Lumin., 1996, 66&67, 383-388.

[46] M. Ichida, A. Nakamura, H. Shinohara, Y. Saitoh, Observation of triplet state of charge-transfer excitons in C60 thin film, Chem. Phys. Lett., 1998, 289, 579-585.

[47] J. Wang, J. Enevold, L. Edman, photochemical transformation of fullerenes, Adv. Funct. Mater., 2013, 23, 3220-3225

[48] P. C. Eklund, A. M. Rao, P. Zhou, Y. Wang, J. M. Holden, photochemical transformation of C60 and C70 films, Thin Solid Film, 1995, 257, 185-203.

[49] Y. Wang, J. M. Holden, Z. H. Dong, X. X. Bi. P. C. Eklund, photo-dimerization kinetics in solid C60 films, Chem. Phys. Lett., 1993, 211, 341-345.

[50] S. Scholz, C. Corten, K. Walzer, D. Kuckling, K. Leo, photochemical reactions in organic semiconductor thin films, Org. Electron., 2007, 8, 709–717.

[51] J. N. Yao, K. Hashimoto, A. Fujishima, photochromism induced in an electrolytically pretreated MoO3 thin film by visible light, Nature, 1992, 355, 624-626.

[52] T. He, J. Yao, photochromic materials based on tungsten oxide, J. Mater. Chem., 2007, 17, 4547-4557.

[53] Y. Ohko, T. Tatsuma, T. Fujii, K. Naoi, C. Niwa, Y. Kubota, A. Fujishima, multicolour photochromism of TiO2 films loaded silver nanoparticles, Nat. Mater., 2003, 2, 29-31.

[54] W. Li, K. H. Hendriks, A. Furlan, W. S. C. Roelofs, S. C. J. Meskers. M. M. Wienk, R. A. J. Janssen, effect of the fibrillary microstructure on the efficiency of high molecular weight diketopyrrolopyrrole-based polymer solar cells, Adv. Mater., 2014, 26(10), 1565-1570.

[55] M. Scarongella, A. A. Paraecattil, E. Buchaca-Domingo, J. D. Douglas, S. Beaupré, T. Mccarthy-Ward, M. Heeney, J.-E. Moser, M. Leclerc, J. M. J. Fréchet, N. Stingelin, N. Banerji, the influence of microstructure on charge separation dynamics in organic bulk heterojunction materials for solar cell applications, J. Mater. Chem. A, 2014, 2, 6218-6230.

[56] B. Gholamkhass, S. Holdcroft, toward stabilization of domains in polymer bulk heterojunction films, Chem. Mater., 2010, 22 (18), 5371-5376.

[57] G. Griffini, J. D. Douglas, C. Piliego, T. W. Holcombe, S. Turri, J. M. J. Fréchet, J. L. Mynar, long-term thermal stability of high efficiency polymer solar cells based on photo-crossinkable donor acceptor conjugated polymers, Adv. Mater., 2011, 23(14), 1660-1664.

[58] O. Haillant, D. Dumbleton, A. Zielnik, an Arrhenius approach to estimating organic pho-tovoltaic module weathering acceleration factors, Sol. Energy Mater. Sol. Cells, 2011, 95, 1889-1895.

[59] S. A. Gevorgyan, M. Jørgensen, F. C. Krebs, K. O. Sylvester-Hvid, A compact multi-chamber setup for degradation and lifetime studies of organic solar cells, Sol. Energy Mater. Sol. Cells, 2011, 95(5), 1389-1397.

[60] R. Betancura, M. Maymóa, X. Eliasa, L. T. Vuonga, J. Martorell, Sputtered NiO as elec-tron blocking layer in P3HT:PCBM solar cells fabricated in ambient air, Sol. Energy Mater. Sol. Cells, 2011, 95(2) 735-739.

[61] M. Jørgensen, K. Norrman, S. A. Gevorgyan, T. Tromholt, B. Andreasen, F. C. Krebs, stability of polymer solar cells, Adv. Mater., 2012, 24, 580-612.

[62] R. R. Søndergaard, M. Hösel, F. C. Krebs, rol-to-roll fabrication of large area functional organic materials, J. Polym. Sci. B: Poly. Phys., 2013, 51, 16-34.

[63] B. Han, K. Pei, Y. L. Huang, X. J. Zhang, Q. K. Rong, Q. G. Lin, Y. F. Guo, T. Y.Sun, C. F. Guo, D. Carnahan, J. W. Gao, K. Kempa, Z. F. Ren, uniform self-forming metallic network as a high-performance transparent conductive electrode, Adv. Mater., 2014, 26, 873-877.

[64] E. Selzer, N. Weiß, L. Bormann, C. Sachse, N. Gaponik, L. Müller-Meskamp, A. Ey-chmüller, K. Leo, highly conductive silver nanowire networks by organic matrix assisted low temperature fusing, Org. Electron., 2014, 15, 3818-3824.

[65] C. Sachse, N. Weiß, N. Gaponik, L. Müller-Meskamp, A. Eychmüller, K. Leo, ITO-free, small-molecule organic solar cells on spray-coated copper-nanowire-based transparent elec-trodes, Adv. Energy Mater., 2014, 4, 1300737.

[66] S. L. Hellstrom, H. W. Lee, Z. Bao, polymer-assisted direct deposition of uniform carbon nanotube bundle networks for high performance transparent electrodes, ACS Nano, 2009, 3(6), 1423-1430.

[67] Y. Y. Choi, S. J. Kang, H. K. Kim, W. M. Choi, S. I. Na, multilayer graphene films as transparent electrodes for organic photovoltaic devices, Sol. Energy Mater. Sol. Cells, 2012, 96, 281-285.

[68] Y. Galagan, B. Zimmermann, E. W. C. Coenen, M. Jørgensen, d. m. Tanenbaum, F. C. Krebs, H. Gorter, S. Sabik, L. H. Slooff, S. C. Veenstra, J. M. Kroon, R. Andriessen, current collecting grids for ITO-free solar cells, Adv. Energy Mater., 2012, 2, 103-110.

[69] M. Hösel, R. R. Søndergaard, M. Jørgensen, F. C. Krebs, fast inline roll-to-roll printing for Indium-Tin-Oxide-free polymer solar cells using automatic registration, Energy Technol. 2013, 1, 102-107.

[70] V. Zardetto, T. M. Brown, A. Reale, A. D. Carlo, substrates for flexible electronics: a practical investigation on the electrical, film flexibility, optical, temperature, and solvent resistance properties, J. Polym. Sci. B: Poly. Phys., 2011, 49, 638–648.

[71] E. Bundgaard, F. C. Krebs, low band gap polymers for organic photovoltaics, Sol. Energy Mater. Sol. Cells, 2007, 91, 954-985.

[72] M. Chen, E. Perzon, M. R. Andersson, S. Marcinkevicius, S. K. M. Jönsson, M. Fahlman, M. Berggren, 1 micron wavelength photo- and electroluminescence from a conjugated polymer, Appl. Phys. Lett., 2004, 84, 3570-3572.

[73] G. Qian, Z. Y. Wang, near-infrared organic compounds and emerging applications, Chem. Asian J., 2005, 5, 1006-1029.

[74] T. Xu, L. Yu, how to design low bandgap polymers for highly efficient organic solar cells, Mater. Today, 2014, 17, 11-15.

[75] Y. Liang, D. Feng, Y. Wu, S. T. Tsai, G. Li, C. Ray, L. Yu, highly efficient solar cell polymers developed via fine-tuning of structural and electronic properties, J. Am. Chem. Soc., 2009, 131, 7792-7799.

[76] C. Winder, N. S. Sariciftci, low bandgap polymers for photon harvesting in bulk heterojunction solar cells, J. Mater. Chem., 2004, 14, 1077.

[77] B. P. Rand, J. Xue, F. Yang, S. R. Forrest, organic solar cells with sensitivity extending into the near infrared, Appl. Phys. Lett., 2005, 87, 233508.

[78] K-J. Huang, Y-S. Hsiao, J-H. Huang, C-W. Chu, P. Chen, W-T. Whang, controlling vertical alignment of phthalocyanine nanofibers on transparent graphene-coated ITO electrodes for organic field emitters, J. Mater. Chem., 2012, 22, 7837-7844.

[79] D-C. Lee, G. M. Morales, Y. Lee, L. Yu, cofacial porphyrin multilayers via layer-by-layer assembly,  Chem. Commun., 2006, 100-102

[80] J. Xue, B. P. Rand, S. Uchida, S. R. Forrest, a hybrid planar mixed molecular heterojunction photovoltaic cell, Adv. Mater., 2005, 17, 66-71.

[81] A. Opitz, B. Ecker, J. Wagner, A. Hinderhofer, F. Schreiber, J. Manara, J. Pflaum, W. Brütting, mixed crystalline films of co-evaporated hydrogen- and fluorine-terminated phthalocyanines and their application in photovoltaic devices, Org. electron., 2009, 10, 1259-1267.

[82] D. Y. Kim, G. Sarasqueta, F. So, SnPc:C60 bulk heterojunction organic photovoltaic cells with MoO3 interlayer, Sol. Energy Mater. Sol. Cells, 2009, 93, 1452-1456.

[83] N. R. Amstrong, D. Placencia, D. Manglesdorf, W. Wang, small molecule organic solar cells with enhanced near-IR photoactivity: the role of texturing and molecular architecture of the active layers on solar cell performance, 2010 IEEE, 978-1-4244-5892-9/10.

[84] R. R. Lunt, V. Bulovic, transparent, near-infrared organic photovoltaic solar cells for window and energy scavenging application, Appl. Phys. Lett., 2011, 98, 113305.

[85] I. H. Campbell, transparent organic photodiodes with high quantum efficiency in the near infrared, Appl. Phys. Lett., 2010, 97, 033303.

[86] C. G. Claessens, U. Hahn, T. Torres, phthalocyanines: from outstanding electronic properties to emerging applications, Chem. Rec., 2008, 8, 75-97.

[87] L. L. Li, E. W. G. Diau, porphyrin-sensitized solar cells, Chem. Soc. Rev., 2013, 42, 291-304.

[88] L. Li, Y. Huang, J. Peng, Y. Cao, X. Peng, highly responsive organic near infrared photodetectors based on a porphyrin small molecule, J. Mater. Chem. C., 2014, 2, 1372-1375.

[89] J. D. Zimmerman, V. V. Diev, K. Hanson, R. R. Lunt, E. K. Yu, M. E. Thompson, S. R. Forrest, Porphyrin-tape/C60 organic photodetectors with 6.5% external quantum efficiency in the near infrared, Adv. Mater., 2010, 22, 2780-2783.

[90] L. Beverina, P. Salice, squaraine compounds: tailored design and synthesis towards a variety of material science applications, Eur. J. Org. Chem., 2010, 1207-1225.

[91] S. So, H. Choi, C. Kim, N. Cho, H. M. Ko, J. K. Lee, J. Ko, novel symmetric squaraine chromphore containing triphenylamine for solution processed small molecule bulk heterojunction solar cells, Sol. Energy Mater. Sol. Cells, 2011, 95, 3433-3441.

[92] J. Park, C. Barolo, F. Sauvage, N. Barbero, C. Benzi, P. Quagliotto, symmetric vs. asymmetric squaraines as photosensitisers in mesoscopic injection solar cells: a structure-property relationship study, Chem. Commun., 2012, 48(22), 2782-2784.

[93] L. Beverina, R. Ruffo, M. M. Salamone, E. Ronchi, M. Binda, D. Natali, M. Sampietro, panchromatic squaraine compounds for broad band light harvesting electronic devices, J. Mater. Chem., 2012, 22, 6704-6710.

[94] G. Chen, H. Sasabe, Y. Sasaki, H. Katagiri, X. F. Wang, T. Sano, Z. Hong, Y. Yang, J. Kido, a series of squaraine dyes: effects of side chain and the number of hydroxyl groups on material properties and photovoltaic performance, Chem. Mater., 2014, 26, 1356-1364.

[95] G. Wei, S. Wang, K. Renshaw, M. E. Thompson, S. R. Forrest, solution-processed squaraine bulk heterojunction photovoltaic cells, ACS Nano, 2010, 4, 1927-1934.

[96] G. Wei, S. Wang, K. Sun, M. E. Thompson, S. R. Forrest, solvent-annealed crystalline squaraine: PC70BM (1:6) solar cells, Adv. Energy Mater., 2011, 1, 184-187.

[97] G. Wei, X. Xiao, S. Wang, K. Sun, K. J. Bergemann, M. E. Thompson, S. R. Forrest, functionalized squaraine donors for nanocrystalline organic photovoltaics, ACS Nano, 2012, 6, 972-978.

[98] J. Qi, L. Ni, D. Yang, X. Zhou, W. Qiao, M. Li, D. Ma, Z. Y. Wang, panchromatic small molecules for UV-Vis-NIR photodetectors with high detectivity, J. Mater. Chem. C, 2014, 2, 2431-2438.

[99] X. Wu, Z. Guo, Y. Wu, S. Zhu, T. D. James, W. Zhu, near-infrared colorimetric and fluorescent Cu2+ sensors based on indoline-benzothiadiazole derivatives via formation of radical cations, ACS Appl. Mater. Interfaces, 2013, 5, 12215-12220.

[100] P. B. Sargent, double-label immunofluorescence with the laser scanning confocal microscope using cyanine dyes, Neuroimage, 1994, 1(4), 288-295.

[101] H. Mustroph, M. Stollenwerk, V. Bressau, current developments in optical data storage with organic dyes. Angew. Chem. Int. Ed Engl., 2006, 45(13), 2016-2035.

[102] R. Hany, B. Fan, F. A. de Castro, J. Heier, W. Kylberg, F. Nüesch, strategies to improve cyanine dye multi-layer organic solar cells, Prog. Photovolt: Res. Appl., 2011, 19, 851857.

[103] X. Chen, X. Peng, A. Cui, B. Wang, L. Wang, R. Zhang, Photostabilities of novel heptamethine 3H-indolenine cyanine dyes with different N-substituents, J. Photoch. Photobio. A, 2006, 181, 79–85.

[104] B. Fan, R. Hany, J-E. Moser, F. Nüesch, enhanced cyanine solar cell performance upon oxygen doping, Org. Electron., 2008, 9, 85-94.

[105] H. Benmansour, F. A. Castro, M. Nagel, J. Heier, R. Hany, F. Nüesch, ionic space charge driven organic photovoltaic devices, Chimia, 2007, 61, 787-791.

[106] A. C. Véron, H. Zhang, A. Linden, F. Nüesch, J. Heier, R. Hany, T. Geiger, NIR-absorbing heptamethine dyes with tailor-made counterions for application in light to energy conversion, Org. Lett., 2014, 16, 1044-1047.

[107] M. Lenes, H. Bolink, ionic space charge effects in solid state organic photovoltaics, ACS Appl. Mater. Interfaces, 2010, 2(12), 3664-3668.

[108] A. Pertegas, D. Tordera, J. J. Serrano-Pérez, E. Orti, H. J. Bolink, light-emitting electrochemical cells using cyanine dyes as the active components, J. Am. Chem. Soc., 2013, 135, 18008-18011.

[109] E. E. Jelley, spectral absorption and fluorescence of dyes in the molecular state, Nature, 1936, 1009-1010.

[110] J. Heier, R. Steiger, R. Hany, F. Nüesch, template synthesis of cyanine dye H-aggregates on nanostructured [6,6]-phenyl C61 butyric acid methyl ester substrates, Phys. Chem. Chem. Phys., 2011, 13, 15714-15722.

[111] J. N. Tisserant, R. Hany, S. Partel, G. L. Bona, R. Mezzenga, J. Heier, dewetting-driven hierarchical self -assembly of small semiconducting molecules, Soft Mater., 2012, 8, 5804-5810.

[112] Q. Li, J. Tan, B. X. Peng, synthesis and characterization of heptamethine cyanine dyes, Molecules, 1997, 2, 91-98.

[113] F. Song, X. Peng, E. Lu, R. Zhang, X. Chen, B. Song, syntheses, spectral properties and photostabilities of novel water-soluble near-infrared cyanine dyes, J. Photoch. Photobio. A, 2004, 168, 53-57.

[114] P. Chen, S. Sun, Y. Hu, Z. Qian, D. Zheng, structure and solvent effect on the photostability of indolenine cyanine dyes, Dyes Pigment., 1999, 41, 227-231.

[115] J. Li, P. Chen, J. Zhao, D. S. Zheng, T. Okazaki, M. Hayami, the influence of molecular chain structure on stability against photooxidation of near-infrared absorbing cyanine dyes, Photogr. Sci. Photochem., 1997, 15, 343-350.

[116] X. Chen, X. Peng, A. Cui, B. Wang, L. Wang, R. Zhang, Photostabilities of novel heptamethine 3H-indolenine cyanine dyes with different N-substituents J. Photoch. Photobio. A, 2006, 181, 79–85.

[117] K. Funabiki, H. Mase, A. Hibino, N. Tanaka, N. Mizuhata, Y. Sakuragi, A. Nakashima, T. Yoshida, Y. Kubota, M. Matsui, synthesis of a novel heptamethine–cyanine dye for use in near-infrared active dye-sensitized solar cells with porous zinc oxide prepared at low temperature, Energy Environ. Sci., 2011, 4, 2186-2192.

[118] T. P. Osedach, A. Iacchetti, R. R. Lunt, T. L. Andrew, P. R. Brown, G. M. Akselrod, V. Bulović, Near-infrared photodetector consisting of J-aggregating cyanine dye and metal oxide thin films Appl. Phys. Lett., 2012, 101, 113303.

[119] C. W. Tang, two-layer organic photovoltaic cell, Appl. Phys. Lett., 1986, 48 (2), 183-185.

[120] A. K. Ghosh, D. L. Morel, T. Feng, R. F. Shaw, C. A. Rowe Jr, photovoltaic and rectification properties of Al/Mg phthalocyanine/Ag Schottky barrier cells, J. Appl. Lett., 1974, 45(1), 230-236.

[121] H. Ohkita, S. Ito, W. C. H. Choy (ed.), Organic Solar Cells, Green Energy and Technology, DOI: 10.1007/978-1-4471-4823-4_5, © Springer-Verlag London 2013.

[122] K. Vandewal, S. Albrecht, E. T. Hoke, K. R. Graham, J. Widmer, J. D. Douglas, M. Schubert, W. R. Mateker, J. T. Bloking, G. F. Burkhard, A. Sellinger, J. M. J. Fréchet, A. Amassian, M. K. Riede, M. D. McGehee, D. Neher, A. Salleo, efficient charge generation by relaxed charge transfer states at organic interfaces, Nat. Mater., 2014, 13, 63-68.

[123] A. Punzi, J. C. Brauer, A. Marchioro, E. Ghadiri, J. De Jonghe and J.-E. Moser, Photoinduced interfacial electron transfer and lateral charge transport in molecular donor–acceptor photovoltaic systems, Chimia, 2011, 65(5), 353-355.

[124] S. E. Park, S. Kim, H. E. Joe, B. Jung, E. Kim, W. Kim, B. K. Min, J. Hwang, fabrication of ordered bulk heterojunction organic photovoltaic cells using nanopatterning and electrohydrodynamic spray deposition methods, Nanoscale, 2012, 4 (24), 7773-7779.

[125] R. A. J. Janssen, J. Nelson, factors limiting device efficiency in organic photovoltaics, Adv. Mater., 2013, 25, 1847-1858.

[126] V. Coropceanu, J. Cornil, D. A. da Silva Filho, Y. Olivier, R. Silbey, J.L. Brédas, charge transport in organic semiconductors, Chem. Rev., 2007, 107, 926-952.

[127] M. Kraus, S. Haug, W. Brütting, A. Opitz, achievement of balanced electron and hole mobility in copper-phthalocyanine field-effect transistors by using a crystalline aliphatic passivation layer, Org. Electron., 2011, 12, 731-735.

[128] A. Devižis, D. Hertel, K. Meerholz, V. Gulbinas, J.-E. Moser, time-independent, high electron mobility in thin PC61BM films: Relevance to organic photovoltaics, Org. Electron., 2014, 15 (12), 3729-3734.

[129] G. W. P. van Pruissen, E. A. Pidko, M. M. Wienk, R. A. J. Janssen, high balanced ambipolar charge carrier mobility in benzodipyrrolidone conjugated polymers, J. Mater. Chem. C, 2014, 2, 731-735

[130] I. Riedel, V. Dyakonov, influence of electronic transport properties of polymer fullerene blends on the performance of bulk heterojunction photovoltaic devices, Phys. Stat. Sol. (a), 2004, 201 (6), 1332-1341.

[131] A. Kokil, K. Yang, J. Kumar, techniques for characterization of charge carrier mobility in organic semiconductors, J. Polym. Sci. Part B Polym. Phys., 2012, 50, 1130-1144.

[132] M. M. Mandoc, L. J. A. Koster, P. W. M. Blom, optimum charge carrier mobility in organic solar cells, Appl. Phys. Lett., 2007, 90, 133504.

[133] M. Abbas, N. Tekin, balanced charge carrier mobilities in bulk heterojunction organic solar cells, Appl. Phys. Lett., 2012, 101, 073302.

[134] L. Sims, U. Hörmann, R. Hanfland, R. C.I. MacKenzie, F. R. Kogler, R. Steim, W. Brütting, P. Schilinsky, investigation of the s-shape caused by the hole selective layer in bulk heterojunction solar cells, Org. Electron., 2014, 15, 2862-2867.

[135] I. P. Murray, S. J. Lou, L. J. Cote, S. Loser, C. J. Kadleck, T. Xu, J. M. Szarko, B. S. Rolczynski, J. E. Johns, J. Huang, L. Yu, L. X. Chen, T. J. Marks, M. C. Hersam, graphene oxide interlayers for robust, high-efficiency organic photovoltaics, J. Phys. Chem. Lett., 2011, 2(24), 3006-3012.

[136] S. Murase, Y. Yang, solution processed MoO3 interfacial layer for organic photovoltaics prepared by a facile synthesis method, Adv. Mater., 2012, 24, 2459-2462.

[137] Z. Tan, L. Li, C. Cui, Y. Ding, Q. Xu, S. Li, D. Qian, Y. Li, solution-processed tungsten oxide as an effective anode buffer layer for high performance polymer solar cells, J. Phys. Chem. C, 2012, 116 (35), 18626-18632.

[138] J. Wagner, M. Gruber, A. Wilke, Y. Tanaka, K. Topczak, A. Steindamm, U. Hörmann, A. Opitz, Y. Nakayama, H. Ishii, J. Pflaum, N. Koch, W. Brütting, identification of different origins for s-shaped current voltage characteristics in planar heterojunction organic solar cells, J. Appl. Phys., 2012, 111, 054509.

[139] S. Esiner, T. Bus, M. M. Wienk, K. Hermans, R. A. J. Janssen, quantification and validation of the efficiency enhancement reached by application of a retroreflective light trapping texture on a polymer solar cell, Adv. Energy Mater., 2013, 3 (8), 1013-1017.

[140] J. Wagner, M. Gruber, A. Hinderhofer, A. Wilke, B. Bröker, J. Frisch, P. Amsalem, A. Vollmer, A. Opitz, N. Koch, F. Schreiber, W. Brütting, high fill factor and open circuit voltage in organic photovoltaic cells with diindenoperylene as donor material, Adv. Func. Mater., 2010, 20, 4295-4303.

[141] U. Hörmann, C.r Lorch, A. Hinderhofer, A. Gerlach, M. Gruber, J. Kraus, B. Sykora, S. Grob, T. Linderl, A. Wilke, A. Opitz, R. Hansson, A. S. Anselmo, Y. Ozawa, Y. Nakayama, H. Ishii, N. Koch, E. Moons, F. Schreiber, W. Brütting, Voc from a morphology point of view: the influence of molecular orientation on the open circuit voltage of organic planar heterojunction solar cells, J. Phys. Chem. C, 2014, 118, 26462-26470.

[142] M. Gruber, M. Rawolle, J. Wagner, D. Magerl, U. Hörmann, J. Perlich, S. V. Roth, A. Opitz, F. Schreiber, P. Müller-Buschbaum, W. Brütting, correlating structure and morphology to device performance of molecular organic donor-acceptor photovoltaic cells based on diindenoperylene (DIP) and C60, Adv. Energy Mater., 2013, 3, 1075-1083.

[143] Z. He, C. Zhong, S. Su, M. Xu, H. Wu, Y. Cao, enhanced power-conversion efficiency in polymer solar cells using an inverted device structure, Nat. Photonics, 2012, 6, 593-597.

[144] V. Gupta, A. K. K. Kyaw, D. H. Wang, S. Chand, G. C. Bazan, A. J. Heeger, Barium: an efficient cathode layer for bulk heterojunction solar cells, Sci. Rep., 2013, 3, 1965.

[145] K. Sun, Z. Xiao, S. Lu, W. Zajaczkowski, W. Pisula, E. Hanssen, J. M. White, R. M. Williamson, J. Subbiah, J. Quyang, A. B. Holmes, W. W. H. Wong, D. J. Jones, a molecular nematic liquid crystalline material for high performance organic photovoltaics, Nat. Commun., 2015, DOI: 10.1038/ncomms7013.

[146] B. Kan, Q. Zhang, M. Li, X. Wan, W. Ni, G. Long, Y. Wang, X. Yang, H. Feng, Y. Chen, solution-processed organic solar cells based on dialkylthiol-substitued benzodithiophene unit with efficiency near 10%, J. Am. Chem. Soc., 2014, 136(44), 15529-15532.

[147] W. Shockley, H. J. Queisser, detailed balance limit of efficiency of p-n junction solar cells, J. Appl. Phys., 1961, 32 (3), 510-519.

[148] M. Gruber, J. Wagner, K. Klein, U. Hörmann, A. Opitz, M. Stutzmann, W. Brütting, thermodynamic efficiency limit of molecular donor-acceptor solar cells and its application to diindenoperylene/C60-based planar heterojunction devices, Adv. Energy Mater., 2012, 2, 1100-1108.

[149] U. Hörmann, J. Kraus, M. Gruber, C. Schuhmair, T. Linderl, S. Grob, S. Kapfinger, K. Klein, M. Stutzman, H. J. Krenner, W. Brütting, quantification of energy losses in organic solar cells from temperature-dependent device characteristics, Phys. Rev. B, 2013, 88, 235307.

[150] A. Wilke, J. Endres, U. Hörmann, J. Niederhausen, R. Schlesinger, J. Frisch, P. Amsalem, J. Wagner, M. Gruber, A. Opitz, A. Vollmer, W. Brütting, A. Kahn and N. Koch, correlation between interface energetics and open circuit voltage in organic photovoltaic cells, Appl. Phys. Lett., 2012, 101, 233301.

[151] M. C. Scharber, D. Mühlbacher, M. Koppe, P. Denk, C. Waldauf, A. J. Heeger, C. J. Brabec, design rules for donors in bulk-heterojunction solar cells-towards 10% energy conversion efficiency, Adv. Mater., 2006, 18, 789-794.

[152] A. De Vos, detailed balance limit of the efficiency of tandem solar cells, J. Phys. D: Appl. Phys., 1980, 13. 839-846.

[153] B. Minnaert, M. Burgelman, efficiency potential of organic bulk heterojunction solar cells, Prog. Photovolt: Res. Appl., 2007, 15, 741-748.

[154] R. R. Lunt, T. P. Osedach, P. R. Brown, J. A. Rowehl, V. Bulovic, practical road map and limits to nanostructured photovoltaics, Adv. Mater., 2011, 23, 5712-5727.

[155] G. Dennler, M.C. Scharber, T. Ameri, P. Denk, K. Forberich, C. Waldauf, C. J. Brabec, design rules for donors in bulk-heterojunction tandem solar cells-towards 15% energy-conversion efficiency, Adv. Mater., 2008, 579-583.

[156] M. C. Scharber, D. Mühlbacher, M. Koppe, P. Denk, C. Waldauf, A. J. Heeger, C. J. Brabec, design rules for donors in bulk-heterojunction solar cells-towards 10% energy conversion efficiency, Adv. Mater., 2006, 18, 789-794.

[157] B. Minnaert, P. Veelaert, guidelines for the bandgap cmbinations and absorption windows for organic tandem and triple junction solar cells, Materials, 2012, 5, 1933-1953.

[158] J. You, L. Dou, K. Yoshimura, T. Kato, K. Ohya, T. Moriarty, K. Emery, C. C. Chen, J. Gao, G. Li, Y. Yang, a polymer tandem solar cell with 10.6% power conversion efficiency, Nat. Commun., 2013, 4, 1446.

[159] Y. Liu, C. C. Chen, Z. Hong, J. Gao, Y. Yang, H. Zhou, L. Dou, G. Li, Y. Yang, solution-processed small molecule solar cells: breaking the 10% power conversion efficiency, Sci. Rep., 2013, 3, 3356.

[160] C. C. Chen, W. H. Chang, K. Yoshimura, K. Ohya, J. You, J. Gao, Z. Hong, Y. Yang, an efficient triple-junction polymer solar cell having a power conversion efficiency exceeding 11%. Adv. Mater., 2014, 26, 5670-5677

[161] A. Hadipour, B. de Boer, P. W. M. Blom, device operation of organic tandem solar cells, Org. Electron., 2008, 9, 617-624.

[162] Y. Yuan, J. Huang, G. Li, intermediate layers in tandem organic solar cells, Green, 2011, 1, 65-80.

[163] S. Sista, Z. Hong, L. Chen, Y. Yang, tandem polymer photovoltaic cells- current status, challenges and future outlook, Energy Environ. Sci., 2011, 4, 1606-1620.

[164] S. Kouijzer, S. Esiner, C. H. Frijters, M. Turbiez, M. M. Wienk, R. A. J. Janssen, efficient inverted tandem polymer solar cells with a solution-processed recombination layer, Ad. Energy Mater., 2012, 2, 945-949.

[165] A. Hadipour, B. de Boer, P. W. M. Blom, organic tandem and multi-junction solar cells, Adv. Funct. Mater., 2008, 18, 169-181.

[166] R. Schueppel, R. Timmreck, N. Allinger, T. Mueller, M. Furno, C. Uhrich, K. Leo, M. Riede, controlled current matching in small molecule organic tandem solar cells using doped space layers, J. Appl. Phys., 2010, 107, 044503.

[167] E. New, T. Howells, P. Sullivan, T. S. Jones, small molecule tandem organic photovoltaic cells incorporating an $\alpha$-NPD optical spacer layer, Org. Electron., 2013, 14, 2353-2359.

[168] J. Gilot, M. M. Wienk, R. A. J. Janssen, optimizing polymer tandem solar cells, Adv. Mater., 2010, 22, E67-E71.

[169] J. Y. Kim, K. Lee, N. E. Coates, D. Moses, T. Q. Nguyen, M. Dante, A. J. Heeger, efficient tandem polymer solar cells fabricated by all solution processing, Science, 2007, 317, 222-225.

[170] L. A. A. Pettersson, L. S. Roman, O. Inganäs, modeling photocurrent action spectra of photovoltaic devices based on organic thin films, J. Appl. Phy., 1999, 86(1), 487

[171] P. Peumans, A. Yakimov, S. R. Forrest, small molecular weight organic thin film photodetectors and solar cells, J. Appl. Phys., 2003, 93 (7), 3693-3723

[172] Y. Long, L. Shen, S. Ruan, W. Yu, Y. Wang, Q. Zeng, J. Luo, top-to-bottom optimization of the optical performance of the tandem organic solar cells with thin metal film as interlayer, Appl. Phys. Lett., 2012, 100, 103304.

[173] W. Eerenstein, L. H. Slooff, S. C. Veenstra, J. M. Kroon, optical modeling as optimization tool for single and double junction polymer solar cells, Thin Solid Films, 2008, 516, 7188-7192.

[174] E. Zimmermann, P. Ehrenreich, T. Pfadler, J. A. Dorman, J. Weickert, L. Schmidt-Mende, erroneous efficiency reports harm organic solar cell research, Nat. Photonics, 2014, 8, 669-672.

[175] J. Gilot, M. M. Wienk, R. A. J. Janssen, measuring the external quantum efficiency of two terminal polymer tandem solar cells, Adv. Funct. Mater., 2010, 20, 3904-3911.

[176] G. Dennler, K. Forberich, T. Ameri, C. Waldauf, P. Denk, C. J. Brabec, K. Hingerl, A. J. Heeger, design of efficient organic tandem cells: on the interplay between molecular absorption and layer sequence, J. Appl. Phys., 2007, 102, 123109.

[177] T. Ameri, N. Li, C. J. Brabec, highly efficient organic tandem solar cells: a follow up review. Energy Environ. Sci., 2013, 6, 2390-2413.

[178] P. Peumans, A. Yakimov, S. R. Forrest, small molecular weight organic thin-film photodetectors and solar cells, J. Appl. Phys., 2003, 93, 3693-3723.

[179] L. Dou, J. You, J. Yang, C. C. Chen, Y. He, S. Murase, T. Moriarty, K. Emery, G. Li, Y. Yang, tandem polymer solar cells featuring a spectrally matched low bandgap polymer, Nat. Photonics, 2012, 6, 180-185.

[180] V. S. Gevaerts, A. Furlan, M. M. Wienk, M. Turbiez, R. A. J. Janssen, solution processed polymer tandem solar cell using efficient small and wide bandgap polymer:fullerene blends, Adv. Mater., 2012, 24, 2130-2134.

[181] W. Li, A. Furlan, K. H. Hendriks, M. M. Wienk, R. A. J. Janssen, efficient tandem and triple junction polymer solar cells, J. Am. Chem. Soc., 2013, 135, 5529-5532.

[182] M. Punke, S. Valouch, S. W. Kettlitz, N. Christ, C. Gärtner, M. Gerken, U. Lemmer, dynamic characterization of organic bulk heterojunction photodetectors, App. Phys. Lett., 2007, 91, 071118.

[183] S. Züfle, N. Christ, S. W. Kettlitz, S. Valouch, U. Lemmer, influence of temperature-dependent mobilities on the nanosecond response of organic solar cells and photodetectors, Appl. Phys. Lett., 2010, 97, 063306.

[184] W. W. Tsai, Y. C. Chao, E. C. Chen, H. W. Zan, H. F. Meng, C. S. Hsu, increasing organic vertical carrier mobility for the application of high speed bilayered organic photodetector, Appl. Phys. Lett., 2009, 95, 213308.

[185] P. E. Keivanidis, P. K. H. Ho, R. H. Friend, N. C. Greenham, the dependence of device dark current on the active layer morphology of solution-processed organic photodetectors, Adv. Func. Mater., 2010, 20, 3895-3903.

[186] K. J. Baeg, M. Binda, D. Natali, M. Caironi, Y. Y. Noh, organic light detectors: photo-diodes and phototransistors, Adv. Mater., 2013, 25, 4267-4295.

[187] S. Valouch, C. Hönes, S. W. Kettlitz, N. Christ, H. Do, M. F. G. Klein, H. Kalt, A. Colsmann, U. Lemmer, solution processed small molecule organic interfacial layers for low dark current polymer photodiodes, Org. Electron., 2012, 13, 2727-2732.

[188] X. Gong, M. Tong, Y. Xia, W. Cai, J. S. Moon, Y. Cao, G. Yu, C. L. Shieh, B. Nilsson, A. J. Heeger, high detectivity polymer photodetectors with spectral response from 300 nm to 1450 nm, Science, 2009, 325, 1665-1667.

[189] M. Binda, A. Iacchetti, D. Natali, L. Beverina, M. Sassi, high detectivity squaraine-based near infrared photodetector with nA/cm2 dark current, Appl. Phys. Lett., 2011, 98, 073303.

[190] S. H. Wu, W. L. Li, B. Chu, Z. S. Su, F. Zhang, C. S. Lee, high performance small mol-ecule photodetector with broad spectral response range from 200 to 900 nm, Appl. Phys. Lett., 2011, 99, 023305.

[191] T. Agostinelli, M. Campoy-Quiles, J. C. Blakesley, R. Speller, D. D. C. Bradley, J. Nel-son, a polymer/fullerene based photodetector with extremely low dark current for x-ray medi-cal imaging applications, Appl. Phys. Lett., 2008, 93, 203305.

[192] M. Ramuz, L. Bürgi, C. Winnewisser, P. Seitz, high sensitivity organic photodiodes with low dark currents and increased lifetimes, Org. Electron., 2008,9,369-376.

[193] L. Li, Y. Huang, J. Peng, Y. Cao, X. Peng, highly responsive organic near-infrared pho-todetectors based on a porphyrin small molecule, J. Mater. Chem. C, 2014, 2, 1372-1375.

[194] R. C. Jones, Proposal of the detectivity D** for detectors limited by radiation noise, J. Opt. Soc. Am., 1960, 50, 1058-1059.

# Chapter II. Transparent OPVs

**Semitransparent organic photovoltaics using a near-infrared absorbing cyanine dye**

Hui Zhang[a], Gaetan Wicht[a], Christina Gretener[b], Matthias Nagel[a], Frank Nüesch[a,c], Yaroslav Romanyuk[b], Jean-Nicolas Tisserant[a], Roland Hany[a]*

[a] H. Zhang, Dr. G. Wicht, Dr. M. Nagel, Prof. F. Nüesch, J.-N. Tisserant, Dr. R. Hany, Empa, Swiss Federal Institute for Materials Science and Technology, Laboratory for Functional Polymers, Überlandstrasse 129, CH-8600 Dübendorf, Switzerland.

[b] C. Gretener, Dr. Y. Romanyuk, Empa, Laboratory for Thin Films and Photovoltaics.

[c] Institut des Matériaux, Ecole Polytechnique Fédéral de Lausanne, EPFL Station 12, CH-1015 Lausanne, Switzerland.

[*] Correspondence should be addressed to  Dr. Roland Hany, Empa, Überlandstr. 129,

8600 CH-Dübendorf, Switzerland

Phone: +41 58 765 4084; fax: +41 58 765 4012;

e-mail: roland.hany@empa.ch

**Declaration:** I fabricated all the devices, performed the AFM, UV-Vis, IPCE and I-V measurements, prepared samples for TEM, carried out all data analysis, contributed to project planning and manuscript preparation.

**Abstract:** A selective near-infrared absorbing heptamethine cyanine dye (Cy7-P) electron donor was used for the fabrication of bilayer solar cells with the acceptor $C_{60}$. Using a reflective metal top electrode, solar cell optimization resulted in an external power conversion efficiency ($\eta$) of 1.5% for layer thicknesses of ~20 nm for Cy7-P and of ~40 nm for $C_{60}$, with using either PEDOT:PSS or $MoO_3$ as anode and $Alq_3$ as cathode buffer layers. Highly transparent devices were then fabricated by using silver/$Alq_3$ cathodes. Average visible transmittance (450 – 670 nm) values of, for example, 67.2% ($\eta = 0.7\%$), 62.1% ($\eta = 0.9\%$) or 50% ($\eta = 1\%$) were obtained for different thickness combinations of silver and $Alq_3$. Optimized solar cells had a maximum transparency of 79.8% at 568 nm. The operational stability under 1 sun illumination was $T_{80} = 30$ hours, after which 80% of the initial cell performance was reached.

**Keywords:** Organic photovoltaics, cyanine dye, transparent solar cell, fullerene

## 1. Introduction

Solution-processed, small molecule-based organic photovoltaic (SM-OPV) cells are attracting interest in research and industrial laboratories due to their potential as low-cost, flexible and lightweight devices for solar energy conversion [1,2]. Power conversion efficiencies ($\eta$) of SM-OPV devices are rapidly increasing. For simple bilayer cells and using $C_{60}$ as electron acceptor, $\eta = 1.5\%$ (using subnaphthalocyanine [3]), $\eta = 2.6\%$ (using azadipyrromethenes [4]), $\eta = 3.3\%$ (using diketopyrrolopyrrole derivatives [5]) or $\eta = 5.7\%$ (using squaraine dyes [6]) have been reported. Bulk heterojunction SM-OPV cells with soluble fullerenes as acceptors performed even better, and $\eta$ ranging between 4.4% and 6.7% were achieved, with donors based on diketopyrroropyrrole [7], thiophenes end-capped with alkyl cyanoacetate [8] or rhodanine groups [9], such as a push-pull thiophene-thiadiazolopyridine chromophore [10].

As for polymeric systems [11], high-performing SM-OPV cells require tailored redox energy levels of the donor-acceptor components, high and balanced charge-carrier mobilities and a film morphology that allows for loss-free charge transport pathways to the electrodes. In addition, a broad optical absorption around the peak (~700 nm) of the solar spectral photon irradiance is prerequisite for efficient light capture and a high resulting photocurrent. Therefore, small molecule dyes for OPV applications have primarily been developed so far that absorb over the whole wavelength region of visible light and into the near-infrared (NIR) region [3-10].

By making the organic layer thin enough, not all of the incoming light is absorbed and the active film becomes semitransparent. Combined with transparent, non-reflecting electrodes, this

has allowed for the fabrication of semitransparent (SM and polymeric) OPV cells that have been proposed for applications such as power-generating windows that provide sun shading at the same time. For example, by using the poly(3-hexylthiophene) / soluble fullerenes material combination, which absorbs in the visible wavelength range between ~400 – 650 nm, semi-transparent solar cells with η between 1.5% and 3% were manufactured [12-15].

Clearly, for many window-integrated applications OPV cells that do not absorb visible light at all would be advantageous. Visible photopic light corresponds to the wavelength range of ~450 – 670 nm, where the relative spectral sensitivity of the human eye is above 5% [16,17]. Not many organic materials with selective NIR absorption are available [18] and important steps towards transparent OPV cells were reported only recently [19]. Using chloroaluminum phthalocyanine as electron donor and $C_{60}$ as acceptor, SM-OPV cells were designed with η = 1.7% and a visible transparency of >55% [17]. In another example, a SM-OPV solar cell with the $Ph_2$-benz-bodipy/$C_{60}$ combination resulted in η = 2.4% with an average transmittance in the 400 – 750 nm wavelength range of 47.9% [20]. Finally, by using a NIR light-sensitive polymer (PBDTT-DPP) as electron donor and [6,6]-phenyl-$C_{61}$-butyric acid methyl ester (PCBM) as electron acceptor, promising solution-processed polymer OPV cells with η ~ 4%, an average visible transmittance (AVT) of 61% and a maximum transmittance of 66% at 550 nm were fabricated [21].

Cyanine dyes are charged polymethine colorants where a usually positive charge is delocal-ized over an odd number of $sp^2$ carbon atoms forming the π-conjugated bridge between elec-tron-donating or –accepting groups [22,23]. Cyanine dyes are characterized by a sharp, very intense absorption band. The absorption maximum is shifted to longer wavelength with in-creasing number of double bonds (~100 nm per additional methine group) [24]; therefore, a desired absorption throughout the visible and into the NIR region (with absorption peak max-ima > 1000 nm [25]) can be adjusted by synthesizing cyanine dyes with the appropriate num-ber of methine units. Similarly, a conjugated polymer that absorbs solely in the NIR wave-length region with an absorption maximum of 1000 nm was obtained by connecting cyanine dyes in a head-to-tail fashion [26].

Cyanine dyes were also studied for photovoltaics. As an important advantage, cyanine dyes are relatively cheap and commercially available in large quantities or they can be synthesized by straightforward chemistry. The best performance (η = 3.7% [27]) for a purely organic solar cell was achieved for a bilayer heterojunction when using a trimethine cyanine dye with a film absorption maximum in the visible at 578 nm as electron donor and $C_{60}$ as acceptor. An

organic salt consisting of a heptamethine cyanine cation and a cyanine anion was used with PCBM in organic bulk heterojunction cells ($\eta \sim 0.4\%$ [28]). Thin films of this cyanine-cyanine salt displayed pronounced light-harvesting properties in the NIR range with peak absorptions at ~820 nm and ~940 nm. In both cases, a non-transparent metal cathode was used as top contact for solar cells [27,28]. A heptamethine cyanine dye was synthesized for use in dye-sensitized solar cells with a maximum spectral response at 800 nm [29].

Here, we report on bilayer solar cells using a commercially available heptamethine dye with terminal benzindol moieties as electron donor and $C_{60}$ as electron acceptor. Solar cell performance was first optimized using a reflective aluminium back contact. In a second step, semi-transparent devices were fabricated by using thin silver/$Alq_3$ top electrodes. The feasibility of cells with an average visible transmittance of over 65% and a performance of 1% was demonstrated. For any semitransparent solar cell application, a compromise must then be made between maximized transparency and performance.

## 2. Experimental

3-Butyl-2-(2-[3-[2-(3-butyl-1,1-dimethyl-1,3-dihydro-benzo[e]indol-2-ylidene)-ethylidene]-2-chloro-cyclohex-1-enyl]-vinyl)-1,1-dimethyl-1H-benzo[e]indolium hexafluorophosphate (Cy7-P, FEW Chemicals), poly(3,4-ethylenedioxythiophene):poly(styrenesulfonate), (PEDOT:PSS, Sigma-Aldrich, conductivity 1 S cm$^{-1}$), 2,2,3,3-tetrafluoropropanol (TFP) and chlorobenzene (CB, Sigma-Aldrich) were used as received.

Indium tin oxide-coated glass substrates (ITO, Thin Film Devices, 140 nm, resistivity 20 Ohms square$^{-1}$) were sequentially cleaned in acetone, ethanol, detergent and de-ionized water. As hole-extracting layer, PEDOT:PSS ($75 \pm 10$ nm) was spin coated onto ITO followed by heating to 120 $^{\circ}$C for 15 min. Alternatively, thin anode films of $MoO_3$ (Alfa Aesar, 99.9995%) were deposited by thermal evaporation from a tungsten boat at a base pressure of $<10^{-6}$ mbar onto unheated ITO substrates which were rotated during deposition. Although we designate $MoO_3$ throughout, Rutherford backscattering spectroscopy on silicon substrates showed that the material was actually slightly oxygen deficient (O/Mo = 2.94).

Cy7-P layers were spin coated from CB solutions inside a nitrogen-filled glove box (< 5 ppm $H_2O$, < 6 ppm $O_2$). Layers with different thicknesses of the $C_{60}$ fullerene (SES Research, 99.9%) and of the exciton blocking layers tris-(8-hydroxyquinoline) aluminium ($Alq_3$, Sigma-Aldrich, 99.995%) or bathocuproine (BCP, Sigma-Aldrich, 96%) were then deposited by thermal sublimation under vacuum at a pressure of $3\times10^{-6}$ mbar. As cathodes, either a 35 nm thick film of Al (Cerac, 99.999%) or Ag (Cerac, 99.99%, different thicknesses) were

evaporated through a shadow mask to define eight solar cells on each substrate with active areas of 3.1 mm$^2$ or 7.1 mm$^2$.

Film thicknesses were determined by profilometry (Ambios XP1), AFM measurements were performed on a Nanosurf Mobile S in tapping mode at a resonance frequency of 170 kHz using silicon cantilevers. Current-voltage (J-V) characteristics were measured using 100 mW cm$^{-2}$ simulated AM 1.5G solar irradiation on a calibrated solar simulator from Spectra-Nova. The incident photon-to-current conversion efficiency (IPCE) was measured using a monochromator and the light from a 300 W Xe lamp together with an AM1.5G filter set. The monochromatic light intensity was determined using a calibrated Si-diode. Absorption spectra for solutions and thin films were measured on a Varian Cary 50 UV-vis spectrophotometer using a quartz cuvette or a glass substrate as baseline. Thin films and solar cells were characterized via illumination through the anode side (glass/ITO) only.

To study the intrinsic lifetime, cells were stored in the glove box in the dark. A homemade airtight transfer box was used to measure cell J-V characteristics outside the glove box. The degradation over a period of 100 h was measured under $N_2$ at 1 sun illumination intensity. For TEM measurements (CM 30 Philips, 300 kV operating voltage), amorphous carbon coated TEM grids (Agar Scientific) were dip-coated in CB (6.5 mg mL$^{-1}$) Cy7-P solutions and were then dried overnight. Optical constants for Cy7-P and Ag were determined by spectroscopic ellipsometry (M-2000, J.A. Woolam Co., Inc.). For the ellipsometry measurement, a 23.1 nm thick Cy7-P film was spin coated from CB onto a silicon wafer, and 12 nm Ag were evaporated onto an ITO/glass substrate. Optical constants were taken from the literature for glass, ITO and PEDOT:PSS [30], for $C_{60}$ [31], for Al [32], for Alq$_3$ [33] and for the 8 nm Ag layer [34]. For thicker Ag layers (12 – 100 nm) the measured values from ellipsometry were taken.

Cyclic voltammetry measurements were recorded on a PGStat μ30 potentiostat (Autolab) using a standard three electrodes cell system with a glassy carbon rotating disc (3 mm in diameter) as the working electrode, a platinum counter electrode and a water-free double junction Ag/AgCl reference electrode system separated by a ceramic and a sleeve diaphragm, respectively (Metrohm). Electrolyte of the inner couple system was 0.1 M tetrabutyl ammonium chloride in acetonitrile, whereas the outer bridging system was 0.1 M tetrabutyl ammonium perchlorate in acetonitrile. Cy7-P (100 mg) and $C_{60}$ (140 mg) were measured in degassed *ortho*-dichlorobenzene (ODCB) solutions (~40 mL) in an argon atmosphere using 0.1 M tetrabutyl ammonium hexafluorophosphate as supporting electrolyte. The ferrocene/ferrocenium (Fc/Fc$^+$) redox couple was used as internal reference. As an approximation of the formal po-

tential of the redox couples, half-wave potentials $E_{1/2} = \frac{1}{2}(E_{pc} + E_{pa})$ were evaluated, with the cathodic and anodic peak potentials, $E_{pc}$ and $E_{pa}$. $E_{1/2}$ for $Fc/Fc^+$ was 1.17 V against the Ag/AgCl reference electrode.

## 3. Results and discussion

### 3.1. Optical, thin film and electrochemical properties of Cy7-P
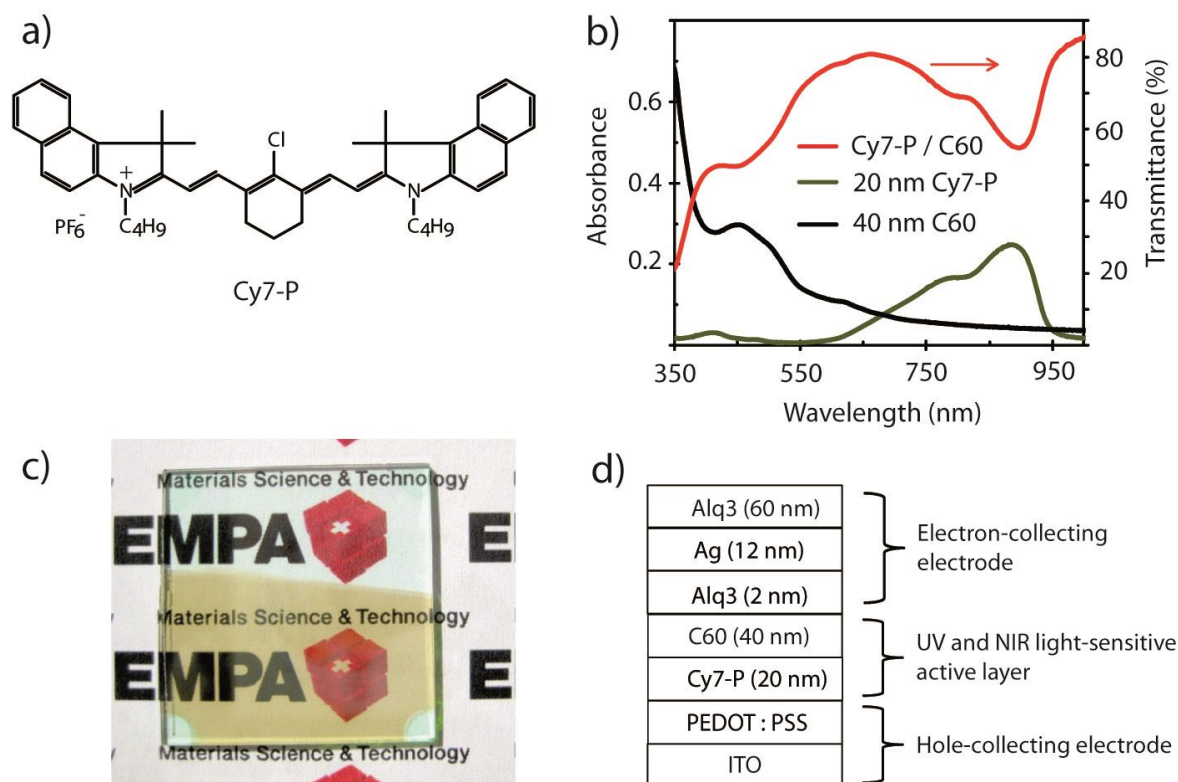


Figure 2- 1 (a) Molecular structure of Cy7-P. (b) Absorbance spectra of separate $C_{60}$ and Cy7-P films, and transmittance spectrum of the corresponding bilayer film. (c) The Empa logo covered with a Cy7-P coated glass plate. $C_{60}$ was evaporated on the lower half. (d) Schematic of the device architecture for a semitransparent Cy7-P/$C_{60}$ solar cell.

Cy7-P (Fig. 2-1a) is a low band gap dye ($\lambda_{max}$ = 839 nm in CB) with a high molar extinction coefficient ($\varepsilon_{(CB, \lambda(839\,nm))}$) = 2.7x10$^5$ L mol$^{-1}$ cm$^{-1}$). From the onset absorption edge $\lambda^{abs}_{onset}$ = 880 nm at higher wavelengths, the optical band gap in CB solution $E_g^{opt}$ = 1.41 eV was determined. For Cy7-P films, the maximum absorption was at $\lambda_{max}$ = 885 nm (Fig. 2-1b). The picture of Fig. 2-1c demonstrates that a 20 nm thick film of Cy7-P is highly transparent to visible light with a faint green color. The lower part of the glass plate (2.5 cm x 2.5 cm) in Fig. 2-1c was covered with an additional 40 nm thick film of $C_{60}$, resulting in a shade of brown for the active, light-absorbing organic layer. This Cy7-P/$C_{60}$ photoactive layer has a maximum visi-

ble transmittance of 80.7% at 666 nm and an AVT of 68.5%, but is strongly absorbing in the UV and NIR wavelength region (Fig. 2-1b).

Cy7-P films were smooth with root mean square, rms, roughnesses < 0.4 nm from AFM images, and rms values did not change upon mild annealing (up to 100 $^{\circ}$C for 1h). TEM experiments were carried out to demonstrate possible film crystallinity. However, from TEM diffraction mode images, no crystallinity could be detected and films appeared amorphous (Fig. 2-2a).
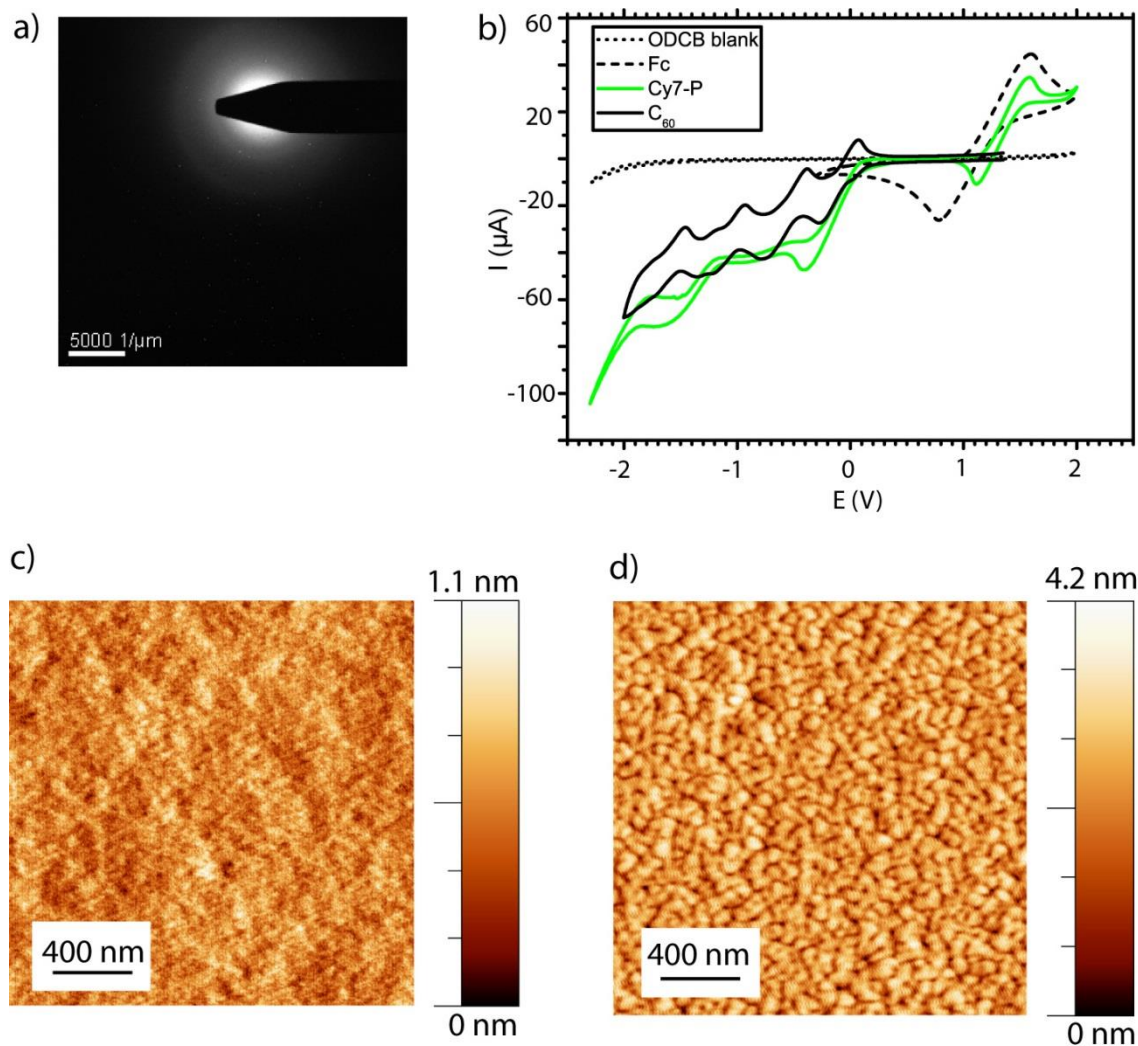


Figure 2- 2 (a) TEM diffraction mode image of a thin Cy7-P film. (b) Cyclic voltammograms of Cy7-P, $C_{60}$ and Fc. (c) AFM phase image of a Cy7-P / PCBM  blend film, and (d) after selective removal of Cy7-P.

In cyclic voltammetry experiments, the first half-wave oxidation potential for Cy7-P was $E_{\frac{1}{2},ox}$ = +0.18 V against Fc/Fc$^{+}$, and the first half-wave reduction potential was $E_{\frac{1}{2},red}$ = -1.31 V against Fc/Fc$^{+}$ (Fig. 2-2b). For $C_{60}$, $E_{\frac{1}{2},red}$ = -1.25 V against Fc/Fc$^{+}$, in agreement with liter-

ature [35] ($E_{½,red}$ = -1.13 V). Assuming that $E_{½,ox}$ and $E_{½,red}$ correspond to the HOMO and LUMO levels, and with an energy level of -5.10 eV vs. vacuum for Fc/Fc$^+$ [36], the redox levels vs. vacuum can be calculated: $C_{60}$ (LUMO) = -3.85 eV, Cy7-P (LUMO) = -3.79 eV, Cy7-P (HOMO) = -5.28 eV. For Cy7-P, the electrochemical band gap ($E_g^{el}$ = 1.49 eV) and the optical band gap differed by 0.08 eV.

Thin films (~100 nm) of spin-coated blends of Cy7-P and PCBM (1:1 weight ratio in CB) were tested for use in bulk heterojunction solar cells. AFM images of as-prepared films showed almost flat surfaces (Fig. 2-2c). Removal of Cy7-P by elution with the selective solvent TFP left the fullerene phase that was composed of a network of individual ~100 nm large PCBM domains (Fig. 2-2d). This blend film was thus composed of scattered PCBM droplets within a continuous film-forming matrix of Cy7-P. The situation resembles morphologies observed for spin coated blends of PCBM and trimethine cyanine dyes, where film formation occurred via a transient bilayer which finally destabilized through effective electrostatic interactions [37]. The Cy7-P/PCBM blend morphology is clearly unfavourable for photovoltaic applications where phase-separated domains with dimensions in the exciton diffusion range and continuous pathways for charge extraction are required. Consequentially, no diode behavior and performance could be measured for corresponding PEDOT:PSS/Cy7-P:PCBM/Al solar cells.

### 3.2. Solar cell optimization

In a first step, Cy7-P/$C_{60}$ bilayer solar cells were systematically optimized for different active layer thicknesses, hole-extracting buffer layers (PEDOT:PSS *vs.* $MoO_3$) and electron-extracting buffer layers ($Alq_3$ *vs.* BCP). For these experiments, a reflective Al back electrode was used. First, Cy7-P layers with thicknesses between ~10 nm and 40 nm were used, with fixed layers for PEDOT:PSS (75 nm), $C_{60}$ (40 nm) and $Alq_3$ (2 nm). The short-circuit current ($J_{sc}$) increased with increasing Cy7-P thickness up to a maximum of $J_{sc}$ = 6.6 mA cm$^{-2}$ at 20 nm, and decreased for thicker films again (Fig. 2-3a). The open-circuit voltage ($V_{oc}$) remained almost constant at ~0.38 V with varying Cy7-P thickness between 20 nm and 40 nm, but $V_{oc}$ decreased markedly to 0.33 V for very thin dye layers. This might be due to the formation of pinholes in thin Cy7-P films. $C_{60}$ then contacts both electrodes at the same time. These direct paths between cathode and anode act as a shunt resistance in parallel with the active part of the device, resulting in a lowering of $V_{oc}$ [38]. Irrespective of the Cy7-P thickness, high fill factors (FF > 58%) were observed. The best performance ($\eta$ = 1.5%) was measured for a Cy7-P thickness of 20 nm (Table 2-1). The average performance from 4 independent cell fabrica-

tion cycles was $J_{sc}$ = 6.2 mA cm$^{-2}$, $V_{oc}$ = 0.38 V, FF = 58.4%, $\eta$ = 1.4%. These cells showed dark currents at -0.5 V of 10$^{-5}$ A cm$^{-2}$ and rectification factors at ±1 V of ~3500.
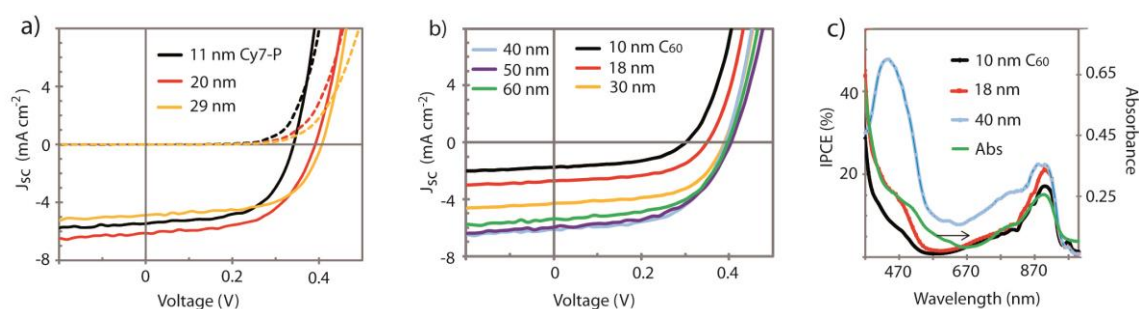


Figure 2- 3 (a) White light (solid lines) and dark (dotted lines) J-V characteristics of ITO/PEDOT:PSS/Cy7-P/C$_{60}$(40nm)/Alq$_3$/Al solar cells with different Cy7-P thicknesses. White light J-V characteristics (b) and IPCE values (c) for corresponding Cy7-P(20nm)/C$_{60}$ solar cells with different C$_{60}$ thicknesses.

Table 2- 1 Selected performance data of Cy7-P(20 nm)/C$_{60}$ (40 nm) bilayer solar cells with Al as cathode.

| Device structure | $J_{sc}$ (mA cm$^{-2}$) | $V_{oc}$ (V) | FF (%) | $\eta$ (%) |
|---|---|---|---|---|
| ITO/Cy7-P/C$_{60}$/2nmAlq$_3$/Al | 4.9 | 0.12 | 46.2 | 0.3 |
| ITO/PEDOT:PSS/Cy7-P/C$_{60}$/Al | 4.3 | 0.29 | 27.6 | 0.3 |
| ITO/PEDOT:PSS/Cy7-P/C$_{60}$/2nmBCP/Al | 5.2 | 0.38 | 53.3 | 1.1 |
| ITO/PEDOT:PSS/Cy7-P/C$_{60}$/2nmAlq$_3$/Al | 6.6 | 0.38 | 58.7 | 1.5 |
| ITO/PEDOT:PSS/Cy7-P/C$_{60}$/9nmAlq$_3$/Al | 1.0 | 0.40 | 16.9 | 0.07 |
| ITO/3nmMoO$_3$/Cy7-P/C$_{60}$/2nmAlq$_3$/Al | 5.6 | 0.40 | 53.2 | 1.2 |
| ITO/5nmMoO$_3$/Cy7-P/C$_{60}$/2nmAlq$_3$/Al | 6.0 | 0.44 | 55.1 | 1.5 |

As a next step, the C$_{60}$ layer thickness (between 10 nm and 60 nm) was varied while keeping the Cy7-P film at 20 nm (Fig. 2-3b). As observed for Cy7-P, $V_{oc}$ collapsed for very thin C$_{60}$ layers. $J_{sc}$ increased sharply with increasing C$_{60}$ thickness and leveled off at ~40 nm. This value corresponds to the exciton diffusion length of C$_{60}$ (40 ± 5 nm [39]). For a layered solar cell configuration, the thicknesses of the active layers should correspond to the exciton diffusion lengths [39]. This is because for thicker films, light is undesirably absorbed in regions too far away from the donor-acceptor heterointerface. The IPCE data shown in Fig. 2-3c confirm that for increasing fullerene layer thickness the additional current is predominantly generated in the wavelength region where C$_{60}$ absorbs.

For bilayer solar cells with $C_{60}$ as acceptor and a wide band gap cyanine dye [40] or copper phthalocyanine [41] as donors, it has been demonstrated that the insertion of a thin electron conducting and exciton blocking layer between $C_{60}$ and the Al cathode greatly improves device performance. These findings could be reconfirmed for the Cy7-P/$C_{60}$ material combination. Omitting such a buffer layer resulted in poor performance (Table 2-1), mainly because of a collapse of FF due to defects at the $C_{60}$/Al cathode interface. Using 2 nm of BCP or $Alq_3$ as buffer layers resulted in an Ohmic contact at the cathode, with $Alq_3$ slightly outperforming BCP. The interlayer has to be chosen very thin, however [42], and a resistive 9 nm thick $Alq_3$ layer suppressed the electron extraction effectively (Table 2-1).

$MoO_3$ is a widely used hole injection material that has been proposed as an effective replacement for PEDOT:PSS [43,44]. $V_{oc}$ values for $MoO_3$ solar cells ($\sim 0.42 \pm 0.02$ V) were larger than for PEDOT:PSS (Table 2-1), probably due to the higher $MoO_3$ valence band energy ($E_v = 5.2 - 5.3$ eV [45]). In contrast, FF were lower, resulting in $\eta \sim 1.5\%$, as was obtained for PEDOT:PSS.

Solar cell performance is currently limited by the $V_{oc}$ of $\sim 0.4$ V. For a related trimethine cyanine dye with the same counter anion $PF_6^-$, that absorbs in the visible, HOMO and LUMO energy levels of -5.5 and -3.4 eV were determined by cyclic voltammetry [46]. The open-circuit voltage of corresponding trimethine cyanine/$C_{60}$ bilayer solar cells was $V_{oc} = 0.65$ V. In general, $V_{oc}$ correlates with the difference of the LUMO of the acceptor ($C_{60}$ for both the trimethine [46] and heptamethine cyanine solar cell in our case) and the HOMO of the donor [36,44]. The difference in $V_{oc}$ (0.65 V – 0.4 V = 0.25 V) between the trimethine cyanine and Cy7-P / $C_{60}$ cells agrees with the difference of the corresponding HOMO energy levels (5.5 eV – 5.28 eV = 0.22 eV). Therefore, the low $V_{oc}$ for Cy7-P solar cells is the direct result of the lower HOMO energy of Cy7-P, as compared to trimethine cyanines.

### 3.3. Towards a transparent Cy7-P solar cell

Starting with a non-transparent 100 nm thick Ag cathode resulted in very similar device characteristics as measured with Al as top contact (Table 2-2). Semitransparent solar cells were then fabricated by replacing the reflective Ag cathode with thinner layers of Ag (8 – 20 nm) [47]. To increase the transparency, $Alq_3$ (20 – 80 nm) was used as an additional external dielectric coating on top of Ag (Fig. 2-1d) [19,20,48]. A comprehensive set of devices with different Ag and $Alq_3$ thickness combinations was fabricated with fixed Cy7-P and $C_{60}$ layers at 20 nm and 40 nm, respectively (Fig. 2-4a,b). Due to interference effects in semitransparent metal films [19], the highest AVT (46.9%) was measured for a 12 nm thick pure Ag layer. For

all Ag thicknesses, the additional Alq$_3$ capping layer considerably improved transmittances, and AVT reached 67.2% for a cathode composed of a 12 nm thick Ag and a 60 nm thick Alq$_3$ layer (Table 2-2). In the wavelength range 400 – 750 nm, the average transmittance for this cell was 57.9%.

Table 2- 2 Selected experimental and calculated average visible transmittances (AVT) and performance data of Cy7-P(20 nm)/C$_{60}$(40 nm) solar cells.

| Device structure, cathode composition | $J_{sc}$ (mA cm$^{-2}$) | $V_{oc}$ (V) | FF (%) | $\eta$ (%) | AVT 450-670 nm (%), exp. | AVT 450-670 nm (%), calc. |
|---|---|---|---|---|---|---|
| 100 nm Ag (non-transparent) | 6.4 | 0.40 | 59.2 | 1.5 | | |
| 8 nm Ag | 3.0 | 0.35 | 47.4 | 0.5 | 42.1 | 42.8 |
| 8 nm Ag / 60 nm Alq$_3$ | 2.6 | 0.36 | 46.9 | 0.4 | 59.4 | 59.7 |
| 12 nm Ag | 4.2 | 0.36 | 51.3 | 0.8 | 46.9 | 47.9 |
| 12 nm Ag / 20 nm Alq$_3$ | 3.7 | 0.39 | 51.3 | 0.7 | 56.0 | 56.3 |
| 12 nm Ag / 40 nm Alq$_3$ | 3.7 | 0.39 | 51.2 | 0.7 | 66.3 | 66.6 |
| 12 nm Ag / 60 nm Alq$_3$ | 3.8 | 0.39 | 49.6 | 0.7 | 67.2 | 69.6 |
| 12 nm Ag / 80 nm Alq$_3$ | 4.0 | 0.39 | 50.1 | 0.8 | 58.8 | 62.4 |
| 16 nm Ag | 5.1 | 0.36 | 46.0 | 0.8 | 39.0 | 39.2 |
| 16 nm Ag / 60 nm Alq$_3$ | 4.7 | 0.40 | 46.3 | 0.9 | 62.1 | 62.6 |
| 20 nm Ag | 5.2 | 0.37 | 53.5 | 1.0 | 29.5 | 31.0 |
| 20 nm Ag / 60 nm Alq$_3$ | 4.8 | 0.39 | 53.3 | 1.0 | 50.0 | 53.7 |
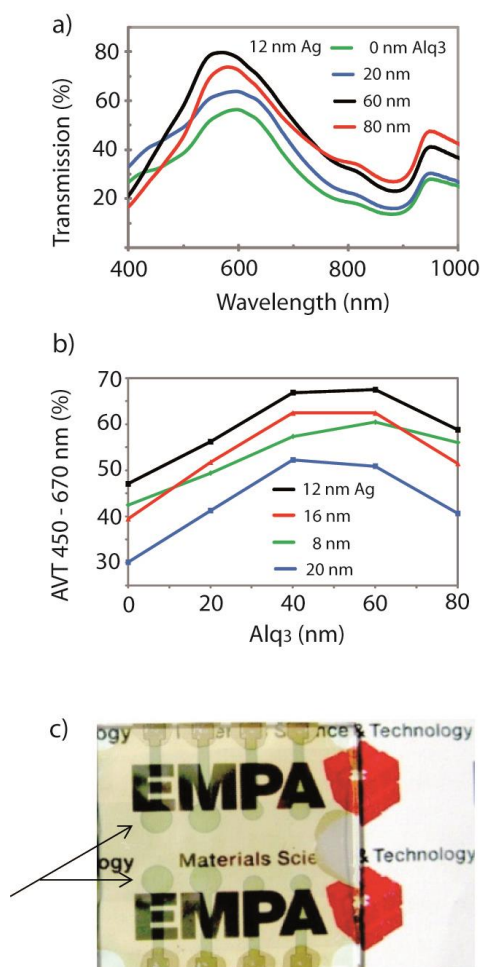
Figure 2- 4 (a) Transmittance spectra of ITO/PEDOT:PSS/Cy7-P(20nm)/C$_{60}$(40nm)/Alq$_3$/Ag(12nm)/Alq$_3$ solar cells with different external Alq$_3$ layer thicknesses. (b) AVT data for solar cells using different thicknesses for the Ag/Alq$_3$ top electrode. (c) Round (arrows) solar cells with a 12 nm thick Ag cathode.

Insight into the influence of the external Alq$_3$ capping layer on the optical electric field distribution in these thin film multilayer devices was obtained from optical simulations. An optical field simulation program (implemented in *Mathematica$^{TM}$*) based on the transfer matrix method [31,39] was used to calculate the normalized spatial distributions of the squared electric field strengths for different individual layer thicknesses. Optical constants were taken from literature or were obtained from ellipsometry measurements for thick Ag films and Cy7-P (Fig. 2-5a, Experimental). As an example, Fig. 2-5b shows simulated optical field distributions for λ = 568 nm of ITO/PEDOT:PSS/20nmCy7-P/40nmC$_{60}$/2nmAlq$_3$/12nmAg/XnmAlq$_3$ stacks with external Alq$_3$ layer thicknesses ranging from 0 – 80 nm. Apparently, the optical electric field distributions inside the device vary considerably by changing the Alq$_3$ thickness. The strength of E$^2$ leaving the device corresponds directly to the transmittance. These calcu-

lated transmittances at $\lambda = 568$ nm were 57% (0 nm Alq$_3$), 65% (20 nm), 81% (60 nm) and 76% (80 nm) (Fig. 2-5b), in good agreement with the experimental values of 54.5% (0 nm Alq$_3$), 62.7% (20 nm), 79.8% (60 nm) and 72.9% (80 nm) (Fig. 2-4a).
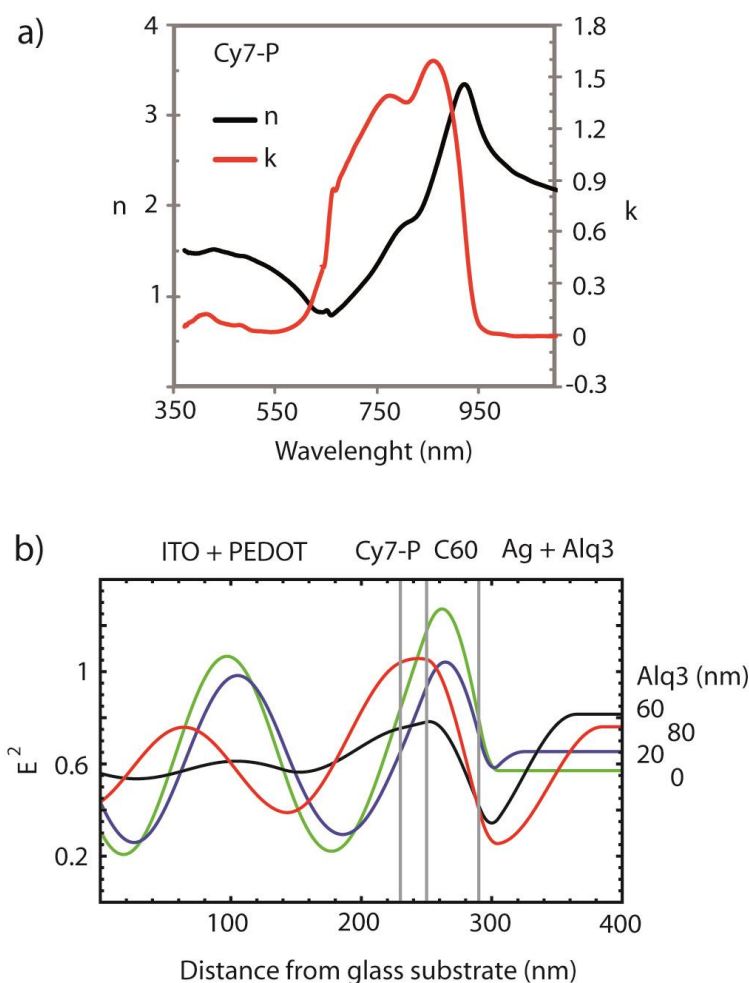


Figure 2- 5 (a) Refractive index (n) and extinction coefficient (k) of Cy7-P. (b) Calculated spatial distributions of the normalized squared optical electric field strengths for $\lambda = 568$ nm inside semitransparent Cy7-P/C$_{60}$ solar cells.

Wavelength-dependent optical modeling was carried out to simulate full transmittance spectra from which calculated AVT were extracted. Data in Table 2-2 demonstrate an excellent agreement between experimental and calculated AVT values. Simulations also suggested that highest AVT will always result for a cathode composed of 12 nm Ag and 60 nm Alq$_3$, irrespective of the Cy7-P (20 – 40 nm) and C$_{60}$ (30 – 50 nm) active layer thicknesses.

For a particular cathode composition, calculated AVT values varied only slightly for different thicknesses of the light-harvesting layers. We also fabricated selected semitransparent solar cells with fixed top cathodes but different thickness combinations of Cy7-P and C$_{60}$ layers

(Fig. 2-6). In agreement with modeling, experimental AVT variations were indeed rather small.

Performance data in Fig. 2-6 showed again highest values for $J_{sc}$ and $\eta$ for layer thicknesses of 20 nm cyanine and 40 nm $C_{60}$, in agreement with results found for cells with an Al top contact. It is obvious that semitransparent solar cells have a lower performance compared to devices that use a highly reflective back metal contact. For thin Ag layers, $J_{sc}$ decreased due to reduced light reflection and a compromise must be found between overall transmittance and solar cell performance (Table 2-2, Fig. 2-4c). Addition of the $Alq_3$ capping layer showed the beneficial influence of increasing AVT strongly with only small losses of $J_{sc}$. For the Cy7-P/$C_{60}$ solar cell, promising semitransparent cathodes could consist of 16 nm or 20 nm thick Ag with a 60 nm thick $Alq_3$ coating, resulting in AVT of over 50% and $\eta$ close to 1% (Table 2-2).
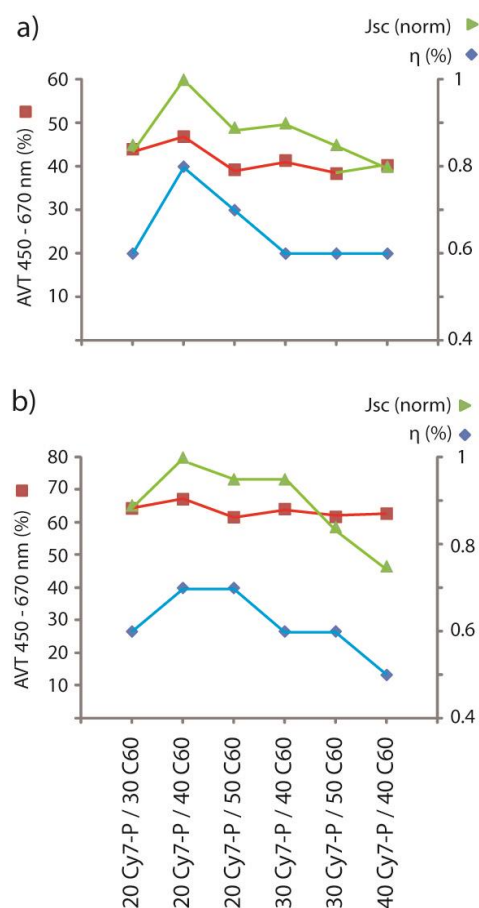


Figure 2- 6 AVT, normalized $J_{sc}$ and $\eta$ for solar cells with different Cy7-P/$C_{60}$ thickness combinations. In (a), the cathode was always 12 nm Ag, in (b) 12 nm Ag/60 nm $Alq_3$. Variations of $V_{oc}$ ($\pm$ 0.01 V) and FF ($\pm$ 3%) were small.

Initial measurements of the stability of Cy7-P films and solar cells showed promising results. Pure Cy7-P films on glass were stored in the glove box at room temperature in the dark. UV-vis spectra suggested that Cy7-P thin films did chemically not degrade over a period of at least two months under inert conditions, as demonstrated by the unchanged absorption at $\lambda =$ 885 nm (data not shown). Performance characteristics for Cy7-P cells under inert storage conditions using a PEDOT:PSS anode layer and different top electrodes are shown in Fig. 2-7a-c. Irrespective of the top electrode used, $V_{oc}$ values increased by ~5% over a period of 28 days. Using a 50 nm thick Ag cathode, $J_{sc}$ and FF were stable over time. For pure 12 nm thin Ag layers, $J_{sc}$ and FF decayed by ~20% and ~50%, respectively. Covering by a 60 nm thick Alq$_3$ layer seems to protect the thin Ag layer and the $J_{sc}$ and FF decay was slower. We note that the careful exclusion of oxygen and water is essential for any solar cell application using cyanines, as the performance of solar cells that were stored at ambient conditions decay completely within 5 hours.
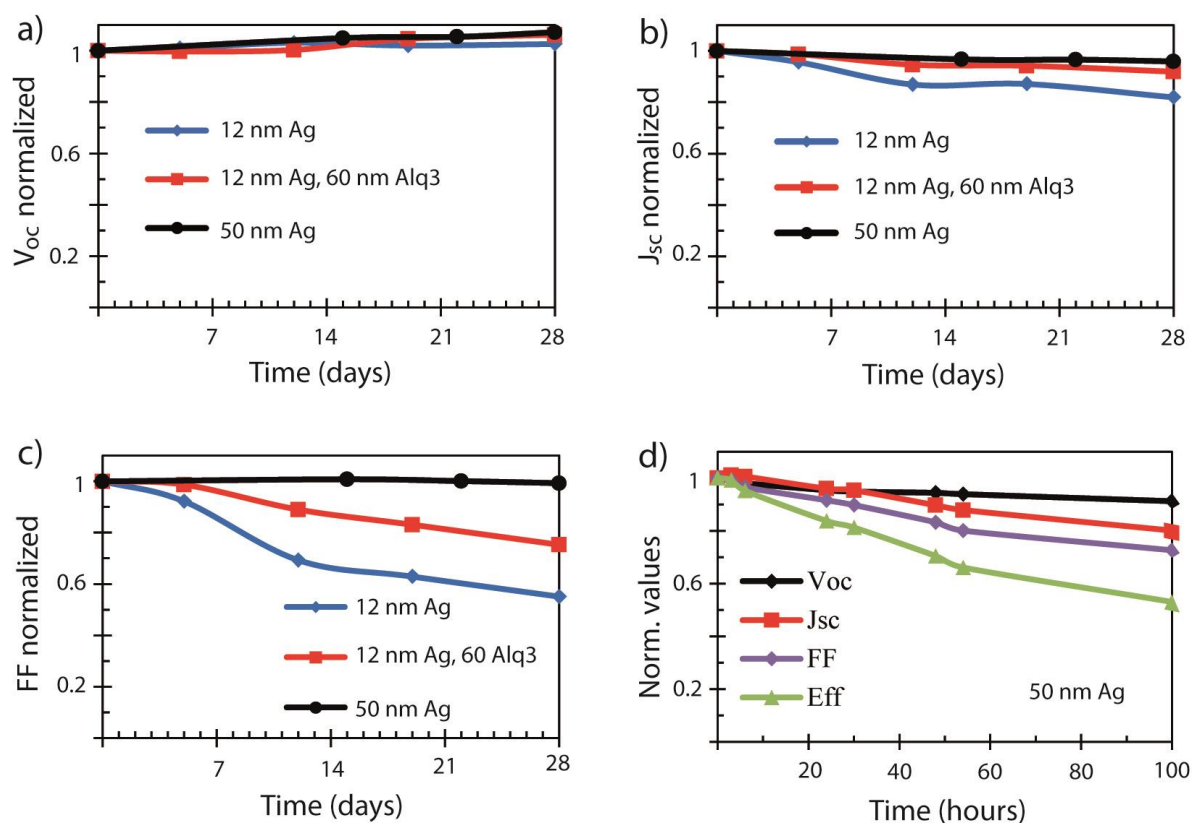


Figure 2- 7 (a-c) Performance characteristics of solar cells stored under N$_2$ at room temperature in the dark. (d) Decay of PV parameters under N$_2$ at 1 sun illumination intensity.

Solar cells were finally exposed to light under N$_2$ (Fig. 2-7d). Cell parameters decayed almost linearly by ~10% ($V_{oc}$), ~20% ($J_{sc}$) and ~30% (FF) over an illumination period of 100 hours. The ISOS protocols [49,50] define the time T$_{80}$ when the performance has decayed to 80% of

the initial value $T_0$ immediately after fabrication (Table 2-2). $T_{80}$ was ~30 hours. After a test period of 100 hours, the performance has decayed to 50% of $T_0$. Clearly, more extensive studies on the degradation are required in future work.

## 4. Conclusions

Here, we introduced cyanine dyes as a suitable class of small molecules for the fabrication of semitransparent organic solar cells with AVT values > 65% and peak transmittances close to 80%. This level of transmittance needs to be increased further to AVT values above 80% for practical display applications in, for example, mobile electronic devices. Therefore, a number of cyanine dyes can be used that are visibly transparent with absorption maxima at 1000 nm and beyond. For the semitransparent Cy7-P/fullerene solar cells demonstrated here, it appears that the visible transmittance can already be substantially increased by replacing $C_{60}$ by a more transparent acceptor material.

## Acknowledgements

## References

[1] M.T. Lloyd, J.E. Anthony, G.G. Malliaras, Photovoltaics from soluble small molecules, materials today 10 (2007) 34.

[2] B. Walker, C. Kim, T.-Q. Nguyen, Small molecule solution-processed bulk heterojunction solar cells, Chem. Mater. 23 (2011) 470.

[3] B. Ma, C.H. Woo, Y. Miyamoto, J.M.J. Fréchet, Solution processing of a small molecule, subnaphthalocyanine, for efficient organic photovoltaic cells, Chem. Mater. 21 (2009) 1413.

[4] S.Y. Leblebici, L. Catane, D.E. Barclay, T. Olson, T.L. Chen, B. Ma, Near-infrared azadipyrromethenes as electron donor for efficient planar heterojunction organic solar cells, ACS Appl. Mater. Interfaces 3 (2011) 4469.

[5] W. Kylberg, P. Sonar, J. Heier, J.-N. Tisserant, C. Müller, F. Nüesch, Z.-K. Chen, A. Dodabalapur, S. Yoon, R. Hany, Synthesis, thin-film morphology, and comparative study of bulk and bilayer heterojunction organic photovoltaic devices using soluble diketopyrrolopyrrole molecules, Energy Environ. Sci. 4 (2011) 3617.

[6] G. Wei, X. Xiao, S. Wang, K. Sun, K.J. Bergemann, M.E. Thompson, S.R. Forrest, Functionalized squaraine donors for nanocrystalline organic photovoltaics, ACS Nano 6 (2012) 972.

[7] B. Walker, A.B. Tamayo, X.-D. Dang, P. Zalar, J.H. Seo, A. Garcia, M. Tantiwiwat, T.-Q. Nguyen, Nanoscale phase separation and high photovoltaic efficiency in solution-processed, small-molecule bulk heterojunction solar cells, Adv. Funct. Mater. 19 (2009) 3063.

[8] Y. Liu, X. Wan, F. Wang, J. Zhou, G. Long, J. Tian, J. You, Y. Yang, Y. Chen, Spin-coated small molecules for high performance solar cells, Adv. Energy Mater. 1 (2011) 771.

[9] Z. Li, G. He, X. Wan, Y. Liu, J. Zhou, G. Long, Y. Zuo, M. Zhang, Y. Chen, Solution processable rhodanine-based small molecule organic photovoltaic cells with a power conversion efficiency of 6.1%, Adv. Energy Mater. 2 (2012) 74.

[10] Y. Sun, G.C. Welch, W.L. Leong, C.J. Takacs, G.C. Bazan, A.J. Heeger, Solution-processed small-molecule solar cells with 6.7% efficiency, Nature Mater. 11 (2012) 44.

[11] C.J. Brabec, S. Gowrisanker, J.J.M. Halls, D. Laird, S. Jia, S.P. Williams, Polymer-fullerene bulk-heterojunction solar cells, Adv. Mater. 22 (2010) 3839.

[12] Y. Galagan, M.G. Debije, P.W.M. Blom, Semitransparent organic solar cells with organic wavelength dependent reflectors, Appl. Phys. Lett. 98 (2011) 043302.

[13] T. Ameri, G. Dennler, C. Waldauf, H. Azimi, A. Seemann, K. Forberich, J. Hauch, M. Scharber, K. Hingerl, C.J. Brabec, Fabrication, optical modeling, and color characterization of semitransparent bulk-heterojunction organic solar cells in an inverted structure, Adv. Funct. Mater. 20 (2010) 1592.

[14] J. Huang, G. Li, Y. Yang, A semi-transparent plastic solar cell fabricated by a lamination process, Adv. Mater. 20 (2008) 415.

[15] Z. Liu, J. Li, Z.-H. Sun, G. Tai, S.-P. Lau, F. Yan, The application of highly doped single-layer graphene as the top electrodes of semitransparent organic solar cells, ACS Nano 6 (2012) 810.

[16] J. Guild, The colorimetric properties of the spectrum, Phil. Trans. Roy. Soc. London A 230 (1932) 149.

[17] R.R. Lunt, V. Bulovic, Transparent, near-infrared organic photovoltaic solar cells for window and energy-scavenging applications, Appl. Phys. Lett. 98 (2011) 113305.

[18] G.M. Fischer, E. Daltrozzo, A. Zumbusch, Selective nir chromophores: bis(pyrrolopyrrole) cyanines, Angew. Chem. Int. Ed. 50 (2011) 1406.

[19] R. Koeppe, D. Hoeglinger, P.A. Troshin, R.N. Lyubovskaya, V.F. Razumov, N.S. Sariciftci, Organic solar cells with semitransparent metal back contacts for power window applications, ChemSusChem. 2 (2009) 309.

[20] J. Meiss, F. Holzmueller, R. Gresser, K. Leo, M. Riede, Near-infrared absorbing semi-transparent organic solar cells, Appl. Phys. Lett. 99 (2011) 193307.

[21] C.-C. Chen, L. Dou, R. Zhu, C.-H. Chung, T.-B. Song, Y.B. Zheng, S. Hawks, G. Li, P.S. Weiss, Y. Yang, Visibly transparent polymer solar cells produced by solution processing, ACS Nano 6 (2012) 7185.

[22] P.-A. Bouit, C. Aronica, L.Toupet, B. Le Guennic, C. Andraud, O. Maury, Continuous symmetry breaking induced by ion pairing effect in heptamethine cyanine dyes: beyond the cyanine limit, J. Am. Chem. Soc. 132 (2010) 4328.

[23] N. Tyutyulkov, J. Fabian, A. Mehlhorn, F. Dietz, A. Tadjer, Polymethine dyes – structure and properties, St. Kliment Ohridski University Press 1991.

[24] R. Hany, B. Fan, F.A. de Castro, J. Heier, W. Kylberg, F. Nüesch, Strategies to improve cyanine dye multi layer organic solar cells, Prog. Photovolt: Res. Appl. 19 (2011) 851.

[25] R.S. Lepkowicz, O.V. Przhonska, J.M. Hales, J. Fu, D.J. Hagan, E.W. Van Stryland, M.V. Bondar, Y.L. Slominsky, A.D. Kachkovski, Nature of the electronic transitions in thia-carbocyanines with a long polymethine chain, Chem. Phys. 305 (2004) 259.

[26] T. Geiger, H. Benmansour, B. Fan, R. Hany, F. Nüesch, Low-band gap polymeric cyanine dyes absorbing in the nir region, Macromol. Rapid Commun. 29 (2008) 651.

[27] E. Berner, T. Jäger, T. Lanz, F. Nüesch, J.-N. Tisserant, G. Wicht, H. Zhang, R. Hany, Influence of crystalline titanium oxide layer smoothness on the performance of inverted organic bilayer solar cells, Appl. Phys. Lett. 102 (2013) 183903.

[28] P.-A. Bouit, D. Rauh, S. Neugebauer, J.L. Delgado, E. di Piazza, S. Rigaut, O. Maury, C. Andraud, V. Dyakonov, N. Martin, A "cyanine-cyanine" salt exhibiting photovoltaic properties, Org. Lett. 11 (2009) 4806.

[29] K. Funabiki, H. Mase, A. Hibino, N. Tanaka, N. Mizuhata, Y. Sakuragi, A. Nakashima, T. Yoshida, Y. Kubota, M. Matsui, Synthesis of a novel heptamethine-cyanine dye for use in near-infrared active dye-sensitized solar cells with porous zinc oxide prepared at low temperature, Energy Environ. Sci. 4 (2011) 2186.

[30] H. Hoppe, N.S. Sariciftci, D. Meissner, Optical constants of conjugated polymer/fullerene based bulk-heterojunction organic solar cells, Mol. Cryst. Liq. Cryst. 385 (2002) [233]/113.

[31] L.A.A. Pettersson, L.S. Roman, O. Inganäs, Modeling photocurrent action spectra of photovoltaic devices based on organic thin films, J. Appl. Phys. 86 (1999) 487.

[32] http://refractiveindex.info

[33] S. Kumar, V.K. Shukla, A. Tripathi, Ellipsometric investigations on the light induced effects on tris(8-hydroxyquinoline) aluminum (Alq3), Thin Solid Films 477 (2005) 240.

[34] C. Charton, M. Fahland, Optical properties of thin Ag films deposited by magnetron sputtering, Surface & Coatings Technology 174-175 (2003) 181.

[35] T. Suzuki, Y. Maruyama, T. Akasaka, W. Ando, K. Kobayashi, S. Nagase, Redox properties of organofullerenes, J. Am. Chem. Soc. 116 (1994) 1359.

[36] C.M. Cardona, W. Li, A.E. Kaifer, D. Stockdale, G.C. Bazan, Electrochemical considerations for determining absolute frontier orbital energy levels of conjugated polymers for solar cell applications, Adv. Mater. 23 (2011) 2367.

[37] J. Heier, J. Groenewold, S. Huber, F. Nüesch, R. Hany, Nanoscale structuring of semiconducting molecular blend films in the presence of mobile counterions, Langmuir 24 (2008) 7316.

[38] H.J. Snaith, N.C. Greenham, R.H. Friend, The origin of collected charge and open-circuit voltage in blended polyfluorene photovoltaic devices, Adv. Mater. 16 (2004) 1640.

[39] P. Peumans, A. Yakimov, S.R. Forrest, Small molecular weight organic thin-film photodetectors and solar cells, J. Appl. Phys. 93 (2003) 3693.

[40] B. Fan, F.A. de Castro, J. Heier, R. Hany, F. Nüesch, High performing doped cyanine bilayer solar cell, Org. Electron. 11 (2010) 583.

[41] Q.L. Song, F.Y. Li, H. Yang, H.R. Wu, X.Z. Wang, W. Zhou, J.M. Zhao, X.M. Ding, C.H. Huang, X.Y. Hou, Small-molecule organic solar cells with improved stability, Chem. Phys. Lett. 416 (2005) 42.

[42] B.E. Lassiter, G. Wei, S. Wang, J.D. Zimmerman, V.V. Diev, M.E. Thompson, S.R. Forrest, Organic photovoltaics incorporating electron conducting exciton blocking layers, Appl. Phys. Lett. 98 (2011) 243307.

[43] V. Shrotriya, G. Li, Y. Yao, C.-W. Chu, Y. Yang, Transition metal oxides as the buffer layer for polymer photovoltaics, Appl. Phys. Lett. 88 (2006) 073508.

[44] R. Steim, F.R. Kogler, C.J. Brabec, Interface materials for organic solar cells, J. Mater. Chem. 20 (2010) 2499.

[45] X. Tong, B.E. Lassiter, S.R. Forrest, Inverted organic photovoltaic cells with high open-circuit voltage, Org. Electron. 11 (2010) 705.

[46] M. Lenes, H.J. Bolink, Ionic space-charge effects in solid state organic photovoltaics, ACS Appl. Mater. Interfaces 2 (2010) 3664.

[47] B. O'Connor, C. Haughn, K.-H. An, K.P. Pipe, M. Shtein, Transparent and conductive electrodes based on unpatterned, thin metal films, Appl. Phys. Lett. 93 (2008) 223304.

[48] B. O'Connor, K.H. An, K.P. Pipe, Y. Zhao, M. Shtein, Enhanced optical field intensity distribution in organic photovoltaic devices using external coatings, Appl. Phys. Lett. 89 (2006) 233502.

[49] M.O. Reese, S.A. Gevorgyan, M. Jørgensen, E. Bundgaard, S.R. Kurtz, D.S. Ginley, D.C. Olson, M.T. Lloyd, P. Morvillo, E.A. Katz, A. Elschner, O. Haillant, T.R. Currier, V. Shrotriya, M. Hermenau, M. Riede, K.R. Kirov, G. Trimmel, T. Rath, O. Inganäs, F. Zhang, M. Andersson, K. Tvingstedt, M. Lira-Cantu, D. Laird, C. McGuiness, S. Gowrisanker, M. Pannone, M. Xiao, J. Hauch, R. Steim, D.M. DeLongchamp, R. Rösch, H. Hoppe, N. Espinosa, A.Urbina, G. Yaman-Uzunoglu, J.-B. Bonekamp, A.J.J.M. van Breemen, C. Girotto, E. Voroshazi, F.C. Krebs, Consensus stability testing protocols for organic photovoltaic materials and devices, Sol. Energy Mater. Sol. Cells 95 (2011) 1253.

[50] D.M. Tanenbaum, M. Hermenau, E. Voroshazi, M.T. Lloyd, Y. Galagan, B. Zimmermann, M. Hösel, H.F. Dam, M. Jørgensen, S.A. Gevorgyan, S. Kudret, W. Maes, L. Lutsen, D. Vanderzande, U. Würfel, R. Andriessen, R. Rösch, H. Hoppe, G. Teran-Escobar, M. Lira-Cantu, A. Rivaton, G.Y. Uzunoğlu, D. Germack, B. Andreasen, M.V. Madsen, K. Norrman, F.C. Krebs, The ISOS-3 inter-laboratory collaboration focused on the stability of a variety of organic photovoltaic devices, RSC Advances 2 (2012) 882.

# Chapter III. Transparent OPDs

**Transparent organic photo-detector using a near-infrared absorbing cyanine dye**

Hui Zhang[1], Sandra Jenatsch[1], Jelissa De Jonghe[2], Frank Nüesch[1,3], Roland Steim[1], Anna C. Véron[1] & Roland Hany[1*]

[1]Empa, Swiss Federal Institute for Materials Science and Technology, Laboratory for Functional Polymers, CH-8600 Dübendorf, Switzerland.

[2]Photochemical Dynamics Group, Institute of Chemical Sciences and Engineering, Ecole Polytechnique Fédérale de Lausanne, EPFL, Station 6, CH-1015 Lausanne, Switzerland.

[3]Institut des Matériaux, Ecole Polytechnique Fédérale de Lausanne, EPFL, Station 12, CH-1015 Lausanne, Switzerland.

Correspondence should be addressed to:    Dr. Roland Hany

Empa / Laboratory for Functional Polymers

CH-8600 Dübendorf - Switzerland

Phone  +41 58 765 4084

E-mail  roland.hany@empa.ch

**Declaration**: I fabricated all the devices, performed the UV-Vis, IPCE, I-V measurements and optical simulations, prepared samples for transient spectroscopy, carried out all data analysis, contributed to manuscript preparation.

**Abstract**: Organic photodetectors are interesting for low cost, large area optical sensing applications. Combining organic semiconductors with discrete absorption bands outside the visible wavelength range with transparent and conductive electrodes allows for the fabrication of visibly transparent photodetectors. Visibly transparent photodetectors can have far reaching impact in a number of areas including smart displays, window-integrated electronic circuits and sensors. Here, we demonstrate a near-infrared sensitive, visibly transparent organic photodetector with a very high average visible transmittance of 68.9%. The transmitted light of the photodetector under solar irradiation exhibits excellent transparency color perception and rendering capabilities. At a wavelength of 850 nm and at -1 V bias, the photoconversion efficiency is 17% and the specific detectivity is $10^{12}$ Jones. Large area photodetectors with an area of 1.6 cm$^2$ are demonstrated.

**Keywords**: cyanine dyes; near infrared; organic; photodetectors; transparent

## Introduction

Photodetectors are present in a vast variety of devices used in private households, industry and research. Organic photodetectors may be well-suited for applications that require large active area, mechanical flexibility, low-cost processing, or wavelength specificity[1]. Applications where organic photodetectors with a narrow spectral response in the near-infrared (NIR) wavelength range would be beneficial are remote control, reflective sensors such as optical communication[1]. Another example can be found in the field of biochemical sensing. A fluorescent molecule can serve as a reporting group when tagged to a biomolecule. When using NIR fluorescent dyes, the background noise caused by the auto-fluorescence of the biosubstrate can be greatly reduced. In addition, the high tissue penetration of NIR light enables *in vivo* imaging applications[2].

Multicolor organic photodetectors with sensitivity extending to the NIR wavelength range have been presented using low band gap polymers[3,4] or small molecules[5-7]. When exclusive NIR light sensing is required, these photodetectors must be operated using a visible light filter. Recently, organic photodetectors with selective NIR sensitivity have been reported[8-10]. These detectors used squaraines and J-aggregated cyanine small molecules with narrow and intense absorption features in the wavelength range from ~ 650 – 850 nm.

Combining organic NIR dyes with transparent, non-reflective electrodes allows for the fabrication of visibly transparent devices, thereby adding new functionality to organic photodetectors, such as integration in displays or invisible electronic circuits[11]. (Semi-)transparent organic solar cells are intensively being investigated for applications such as building-integrated

photovoltaics or chargers of portable electronics[12,13], but only few attempts were made to demonstrate transparent organic photodetectors. A visibly transparent photoconductor was reported using a naphthalocyanine molecule with an absorption maximum at ~1000 nm[14]. Semitransparent photodetectors with an average visible transmittance (AVT) of 45% were fabricated with molecules that absorb strongly in the ultraviolet and NIR region but relatively weakly in the visible[6]. A stacked device was reported that consisted of an organic light-emitting diode (OLED) and a semitransparent (AVT ~45%) photodiode[15]. The device acts as an image sensor by emitting light from the OLED through the photodiode onto a surface and detecting reflected light by the photodiode.

**Results and Discussion**

Here, we demonstrate a sensitive, fast responding and transparent organic photodetector with a high average visible transmittance of over 65%. The transmitted light of the photodetector under solar irradiation exhibits excellent transparency color perception and rendering capabilities. The photodetector consists of a $TiO_2$ electron transport layer[16] on ITO that is sensitized by a near-infrared absorbing heptamethine cyanine dye layer, Cy7-T (Figure 3-1a). Recently, we fabricated transparent organic photovoltaic cells using Cy7-T with an average visible transmittance of 66% and a power conversion efficiency of 2.2%[17]. The device further contains poly-$C_{60}$ (photo-polymerized $C_{60}$) and MeO-TPD (N,N,N',N'-Tetrakis-(4-methoxyphenyl) benzidine) interfacial layers that are inserted to reduce the dark current (Figure 3-1b and 3-1c).
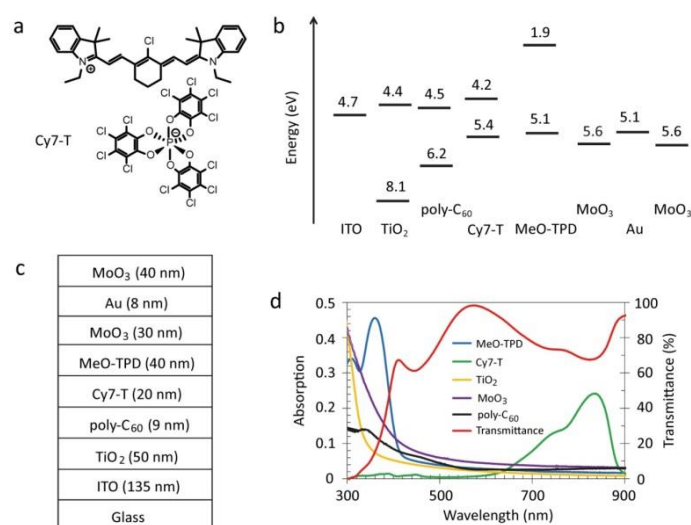


Figure 3- 1 Molecular structure of the cyanine dye, schematic of the device architecture and absorption spectra.

(a) Chemical structure of the cyanine dye Cy7-T with the anion Δ-TRISPHAT. (b) Energy level diagram of the photodiode. (c) Schematic representation of the photodiode with an average visible transmittance (AVT$_{450-670 \, nm}$) of 68.9%. (d) Absorption spectra[1] of individual materials with thicknesses indicated in (c), and the transmittance spectrum of the layer stack ITO/TiO$_2$/poly-C$_{60}$/Cy7-T/MeO-TPD/MoO$_3$.

Light absorption in the visible is small for all materials and the transmittance of the multilayer stack, excluding the top electrode, is above 90% between 530 and 640 nm (Figure 3-1d). Photodetectors were fabricated with either non-transparent 80 nm thick Ag anodes or a semitransparent Au / MoO$_3$ top contact (Figure 3-1c). Gold was the hole-collecting electrode and MoO$_3$ an additional external dielectric coating to increase the device transmittance. Wavelength-dependent optical modelling was carried out for different Au and MoO$_3$ film thickness combinations to simulate full transmittance spectra from which calculated average visible transmittance values were extracted. For pure Au layers, AVT values increased monotonically with decreasing thickness. However, a balance must be achieved between optical transparency and electrical conductivity (Supplementary Information 3-S1). A low electrode sheet resistance is important for photodetector scale-up, in order to reduce losses in transporting charge to external circuitry. To ensure that Au is forming a continuous film in a reproducible way the gold thickness was fixed to 8 nm (AVT$_{390-720 \, nm, \, calc.}$ = 64%)[18]. This value increased to a maximum of AVT$_{390-720 \, nm, \, calc.}$ = 71.5% when adding 40 nm MoO$_3$ on top. The optical electric field distribution inside the device varies considerably by changing the MoO$_3$ thickness. As an example, Figure 3-2a shows simulated normalized spatial distributions of the squared electric field strengths at λ = 620 nm for MoO$_3$ layer thicknesses ranging from 0 to 60 nm. The strength of E$^2$ leaving the device corresponds directly to the transmittance. For a 40 nm thick MoO$_3$ layer, the calculated transmittance was 86.4% at λ = 620 nm, in fair agreement with the experimental value of 77.8% (Figure 3-2b).

---

[1] Absorption (A) in this chapter is equal to $Log_{10}(\frac{I_0}{I})$, where $I_0$ is the incident light intensity and $I$ is the transmitted light intensity.
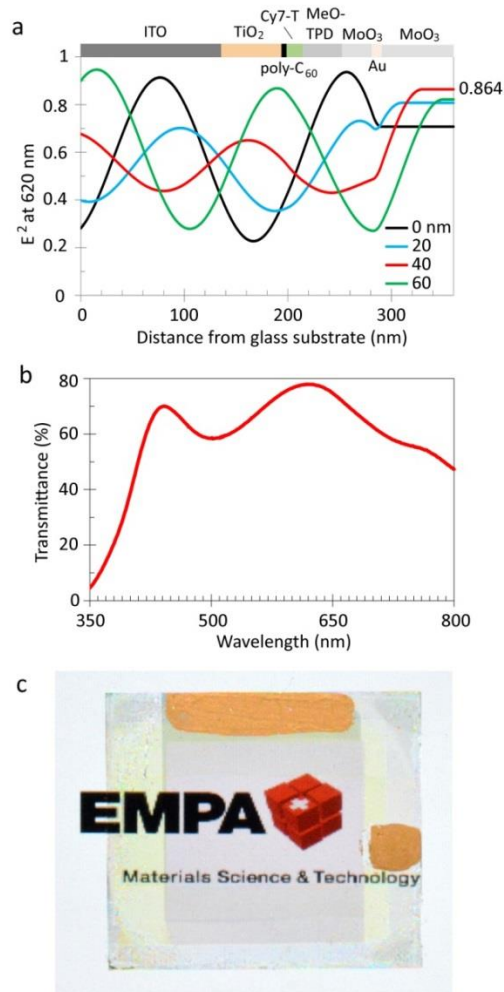
Figure 3- 2 Optical device properties.

(a) Calculated spatial distribution of the normalized squared optical electric field strengths for $\lambda = 620$ nm inside transparent photodetectors. (b) Transmittance spectrum and (c) image of the transparent photodetector with an active area of 1.6 $cm^2$.

The value of the AVT of the photodetector depends on the definition of the visible wavelength range. Common assessments for the visible range are defined for photopic responses > 0.1% or > 5% peak sensitivity, resulting in visible spectral ranges of ~390 – 720 nm and ~ 450 – 670 nm, respectively[19]. For these wavelength ranges, experimental average visible transmittance values are $AVT_{390\text{-}720 \text{ nm, exp.}} = 66.4\%$ and $AVT_{450\text{-}670 \text{ nm, exp.}} = 68.9\%$.

The photodetector exhibits a very high and uniform measured transmittance over a large range of the visible spectrum, resulting in a greyish and color neutral appearance (Figure 3-2c). There are several ways how the measured transmitted light can be related to the human perception of transparency and color. Since the sensitivity of the human eye is different for every

visible wavelength, the human perception of transparency (HPT) can differ from the radiometric AVT value. To calculate HPT, the measured transmittance is folded with the eye sensitivity[20]. A HPT$_{390\text{-}720\text{ nm}}$ value of 68.4% was obtained, in good agreement with the AVT value. For analyzing the transparency color perception, color coordinates were calculated in the CIE 1931 color space. As light source, we used the AM1.5 solar spectrum folded with the transmittance spectrum of the photodetector[21]. Color coordinates were (0.350, 0.342), very close to the so called "white point" (1/3, 1/3). This implies that the transparency color perception is similar to the color perception of the original light source and the device is acting nearly as a neutral density filter.

The color rendering index (CRI) is a quantitative measure for how well a light source, in our case the transmitted light from the photodetector, renders the colors of objects in comparison to a reference light source. CRI was evaluated following published procedures[21,22]. Therefore, the special color rendering index (sCRI) was calculated for eight standard test color samples. The correlated color temperature of the photodetector was T = 4760 K and the blackbody irradiator was used as the reference light. A CRI of 100 means that the eight specified colors have the same appearance when illuminated by the transmitted light from the photodetector or by the reference light source, by definition. We obtained eight sCRI values (96, 96, 98, 98, 96, 95, 98, 98) and from these, a general (i.e. the mean) CRI of 96.7. This high general CRI implies an excellent color rendering capacity that is comparable with the highest reported CRI values for semitransparent organic solar cells[22].
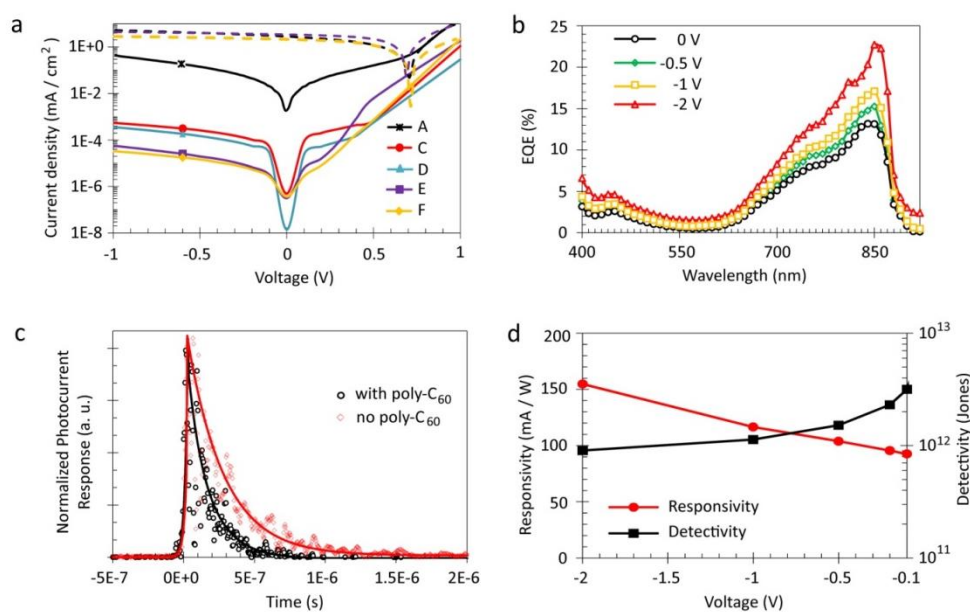


Figure 3- 3 Electrical device properties.

(a) Current-voltage (J-V) characteristics of photodetectors measured in the dark (solid lines) and under 1 sun illumination (dashed lines). Labels designate devices shown in Table 1. (b) External quantum efficiency versus wavelength for a transparent photodetector (device F) at various biases. (c) Photocurrent response of photodetectors (device F) to a 5 ns long light pulse at 850 nm. (d) Responsivity and specific detectivity at 850 nm of photodetector F for different applied biases.

To tune the electrical properties of the photodetector, we omitted in a first step the interfacial layers and fabricated $TiO_2$ / Cy7-T heterojunction devices (Table 3-1, device A). Operated in the photovoltaic mode under 1 sun illumination, the short-circuit current was $J_{sc} = 2.7$ mA cm$^{-2}$, the open-circuit voltage $V_{oc} = 0.74$ V, and the fill factor FF = 37%, resulting in a power conversion efficiency of $\eta = 0.7\%$ (Figure 3-3a). This confirms the electron transfer process from the photoexcited dye into the $TiO_2$ conduction band, and the regeneration of the Cy7-T ground state by hole transfer across $MoO_3$.

However, the dark current ($J_d = 4.3$ x $10^{-1}$ mA cm$^{-2}$ at -1 V) is too high for using device A as a photodetector. The dark current is an inherent source of detector noise, and the entity of noise determines the lower limit of light detection. In general, applying a reverse bias across a photodetector increases its speed of response. However, the dark current tends to increase as well with applied reverse bias resulting in an increase of the shot noise. Therefore, the choice of operation mode is a trade-off between the required speed of response and the maximum noise that can be accepted in the actual application.

A major contribution to the dark current in organic photodetectors under reverse bias is the injection of charge carriers through the electrode contacts into the semiconductor materials[1,9,23]. A proven strategy to suppress these injection processes is the use of interfacial blocking layers[1,4,9]. We selected MeO-TPD as suitable electron blocking layer (Supplementary Information 3-S2). MeO-TPD does not absorb light in the visible and has a high LUMO energy to block electron injection. In addition, the HOMO energies of MeO-TPD and Cy7-T closely match, which is essential for efficient photogenerated carrier collection. $TiO_2$ / Cy7-T / MeO-TPD devices with increasing thickness of MeO-TPD were fabricated (Table 3-1, B − D). From spectral response measurements, we observed no photocurrent generation in the wavelength range below 400 nm where MeO-TPD absorbs light. This means that MeO-TPD acts solely as an electron blocking and hole transporting layer. The optimum layer thickness of 40 nm MeO-TPD resulted in a dark current reduction by three orders of magnitude ($J_d = 5.5$ x $10^{-4}$ mA cm$^{-2}$ at -1 V; Table 3-1, C) while reducing $J_{sc}$ from 2.73 mA cm$^{-2}$ for device A to 1.70 mA cm$^{-2}$ only slighty. The dark current decreased further by increasing the MeO-TPD thick-

ness to 100 nm, but $J_{sc}$ collapsed due to the strong increase in the series resistance (Table 3-1, D).

Table 3- 1 Current-voltage characteristics of ITO / TiO$_2$(50 nm) / poly-C$_{60}$ / Cy7-T(20 nm) / MeO-TPD / MoO$_3$(30 nm) / (top electrode) photodiodes.

| Device[a] | poly-C$_{60}$ | MeO-TPD | $J_d$ at 0 V[b] | $J_d$ at -1 V | $R_{sh}$ | $R_s$ | $J_{sc}$ |
|---|---|---|---|---|---|---|---|
| | (nm) | (nm) | (mA cm$^{-2}$) | (mA cm$^{-2}$) | (kΩ cm$^2$) | (Ω cm$^2$) | (mA cm$^{-2}$) |
| A | 0 | 0 | $1.9 \times 10^{-3}$ | $4.3 \times 10^{-1}$ | 3.9 | 5 | 2.73 |
| B | 0 | 10 | $7.1 \times 10^{-4}$ | $5.7 \times 10^{-2}$ | 20 | 40 | 2.01 |
| C | 0 | 40 | $4.9 \times 10^{-7}$ | $5.5 \times 10^{-4}$ | $2 \times 10^3$ | 53 | 1.70 |
| D | 0 | 100 | $1.4 \times 10^{-8}$ | $3.6 \times 10^{-4}$ | $4 \times 10^3$ | 400 | 0.50 |
| E | 9 | 40 | $3.2 \times 10^{-7}$ | $5.7 \times 10^{-5}$ | $28 \times 10^3$ | 83 | 3.40 |
| F[c] | 9 | 40 | $3.7 \times 10^{-7}$ | $3.3 \times 10^{-5}$ | $30 \times 10^3$ | 63 | 1.99 |
| G | 9 | 40 | $2.7 \times 10^{-7}$ | $6.9 \times 10^{-5}$ | $20 \times 10^3$ | 260 | 2.05 |

[a]The top electrode for devices A – E was 80 nm Ag, for the transparent devices F and G gold (8 nm) / MoO$_3$ (40 nm). The device area was 3.1 mm$^2$ for A – F, and 1.6 cm$^2$ for G; [b]$J_d$ denotes the dark current, $R_{sh}$ the shunt resistance, $R_s$ the series resistance, and $J_{sc}$ the short-circuit current density measured at 100 mW cm$^{-2}$ simulated AM1.5G solar irradiation; [c]Rectification of the dark current at ±1V was $6.6 \times 10^4$.

A C$_{60}$ film was evaporated onto TiO$_2$ and photo-polymerized by illumination (Supplementary Information 3-S3)[24]. Poly-C$_{60}$ is partially insoluble in the solvent chlorobenzene that was used to spin coat the Cy7-T film on top. In agreement with results from related Cy7 / C$_{60}$ photovoltaic cells, we observed a strong increase of the forward injection current under illumination compared to the dark current (Figure 3a)[17,25]. This photoconductivity effect[26] probably originates from light absorption in the C$_{60}$ layer[27,28]. Insertion of the C$_{60}$ interfacial layer between TiO$_2$ and Cy7-T improved the performance of the photodetector in several ways. First, the use of poly-C$_{60}$ reduced the dark current further by one order of magnitude ($J_d = 5.7 \times 10^{-5}$ mA cm$^{-2}$ at -1 V; Table 3-1, E). Secondly, external quantum efficiency (EQE) measurements (Figure 3-3b) showed a small current contribution resulting from direct poly-C$_{60}$ excitation in

the wavelength region below 550 nm. This is much less, however, than the observed doubling of the short-circuit current when inserting poly-$C_{60}$ ($J_{sc}$ = 3.4 mA cm$^{-2}$). This suggests that poly-$C_{60}$ can assist in efficient charge separation between Cy7-T and $TiO_2$ and prevents back recombination. Such a beneficial role of interfacial modifiers in hybrid solar cells incorporating both organic and inorganic materials has been demonstrated several times[29,30].

The enhanced charge transfer process across the metal oxide – organic interface resulted also in a faster response speed of the photodiode. The temporal electrical response to nanosecond optical excitation at zero applied bias was used to probe photogenerated carrier extraction. The response decayed over ~2 µs when omitting poly-$C_{60}$ (Figure 3-3c), but light detection was well accomplished within 1 µs when adding poly-$C_{60}$, potentially allowing for applications requiring response frequencies up to 1 MHz. Optimized non-transparent and transparent devices (Table 3-1, E and F) showed very similar dark current values. Replacing the highly reflective back metal contact with a transparent electrode resulted in a lower $J_{sc}$ value, as expected. Finally, we were able to fabricate photodetectors with larger active area without significant performance losses (Table 3-1, G). Large-area organic photodetectors have promising applications in X-ray medical imaging or industrial quality control, particularly because of the potential reductions in the costs when producing devices of several square centimeter[31].

To characterize the photodiode sensitivity, we determined the specific detectivity D* (in units of cm Hz$^{\frac{1}{2}}$ W$^{-1}$ or Jones). D* is given as $(A \Delta f)^{\frac{1}{2}} R / J_n$, where A is the effective area of the detector in cm$^2$, $\Delta f$ the electrical bandwidth in Hz, R the responsivity in A W$^{-1}$, and $J_n$ the noise current in A. With the assumption that under reverse bias the shot noise from the dark current is the dominant contribution to the overall electronic noise of the device[1,3,4,9], the specific detectivity can be expressed as $D* = R / (2q J_d)^{\frac{1}{2}}$, where q is the absolute value of the electron charge and $J_d$ is the dark current density (Table 3-1). The responsivity is given by $R = J_{ph} / I_{light}$, where $J_{ph}$ is the photocurrent and $I_{light}$ is the incident light intensity. To determine R, EQE values were measured under short-circuit conditions and under reverse bias (Figure 3-3b). The maximum EQE (at λ = 850 nm) increased from 13% electron per photon at zero bias to 23% at -2 V. Correspondingly, R increased with reverse bias to a maximum value of R = 165 mA W$^{-1}$ at -2 V (Figure 3-3d). Specific detectivities were calculated based on the responsivity values and the dark current values (Figure 3-3d). D* monotonically decreased with increasing reverse bias from $D* = 3 \times 10^{12}$ Jones at -0.1 V to $1 \times 10^{12}$ Jones at -2 V. The trend of D* demonstrates that the key to obtaining a high detector sensitivity is a high responsivity while keeping the dark current low.

We note that specific detectivities were calculated using responsivity values that were measured using light intensities in the ~ 0.1 mW cm$^{-2}$ range. The linearity of the photodetector's responsivity was addressed by measuring the photocurrent for different light intensities (Supplementary Information 3-S4). We applied light intensities ranging from $10^2 - 10^{-3}$ mW cm$^{-2}$ and measured a linear response of the photocurrent. Care must be taken when organic photodetectors are used to detect much lower light intensities, such as a few nW cm$^{-2}$ in medical X-ray imaging[31]. This is because of the density of charge traps that is usually higher than in inorganic semiconductor materials. Trapped charges cause enhanced recombination and are extracted at a reduced speed from the organic material, deteriorating the responsivity and the bandwidth of the photodetector. These effects become important when the charge density generated by low-level light conditions is comparable to the charge trap density.

The figure of merits of our photodetector at $\lambda = 850$ nm, such as photoconversion efficiencies of 13% - 23% and specific detectivities of ~$10^{12}$ cm Hz$^{\frac{1}{2}}$ W$^{-1}$, compare favourably with results presented so far for selective NIR organic photodiodes[9,10]. Ultimately, the required level of device transparency and photometric perception will depend on the type of application. For example, a dual wavelength range specific photodetector can be envisioned by stacking a transparent NIR detector with a detector that selectively senses visible light. In that case the required transparency would be relatively low, because the combined photodetector appears colored or grey, respectively. On the other hand, reasonable transparency perception and good color rendering properties will be required for display or window-integrated applications.

**Methods**

Photodetectors were fabricated in a glove box under $N_2$ atmosphere ($H_2O < 1$ ppm, $O_2 < 10$ ppm). $TiO_2$ films were prepared on cleaned ITO glass substrates (Geomatec, resistivity ~11 Ohms square$^{-1}$) via a sol-gel process using titanium iso-propoxide as precursor[16]. Spin coated $TiO_2$ films were heated within 3 h to 460 $^{\circ}$C in air, were kept for 2 h at that temperature, and were then cooled to room temperature. Before deposition of the active layers, $TiO_2$ coated substrates were heated for 10 min at 120 $^{\circ}$C inside the glove box. Cy7-T was synthesized as described[17] and spin coated as a 20 nm thick film from chlorobenzene solution. Layers of $C_{60}$ (SES Research, 99.5% or 99.9%), MeO-TPD (Sigma-Aldrich, 98%) and $MoO_3$ (Sigma Aldrich, 99.99%) were deposited by thermal evaporation ($< 5\times10^{-6}$ mbar). $C_{60}$ was photopolymerized under illumination (100 mW cm$^{-2}$, $N_2$) for 12 h. Ag (Cerac, 99.99%) and Au (Kurt J. Lesker, 99.99%) was evaporated through a shadow mask to define devices with active areas of 3.1 mm$^2$, 7.1 mm$^2$, or 1.6 cm$^2$.

Absorption and transmission spectra were measured on a Varian Cary 50 UV-vis spectrophotometer. For the transmission spectrum shown in Figure 1d, glass was defined as the baseline. For the spectrum shown in Figure 2b, air was defined as the baseline. Film thicknesses were determined by profilometry (Ambios XP1). White light J-V characteristics were measured using 100 mW cm$^{-2}$ simulated AM1.5G solar irradiation on a calibrated solar simulator from Spectra-Nova. EQE was measured using a monochromator and the light from a 300 W Xe lamp together with an AM1.5G filter set. The monochromatic light intensity was determined using a calibrated Si-diode. Bias on the device was applied using a Keithley 2400 sourcemeter. Photodiodes were characterized via illumination through the glass / ITO side only. For dark current measurements, devices were serially connected with resistors and currents were recorded using a Keithley 2000 multimeter by measuring the voltage drop.

Transient photocurrent experiments were carried out using a frequency-tripled Q-switched Nd:YAG laser (Ekspla NT-342) running at 20 Hz repetition rate. The excitation wavelength at 850 nm was generated by an optical parametric oscillator (idler output, 5 ns FWHM) and attenuated by grey filters (0.5 - 220 μJ cm$^{-2}$). Temporal responses (photocurrent into $50 - 500\ \Omega$ loads) were measured with no bias applied on an oscilloscope (Tektronix DPO 7104C). Full lines in Figure 3c correspond to the best exponential fit.

Energy values shown in Figure 1b were taken from the literature: ITO[32], TiO$_2$[33], Cy7-T[17], MeO-TPD[34], Au[35] and MoO$_3$[24]. For poly-C$_{60}$, values from C$_{60}$[36] were adopted. The thickness of the transparent Au / MoO$_3$ electrode was optimized using the optical model implemented in Setfos (www.fluxim.ch). Optical constants were taken from the literature: ITO[37], TiO$_2$[38], MeO-TPD[39], MoO$_3$[40] and for Au from the Setfos database. For poly-C$_{60}$, values from C$_{60}$[41] were adopted. Optical constants for Cy7-T were determined by spectroscopic ellipsometry (Supplementary Information 3-S5).

**References**

1. Baeg, K.-J., Binda, M., Natali, D., Caironi, M. & Noh, Y.-Y. Organic light detectors: photodiodes and phototransistors. *Adv. Mater.* **25**, 4267-4295 (2013).

2. Guo, Z., Park, S., Yoon, J. & Shin, I. Recent progress in the development of near-infrared fluorescent probes for bioimaging applications, *Chem. Soc. Rev.* **43**, 16-29 (2014).

3. Yao, Y., et al. Plastic near-infrared photodetectors utilizing low band gap polymer, *Adv. Mater.* **19**, 3979-3983 (2007).

4. Gong, X., et al. High-detectivity polymer photodetectors with spectral response from 300 nm to 1450 nm, *Science* **325**, 1665-1667 (2009).

5. Li, L., Huang, Y., Peng, J., Cao, Y. & Peng, X. Highly responsive organic near-infrared photodetectors based on a porphyrin small molecule, *J. Mater. Chem. C* **2**, 1372-1375 (2014).

6. Qi, J., et al. Panchromatic small molecules for uv-vis-nir phtotodetectors with high detectivity, *J. Mater. Chem. C* **2**, 2431-2438 (2014).

7. Zimmerman, J. D., et al. Porphyrin-tape/$C_{60}$ organic photodetectors with 6.5% external quantum efficiency in the near infrared, *Adv. Mater.* **22**, 2780-2783 (2010).

8. Arca, F., Sramek, M., Tedde, S. F., Lugli, P. & Hayden, O. Near-infrared organic photodiodes, *IEEE J. Quantum Electron.* **49**, 1016-1025 (2013).

9. Binda, M., et al. High detectivity squaraine-based near infrared photodetector with $nA/cm^2$ dark current, *Appl. Phys. Lett.* **98**, 073303 (2011).

10. Osedach, T. P., et al. Near-infrared photodetector consisting of j-aggregating cyanine dye and metal oxide thin films, *Appl. Phys. Lett.* **101**, 113303 (2012).

11. Wager, J. F., Keszler, D. A. & Presley, R. E. *Transparent Electronics* (Springer, New York, 2008).

12. Chen, C.-C., et al. Visibly transparent polymer solar cells produced by solution processing, *ACS Nano* **6**, 7185-7190 (2012).

13. Lunt, R. R. & Bulovic, V. Transparent, near-infrared organic photovoltaic solar cells for window and energy-scavenging applications, *Appl. Phys. Lett.* **98**, 113305 (2011).

14. Campbell, I. H. Transparent organic photodiodes with high quantum efficiency in the near infrared, *Appl. Phys. Lett.* **97**, 033303 (2010).

15. Komatsu, T., Sakanoue, K., Fujita, K. & Tsutsui, T. Transparent organic photodiodes stacked with electroluminescence devices, *Proc. of SPIE* **5938**, 593816-1-593186-8 (2005).

16. Berner, E., et al. Influence of crystalline titanium oxide layer smoothness on the performance of inverted organic bilayer solar cells, *Appl. Phys. Lett.* **102**, 183903 (2013).

17. Véron, A. C., et al. Nir-absorbing heptamethine dyes with tailor-made counterions for application in light to energy conversion, *Org. Lett.* **16**, 1044-1047 (2014).

18. Echlin, P. *Handbook of Sample Preparation for Scanning Electron Microscopy and X-Ray Microanalysis* (Springer, New York, 2009).

19. Guild, J. The colorimetric properties of the spectrum, *Philosophical Transactions of the Royal Society London A* **230**, 149-187 (1932).

20. Ameri, T., et al. Fabrication, optical modeling, and color characterization of semitransparent bulk-heterojunction organic solar cells in an inverted structure, *Adv. Funct. Mater.* **20**, 1592-1598 (2010).

21. Colsmann, A., et al. Efficient semi-transparent organic solar cells with good transparency color perception and rendering properties, *Adv. Energy Mater.* **1**, 599-603 (2011).

22. Chen, K.-S., et al. Semi-transparent polymer solar cells with 6% PCE, 25% average visible transmittance and a color rendering index close to 100 for power generating window applications, *Energy Environ. Sci.* **5**, 9551-9557 (2012).

23. Keivanidis, P. E., Ho, P. K. H., Friend, R. H. & Greenham, N. C. The dependence of device dark current on the active-layer morphology of solution-processed organic photodetectors, *Adv. Funct. Mater.* **20**, 3895-3903 (2010).

24. Zhang, H., et al. Photochemical transformations in fullerene and molybdenum oxide affect the stability of bilayer organic solar cells, *Adv. Energy Mater.* **5**, 1400734 (2015).

25. Zhang, H., et al. Semitransparent organic photovoltaics using a near-infrared absorbing cyanine dye, *Solar Energy Mater. Solar Cells* **118**, 157-164 (2013).

26. Gebeyehu, D., et al. The interplay of efficiency and morphology in photovoltaic devices based on interpenetrating network of conjugated polymers with fullerenes, *Syn. Met.* **118**, 1-9 (2001).

27. Jeong, W.-I., Lee, Y. E., Shim, H.-S., Kim, T.-M., Kim, S.-Y. & Kim, J.-J. Photoconductivity of $C_{60}$ as an origin of bias-dependent photocurrent in organic photovoltaics, *Adv. Funct. Mater.* **22**, 3089-3094 (2012).

28. Tress, W., Leo, K. & Riede, M. Photoconductivity as loss mechanism in organic solar cells, *Phys. Status Solidi RRL* **7**, 401-405 (2013).

29. Lin, Y.-Y., et al. Interfacial nanostructuring on the performance of polymer/$TiO_2$ nanorod bulk heterojunction solar cells, *J. Am. Chem. Soc.* **131**, 3644-3649 (2009).

30. Eom, S. H., et al. Roles of interfacial modifiers in hybrid solar cells: inorganic/polymer bilayer vs inorganic/polymer:fullerene bulk heterojunction, *ACS Appl. Mater. Interfaces* **6**, 803-810 (2014).

31. Arca, F., et al. Interface trap states in organic photodiodes, *Sci. Rep.* **3**, 1324 (2013).

32. Nüesch, F., Rotzinger, F., Si-Ahmed, L. & Zuppiroli, L. Chemical potential shifts at organic device electrodes induced by grafted monolayers, *Chem. Phys. Lett.* **288**, 861-867 (1998).

33. Kim, J. Y., et al. New architecture for high-efficiency polymer photovoltaic cells using solution-based titanium oxide as an optical spacer, *Adv. Mater.* **18**, 572-576 (2006).

34. He, G., et al. Ulta-high efficiency electrophosphorescent p-i-n OLEDs with double emission layers, *Proceedings of SPIE* **5519**, 42-47 (2004).

35. Araujo de Castro, F., Heier, J., Nüesch, F. & Hany, R. Origin of the kink in current-density versus voltage curves and efficiency enhancement of polymer-$C_{60}$ heterojunction solar cells, *IEEE J. of selected topics in quantum electronics* **16**, 1690-1699 (2010).

36. Peumans, P., Yakimov, A. & Forrest, S. R. Small molecular weight organic thin-film photodetectors and solar cells, *J. Appl. Phys.* **93**, 3693-3723 (2003).

37. Hoppe, H., Sariciftci, N. S. & Meissner, D. Optical constants of conjugated polymer/fullerene based bulk-heterojunction organic solar cells, *Mol. Cryst. Liq. Cryst.* **385**, 113-119 (2002).

38. Wang, X., Wu, G., Zhou, B. & Shen, J. Optical constants of crystallized $TiO_2$ coatings prepared by sol-gel process, *Materials* **6**, 2819-2830 (2013).

39. Maennig, B., et al. Organic p-i-n solar cells, *Appl. Phys. A* **79**, 1-14 (2004).

40. Al-Kuhaili, M. F., Durrani, S. M. A., Bakhtiari, I. A. & Al-Shukri, A. M. Optical constants and thermocoloration of pulsed laser deposited molybdenum oxide thin films, *Optics Commun.* **283**, 2857-2862 (2010).

41. Pettersson, L. A. A., Roman, L. S. & Inganäs, O. Modeling photocurrent action spectra of photovoltaic devices based on organic thin films, *J. Appl. Phys.* **86**, 487-496 (1999).

**Author contributions**

Devices were fabricated by H.Z., the dye was synthesized by A.C.V, transient spectroscopy was measured by J.De J., ellipsometry measurements were carried out by S.J, R.H., R.S. and F.N. contributed to project planning and manuscript preparation.

# Supplementary Information

**Transparent Organic Photodetector using a Near-Infrared Absorbing Cyanine Dye**

Hui Zhang, Sandra Jenatsch, Jelissa De Jonghe, Frank Nüesch, Roland Steim, Anna C. Véron, and Roland Hany[*]

**Supplementary Information 3S-1**

The growth mode of thin metal films depends on the metal type, substrate, film deposition method, or temperature. Large scale coalescence of metal islands during deposition eventually forms a continuous layer that allows for electrical conduction over macroscopic distances. The best compromise between increasing conductivity and decreasing transparency is close to that coalescence point. For Ag deposited on $MoO_3$, sheet resistance values of ~45 Ω square$^{-1}$ (8 nm Ag) or ~10 Ω square$^{-1}$ (10 nm Ag) were measured[S11]. In reference S12, these sheet resistance values were reported as ~95 Ω square$^{-1}$ (8 nm Ag) and ~40 Ω square$^{-1}$ (12 nm Ag). The conductivity for thin Au films on $MoO_3$ seems to be even slightly higher, and sheet resistances <10 Ω square$^{-1}$ were measured for 10 nm thick Au films[S13]. In all cases, sheet resistances decreased with increasing metal film thickness. We calculated AVT values of photodetectors with different thickness combinations of the top Au / $MoO_3$ electrode (Figure S1). For a 40 nm thick $MoO_3$ layer, AVT values are 71.5% and 68% for Au thicknesses of 8 nm and 12 nm, respectively. This indicates that when the electrode sheet resistance value needs to be decreased, this can be accepted with a relatively small drop in the AVT .
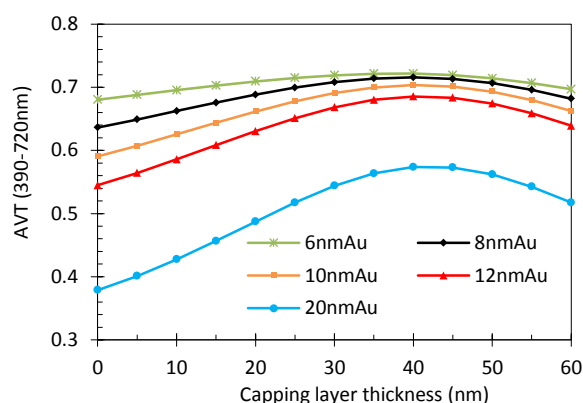


Figure 3S- 1 Calculated average visible transmittance (AVT) values for different thickness combinations of the top Au / $MoO_3$ electrode.

S11. Schubert, S., Hermenau, M., Meiss, J., Müller-Meskamp, L. & Leo, K. Oxide sand-wiched metal thin-film electrodes for long-term stable organic solar cells, *Adv. Funct. Mater.* 22, 4993-4999 (2012).

S12. Tian, B., Williams, G., Ban, D. & Aziz, H. Transparent organic light-emitting devices using a $MoO_3/Ag/MoO_3$ cathode, *J. Appl. Phys.* 110, 104507 (2011).

S13. Wrzesniewski, E., Eom, S.-H., Hammond, W. T., Cao, W. & Xue, J. Transparent oxide/metal/oxide trilayer electrode for use in top-emitting organic light-emitting diodes, *J. Photonics for Energy* 1, 011023 (2011).

**Supplementary Information 3S-2**
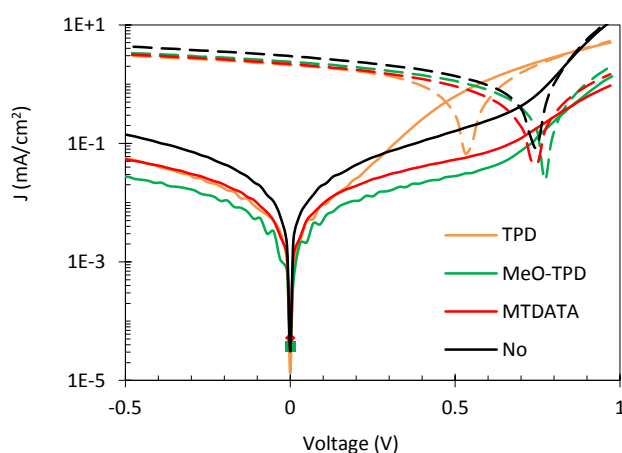


Figure 3S- 2 Current-voltage characteristics in the dark (full lines) and under illumination

(dotted lines, 100 mW cm$^{-2}$) of ITO / $TiO_2$(50 nm) / Cy7-T(20 nm) / EBL(10 nm) / $MoO_3$(30 nm) / Ag(80 nm) devices using different electron-blocking layers EBL. m-MTDATA is 4,4,4',4'-Tris[(3-methylphenyl) phenyla-mino] triphenylamine (Sigma-Aldrich, ≥99.0%), TPD is N,N'-Bis(3-methylphenyl)-N,N'-diphenylbenzidine (Sigma-Aldrich, 99%).

Table 3S- 1 Device performance / parameters for J-V curves shown in Figure 3S-2.

| EBL[a)] | | | | Device performance | | | | |
|---|---|---|---|---|---|---|---|---|
| | HOMO | LUMO | Hole mobility | $V_{oc}$ | $J_{sc}$ | Eff | FF | $r_{p/d}$ [b)] |
| | (eV) | (eV) | (cm$^2$ V$^{-1}$ s$^{-1}$) | (V) | (mA cm$^{-2}$) | (%) | (%) | (at -0.1 V) |
| no | | | | 0.74 | 2.73 | 0.75 | 37 | $1.5\times10^2$ |
| m-MTDATA | -5.1 | -2.0 | $3\times10^{-5}$ | 0.74 | 2.20 | 0.50 | 31 | $2.2\times10^2$ |
| TPD | -5.4 | -2.4 | $1.4\times10^{-3}$ | 0.51 | 2.16 | 0.40 | 37 | $2.6\times10^2$ |
| MeO-TPD | -5.1 | -1.9 | $1.1\times10^{-3}$ | 0.77 | 2.01 | 0.50 | 32 | $4.9\times10^2$ |

[a)] HOMO, LUMO energies and hole mobility values were taken from

He, G., Walzer, K., Pfeiffer, M., Leo, K., Pudzich, R. & Salbeck, J. *Proceedings of SPIE* **5519**, 42-47 (2004);

Kulshreshtha, C., Choi, J. W., Kim, J.-k., Jeon, W. S., Suh, M. C., Park, Y. & Kwon, J. H. *Appl. Phys. Lett.* **99**, 023308 (2011);

Shirota, Y. *J. Mater. Chem.* **10**, 1-25 (2000);

Lee, J., Kim, S.-Y., Kim, C. & Kim, J.-J. *Appl. Phys. Lett.* **97**, 083306 (2010);

Goushi, K., Yoshida, K., Sato, K. & Adachi, G. *Nature Photon.* **6**, 253-258 (2012).

[b)] $r_{p/d}$ is the ratio between the photocurrent and the dark current.

We observed that for comparable $J_{sc}$ current values, the dark current was smallest when using MeO-TPD, resulting in the largest value for $r_{p/d}$.

## Supplementary Information 3S-3
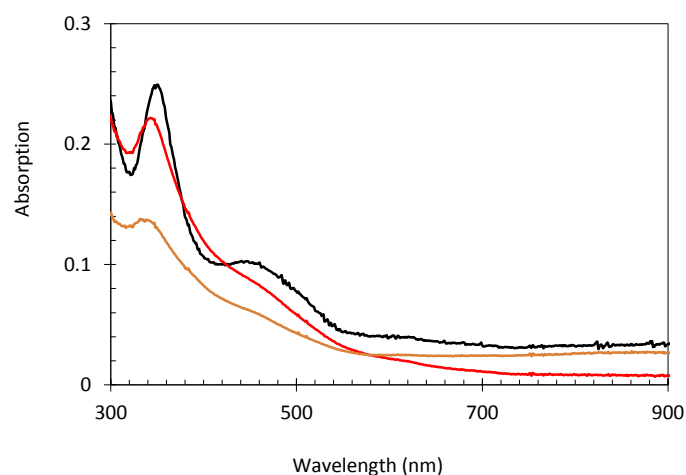


Figure 3S- 3 Absorption spectra of a ~15 nm thick $C_{60}$ film

after evaporation (black line), after illumination (100 mW cm$^{-2}$) for 12 h under nitrogen atmosphere (red line), and after spin coating with chlorobenzene (orange line). During light exposure $C_{60}$ polymerizes [S3] and becomes partially insoluble in chlorobenzene. The $C_{60}$ film thickness after solvent treatment is ~ 9 nm.

S3. Zhang, H., Borgschulte, A., Castro, F. A., Crockett, R., Gerecke, A. C., Deniz, O., Heier, J., Jenatsch, S., Nüesch, F., Sanchez-Sanchez, C., Zoladek-Lemanczyk, A. & Hany, R. *Adv. Energy Mater.* **5**, 1400734 (2014).

## Supplementary Information 3S-4
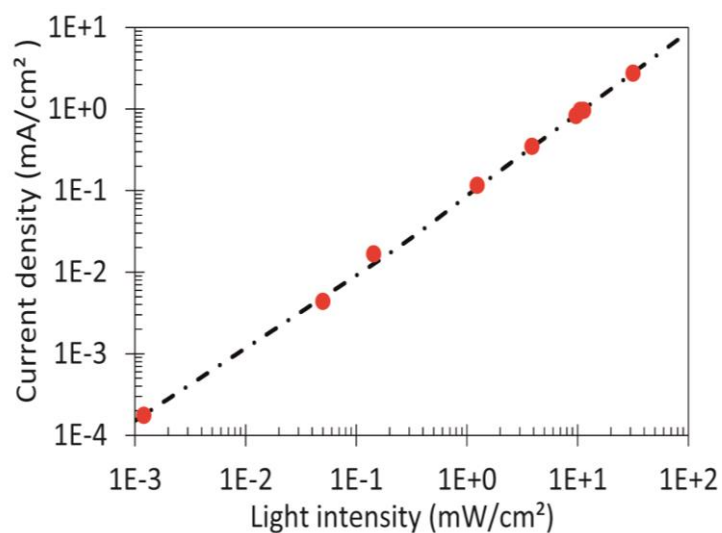
Figure 3S- 4 Photocurrent versus light intensity (wavelength range 780 – 880 nm).


## Supplementary Information 3S-5
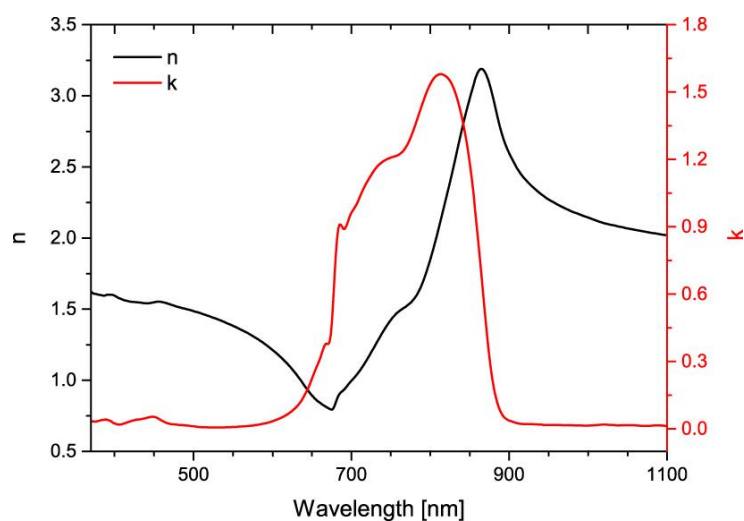


Figure 3S- 5 Refractive index (n) and extinction coefficient (k) of Cy7-T.

Optical constants for Cy7-T were determined by spectroscopic ellipsometry (M-2000, J.A. Woolam Co., Inc.).

For the ellipsometry measurements, cyanine films were spin coated from chlorobenzene onto silicon wafers.

# Chapter IV. Tandem OPVs

**Cyanine Tandem- and Triple-Junction Solar Cells**

Hui Zhang[1], Bjoern Niesen[2], Erwin Hack[3], Roland Hany[1], Frank Nüesch[1,4,*]

[1]Empa, Swiss Federal Institute for Materials Science and Technology, Laboratory for Functional Polymers, CH-8600 Dübendorf, Switzerland.

[2]Ecole Polytechnique Fédérale de Lausanne (EPFL), IMT, Photovoltaics and Thin Film Electronics Laboratory, Breguet 2, CH-2000 Neuchâtel, Switzerland

[3]Empa, Swiss Federal Institute for Materials Science and Technology, Reliability Science and Technology, CH-8600 Dübendorf, Switzerland.

[4]Institut des Matériaux, Ecole Polytechnique Fédérale de Lausanne, EPFL, Station 12, CH-1015 Lausanne, Switzerland.

* Correspondence should be addressed to      Prof. Dr. Frank Nüesch

Empa

Überlandstr. 129

CH-8600 Dübendorf

Switzerland

Phone: +4158 765 4740; fax: +41 58 765  4012;

e-mail: frank.nueesch@empa.ch

**Declaration**: I fabricated all the devices, performed the AFM, UV-Vis, IPCE, I-V measurements and optical simulation, prepared samples for ellipsometry, carried out all data analysis, contributed to project planning and manuscript preparation.

**Abstract**: Ultrathin bilayer heterojunction solar cells using cyanine electron donors and electron acceptor $C_{60}$ are used to fabricate monolithically stacked tandem and triple junction devices. Sub-cell stack sequences as well as $C_{60}$ layer thicknesses are optimized by optical modelling and maximum efficiency is corroborated experimentally. The highest power conversion efficiency of 4.3% under full sun irradiation is achieved with a tandem cell where heptamethine and trimethine cyanine dyes are used in the front and back cell, respectively. The open circuit voltage matches the sum of the two respective open circuit voltages of the individual single junction solar cells within 3%. Triple junction cells using an additional sub-cell with a pentamethine cyanine suffer from electrical series resistance. At low light irradiation intensity, however, both triple and tandem solar cells reach power conversion efficiencies above 5% in agreement with the performance increase predicted from numerical simulation.

## 1. Introduction

Cyanine dyes are well known as sensitizers in silver halide photography[1], as fluorescent biomarkers[2] or as light-absorbing layer in optical data storage devices[3]. These polymethine dyes have rarely been used as solid organic semiconductors but show high promise due to very high absorption coefficients, tuneable absorption spectrum and the ability to form aggregates with highly delocalized excitons[4]. Facile and cost effective synthesis of soluble cyanines with good film forming properties add to the merits of this materials class as active semiconductors in organic photovoltaic devices (OPV)[5]. The first use of cyanine dyes as solid organic semiconductor material dates back to 1965 when Meier et al. discovered photoconductivity in this class of materials[6]. Much later first attempts were undertaken to use trimethine carbocyanine dyes as donors and acceptors in planar bilayer heterojunction devices[7]. Even though maximum external quantum efficiencies of close to 75% were achieved[8], best power conversion efficiencies (PCE) of 3.7% in cyanine devices[9] still lag behind other small molecular semiconductors[10] and polymers[11-16] that recently reached PCE in excess of 8%. The main reason for this shortcoming lies in the narrow absorption band of cyanine dyes, but also in the rather low charge carrier mobility which limits the active layer thickness to 20 nm-30 nm[17]. While the small width of the absorption spectrum limits photocurrent in single junction devices, well defined complementary absorption spectra are beneficial in multi-junction devices.

Organic multi-junction solar cells have been realized as a stacked assembly of single junction devices being electrically connected either in series or in parallel[18]. First multijunction solar

cells were simple mechanical stacks that hardly enabled to increase the power conversion efficiency in comparison with the constituting single junction solar cells[19-20]. In some work, the tandem cells were constructed out of single junctions employing the same materials which raised the efficiency due to an increased collection of photons and charge carriers. By now, design rules are well established to optimize efficiency in monolithically stacked multijunction organic solar cells. Optical and electrical modelling are invaluable tools for hitting the maximum efficiency spot in the fabrication of these multilayer solar cells. When organic semiconductors with non-overlapping absorption spectra can be used, optical device optimization is particularly eased[21-23]. For example, it enables to position the low band-gap material to the front in order to optimize absorption[24]. To date, tandem[25-26] and triple-junction[27] devices with PCE exceeding 10% and 11%, respectively, have been reported. In both cases the multijunction solar cell outperformed the best constituting single junction cell by about 30%. The big challenge for further improvements is to find organic semiconductors with complementary bandgaps in the near infrared domain as well as transparent and lossless recombination layers between the monolithically stacked cells. Furthermore, solution processed cells with low energy input are of particular economic and ecologic interest. Owing to their wide range of bandgaps, high extinction coefficients and solution processability, cyanine dyes are interesting candidates for organic multijunction solar cells.

In previous work, we have demonstrated single junction solar cells based on trimethine dyes (Cy3-P) with a band gap of ~1.8 eV[28] as well as NIR absorbing heptamethine dyes[29] (Cy7-T) with a band gap of 1.2 eV using a simple bilayer structure with $C_{60}$ as electron acceptor. In this work we investigate tandem solar cells with Cy3-P and Cy7-T as well as triple-junction solar cells using the latter dyes and a complementary absorbing pentamethine cyanine dye (Cy5-P). We optimized the multilayer structures by varying the thickness of the $C_{60}$ acceptor layers and changing the sub-cell sequence of the multijunction architecture using optical modelling based on transfer matrix formalism. Also, an efficient recombination layer composed of $MoO_3$ and a very thin metal layer was optimized by varying the metal and its nominal thickness. The maximum efficiency reached for tandem solar cells at AM1.5G solar irradiation conditions was 4.3% which is approximately 34% higher than the efficiency of the best single junction cell employed in the stack. Triple-junction devices were optimized in the same way as tandem cells and reached 3.6% at full solar irradiation. Tandem and triple-junction devices both reached a PCE of 5.2% at one tenth of the full sun intensity.

## 2. Experimental

## 2.1. Device fabrication

All single, tandem and triple-junction solar cells were fabricated and stored in a glove box under nitrogen ($H_2O$ < 1 ppm, $O_2$ < 10 ppm). Indium tin oxide-coated glass substrates (ITO, Thin Film Devices, 140 nm, resistivity 20 Ohm/square) were sequentially cleaned in acetone, ethanol, detergent and de-ionized water. Layers of electron acceptor $C_{60}$ (SES Research, 99.5% or 99.9%), anode buffer $MoO_3$ (Sigma Aldrich, 99.99%) , recombination metals Ag (Kurt J. Lesker, 99.99%), Al (Kurt J. Lesker, 99.999%) and Au (Kurt J. Lesker, 99.99%) as well as cathode buffer tris(8-hydroxyquinolinato)aluminium ($Alq_3$, Sigma-Aldrich, 99.995%) were deposited by thermal evaporation under high vacuum (< $5\times10^{-6}$ mbar). Active electron donor films consisting of cyanine dyes 1-ethyl-2-[3-(1-ethyl-3,3-dimethyl-1,3-dihydro-indol-2-ylidene)-propenyl]-3,3-dimethyl-3H-indolium hexafluorophosphate (Cy3-P, FEW Chemicals), 1,3,3-trimethyl-2-[5-(1,3,3-trimethyl-1,3-dihydro-indol-2-ylidene)-penta-1,3-dienyl]-3H-indolium hexafluorophosphate (Cy5-P, FEW Chemicals) and heptamethine cyanine dye 2-[2-[2-chloro-3-[2-(1-ethyl-1,3-dihydro-3,3-dimethyl-2H-indol-2-ylidene)ethylidene]-1-cyclohexen-1-yl]ethenyl]-1-ethyl-3,3-dimethyl-3H-indolium trisphate (Cy7-T, synthesized in our group) were spin coated from filtered 2,2,3,3-tetrafluoropropanol (TFP, Sigma-Aldrich) or chlorobenzene (CB, Sigma-Aldrich) solutions. The top silver electrode (Cerac, 99.99%) was evaporated through a shadow mask to define devices with active areas of 3.1 mm$^2$ or 7.1 mm$^2$.

Bilayer single-junction devices with the general architecture ITO/$MoO_3$ (10 nm)/Cyanine dye (20 nm)/$C_{60}$ (40 nm)/$Alq_3$ (2 nm)/Ag (100 nm) were fabricated by subsequent deposition steps on cleaned ITO substrates. The cyanine donor layers were deposited from solution and left for 2 h under vacuum before depositing the $C_{60}$ electron acceptor. TFP was used for Cy3-P and Cy5-P whereas CB was used in the case of Cy7-T. All other layers were deposited in the same vacuum chamber.

Tandem devices were fabricated by using ten consecutive deposition steps to form two stacked junctions with general architecture ITO/$MoO_3$ (10 nm)/ Cy7-T (20 nm)/$C_{60}$ ($x$ nm)/$Alq_3$ (2 nm)/RL ($z$ nm)/$MoO_3$ (10 nm)/ Cy3-P (20 nm)/$C_{60}$ ($y$ nm)/$Alq_3$ (2 nm)/Ag (100 nm). The recombination layer (RL) consisted of evaporated Au with nominal thickness $z$ varying form 0.1 nm to 1nm. For comparison, Ag and Al were also used. In the best performing device structure (Tan 7-3), the $C_{60}$ layer of the front cell had varying thicknesses $x$ ranging from 14 nm to 35 nm, while the $C_{60}$ thicknesses of the back cell was varied between 25 nm and 40 nm.

Triple-junction solar cells consisted of fifteen deposited layers with the general structure ITO/MoO$_3$ (10 nm)/ Cy7-T (20 nm)/C$_{60}$ ($x$ nm)/Alq$_3$ (2 nm)/Au (0.5 nm)/MoO$_3$ (10 nm)/ Cy3-P or Cy5-P (20 nm)/C$_{60}$ ($y$ nm)/Alq$_3$ (2 nm)/Au (0.5 nm)/MoO$_3$ (10 nm)/ Cy5-P or Cy3-P (20 nm)/C$_{60}$ (20 nm)/Alq$_3$ (2 nm)/Ag (100 nm). Two promising sequences, both comprising Cy7-T as front cell were investigated. The first (Tri 7-3-5) embeds Cy3-P in the middle cell and Cy5-P in the back cell, while the second (Tri 7-5-3) incorporates Cy5-P in the middle cell and Cy3-P in the back cell. As for single and tandem devices, only the cyanine films were deposited from solution, the other layers being deposited by vapor deposition under vacuum.

*2.2. Methods*

For solar cell characterization, the substrates were sealed in a vacuum tight box with current feedthroughs and an optical window. Current-voltage characteristics of the solar cells were measured by a Keithley 2400 source/measure unit in the dark and under simulated AM1.5G solar irradiation of 100 mW cm$^{-2}$ from a calibrated solar simulator (Spectra-Nova). For reduced irradiation conditions, the white light intensity $P_{in}$ was passed through neutral density filters (Andover Corporation Optical Filter). Open-circuit voltage ($V_{OC}$) and short-circuit current-density ($J_{SC}$) were obtained directly from the current-voltage characteristics. Power conversion efficiencies (*PCE*) were calculated as $PCE = FF \times V_{OC} \times J_{SC} \times P_{in}^{-1}$, where

$FF = (J \times V)_{max} \times V_{OC}^{-1} \times J_{SC}^{-1}$ and $(J \times V)_{max}$ relates to the current-density and voltage measured at the maximum power point. A Cornerstone 130 monochromator (Oriel) was used together with a 300 W Xe lamp to measure the incident photon-to-current conversion efficiencies (IPCE). They were calculated as $IPCE = \dfrac{hc}{\lambda e} \times J_{SC} \times P_{in}^{-1}$ where $h$ is Planck's constant, $e$ is the elementary charge and $\lambda$ is the monochromatic irradiation wavelength. The monochromatic light intensity was determined using a calibrated Si-diode. Reflection losses at the solar cell substrate were not considered in the calculation.

The IPCE of multijunction solar cells was measured with a custom-built spectral response setup equipped with lock-in amplifiers, a monochromator, and a xenon lamp whose light was chopped at a frequency of 43 Hz, without applying a bias voltage. The individual sub cells were measured utilizing appropriate combinations of blue, red, and near-infrared bias light, to generate high photocurrents in the sub cells not being measured. For this purpose, a halogen lamp with optical filters and LEDs were used. Specifically, for tandem cells, the Cy3-P IPCE was measured using a long pass filter with a cut-off wavelength of 630 nm (Schott RG-630) and the Cy7-T sub cell IPCE was measured using a Schott BG-23 band pass filter and a blue

LED (470 nm emission peak). For triple-junction cells, the Cy3-P sub cell IPCE was measured with a RG-630 long pass filter and a blue LED, the Cy5-P sub cell IPCE with a RG-830 long pass filter and a blue LED, and the Cy7-T sub cell IPCE with a BG-23 band pass filter and a red LED (emission peak at 650 nm).

Absorption spectra were measured on a Varian Cary 50 UV-vis spectrophotometer. Film thicknesses were determined by profilometry (Ambios XP1).

Optical constants *n* and *k* (see Supplementary Information) for Cy3-P, Cy5-P and Cy7-T were determined by spectroscopic ellipsometry (M-2000, J.A.Woolam Co., Inc.) and served as input for the optical modeling based on the software setfos (www.fluxim.ch). The modelling took into account the full device layer stack including the conducting ITO glass substrate.

## 3. Results and discussion

Cyanine dyes are characterized by a cationic chromophore with two end-standing nitrogens connected by a polymethine bridge. The absorption spectra of these dyes in solution are characterized by a narrow absorption spectrum and a huge maximum extinction coefficient, e.g. for Cy7-T the molar extinction coefficient at the maximum absorption wavelength of 796 nm reaches up to 360000 $M^{-1}cm^{-1}$ in CB. When coated as a thin solid film, the absorption maximum is red shifted and significantly broadened due to intermolecular interaction of the conjugated pi-systems, which is particularly important for dyes with strong transition dipole moments. The molecular structures and thin film absorption spectra of the cyanines Cy3-P, Cy5-P and Cy7-T as well as fullerene $C_{60}$ are shown in Fig.4-1. By combining the tri-, penta- and heptamethine dyes, solar light in the range between 450 nm and 900 nm can be captured. As deduced from the intersection of the absorption onset with the axis of abscissae, band gap energies of 1.8 eV (Cy3-P), 1.4 eV (Cy5-P) and 1.2 eV (Cy7-T) are obtained. It appears that the bandgaps of 1.8 eV and 1.2 eV would be quite ideal for inorganic semiconductor tandem cells, but that a lower bandgap would be needed for ideal triple layer devices. However, given the fact that the bandwidth of organic conjugated materials is much smaller than for inorganic semiconductors, organic multi-junction solar cells require case-by-case optimization.
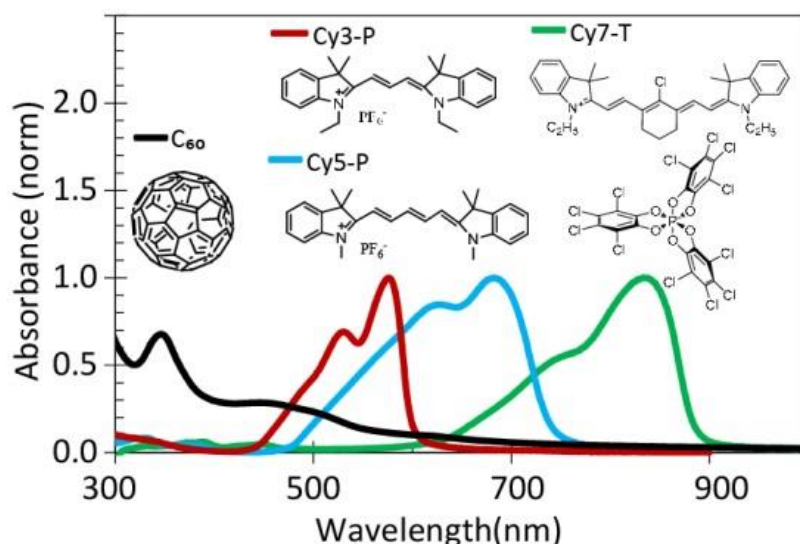
Figure 4- 1 Absorption spectra and molecular structures of $C_{60}$, Cy3-P, Cy5-P and Cy7-T

The performances of single junction solar cells composed of the different materials as well as the characteristic energy levels of the highest occupied molecular orbital (HOMO) and lowest unoccupied molecular orbital (LUMO) are given in Table 4-1. We have previously optimized the cyanine layer thickness in bilayer heterojunction solar cells and found that the optimum cyanine film thickness of 20 nm balances light absorption, exciton diffusion and charge carrier transport. Despite the small cyanine layer thickness used for all three devices, PCE of about 3% could be obtained for all three cyanine solar cells. More important for constructing multijunction devices is the fact that the short circuit current-density is matched between the cells, which is not the case for the optimized single layer devices in Table 4-1. For comparing modelled current densities with experimentally determined ones, light absorption was simulated using setfos software. The optical model implemented in the setfos absorption module is based on a modified transfer matrix formalism that allows calculating the photon flux across any optical stack. Input regarding layer thicknesses as well as the optical constants *n* and *k* as a function of wavelength are required to compute the optical electric field distribution through the multilayer device in a coherent way. Thicker layers such as the 1 mm thick glass substrate are treated in an incoherent way. If it is assumed that every absorbed photon in the electron donor and acceptor material generates one photon in the external electric circuit, the maximum short circuit current $J_{sc,max}$ can be computed. A series of single junction cells with different active layer thicknesses were fabricated to determine the average ratio of $J_{SC, exp}/ J_{SC, max}$, these values were then used as input to calculate $J_{SC, cal}$ for multijunction cells. We found that the experimental values $J_{sc,exp}$ are about 75% of the theoretical maximum and reflect losses due to either exciton diffusion, exciton dissociation or charge carrier collection. The high se-

ries resistance imposed by the low hole mobility in cyanine films accounts for part of these losses, but for the ultrathin cyanine layers used, the FF of 50-60% is nevertheless appreciably high for organic solar cell devices. The precise origin of the major bottleneck in this class of semiconductors is not fully understood, but is believed to be partly due to charge trapping induced by structural disorder. The exciton diffusion limitation accounts for another part of the loss and is governed by the very short luminescence lifetime in cyanine films of about 50 ps. Efficient excited state quenching in pure cyanine films occurs via twisted excited state intermediates also leading to cis isomers. Exciton localization in the disordered films is another possible mechanism that has been evidenced.

Table 4- 1 Experimental performances of single junction cyanine solar cells

| *Device* | *LUMO* /eV | *HOMO* /eV | $V_{OC}$ /V | $J_{SC,exp}$ /mAcm$^{-2}$ | *FF* /% | $\eta$ /% | $\eta_{best}$ /% |
|---|---|---|---|---|---|---|---|
| single Cy7-T cells (CB) | 4.2 | 5.4 | 0.63 | 7.1 | 52 | 2.3 | 2.8 |
| single Cy5-P cells (TFP) | 4.0 | 5.4 | 0.64 | 7.2 | 62 | 2.8 | 2.9 |
| single Cy3-P cells (TFP) | 3.9 | 5.7 | 0.90 | 6.2 | 55 | 3.0 | 3.2 |

All single junction devices have the same architecture ITO/MoO$_3$ (10 nm)/Cyanine dye (20 nm)/C$_{60}$ (40 nm) /Alq$_3$ (2 nm)/Ag (100 nm). The solvents used to deposit the cyanine films are also indicated (CB: chlorobenzene, TFP: tetrafluoropropanol)

An ideal tandem device configuration using inorganic semiconductors has the wide band gap subcell positioned to the front, followed by smaller bandgaps with the smallest bandgap to the very back of the multijunction stack. However, due to the specific absorption profiles and interference effects in thin layer organic solar cells, certain devices in reversed layer sequence are performing better[30-31].

Given the large number of stacked layer possibilities in multijunction devices, it is tedious to optimize the performance experimentally by altering the cell configuration in the stack and by varying the active layer thicknesses. Therefore the first step was to simulate tandem and triple-junction solar cells based on the single junction devices described above. For this purpose we used the optical module in setfos to calculate the $J_{SC,cal}$. To estimate the maximum PCE of the multiple junction devices, the open circuit voltage $V_{OC}$ is assumed to be equal to the sum of the open circuit voltages of the constituting sub cells (data taken from Table 4-1) and FF=65% was taken for the fill factor. Besides the different combinations of cell sequences, device optimization also includes variation of the C$_{60}$ layer thickness from 6 nm to 40 nm for

each sub-cell in the multilayer device. Due to the physical constraints of cyanine bilayer heterojunction devices explained above, all cyanine layer thicknesses were fixed to 20 nm. Recombination layers consisting of an $Alq_3$ (2 nm)/Au (1 nm)/ $MoO_3$ (10 nm) structure were taken for the simulations. Fig.4-2 displays the optimization procedure to find the ideal $C_{60}$ layer thickness in the subcells composed of a tandem device using Cy7-T and Cy3-P. Clearly, higher efficiencies are obtained when Cy7-T is used as the front cell (denoted as Tan 7-3) reaching a PCE up to 5.2 % while tandem cells with Cy3-P as the front cell reach only about 4.1%. Closer inspection of the light intensity distribution through the multilayer stack for the different device types reveals that the maximum NIR light intensity at 840 nm is always located in the front cells due to the thin active layer thickness for both sub-cells (see supplementary material Fig.4S-1).
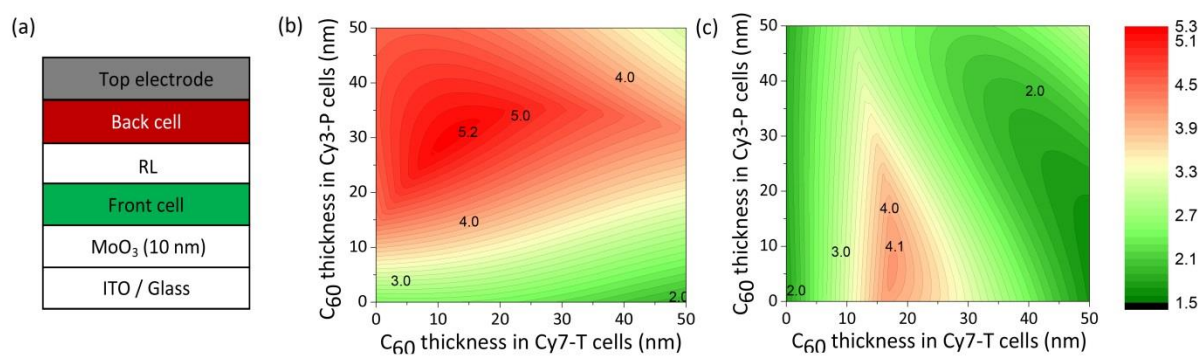


Figure 4- 2 Tandem device architecture (a) and simulated efficiencies of tandem devices (b) Tan 7-3 and (c) Tan 3-7.

A similar nomenclature is used for triple junction devices. For example Tri 7-5-3 means that the cell incorporating Cy7-T is used as front cell, the one using Cy5-P constitutes the middle cell and Cy3-P the back cell, respectively. Fig.4-3 displays all the calculated efficiency results of tandem and triple-junction devices that were obtained by optimizing the $C_{60}$ layer thicknesses as described above. Additionally, the single layer devices (e.g. single Cy3) of Table 4-1 are also included. The latter provide the highest short circuit densities but have lower efficiencies when compared to the multi junction devices. Clearly, Tan 7-3 outperforms all other tandem device configurations and was therefore chosen for experimental investigation. Regarding triple-junction solar cells, Tri 7-5-3, Tri 3-7-5 and Tri 7-3-5 revealed the highest efficiencies. Due to experimental difficulties of coating CB solutions of Cy7-T in Tri 3-7-5 devices without re-dissolving the underlying $C_{60}$ layer, only triple layer devices Tri 7-5-3 and Tri 7-3-5 were chosen for further experimental investigations.
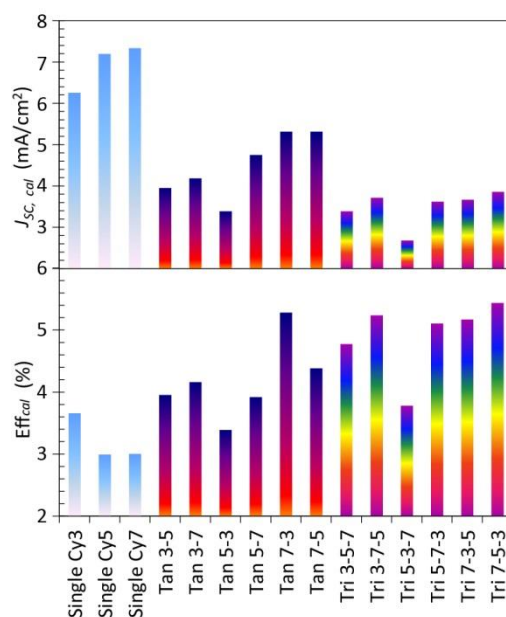
Figure 4- 3 Calculated current density and efficiency of single junction and multi-junction devices with different layer sequences.

The fabrication of monolithically stacked multjunction devices is analogous to single junction device fabrication, but bears additional difficulties. First, a recombination layer is necessary between two subsequent sub-cells in the stack. Negative charges from the front cell have to recombine with positive charges from the back cell through an Ohmic contact, such that no voltage drop occurs across the interface. In classical inorganic tandem solar cells this is achieved by a tunneling contact between highly p- and n-doped layers. A similar approach has been adopted for organic solar cells deposited by vapor deposition[32]. Though, the difficulty is to avoid parasitic absorption and therefore the most widely used approach consists of using a combination of oxide films and ultrathin metallic layers. The advantage of connecting the subcells in series is the fact that lateral conductivity is not required for the recombination layer. In order to increase optical transmission, the thin metallic layer therefore must not be continuous and can consist of fine clusters or even metallic nanowires[33]. If solution processing is applied, the intermediate layer also serves as protecting layer in order to avoid diffusion of solvent into the underlying layers. Therefore the oxide layer in the stack has to be continuous and preferably dense. In this work we used a combination of ultrathin metal layers evaporated on $Alq_3$ covered by a 10 nm thick $MoO_3$ layer. This system provides an excellent recombination path between n- and p-contacts of front and back cell, respectively. Numerous works confirmed that various metals such as Au, Ag or Al do form Ohmic contacts to $C_{60}$ when evaporated on a thin $Alq_3$ layer[8]. To find the optimum recombination layer in the cyanine devices

presented in this work, tandem solar cells with Tan 7-3 architecture were fabricated using different thin metal recombination layers.
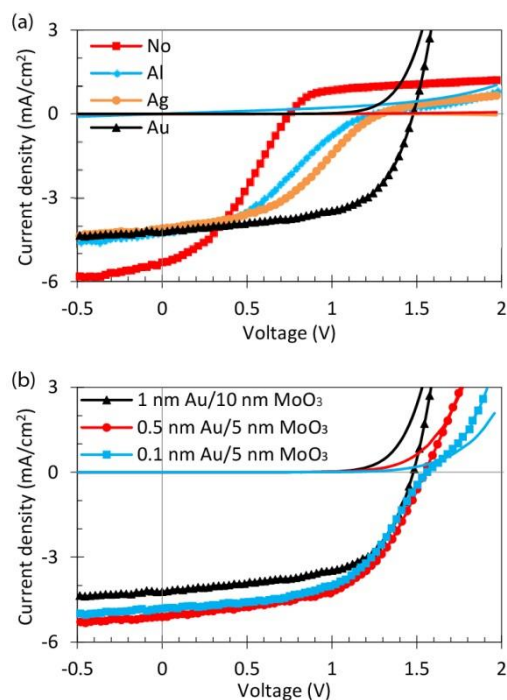


Figure 4- 4 (a) dark and light J-V curves of devices Tan 7-3 for different metals Al (1 nm), Ag (1 nm) and Au (1 nm) as internal recombination centers and combinations with 2 nm Alq$_3$/ metal/ 10 nm MoO$_3$, (b) thickness variation of RL layer combinations using Au, the other layers thicknesses were kept the same as for device 0 in Table 4-2

In absence of the highly conductive metal layer a strong S-shape and reverse diode characteristics under forward bias is evidenced (see Fig.4-4a). Such behavior has already been observed in tandem devices missing a recombination layer[34-35]. Reverse diode behavior can therefore originate from inverse junction formation between Cy3-P and C$_{60}$ across the non-continuous MoO$_3$ layer. The growth of thin MoO$_3$ layers on gold is known to proceed via a first, strongly interacting oxide monolayer that serves as wetting layer for the subsequent oxide layer[36]. Therefore the growth of the oxide intermediate layer depends also on the metal clusters being used as intermediate layers. Thin 1 nm films of Al or Ag did not provide the same quality of recombination layer and lead to S-shapes and reduced $V_{oc}$ in the tandem devices (Fig.4-4a). AFM analysis of 10 nm thick MoO$_3$ films deposited on Au, Ag or Al films reveal the lowest film roughness on gold surfaces, thus supporting a more compact and continuous MoO$_3$ film (see supplementary materials Fig. 4S-2). Still, the thickness of MoO$_3$ was quite crucial since layers thinner than 5 nm always lead to low fill factors and S-shaped current-voltage characteristics. We attribute this behavior to the interdiffusion of Cy3-P when

spin coating the back cell on top of the noncontiguous $MoO_3$. In order to search for maximum cell performance, reflectivity and electrical resistance of the RL were minimized by further reducing the gold and $MoO_3$ thickness to 0.1 nm and 5 nm, respectively (see Fig.4-4b). It has to be pointed out, however, that the device yield was lower than 40% in this case.

Table 4- 2 Experimental and calculated $J_{SC}$s for tandem devices Tan 7-3 with different $C_{60}$ layer thickness

| Device | $C_{60}$ [a] thickness /nm | $V_{OC}$ /V | $J_{SC, exp}$ /mAcm$^{-2}$ | $J_{SC,cal}$ /mAcm$^{-2}$ | FF / % | $\eta$ / % | $\eta_{best}$ / % |
|---|---|---|---|---|---|---|---|
| 0 | 14, 32 | 1.46 | 4.52 | 5.31 | 59.6 | 3.93 | 3.98 |
| 1 | 15, 25 | 1.49 | 3.98 | 4.89 | 58.6 | 3.48 | 3.77 |
| 2 | 15, 30 | 1.49 | 4.01 | 5.17 | 57.5 | 3.45 | 3.51 |
| 3 | 15, 35 | 1.44 | 3.94 | 5.12 | 58.3 | 3.31 | 3.40 |
| 4 | 15, 40 | 1.43 | 3.82 | 4.94 | 59.2 | 3.23 | 3.61 |
| 5 | 20, 35 | 1.42 | 3.69 | 5.12 | 59.5 | 3.13 | 3.18 |
| 6 | 25, 35 | 1.44 | 3.78 | 4.98 | 59.2 | 3.22 | 3.56 |
| 7 | 35, 35 | 1.43 | 3.05 | 4.65 | 61.1 | 2.67 | 2.78 |
| 8[b] | 14, 32 | 1.52 | 4.99 | 5.41 | 55.3 | 4.19 | 4.31 |
| 9[c] | 14, 32 | 1.55 | 4.81 | 5.41 | 53.3 | 3.98 | 4.10 |

a) x, y refer to the $C_{60}$ thicknesses in the front and back cells, respectively. device 0-7 RL layer: 2 nm $Alq_3$/1 nm Au / 10 nm $MoO_3$, b) RL layer: 2 nm $Alq_3$/0.5 nm Au /5 nm $MoO_3$ , averaged from 3 independent devices (24 cells) , c) RL layer: 2 nm $Alq_3$/0.1 nm Au/5 nm $MoO_3$.

In order to optimize tandem devices experimentally and to verify the modeling results, multi-layer solar cells with different $C_{60}$ layer thicknesses were fabricated using a recombination layer incorporating a 1 nm thick Au layer and a 10 nm thick $MoO_3$ film. For further optimization, thinner gold and $MoO_3$ films were also used in specific cases (see Table 4-2). Given the short exciton diffusion length and limited hole transport mobility of cyanine films, the layer thicknesses of all cyanine donor films were kept to 20 nm, same as in optimized single junction devices. As shown in Table 4-2 the variation of the $C_{60}$ thicknesses in the front and back cell greatly influences the efficiency of the tandem devices. The open circuit voltage of 1.4 V to 1.5 V is only slightly affected and in the best case comes very close to the sum of $V_{OC}$ of the two single junction cells (the difference is only 2.6%). On the other hand, the short circuit current density $J_{SC,exp}$ varies considerably from 3 mA/cm$^2$ to 5 mA/cm$^2$. Given the good qualitative agreement with the modeled short circuit current $J_{SC,cal}$, we conclude that the efficiency differences correlate with the light absorption profiles in the different multilayer stacks. The average ratio $J_{SC,exp}/J_{SC,cal}$ of 80±6% indicates that important losses are reducing the power

conversion efficiency besides incomplete light absorption. As explained before, losses could be due to exciton diffusion, exciton dissociation or charge transport. The latter point was assessed by reducing the full sun light irradiation intensity from 100% to 10% using neutral density filters (Fig.4-5). The efficiency at one tenth of the solar irradiation intensity is about 5.3%, which is very close to the calculated maximum values as shown in Fig.4-3. Since $J_{SC,exp}$ in single junction solar cells depends linearly on light intensity, we attribute the current loss in tandem devices to charge accumulation at the recombination layer. As we will show below, the loss is even more pronounced for triple junction solar cells using two such junctions.
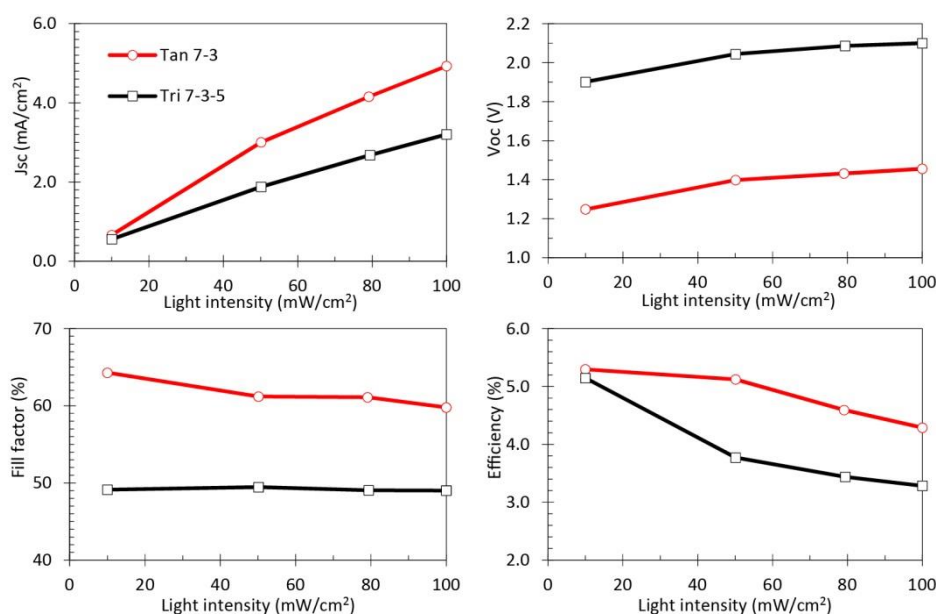


Figure 4- 5 $J_{SC}$, $V_{OC}$, *FF* and efficiency of the tandem cell and triple cell as functions of light intensity

Triple junction devices were constructed with Cy7-T incorporated in the front cel. In analogy to tandem devices, we varied the $C_{60}$ layer thicknesses of the individual junctions in the triple layer device stack (Table 4-3). This time, $V_{OC}$ varied quite substantially from 1.47 V to 2.11 V. The reason is not so clear until now, but we identified that coating Cy3-P on a Cy5-P cell as the problematic step leading to inhomogeneous films. In the optimized Tri-7-3-5 cell, $V_{OC}$ remarkably approaches the sum of the single junction cells (difference of 4.6%). The short circuit current $J_{SC,exp}$ showed less variation from 3.03mA/cm$^2$ to 3.61 mA/cm$^2$. Again, a good qualitative agreement of the experimental current density values with the modeled ones is observed. The intensity dependence shown in Fig.4-5 underlines the losses of $J_{SC,exp}$. As a matter of fact the efficiency of triple junction solar cells of 5.2% measured at 0.1 solar irradiation intensity comes very close to the one for tandem cells of 5.3% measured under the same condi-

tions. Almost identical efficiencies for ideal devices have indeed been predicted by the modeling studies.

Table 4- 3 Experimental and calculated $J_{SC}$s for triple junction devices Tri 7-3-5 and Tri 7-5-3 with different $C_{60}$ layer thicknesses

| Devices | $C_{60}$[a] thickness /nm | $V_{OC}$ /V | $J_{SC, exp}$ /mAcm$^{-2}$ | $J_{SC,cal}$ /mAcm$^{-2}$ | FF / % | $\eta$ / % | $\eta_{best}$ / % |
|---|---|---|---|---|---|---|---|
| Tri 7-5-3 | 10, 12, 20 | 1.87 | 3.21 | 3.81 | 54.9 | 3.3 | 3.5 |
| Tri 7-5-3 | 8, 10, 20 | 1.47 | 3.61 | 3.86 | 49.4 | 2.6 | 3.0 |
| Tri 7-5-3 | 10, 10, 20 | 1.81 | 3.00 | 3.79 | 51.8 | 2.8 | 2.9 |
| Tri 7-3-5 | 8, 10, 20 | 2.08 | 3.38 | 3.66 | 47.4 | 3.3 | 3.5 |
| Tri 7-3-5 | 10, 12, 20 | 2.11 | 3.03 | 3.54 | 50.3 | 3.2 | 3.6 |
| Tri 7-3-5 | 10, 10, 20 | 2.03 | 3.22 | 3.58 | 46.1 | 3.0 | 3.2 |

a) x,y,z refer to the $C_{60}$ thicknesses in the bottom, middle and top sub-cell, respectively

In order to verify the short term stability of the multijunction solar cells, tandem and triple junction devices were aged in inert nitrogen atmosphere for more than one month in the absence of light. At room temperature, an initial degradation of the power conversion efficiency of 35% set in during the first 10 days (Fig.4-6c). After this initial aging period the PCE stabilized and stayed constant for the next 40 days. When the same type of aging was carried out at the lowered temperature of -15°C, PCE did not noticeably change during the first 15 days of aging (Fig.4-6c). Looking at the device characteristics (Fig.4-6c) it appears that the $V_{OC}$ stayed unaffected by aging while the fill factor and to a lesser extent also $J_{SC}$ were most seriously reduced. The precise nature of this stabilization is not fully understood at the moment. However, since this phenomenon is not observed in single junction devices, there is strong evidence that deterioration of FF and $J_{SC}$ is related to the reconstruction of the RL. Gold atoms and clusters are able to diffuse into the organic layer during evaporation. They may also diffuse at organic interfaces and agglomerate. As we have shown in Fig.4-4, the effectiveness of the RL depends strongly on Au nanocluster formation. If the clusters are more widely spaced from each other, e.g. when agglomerating at the interface, negative photogenerated charges may not be removed quickly enough by the RL and would therefore charge up the interface and lead to an S-shaped I-V curve. At low temperature, diffusion processes are slowed down which we also observe by the striking stabilization of PCE when reducing the storage temperature of devices.
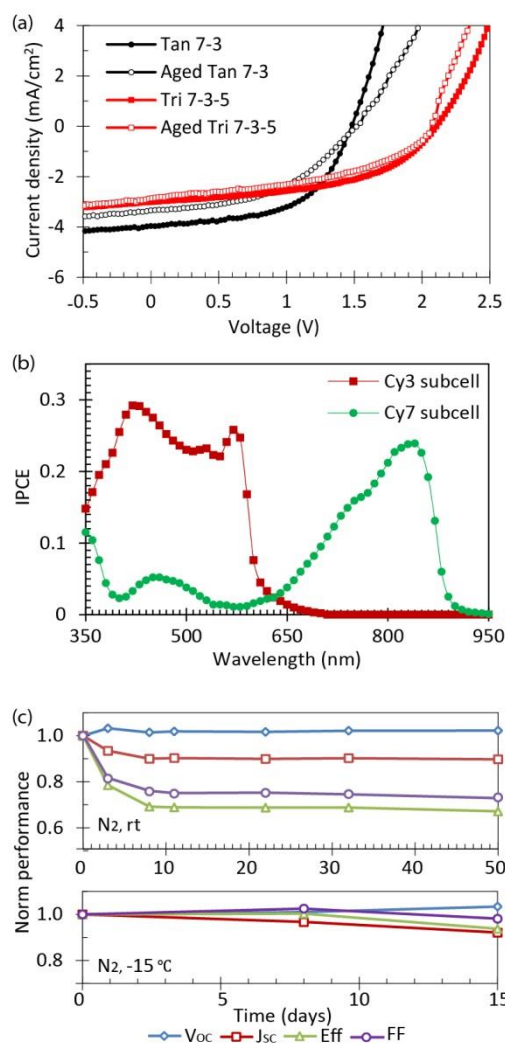
Figure 4- 6 a) Current-voltage characteristics of a tandem device Tan 7-3 and triple junction device Tri 7-3-5 freshly prepared (full symbols) and after 10 days of aging in the dark under nitrogen (empty symbols). b) IPCE spectrum of tandem device Tan 7-3 after 10 days of aging in the dark, (c) degradation trend of the performance of tandem device Tan 7-3 at room temperature and at -15°C.

To avoid effects of aging, stabilized tandem devices were used for the IPCE measurements as described in the experimental section. The maximum quantum efficiency is rather low and reflects not only the aging of the devices, but also the fact that bilayer heterojunctions are used in this work. IPCE measurements of the individual sub-cells in the tandem stack show almost identical spectra as compared with single junction solar cells, except for the lower quantum yield in the region where $C_{60}$ absorbs. This comes from the smaller $C_{60}$ thickness used in the Cy7-T front cell as compared to optimized single layer junctions. In accordance to numerical simulation, current matching is obtained by decreasing the $C_{60}$ layer thickness of the Cy7-T based front cell with respect the $C_{60}$ layer thickness used in the back cell. When integrating

the IPCE in Fig.4-6b with the AM1.5G solar irradiation spectrum, we obtain a short circuit current density $J_{SC}$ of 3.50 mA/cm$^2$ and 3.12 mA/cm$^2$ for Cy3-P and Cy7-T based sub-cells, respectively. The currents match quite well and indeed, the short circuit current coming from the Cy7-T cell is limiting $J_{SC}$ as predicted by modelling. Furthermore, the integrated IPCE spectra correspond quite well to the $J_{SC}$ of stabilized devices measured under white light irradiation (Fig.4-6a).

The IPCE spectra also reveal the fact that only very little photocurrent is produced between 600 nm and 700 nm which led us to the investigation of triple junction devices using Cy5-P with an absorption maximum in precisely above spectral region. As we have elucidated experimentally and by modelling, addition of the supplementary cyanine junction absorbing in this range does not increase the power conversion efficiency with respect to the tandem device (see Fig.4-3). To investigate this effect experimentally, we attempted to measure the IPCE of triple junction solar cells. Unfortunately, this was not possible with our setup, mainly because the Cy5-P sub-cell could not be saturated selectively. Therefore the IPCE spectra of the front Cy7-T and middle Cy3-P cell always showed a contribution of the Cy5-P cell (supplementary materials Fig.4S-3). By integrating the IPCE spectra of the individual cells in the stack with the AM1-5G spectrum, it clearly appears that $J_{SC}$= 1.58 mA/cm$^2$ in the Cy3-P based middle cell of the triple junction solar cell is about 35% lower than in the bottom and top cell, which contradicts the much higher current density of $J_{SC}$= 2.8 mA/cm$^2$ observed under white light irradiation of the stabilized triple junction cell Tri 7-3-5.

## 4. Conclusion

Soluble trimethine, pentamethine and heptamethine cyanine dyes with bandgaps of 1.2 eV, 1.4 eV and 1.8 eV, respectively, were used to construct tandem and triple junction devices. This result is remarkable, if one considers that cyanine dye semiconductors with low charge carrier mobility were employed in this work. Optical simulation of the devices revealed losses in the extracted current of 25% if an internal quantum efficiency of 1 is assumed. The modelling studies showed also that tandem and triple junction architectures constructed by stacking cyanine bilayer solar cells with different bandgaps and optimizing the C$_{60}$ electron acceptor thicknesses of the sub-cells could increase efficiency by 50 % with respect to the best single junction solar cells. At full AM1.5G simulated sunlight irradiation an appreciable increase of 34% was observed which is believed to be limited by the series resistance induced by the recombination layers. At low light intensity, the power conversion efficiency increase over the best single junction device was over 60% and demonstrates the potential of multijunction de-

vices made from bilayer heterojunction sub-cells. Future work has now to address stability and efficiency of the recombination layers.

**References**

[1] James, T. H., The Theory of the Photographic Process. 4th ed.; Macmillan, New York: 1977.

[2] Sargent, P. B., Double-Label Immunofluorescence with the Laser-Scanning Confocal Microscope Using Cyanine Dyes. Neuroimage 1994, 1 (4), 288-295.

[3] Mustroph, H.; Stollenwerk, M.; Bressau, V., Current Developments in Optical Data Storage with Organic Dyes. Angewandte Chemie-International Edition 2006, 45 (13), 2016-2035.

[4] Mishra, A.; Behera, R. K.; Behera, P. K.; Mishra, B. K.; Behera, G. B., Cyanines During the 1990s: A Review. Chem Rev 2000, 100 (6), 1973-2011.

[5] Heterocyclic Polymethine Dyes: Synthesis, Properties and Applications. Springer-Verlag: Berlin, 2008.

[6] Meier, H., Organic Dyes as Photoelectric Semiconductors. Angewandte Chemie-International Edition 1965, 4 (8), 619-635.

[7] Meng, F. S.; Chen, K. C.; Tian, H.; Zuppiroli, L.; Nuesch, F., Cyanine Dye Acting Both as Donor and Acceptor in Heterojunction Photovoltaic Devices. Applied Physics Letters 2003, 82 (21), 3788-3790.

[8] Fan, B.; de Castro, F. A.; Heier, J.; Hany, R.; Nuesch, F., High Performing Doped Cyanine Bilayer Solar Cell. Organic Electronics 2010, 11 (4), 583-588.

[9] Berner, E.; Jaeger, T.; Lanz, T.; Nueesch, F.; Tisserant, J.-N.; Wicht, G.; Zhang, H.; Hany, R., Influence of Crystalline Titanium Oxide Layer Smoothness on the Performance of Inverted Organic Bilayer Solar Cells. Applied Physics Letters 2013, 102 (18).

[10] Liu, Y.; Chen, C.-C.; Hong, Z.; Gao, J.; Yang, Y.; Zhou, H.; Dou, L.; Li, G.; Yang, Y., Solution-Processed Small-Molecule Solar Cells: Breaking the 10% Power Conversion Efficiency. Scientific Reports 2013, 3, 3356.

[11] Liu, Y.; Zhao, J.; Li, Z.; Mu, C.; Ma, W.; Hu, H.; Jiang, K.; Lin, H.; Ade, H.; Yan, H., Aggregation and Morphology Control Enables Multiple Cases of High-Efficiency Polymer Solar Cells. Nature Communications 2014, 5, 5293.

[12] Lu, L.; Xu, T.; Chen, W.; Landry, E. S.; Yui, L., Ternary Blend Polymer Solar Cells with Enhanced Power Conversion Efficiency. Nature Photonics 2014, 8 (9), 716-722.

[13] Guo, X.; Zhou, N.; Lou, S. J.; Smith, J.; Tice, D. B.; Hennek, J. W.; Ponce Ortiz, R.; Lopez Navarrete, J. T.; Li, S.; Strzalka, J.; Chen, L. X.; Chang, R. P. H.; Facchetti, A.; Marks, T. J., Polymer Solar Cells with Enhanced Fill Factors. Nature Photonics 2013, 7 (10), 825-833.

[14] He, Z.; Zhong, C.; Su, S.; Xu, M.; Wu, H.; Cao, Y., Enhanced Power-Conversion Efficiency in Polymer Solar Cells Using an Inverted Device Structure. Nature Photonics 2012, 6 (9), 591-595.

[15] Lu, L.; Xu, T.; Chen, W.; Lee, J. M.; Luo, Z.; Jung, I. H.; Park, H. I.; Kim, S. O.; Yu, L., The Role of N-Doped Multiwall Carbon Nanotubes in Achieving Highly Efficient Polymer Bulk Heterojunction Solar Cells. Nano Letters 2013, 13 (6), 2365-2369.

[16] Woo, S.; Kim, W. H.; Kim, H.; Yi, Y.; Lyu, H.-K.; Kim, Y., 8.9% Single-Stack Inverted Polymer Solar Cells with Electron-Rich Polymer Nanolayer-Modified Inorganic Electron-Collecting Buffer Layers. Advanced Energy Materials 2014, 4 (7), 1301692.

[17] Jenatsch, S.; Hany, R.; Veron, A. C.; Neukom, M.; Zufle, S.; Borgschulte, A.; Ruhstaller, B.; Nüesch, F., Influence of Molybdenum Oxide Interface Solvent Sensitivity on Charge Trapping in Bilayer Cyanine Solar Cells. Journal of Physical Chemistry C 2014, 118 (30), 17036-17045.

[18] Etxebarria, I.; Furlan, A.; Ajuria, J.; Fecher, F. W.; Voigt, M.; Brabec, C. J.; Wienk, M. M.; Slooff, L.; Veenstra, S.; Gilot, J.; Pacios, R., Series Vs Parallel Connected Organic Tandem Solar Cells: Cell Performance and Impact on the Design and Operation of Functional Modules. Solar Energy Materials and Solar Cells 2014, 130, 495-504.

[19] Kawano, K.; Ito, N.; Nishimori, T.; Sakai, J., Open Circuit Voltage of Stacked Bulk Heterojunction Organic Solar Cells. Applied Physics Letters 2006, 88 (7).

[20] Shrotriya, V.; Wu, E. H. E.; Li, G.; Yao, Y.; Yang, Y., Efficient Light Harvesting in Multiple-Device Stacked Structure for Polymer Solar Cells. Applied Physics Letters 2006, 88 (6), 064104.

[21] Li, W. W.; Furlan, A.; Hendriks, K. H.; Wienk, M. M.; Janssen, R. A. J., Efficient Tandem and Triple-Junction Polymer Solar Cells. J Am Chem Soc 2013, 135 (15), 5529-5532.

[22] Kim, J. Y.; Lee, K.; Coates, N. E.; Moses, D.; Nguyen, T. Q.; Dante, M.; Heeger, A. J., Efficient Tandem Polymer Solar Cells Fabricated by All-Solution Processing. Science 2007, 317 (5835), 222-225.

[23] Dou, L. T.; You, J. B.; Yang, J.; Chen, C. C.; He, Y. J.; Murase, S.; Moriarty, T.; Emery, K.; Li, G.; Yang, Y., Tandem Polymer Solar Cells Featuring a Spectrally Matched Low-Bandgap Polymer. Nature Photonics 2012, 6 (3), 180-185.

[24] Cheyns, D.; Rand, B. P.; Heremans, P., Organic Tandem Solar Cells with Complementary Absorbing Layers and a High Open-Circuit Voltage. Applied Physics Letters 2010, 97 (3), 033301.

[25] Liu, Y.; Chen, C.-C.; Hong, Z.; Gao, J.; Michael Yang, Y.; Zhou, H.; Dou, L.; Li, G.; Yang, Y., Solution-Processed Small-Molecule Solar Cells: Breaking the 10% Power Conversion Efficiency. Scientific reports 2013, 3, 3356-3356.

[26] You, J. B.; Dou, L. T.; Yoshimura, K.; Kato, T.; Ohya, K.; Moriarty, T.; Emery, K.; Chen, C. C.; Gao, J.; Li, G.; Yang, Y., A Polymer Tandem Solar Cell with 10.6% Power Conversion Efficiency. Nature Communications 2013, 4.

[27] Chen, C. C.; Chang, W. H.; Yoshimura, K.; Ohya, K.; You, J. B.; Gao, J.; Hong, Z. R.; Yang, Y., An Efficient Triple-Junction Polymer Solar Cell Having a Power Conversion Efficiency Exceeding 11%. Advanced Materials 2014, 26 (32), 5670-+.

[28] Wicht, G.; Buecheler, S.; Dietrich, M.; Jaeger, T.; Nueesch, F.; Offermans, T.; Tisserant, J.-N.; Wang, L.; Zhang, H.; Hany, R., Stability of Bilayer Trimethine Cyanine Dye/Fullerene Organic Solar Cells. Solar Energy Materials and Solar Cells 2013, 117, 585-591.

[29] Veron, A. C.; Zhang, H.; Linden, A.; Nueesch, F.; Heier, J.; Hany, R.; Geiger, T., Nir-Absorbing Heptamethine Dyes with Tailor-Made Counterions for Application in Light to Energy Conversion. Organic Letters 2014, 16 (4), 1044-1047.

[30] Ameri, T.; Li, N.; Brabec, C. J., Highly Efficient Organic Tandem Solar Cells: A Follow up Review. Energy & Environmental Science 2013, 6 (8), 2390-2413.

[31] Dennler, G.; Forberich, K.; Ameri, T.; Waldauf, C.; Denk, P.; Brabec, C. J.; Hingerl, K.; Heeger, A. J., Design of Efficient Organic Tandem Cells: On the Interplay between Molecular Absorption and Layer Sequence. Journal of Applied Physics 2007, 102 (12), 123109.

[32] Timmreck, R.; Olthof, S.; Leo, K.; Riede, M. K., Highly Doped Layers as Efficient Electron-Hole Recombination Contacts for Tandem Organic Solar Cells. Journal of Applied Physics 2010, 108 (3), 033108.

[33] Li, N.; Stubhan, T.; Krantz, J.; Machui, F.; Turbiez, M.; Ameri, T.; Brabec, C. J., A Universal Method to Form the Equivalent Ohmic Contact for Efficient Solution-Processed Organic Tandem Solar Cells. Journal of Materials Chemistry A 2014, 2 (36), 14896-14902.

[34] Timmreck, R.; Olthof, S.; Leo, K.; Riede, M. K., Highly Doped Layers as Efficient Electron-Hole Recombination Contacts for Tandem Organic Solar Cells. Journal of Applied Physics 2010, 108 (3).

[35] Macko, J. A.; Lunt, R. R.; Osedach, T. P.; Brown, P. R.; Barr, M. C.; Gleason, K. K.; Bulovic, V., Multijunction Organic Photovoltaics with a Broad Spectral Response. Physical Chemistry Chemical Physics 2012, 14 (42), 14548-14553.

[36] Quek, S. Y.; Biener, M. M.; Biener, J.; Friend, C. M.; Kaxiras, E., Tuning Electronic Properties of Novel Metal Oxide Nanocrystals Using Interface Interactions: Moo3 Monolayers on Au(111). Surface Science 2005, 577 (2-3), L71-L77.

# Supplementary materials

**Cyanine Tandem- and Triple-Junction Solar Cells**

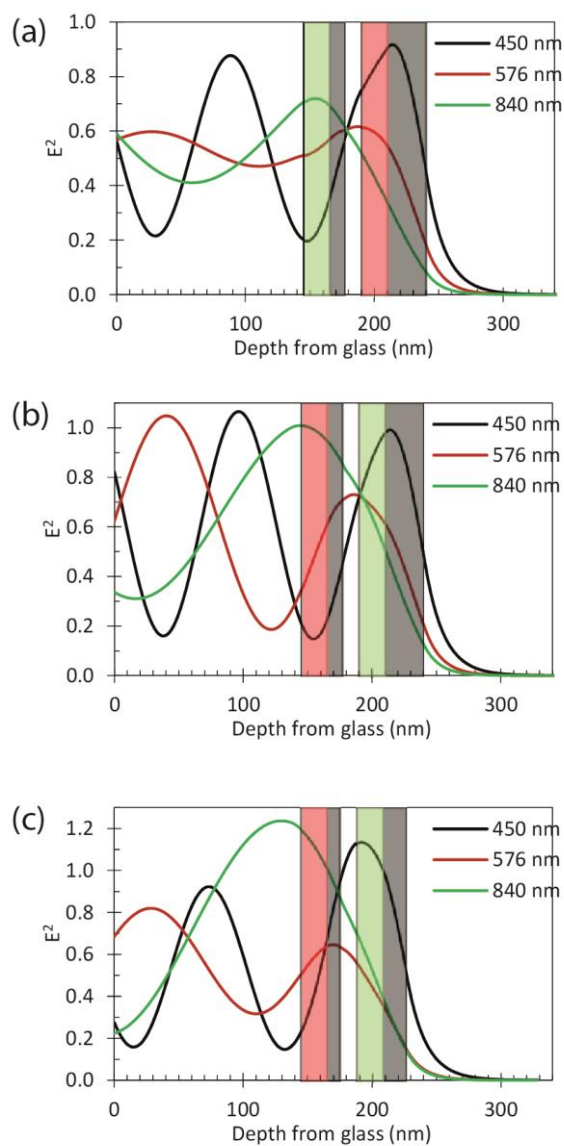Hui Zhang, Bjoern Niesen, Erwin Hack, Roland Hany, Frank Nüesch



Figure 4S- 1 Normalized optical electric field distribution for device (a) Tan 7-3 (14, 32), (b) Tan 3-7 (14, 32) and (c) Tan 3-7 (12, 18) at wavelengths of 450 nm, 576 nm and 840 nm
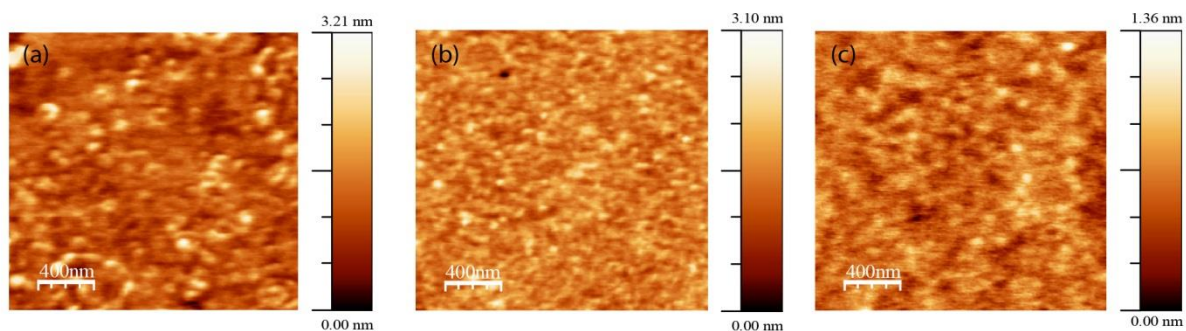
Figure 4S- 2 AFM images of 10 nm $MoO_3$ on top of 1 nm (a) Al, (b) Ag and (c) Au surfaces
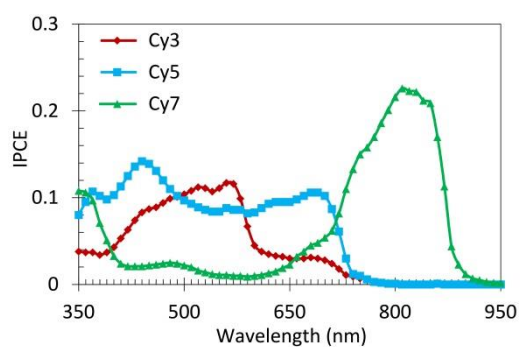


Figure 4S- 3 IPCE spectra of Tri 7-3-5 after 2 days of aging in the dark

# Chapter V. Stability of OPVs

**Photochemical Transformations in Fullerene and Molybdenum Oxide Affect the Stability of Bilayer Organic Solar Cells**

*Hui Zhang, Andreas Borgschulte, Fernando A. Castro, Rowena Crockett, Andreas C. Gerecke, Okan Deniz, Jakob Heier, Sandra Jenatsch, Frank Nüesch, Carlos Sanchez-Sanchez, Alina Zoladek-Lemanczyk, and Roland Hany*[*]

H. Zhang, Dr. J. Heier, S. Jenatsch, Prof. F. Nüesch, Dr. R. Hany, Empa, Swiss Federal Laboratories for Materials Science and Technology, Laboratory for Functional Polymers, Überlandstrasse 129, CH-8600 Dübendorf, Switzerland, E-mail: roland.hany@empa.ch

Dr. A. Borgschulte, Empa, Swiss Federal Laboratories for Materials Science and Technology, Laboratory for Hydrogen and Energy, Überlandstrasse 129, CH-8600 Dübendorf, Switzerland

Dr. F. A. Castro, Dr. A. Zoladek-Lemanczyk, NPL, National Physical Laboratory, Materials Division, Hampton Rd, Teddington TW11 0LW, UK

Dr. R. Crockett, Empa, Swiss Federal Laboratories for Materials Science and Technology, Laboratory for Nanoscale Materials Science, Überlandstrasse 129, CH-8600 Dübendorf, Switzerland

Dr. A. C. Gerecke, Empa, Swiss Federal Laboratories for Materials Science and Technology, Laboratory for Analytical Chemistry, Überlandstrasse 129, CH-8600 Dübendorf, Switzerland

O. Deniz, Dr. C. Sanchez-Sanchez, Empa, Swiss Federal Laboratories for Materials Science and Technology, Laboratory nanotech@surfaces, Überlandstrasse 129, CH-8600 Dübendorf, Switzerland

S. Jenatsch, Prof. F. Nüesch, Institut des Matériaux, Ecole Polytechnique Fédéral de Lausanne, EPFL Station 12, CH-1015 Lausanne, Switzerland

**Declaration**: I fabricated all the devices, performed the Fluorescence, AFM, UV-Vis, IPCE and I-V measurements, prepared samples for UPS, XPS and ESI-HRMS, carried out all data analysis, contributed to project planning and manuscript preparation.

**Abstract**: Thin films of fullerene $C_{60}$ and molybdenum oxide ($MoO_3$) are ubiquitously used as electron acceptor material and hole extraction interfacial layer for the fabrication of organic photovoltaic (OPV) cells. It is well known that light exposure induces color changes in $MoO_3$ (photochromism) and the formation of intermolecular bonds between $C_{60}$ molecules (photo-polymerization). The influence of these photoinduced reactions on the long-term stability of OPV cells, however, has not previously been studied in detail. We present a study and discuss the early (< 5 days) aging mechanisms occurring in illuminated ITO/$MoO_3$/organic cyanine dye/$C_{60}$/$Alq_3$/Ag bilayer solar cells under nitrogen atmosphere. We identify a degradation process at the organic heterojunction and the formation of $Mo^{5+}$ species during illumination that adversely affect cell behavior. For these widely used materials, our results suggest that light processing is a first necessary step before OPV characteristics can be meaningfully rated.

**Keywords**: fullerene, molybdenum oxide, photopolymerization, photochromism, organic solar cell

## 1. Introduction

Rapid progress is made in the field of organic photovoltaics and power conversion efficiencies of 8-10% have repeatedly been reported.[1-3] As exciting as these advances are, an important requirement for their commercialization is the demonstration of OPV cells that maintain the initial performance over an operating time of several years. However, increasing the lifetime of OPV cells remains a major challenge, with extrinsic (water, oxygen or light) and intrinsic (e.g. morphology changes) stress factors inducing cell degradation in a complex and often interrelated way.[4-8]

Buckminsterfullerene $C_{60}$ and molybdenum trioxide $MoO_3$ are very widely used materials in OPV cells. $C_{60}$ has been a key molecule in the development of the entire OPV field and is still frequently used as electron acceptor material.[9-12] More recently, $MoO_3$ has been recognized as a promising anode interfacial layer in OPV cells. The low charge injection/extraction barrier at $MoO_3$/organic interfaces is believed to be due to the favorable energy level alignment between the high work function value of $MoO_3$ and the highest occupied molecular orbital of an organic molecule.[13] However, due to the complex chemistry of that material and the strong impact of sample preparation history on the electronic properties, a coherent understanding of the hole extraction process across $MoO_3$ in OPV cells is still lacking.[14-21] Thin $MoO_3$ films have been deposited by thermal evaporation[22] or via coating-processes using precursor solutions or nanoparticle dispersions.[14,20,23-25]

It is well known that both $C_{60}$ and $MoO_3$ are photosensitive materials, but possible implications on the stability of OPV cells are largely unidentified. Visible and UV light exposure of oxygen-free solid $C_{60}$ can transform monomers into dimers, oligomers and polymers via the formation of intermolecular bonds in a 2+2 cyclo-addition process.[26,27] The thermal decomposition reaction back to the monomers must be taken into account for temperatures above 100 °C.[28] The distance between neighboring $C_{60}$ molecules decreases by ~10% when a weak van der Waals bond is replaced by two covalent bonds. Therefore, the polymerization reaction is associated with a decrease of the bulk volume.[29,30] A similar photochemical reaction occurs for [6,6]-phenyl $C_{61}$-butyric acid methyl ester (PCBM) films. Exposing PCBM monomers to light leads to the formation of dimers, although higher oligomers are not produced, probably for steric reasons. The importance of this process has been realized for high-resolution electronic active pattering purposes of fullerene thin films.[31,32] In the OPV field, the PCBM dimerization has recently been found to be responsible either for a device performance loss, due to a reduced electron mobility, or an enhanced morphological stability of the active blend film, resulting in an increase of the overall cell lifetime under modest thermal stress conditions.[33,34]

Thin films of $MoO_3$ can be permanently coloured blue by excitation using UV light.[35] The photochromic mechanisms are still not fully resolved and controversially discussed. The occurrence of optical absorption in the visible and near-infrared wavelength region is associated with oxygen vacancies and the presence of lower valence $Mo^{5+}$ states in $MoO_{3-x}$[36-38] since pure $MoO_3$ shows little photochromism.[35,39] In one model, it is proposed that colour centres are formed when photo-excited electrons are trapped in oxygen vacancies.[38] These trapped electrons can be excited into the conduction band by red light resulting in a blue film colour. In the presence of hydrogen donors, an additional mechanism must be considered. When excited with UV light, electrons and holes are formed in $MoO_3$, followed by reaction of the holes with surface-absorbed molecules, causing the film to be negatively charged. The positive ions on the surface then diffuse into the film driven by Coulomb force, forming the hydrogen molybdenum bronze $H_xMo_x^{5+}Mo_{1-x}^{6+}O_3$.[19,40] The film colour develops due to charge transfer between $Mo^{5+}$ and neighbouring $Mo^{6+}$. A similar charge transfer can occur after self-trapping of excited electrons in low-energy sites leading to $Mo^{5+}$.[35] Irrespective of the processes leading to film colour, the presence of $Mo^{5+}$ seems to be a necessity. Notably, the $Mo^{5+}$ content has been reported to increase during illumination, concomitant with the increase of the visible absorption.[35,38,39]

Interestingly, it seems that despite these extensive research activities on the phototransformations occurring in $C_{60}$ and $MoO_3$ thin films, their importance in conjunction with the stability of OPV cells containing these materials has not been identified and addressed to date.[8,41-50] Here, we present a detailed study on the early aging mechanisms in such solar cells during illumination and link degradation to the occurrence of photopolymerization in $C_{60}$ and photochromism in $MoO_3$ directly. To avoid morphological stability issues known from blended organic donor-acceptor films, we have chosen a simple bilayer film design composed of an organic cyanine dye (Cy3-P) donor / $C_{60}$ acceptor heterojunction.[51] OPV cells were fabricated in the so-called regular geometry by sandwiching the organic film between an ITO/$MoO_3$ anode and an Ag cathode. In this architecture, impinging light travels first through $MoO_3$ followed by the organic bilayer. Thereby, both photosensitive materials are simultaneously exposed to sunlight and can be studied at the same time.

## 2. Results and Discussion

### 2.1. Kinetics of Phototransformations

Figure 5-1 shows the temporal evolution of UV-vis spectra for thin films of Cy3-P, $C_{60}$ and $MoO_3$ that were irradiated for 24 h under OPV device relevant conditions at 1 sun intensity. No changes are observed for the dye film indicating that Cy3-P is photostable when illuminated in the absence of oxygen and water (Figure 5-1a).[51] For $C_{60}$, the energy of the lowest, optically forbidden, singlet excitation is at about 1.9 eV, the spectral intensity in the region 2.4-2.8 eV is due to charge-transfer-type excitations between molecules in the film, and the first allowed electronic transitions is at about 3.6 eV.[27,52,53] Upon irradiation, the $C_{60}$ absorption band at 349 nm broadens and the maximum blueshifts slightly to 342 nm after 24 h (Figure 5-1b). Note the characteristic increase in absorption at 321 nm during illumination. No further changes in absorption were observed for irradiation times longer than 24 h. For $MoO_3$, illumination continuously increases the absorption in the near-infrared region (Figure 5-1c). Changes in the UV-vis absorption spectra are best visualized for pure $C_{60}$ and $MoO_3$ films, but very similar trends were observed for Cy3-P/$C_{60}$ and $MoO_3$/Cy3-P bilayer films and for the full ITO/$MoO_3$/Cy3-P/$C_{60}$ solar cell layer stack as well (Figure 5-S1).
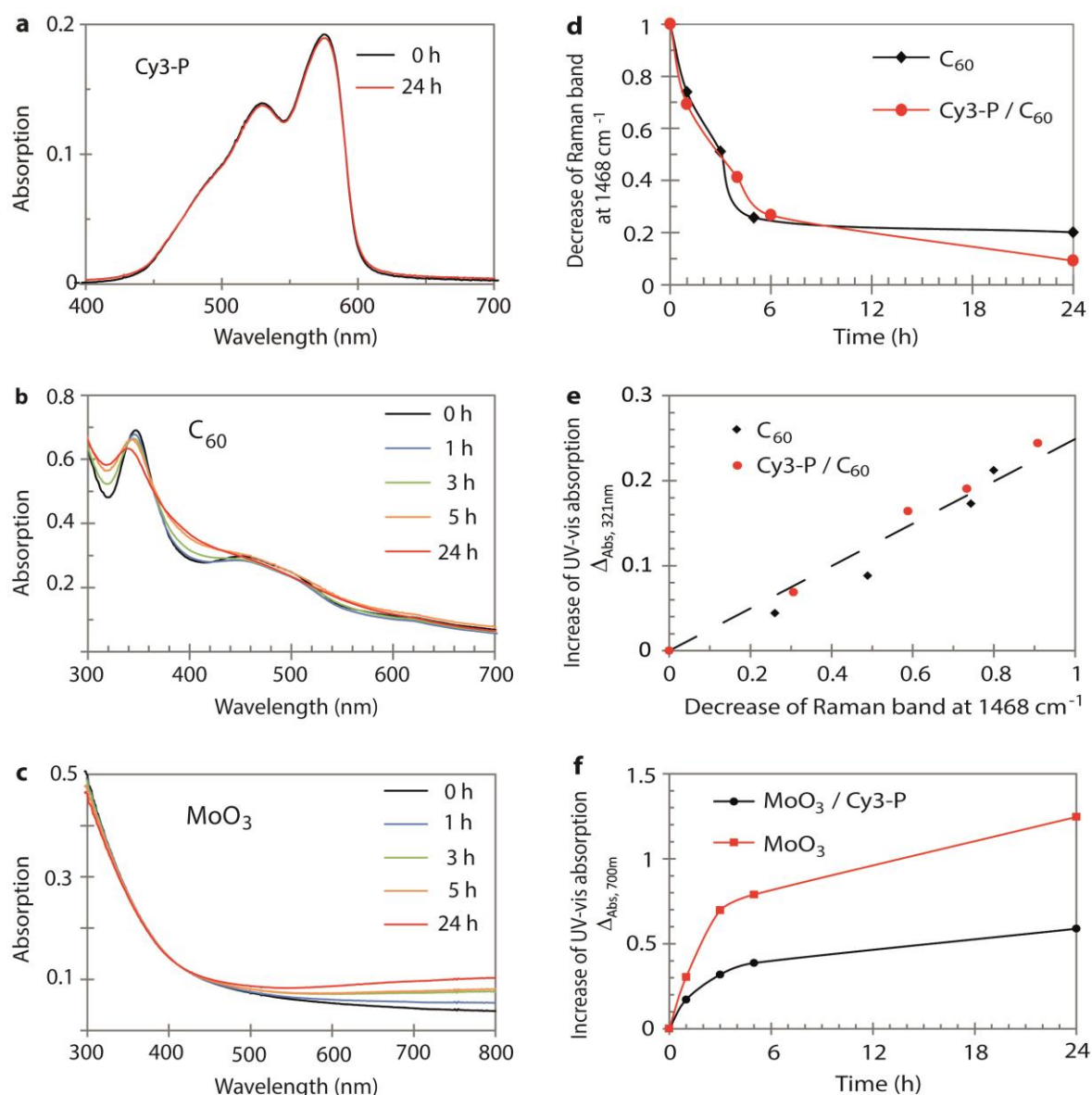
Figure 5- 1. Absorption spectra and kinetics of phototransformations.

UV-vis absorption[2] spectra of films on glass upon illumination by a xenon lamp at 1 sun intensity under nitrogen of (a) 20 nm cyanine dye Cy3-P, (b) 40 nm $C_{60}$, (c) 30 nm $MoO_3$. (d) Kinetics of light-induced $C_{60}$ transformation from Raman spectra. (e) Correlation between changes in UV-vis ($\Delta_{Abs,321nm}=$

$\frac{Abs_{t,321nm}-Abs_{t=0,321nm}}{Abs_{t=0,321nm}}$) and Raman spectra. (f) Kinetics of light-induced $MoO_3$ transformation from UV-vis spec-

tra ($\Delta_{Abs,700\,nm}=\frac{Abs_{t,700nm}-Abs_{t=0,700nm}}{Abs_{t=0,321nm}}$).

For $C_{60}$, changes in the UV-vis spectrum are due to the light-induced dimerization, oligomeri-zation and finally three-dimensional polymerization between fullerene molecules.[26] This re-action can be followed by Raman spectroscopy (Figure 5-S2).[28] We used the decrease of the

---

[2] Absorption (A) in this chapter is equal to $Log_{10}(\frac{I_0}{I})$, where $I_0$ is the incident light intensity and $I$ is the transmit-ted light intensity.

1468 cm$^{-1}$ band representing the pristine $C_{60}$ molecules as a direct measure for the kinetics of the dimerization reaction (Figure 5-1d). The reaction proceeds rapidly during the first ~6 h with a dimerization yield of ~70% and then levels off, both for pure $C_{60}$ and Cy3-P/$C_{60}$ films. We found a good correlation between Raman data and the relative increase of the UV-vis absorption at 321 nm (Figure 5-1e). Therefore, UV-vis spectroscopy can be used as a convenient tool to follow the light-induced $C_{60}$ transformation. Even after 24 h light irradiation, however, the polymerization is not complete and $C_{60}$ monomers, oligomers and polymer chains coexist in the film, as inferred from Raman spectra. Despite this incomplete transformation, $C_{60}$ films became insoluble in the solvent toluene during light processing (Figure 5-S3), confirming the intermolecular bond formation process.[26,28,29]

The kinetics of the $MoO_3$ phototransformation was evaluated from the increase in the absorption spectra at 700 nm (Figure 5-1f). Similar to $C_{60}$, changes are most pronounced during the first few hours of illumination, but pure $MoO_3$ films transform more effectively than $MoO_3$/Cy3-P bilayers. Optical modeling showed that the integrated absorbance is ~ 6% higher for a pure $MoO_3$ sample compared to the one with an additional Cy3-P layer (Figure 5-S4 and Figure 5-S5). This is much less than the observed difference in Figure 5-1f. Therefore, it is likely that the reaction routes leading to film coloration are different when comparing pure $MoO_3$ with a metal oxide that is covered with an organic layer.

## 2.2. Device Performance During Light Processing

Figure 5-2 shows the J-V characteristics for a cell during 24 h illumination. At time = 0, $V_{oc}$ = 0.86 V, $J_{sc}$ = 4.4 mA cm$^{-2}$ and FF = 68% were measured, resulting in a power conversion efficiency of $\eta$ = 2.6%. For longer times, both $V_{oc}$ and $J_{sc}$ decayed in a two-step process, and a fast initial decrease during the first ~ 6 h leveled off for longer irradiation times. This trend very much resembles the kinetics of phototransformations observed in $C_{60}$ and $MoO_3$. Fill factors (FF) of our solar cells were high and changes in FF were small. During the first hour, FF increased to 73% and then slightly decreased to a final value of 65%. Similar small relative FF changes of less than 10% were found throughout this study (Figure 5-S6).

We have measured the stability of cells using three different approaches in order to identify the critical materials inducing degradation and to rate their relative importance. In a first set of experiments, individual layer stacks were pre-irradiated for 24 h at room temperature before completing the cells. J-V characteristics of these devices were then measured for another 24 h under continuous irradiation. Because each additional layer also creates an interface with the subjacent material, J-V trends cannot be related clearly to bulk material or interface processes

without further experiments. Starting values of $V_{oc}$ and $J_{sc}$ are indicated in Figure 5-2c and 5-2d ($\blacktriangledown 1 - 4$), the temporal development over the following 24 h is shown in Figure 5-2e and 5-2f. It should be noted that we can only extract trends from this analysis rather than quantitative data. First, the scattering in currents from different samples was relatively large ($\pm$ (0.2–0.4) mA cm$^{-2}$, Table 5-S1). In addition, the amount of light absorbed by individual materials changes when present in different layer stacks. When a full device is illuminated, the top Ag electrode acts as a mirror and light that is not absorbed is reflected back through the active layers.
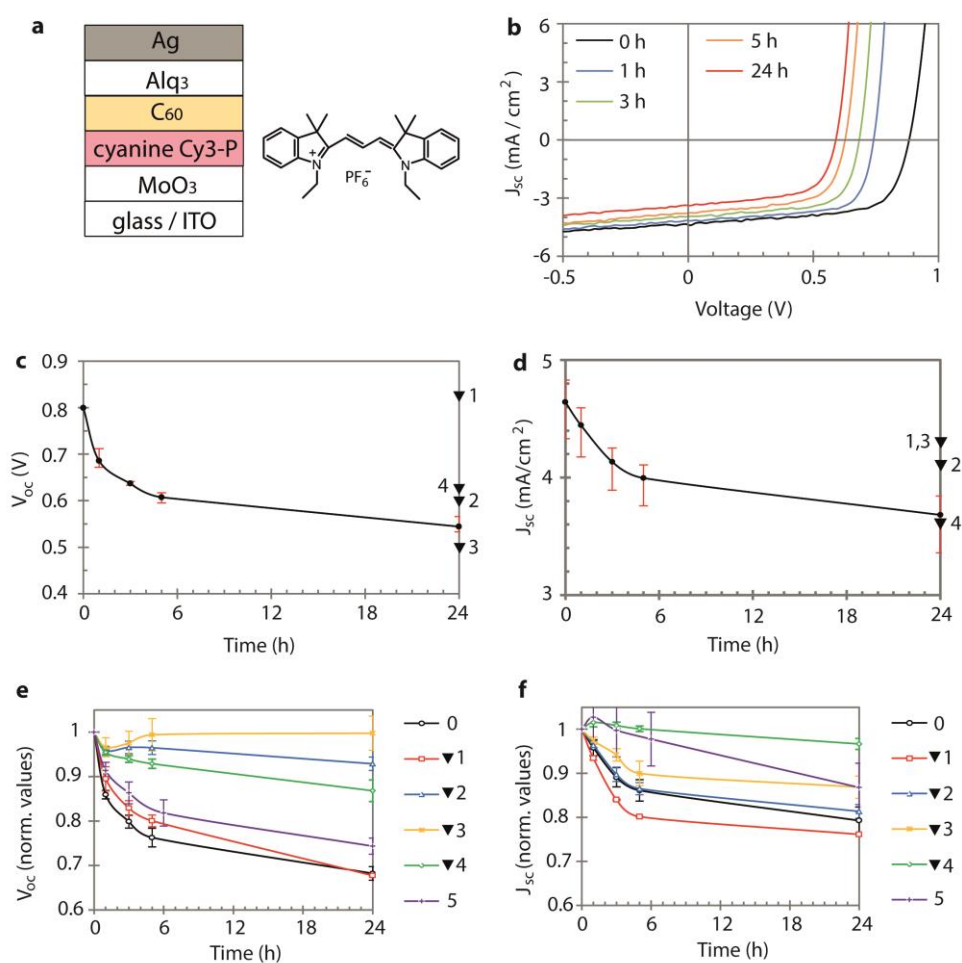


Figure 5- 2. Cell performance during white light illumination.

(a) Schematic representation of the cyanine dye/C$_{60}$ solar cell and the molecular structure of Cy3-P. (b) Current-voltage characteristics of glass/ITO/MoO$_3$/Cy3-P/C$_{60}$/Alq$_3$/Ag solar cells upon illumination at 1 sun intensity under nitrogen at 43 $^{o}$C. Temporal development of (c) the open-circuit voltage ($V_{oc}$) and (d) the short-circuit current ($J_{sc}$), shown are average values from 5 cells. $\blacktriangledown$ denote starting values using individual layer stacks that were pre-irradiated for 24 h before completing the device, $\blacktriangledown 1 = $ ITO, $\blacktriangledown 2 = $ ITO/MoO$_3$, $\blacktriangledown 3 = $ ITO/MoO$_3$/Cy3-P, $\blacktriangledown 4$

= ITO/MoO$_3$/Cy3-P/C$_{60}$/Alq$_3$. Temporal development of normalized (e) V$_{oc}$ and (f) J$_{sc}$ upon illumination. Labels 0 and 5 indicate complete cells that were irradiated at 43 $^o$C and at - 30 $^o$C, respectively.

Pre-irradiation of a glass/ITO substrate (▼1) had no influence on the initial cell performance and the subsequent degradation followed the typical two-stage behavior. On the other hand, pre-irradiation of MoO$_3$-containing layers resulted in decreased, but stable for the long-term, V$_{oc}$ values after cell fabrication, with values almost matching those of an untreated cell after 24 h illumination (Figure 5-2c and 5-2e). This result strongly suggests that mainly MoO$_3$ is responsible for the observed voltage decay, since pre-irradiation of this layer alone is suffi-cient to induce the observed changes.

The results in Figure 5-2d further show that pre-irradiation of a C$_{60}$-containing layer (▼4) in-duced the largest drop in starting current, indicating the adverse influence of the photopoly-merization reaction. During further illumination, however, the current remained stable. Addi-tionally, pre-treated MoO$_3$ and MoO$_3$/Cy3-P cells started at reduced current values, but these devices showed the known current decay trend, due to the proceeding C$_{60}$ phototransfor-mation. An interesting question is whether the overall long-term stability can be improved by a pre-irradiation step of individual layers before the cell is completed. This is not the case, since un-treated and pre-irradiated cells all ended up a η = 1.3% (Table 5-S1) after 24 h of il-lumination. This corresponds to a performance loss of 50%.

In a further approach, we were able to separate the phototransformation kinetics of C$_{60}$ and MoO$_3$ to some extent by lowering the temperature during illumination. It is well known that C$_{60}$ molecules rotate above ~ -15 $^o$C almost freely about their lattice positions. Below that temperature the rotation becomes restricted and finally freezes below ~ -190 $^o$C.[54] It has fur-ther been shown that the photopolymerization efficiency is correlated with the C$_{60}$ rotation rate. For low temperatures, the reaction is effectively absent, and at the threshold temperature the polymerization starts.[28]

Cell stability was measured at -30 $^o$C. At this temperature, the C$_{60}$ photopolymerization is considerably slowed down and reached 20% after 24 h of illumination. This corresponds to a degree of transformation that is attained after ~ ½ h at 43 $^o$C. On the other hand, no tempera-ture dependence was found for the photoreaction of MoO$_3$ (Figure 5-S7). Voltage trends at low and high temperatures were identical (Figure 5-2e, labels 0 and 5). This supports our above findings that mainly the phototransformation in MoO$_3$ is responsible for the drop in V$_{oc}$. We can further approximate that at 43 $^o$C phototransformations in C$_{60}$ and MoO$_3$ almost equally contribute to the observed current decay (Figure 5-2f).
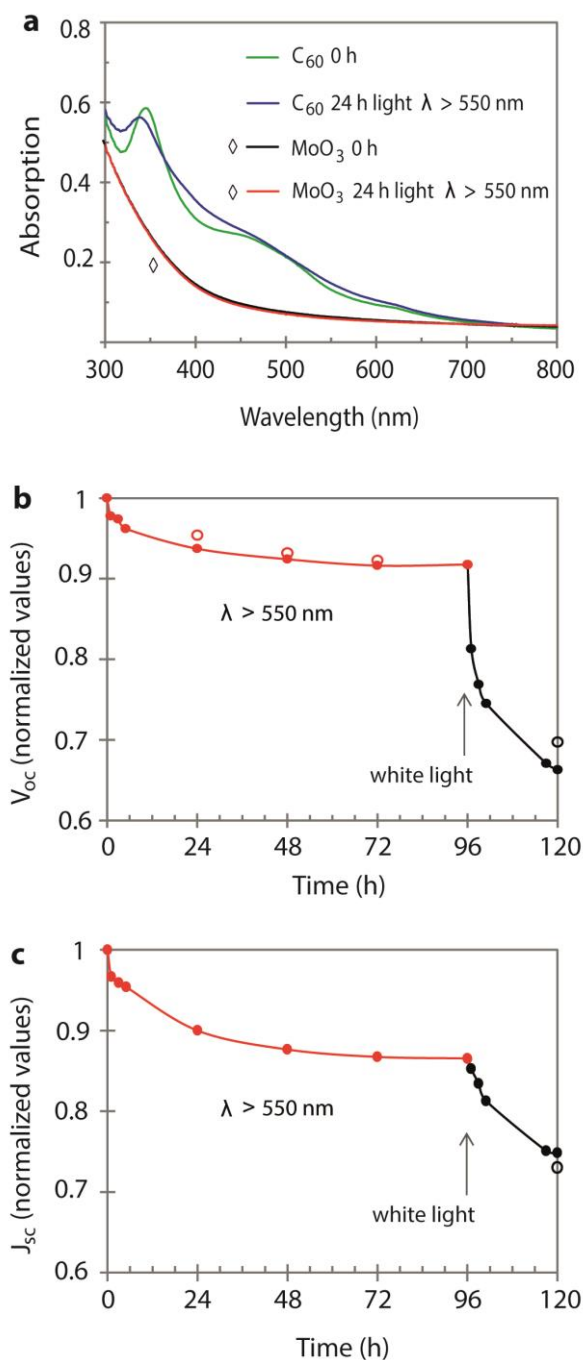
Figure 5- 3. Cell performance using selective irradiation wavelengths.

(a) UV-vis absorption spectra of $C_{60}$ and $MoO_3$ films upon illumination with a xenon lamp at room temperature and using a cutoff filter that blocks light at wavelengths below 550 nm. Temporal development of (b) $V_{oc}$ and (c) $J_{sc}$ upon illumination. During the first 96 h, a cutoff filter was used. Open circles indicate measurements after cooling the cell to room temperature.

Finally, irradiation in selective wavelength regions was used to address the influence of phototransformations in $C_{60}$ and $MoO_3$ on cell stability individually. We used a cutoff filter that blocks light at wavelengths below 550 nm to separately excite $C_{60}$ from $MoO_3$.[13,18] Illuminat-

ing $MoO_3$ with filtered light did not induce any changes in the UV-vis absorption spectrum, but the polymerization of $C_{60}$ still took place (Figure 5-3a). After 24 h, the $C_{60}$ photo transformation reached a degree of about 50%, lower than the 80-90% transformation observed when white light was used.

J-V characteristics were measured over a period of 120 h and for the first 96 h of illumination filtered light was used. During the first 24 h $V_{oc}$ decayed by ~ 6% only (Figure 5-3b), much less than the ~ 32% when using white light. In addition, part of the $V_{oc}$ drop is due to heating the cell during illumination.[55] Open circles in Figure 5-3b indicate $V_{oc}$ values measured after storage in the dark allowing the cell to cool down to room temperature. During 24 - 96 h of illumination, $V_{oc}$ remained essentially constant. This clearly confirms that the major part of $V_{oc}$ degradation is not induced by the $C_{60}$ photopolymerization. After 96 h the filter was removed and white light was used for illumination. The drop in $V_{oc}$ during the time period 96 - 120 h must be due to photoinduced transformations in $MoO_3$ and/or at the metal oxide/Cy3-P interface, since the $C_{60}$ polymerization has already taken place using filtered light. The $J_{sc}$ trend over a period of 120 h illumination supports our findings that both phototransformations in $C_{60}$ and $MoO_3$ contribute approximately equally to the current decrease (Figure 5-3c). $J_{sc}$ drops by ~ 13% during the first 96 h of filtered light illumination due to the polymerization of $C_{60}$, and another ~ 12% due to $MoO_3$ when using white light during 96-120 h.

## 2.3. Degradation Mechanisms

It is clear that temporal trends in UV-Vis spectra and J-V characteristics cannot be linked to specific failure mechanisms directly.[5] The unchanging dye absorption spectrum during illumination and the similar J-V characteristics of cells using pre-irradiated $MoO_3$ and $MoO_3$/Cy3-P layers indicate that the bulk of the dye film is stable and that the influence of Cy3-P on degradation must be small. This is also supported by the relative stability of cells during 96 h illumination using wavelengths above 550 nm where a Cy3-P film has actually the absorption maximum ($\lambda_{max}$ = 578 nm). To detect small amounts of Cy3-P degradation products at the metal oxide/dye interface, we carried out ESI-HRMS experiments (Supporting Information 5-S8). Also these measurements confirmed the photostability of Cy3-P and no transformation products could be clearly assigned to photoinduced reactions during white light illumination under nitrogen. The experimental observation (Figure 5-1f) that the increase in visible absorbance is relatively suppressed for $MoO_3$ when coated with Cy3-P remains unexplained at this time, but probably cannot be linked to the chemical instability of Cy3-P. A similar result on the complex metal oxide/organic interface has been reported recently, and it

was found that the evolution of $Mo^{5+}$ states upon thermal annealing was larger for pure $MoO_3$ when compared to a $MoO_3$/organic layer.[20]

We now consider the impact of light-induced $C_{60}$ polymerization on cell performance. Firstly, it has been reported that the $C_{60}$ electron mobility $\mu_e$ drops by 10% upon full polymerization.[29] In our case the transformation is not complete, and a partial polymerization is expected to induce the formation of traps due to spatial and/or energetic heterogeneity, effectively lowering $\mu_e$ further. By opto-electrical simulations (Supporting Information 5-S9), however, we could show that a lowering of $\mu_e$ over 2 orders of magnitude (from $8 \cdot 10^{-2}$ to $8 \cdot 10^{-4}$ $cm^2$ $V^{-1}$ $s^{-1}$) does not explain the observed drop in $J_{sc}$ and $V_{oc}$ (Figure 5-3). This is supported by the very high fill factors of our devices.
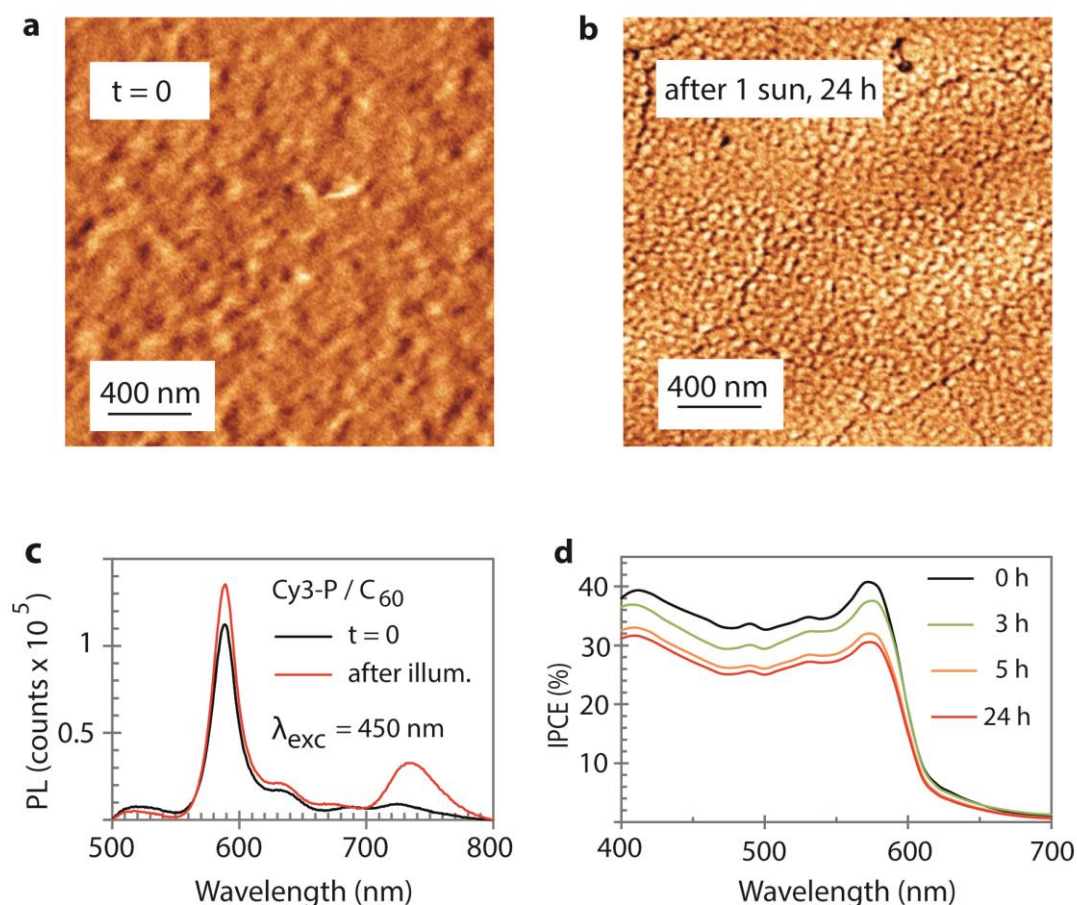


Figure 5- 4. Effects of $C_{60}$ photopolymerization.

AFM phase images of a Cy3-P/$C_{60}$ film (a) before and (b) after illumination. (c) Fluorescence spectra on glass/$MoO_3$ substrates of a bilayer film with simultaneous excitation of the dye and $C_{60}$. Emission signals are shown for as-prepared films, and after 96 h irradiation with filtered ($\lambda > 550$ nm) light. For Cy3-P, the emission peak is at $\lambda = 589$ nm. The emission peak of pristine $C_{60}$ is at $\lambda = 725$ nm with a shoulder at 693 nm, after illumination the emission shifts to $\lambda = 734$ nm. (d) Incident photon-to-current conversion efficiency (IPCE) spectra during illumination at 1 sun intensity.

Next, we examine the impact of the volume decrease of a $C_{60}$ film upon polymerization. We suggested previously that this could result in the formation of voids effectively decreasing the contact area between $C_{60}$ and the adjacent layers.[51] AFM images of pristine and illuminated Cy3-P/$C_{60}$ bilayer films are shown in Figure 5-4. Before illumination, the film is pinhole-free with a root-mean square (rms) roughness of 1.6 nm. During phototransformation, cracks are formed and the topography smoothens (rms roughness 0.3 nm). At the $C_{60}$/top metal interface, a decrease of the physical contact area would diminish the active electrode area leading to a reduction in charge extraction. This phenomenon has been experimentally found for solar cells using a calcium/aluminium electrode and resulted in a rapid decay of $J_{sc}$, while FF and $V_{oc}$ remained relatively stable.[56] We found the same $J_{sc}$ values for full cells that were illuminated for 24 h and for devices were the Ag electrode was evaporated only after pre-irradiation of the ITO/MoO$_3$/Cy3-P/$C_{60}$/Alq$_3$ layer stack (Figure 5-2d). This indicates that in our case a reduction of the contact area between $C_{60}$ and Ag is probably not occurring.

To examine a possible formation of voids at the hidden dye/$C_{60}$ heterojunction, we used fluorescence spectroscopy as a probe that is sensitive to a changing charge generation yield. By comparing bilayer film spectra before and after illumination, we indeed observed a substantial increase of the dye emission (Figure 5-4c, Figure 5-S10). Additionally, the $C_{60}$ emission increased after light treatment with a concomitant redshift due to the fullerene polymerization, in agreement with literature.[26,34] This supports the proposal that, due to a reduction of the interface contact area when the polymerizing $C_{60}$ film contracts, a fraction of excitons in Cy3-P and $C_{60}$ cannot be separated anymore and must decay partly by fluorescence. This scenario is further consistent with the spectrally resolved external quantum efficiency data displayed in Figure 5-4d. During illumination, IPCE values uniformly decreased across the entire spectral range where $C_{60}$ and Cy3-P absorb. This excludes degradation processes which affect the exciton diffusion lengths in Cy3-P or $C_{60}$ individually, since then the IPCE change would exhibit a wavelength dependency.

We cannot clearly relate the small relative (8%) $V_{oc}$ drop during 96 h of filtered light illumination to the $C_{60}$ photopolymerization. Again, initial $V_{oc}$ values of cells fabricated by evaporating the top metal electrode after a pre-illumination period were lowered, excluding an adverse effect occurring at the $C_{60}$/Ag interface during photopolymerization. In addition, the reduced charge generation yield at the heterojunction does not induce a $V_{oc}$ drop (Supporting Information 5-S9). In principle, an increase of the energy of the $C_{60}$ lowest unoccupied molecular orbital could explain the observed $V_{oc}$ decay.[57,58] It appears, however, that while

polymerization of $C_{60}$ induces a small decrease of the optical bandgap (as inferred from photoluminescence), this change is primarily associated with an energy shift of the highest occupied molecular orbital, as measured by UPS (Figure 5-S11).[59,60]

Our results show that illumination of a $MoO_3$ thin film with UV light induces a substantial drop in cell performance over time. We can connect this trend with the photochromic phenomenon in $MoO_3$, and thereby to the presence of $Mo^{5+}$ species directly. XPS was used to detect the presence of reduced Mo species (Figure 5-S12). Experiments were carried out for as-deposited $MoO_3$ films and after 24 h illumination. While for untreated films $Mo^{5+}$ was not detected, $Mo^{5+}/Mo^{6+}$ was ~ 0.03 after 24 h. This clearly confirms that during illumination $Mo^{5+}$ is formed and that these species are closely linked to the occurrence of photochromism. Slightly sub-stoichiometric $MoO_{x<3}$ is n-doped,[13,14,19,37] with the presence of $Mo^{5+}$ resulting in the formation of isolated, occupied gap states during illumination close to the conduction band.[13,15] These states cause the Fermi level ($E_F$) to be shifted upwards, thus reducing the work function. UPS spectra were measured on as-prepared and illuminated $MoO_3$ films (Figure 5-S13). The work function for untreated $MoO_3$ was measured at ~5.6 eV, and was reduced to ~5.3 eV after illumination, consistent with the expected trend. At the same time, a substantial amount of gap states arose between 1 eV and 2 eV below $E_F$.

Cy3-P has a deep-lying HOMO energy of ~5.7 eV, as measured by cyclic voltammetry.[61] This suggests a balanced energetic situation at the $MoO_3$/dye interface for short illumination times, allowing for efficient hole extraction via electrons that travel towards the organic interface and recombine with photogenerated holes. During illumination, the reduction of the work function results in an unfavorable change in the energy alignment between $MoO_3$ and Cy3-P, reducing cell performance.

In general, the presence of $Mo^{5+}$ and their subtle influence on solar cell performance is not fully elucidated so far and results seem to be contradictory in some cases. Using the poly(3-hexylthiophene), P3HT, /PCBM material system and ITO/$MoO_3$ as anode, it was reported that an increased density of $Mo^{5+}$ is detrimental to the device performance.[20] These findings are contrary to the results of experiments that showed that $Mo^{5+}$ can play a dominating role in improving cell performance.[21] For P3HT/PCBM OPV cells, it was found that $V_{oc}$ and $J_{sc}$ were reduced when using a $MoO_3$ hole collection layer as compared to poly(3,4-ethylenedioxythiophene):poly(styrene sulfonate).[17] At the same time, FF was enhanced due to the reduced series resistance in $MoO_x$. This was explained by charge recombination at $Mo^{5+}$ gap states.

One issue relates to the varying reported values of electronic states in $MoO_3$ that so sensitively depend on the processing history before characterizing the device. For example, the electron affinity, work function and ionization energy of vacuum-deposited $MoO_3$ are at 6.7, 6.9 and 9.5 eV, respectively.[16] A short air exposure reduces the values by about 1 eV.[17] A quick shift to lower values was even found for $MoO_3$ samples that were stored under nitrogen for several hours, due to residual water in the glovebox.[18]

For organic molecules in contact with metal oxides, it was observed that energy level alignment between the materials donor and acceptor states occurs when the organic's ionization energy equals the substrate's Fermi energy.[13] Ground state electron transfer was also observed from organic semiconductors to freshly evaporated $MoO_3$.[18] De-doping over time was explained by changes in the $MoO_3$ energy levels, resulting in a suppression of charge transfer when the $MoO_3$ electron affinity becomes smaller than the ionization energy of the organic material.

These results imply that the influence of the $MoO_3$ photochromism on OPV cell stability might depend sensitively on the ionization energy of the used organic donor material and must be studied from case to case. We note that the photochromism is not limited to the pure metal oxide and the $MoO_3$/Cy3-P material system we studied here in detail. In preliminary work, we found similar absorbance changes in illuminated $MoO_3$ when coated with P3HT or PTB7 (Figure 5-S14), notably polymers that are among the most widely used and best-performing OPV materials. Possible implications on the long-term stability of these OPV cells are the subject of ongoing work.

## 3. Conclusions

Our results suggest that for regular OPV cell architectures comprising $MoO_3$ and $C_{60}$, performances should be measured and reported only after a preceding light processing step. The polymerization of $C_{60}$ appears to be an inevitable consequence when exposed to light, and when using sunlight the relevant photochemistry influencing device behavior develops over a timescale of a few hours. The same timescale was found here for the film coloration to occur in $MoO_3$, but in the general case, this might be sensitive to the chemical and electronic nature of the overlying organic donor layer. There are two apparent routes to prevent the photochromic effect in $MoO_3$. In the regular device geometry, a filter that blocks light at wavelengths below ~ 400 nm can be used, corresponding to the optical bandgap of $MoO_3$. This prevents film coloring but such OPV cell will display a lowered performance, because a considerably fraction of current is generated in the UV wavelength region, typically due to light

absorption by the fullerene component. The second possibility is to use $MoO_3$ in the so-called inverted device structure. In this geometry, the metal oxide is situated next to the top electrode and protected by the underlying organic materials that will absorb most of the impinging light.

## 4. Experimental Section

Solar cells with active areas of 3.1 and 7.1 mm$^2$ in the configuration glass/140 nm ITO/30 nm $MoO_3$/20 nm Cy3-P/40 nm $C_{60}$/2 nm Alq$_3$/80 nm Ag were fabricated as reported.[51] Materials were ITO (Geomatec, resistivity 20 Ohms square$^{-1}$), 1-ethyl-2-[3-(1-ethyl-3,3-dimethyl-1,3-dihydro-indol-2-ylidene)-propenyl]-3,3-dimethyl-3H-indolium hexafluorophosphate (Cy3-P, FEW Chemicals), $MoO_3$ (Sigma Aldrich, 99.99%), $C_{60}$ (SES Research, 99.5% or 99.9%), tris-(8-hydroxyquinoline) aluminium (Alq$_3$, Sigma-Aldrich, 99.995%) and Ag (Cerac, 99.99%). All evaporations were carried out in the same vacuum chamber (~$4 \cdot 10^{-6}$ mbar) with deposition rates of 0.2 Å s$^{-1}$ for $C_{60}$, Alq$_3$ and $MoO_3$, and of 0.5 Å s$^{-1}$ for Ag.

Film thicknesses were determined by profilometry (Ambios XP1). AFM measurements were performed on a Nanosurf Mobile S in tapping mode at a resonance frequency of 170 kHz using silicon cantilevers. Current-voltage (J-V) characteristics were measured using 100 mW cm$^{-2}$ simulated AM 1.5G solar irradiation on a calibrated solar simulator from Spectra-Nova. IPCE spectra were measured using a monochromator and the light from a 300 W Xe lamp together with an AM1.5G filter set. The monochromatic light intensity was determined using a calibrated Si-diode. Raman measurements were performed in ambient conditions with a Horiba Labram Evolution 800 spectrometer. Absorption spectra were measured on a Varian Cary 50 UV-vis spectrophotometer. Fluorescence spectra were measured on Horiba Jobin Yvon Fluorolog. Electrospray-high resolution mass (ESI-HRMS) measurements were performed on an Agilent 6530 QTOF mass spectrometer. Ultraviolet photoelectron spectroscopy (UPS) measurements were performed in an OMICRON photoelectron spectrometer under UHV (5x10$^{-11}$ mbar range) conditions. A discharge lamp (He I: *hv*: 21.2 eV) and VSW EAC 300HR energy analyzer were used. $MoO_3$ samples were biased at -9.6 V relative to the spectrometer and measured at room temperature. The Fermi level of the spectrometer was determined by measuring the Fermi edge of a Cu crystal. A 300 W Xe lamp was used as a light source for illumination of $C_{60}$ films between consecutive UPS spectra. In situ X-ray photoelectron spectroscopy (XPS) surface analysis was performed in a modified VG EscaLab spectrometer with a base pressure below 10$^{-9}$ mbar. XPS spectra were collected with a SPECS PHOIBOS 100 analyzer using a non-monochromatic x-ray source (Mg K alpha: 1253.6 eV). The binding en-

ergy was re-calibrated using the O1s peak set to 530.0 eV. Further experimental details on Raman, ESI-HRMS, UPS and XPS measurements are given in the Supporting Information.

Samples were never exposed to ambient atmosphere during fabrication and light processing. Devices were fabricated in a glove box under nitrogen ($H_2O$ < 1 ppm, $O_2$ < 10 ppm) and were then mounted into a homemade air-tight transfer box. J-V characteristics were measured and light processing was carried out outside the glovebox using the solar simulator. The actual temperature in the transfer box during illumination at ambient was 43 $^o$C. For the pre-irradiation of individual layer stacks, samples were transferred under $N_2$ into a separate glove box ($H_2O$ < 1 ppm, $O_2$ < 1 ppm). Light from a Xe lamp was directed from outside into the glove box and the intensity was adjusted to ~1 sun with a radiant power meter from LOT Oriel using a calibrated thermopile. Similarly, experiments at -30 $^o$C were carried out in a climate chamber equipped with a glass front door. Cells were placed in the transfer box and the Xe lamp with an intensity of 60-70 mW cm$^{-2}$ was directed from outside into the chamber. The J-V characteristics during light processing were measured in-situ at -30 $^o$C.

## Acknowledgements

## References

[1] Z. He, C. Zhong, S. Su, M. Xu, H. Wu, Y. Cao, *Nature Photon.* **2012**, *6*, 591.

[2] Y. Liu, C.-C. Chen, Z. Hong, J. Gao, Y. (M.) Yang, H. Zhou, L. Dou, G. Li, Y. Yang, *Scientific reports* **2013**, 3:3356, DOI:10.1038/srep03356.

[3] M. A. Green, K. Emery, Y. Hishikawa, W. Warta, E. D. Dunlop, *Prog. Photovolt: Res. Appl.* **2012**, *20*, 12.

[4] M. Jørgensen, K. Norrman, F. C. Krebs, *Solar Energy Mater. Solar Cells* **2008**, *92*, 686.

[5] C. J. Brabec, S. Gowrisanker, J. J. M. Halls, D. Laird, S. Jia, S. P. Williams, *Adv. Mater.* **2010**, *22*, 3839.

[6] M. Jørgensen, K. Norrman, S. A. Gevorgyan, T. Tromholt, B. Andreasen, F. C. Krebs, *Adv. Mater.* **2012**, *24*, 580.

[7] N. Grossiord, J. M. Kroon, R. Andriessen, P. W. M. Blom, *Org. Electron.* **2012**, *13*, 432.

[8] D. M. Tanenbaum, M. Hermenau, E. Voroshazi, M. T. Lloyd, Y. Galagan, B. Zimmermann, M. Hösel, H. F. Dam, M. Jørgensen, S. A. Gevorgyan, S. Kudret,

W. Maes, L. Lutsen, D. Vanderzande, U. Würfel, R. Andriessen, R. Rösch, H. Hoppe, G. Teran-Escobar, M. Lira-Cantu, A. Rivaton, G. Y. Uzunoğlu, D. Germack, B. Andreasen, M. V. Madsen, K. Norrman, F. C. Krebs, *RSC Advances* **2012**, *2*, 882.

[9] N. S. Sariciftci, D. Braun, C. Zhang, V. I. Srdanov, A. J. Heeger, G. Stucky, F. Wudl, *Appl. Phys. Lett.* **1993**, *62*, 585.

[10] G. Yu, J. Gao, J. C. Hummelen, F. Wudl, A. J. Heeger, *Science* **1995**, *270*, 1789.

[11] P. Peumans, S. R. Forrest, *Appl. Phys. Lett.* **2001**, *79*, 126.

[12] A. W. Hains, Z. Liang, M. A. Woodhouse, B. A. Gregg, *Chem. Rev.* **2010**, *110*, 6689.

[13] M. T. Greiner, M. G. Helander, W.-M. Tang, Z.-B. Wang, J. Qiu, Z.-H. Lu, *Nature Mater.* **2012**, *11*, 76.

[14] J. Meyer, R. Khalandovsky, P. Görrn, A. Kahn, *Adv. Mater.* **2011**, *23*, 70.

[15] M. T. Greiner, L. Chai, M. G. Helander, W.-M. Tang, Z.-H. Lu, *Adv. Funct. Mater.* **2012**, *22*, 4557.

[16] M. Kröger, S. Hamwi, J. Meyer, T. Riedl, W. Kowalsky, A. Kahn, *Org. Electron.* **2009**, *10*, 932.

[17] S. R. Hammond, J. Meyer, N. E. Widjonarko, P. F. Ndione, A. K. Sigdel, A. Garcia, A. Miedaner, M. T. Lloyd, A. Kahn, D. S. Ginley, J. J. Berry, D. C. Olson, *J. Mater. Chem.* **2012**, *22*, 3249.

[18] M. C. Gwinner, R. Di Pietro, Y. Vaynzof, K. J. Greenberg, P. K. H. Ho, R. H. Friend, H. Sirringhaus, *Adv. Funct. Mater.* **2011**, *21*, 1432.

[19] F. Xie, W. C. H. Choy, C. Wang, X. Li, S. Zhang, J. Hou, *Adv. Mater.* **2013**, *25*, 2051.

[20] J. J. Jasieniak, J. Seifert, J. Jo, T. Mates, A. J. Heeger, *Adv. Funct. Mater.* **2012**, *22*, 2594.

[21] B. Dasgupta, W. P. Goh, Z. E. Ooi, L. M. Wong, C. Y. Jiang, Y. Ren, E. S. Tok, J. Pan, J. Zhang, S. Y. Chiam, *J. Phys. Chem. C* **2013**, *117*, 9206.

[22] V. Shrotriya, G. Li, Y. Yao, C.-W. Chu, Y. Yang, *Appl. Phys. Lett.* **2006**, *88*, 073508.

[23] T. Stubhan, T. Ameri, M. Salinas, J. Krantz, F. Machui, M. Halik, C. J. Brabec, *Appl. Phys. Lett.* **2011**, *98*, 253308.

[24] S. Murase, Y. Yang, *Adv. Mater.* **2012**, *24*, 2459.

[25] K. Zilberberg, J. Meyer, T. Riedl, *J. Mater. Chem. C* **2013**, 1, 4796.

[26] A. M. Rao, P. Zhou, K.-A. Wang, G. T. Hager, J. M. Holden, Y. Wang, W.-T. Lee, X.-X. Bi, P. C. Eklund, D. S. Cornett, M. A. Duncan, I. J. Amster, *Science* **1993**, *259*, 955.

[27] M. Suzuki, T. Iida, K. Nasu, *Phys. Rev. B* **2000**, *61*, 2188.

[28] P. C. Eklund, A. M. Rao, P. Zhou, Y. Wang, J. M. Holden, *Thin Solid Films* **1995**, *257*, 185.

[29] A. Dzwilewski, T. Wågberg, L. Edman, *Phys. Rev. B* **2007**, *75*, 075203.

[30] H. Tanimoto, K. Yamada, H. Mizubayashi, Y. Matsumoto, H. Naramaoto, S. Sakai, *Appl. Phys. Lett.* **2008**, *93*, 151919.

[31] J. Wang, C. Larsen, T. Wågberg, L. Edman, *Adv. Funct. Mater.* **2011**, *21*, 3723.

[32] J. Wang, J. Enevold, L. Edman, *Adv. Funct. Mater.* **2013**, *23*, 3220.

[33] A. Distler, T. Sauermann, H.-J. Egelhaaf, S. Rodman, D. Waller, K.-S. Cheon, M. Lee, D. M. Guldi, *Adv. Energy Mater.* **2014**, *4*, 1300693.

[34] Z. Li, H. C. Wong, Z. Huang, H. Zhong, C. H. Tan, W. C. Tsoi, J. S. Kim, J. R. Durrant, J. T. Cabral, *Nature Commun*. **2013**, 4:2227, DOI:10.1038/ncomms3227.

[35] T. He, J. Yao, *J. Photochem. Photobiol. C: Photochem. Rev.* **2003**, *4*, 125.

[36] Y. A. Pastrana, J. Torres, L. D. López-Carreño, H. M. Martínez, *J. Supercond. Nov. Magn.* **2013**, *26*, 2475.

[37] M. Vasilopoulou, L. C. Palilis, D. G. Georgiadou, S. Kennou, I. Kostis, D. Davazoglou, P. Argitis, *Appl. Phys. Lett.* **2012**, *100*, 013311.

[38] S. K. Deb, J. A. Chopoorian, *J. Appl. Phys.* **1966**, *37*, 4818.

[39] M. Rouhani, Y. L. Foo, J. Hobley, J. Pan, G. S. Subramanian, X. Yu, A. Rusydi, S. Gorelik, *Appl. Surface Sci.* **2013**, *273*, 150.

[40] A. Gavrilyuk, U. Tritthart, W. Gey, *Solar Energy Mater. Solar Cells* **2011**, *95*, 1846.

[41] F. C. Krebs, K. Norrman, *Prog. Photovolt: Res. Appl.* **2007**, *15*, 697.

[42] Q. L. Song, M. L. Wang, E. G. Obbard, X. Y. Sun, X. M. Ding, X. Y. Hou, C. M. Li, *Appl. Phys. Lett.* **2006**, *89*, 251118.

[43] M. Hermenau, S. Schubert, H. Klumbies, J. Fahlteich, L. Müller-Meskamp, K. Leo, M. Riede, *Solar Energy Mater. Solar Cells* **2012**, *97*, 102.

[44] G. Teran-Escobar, D. M. Tannenbaum, E. Voroshazi, M. Hermenau, K. Norrman, M. T. Lloyd, Y. Galagan, B. Zimmermann, M. Hösel, H. F. Dam, M. Jørgensen, S. Gevorgyan, S. Kudret, W. Maes, L. Lutsen, D. Vanderzande, U. Würfel, R. Andriessen, R. Rösch, H. Hoppe,

A. Rivaton, G. Y. Uzunoğlu, D. Germack, B. Andreasen, M. V. Madsen, E. Bundgaard, F. C. Krebs, M. Lira-Cantu, *Phys. Chem. Chem. Phys.* **2012**, *14*, 11824.

[45] R. Lessmann, Z. Hong, S. Scholz, B. Maennig, M. K. Riede, K. Leo, *Org. Electron.* **2010**, *11*, 539.

[46] X. Tong, N. Wang, M. Slootsky, J. Yu, S. R. Forrest, *Solar Energy Mater. Solar Cells* **2013**, *118*, 116.

[47] Z. Tan, D. Qian, W. Zhang, L. Li, Y. Ding, Q. Xu, F. Wang, Y. Li, *J. Mater. Chem. A* **2013**, *1*, 657.

[48] Y. Kanai, T. Matsushima, H. Murata, *Thin Solid Films* **2009**, *518*, 537.

[49] S. Schubert, M. Hermenau, J. Meiss, L. Müller-Meskamp, K. Leo, *Adv. Funct. Mater.* **2012**, *22*, 4993.

[50] G. Williams, Q. Wang, H. Aziz, *Adv. Funct. Mater.* **2013**, *23*, 2239.

[51] G. Wicht, S. Bücheler, M. Dietrich, T. Jäger, F. Nüesch, T. Offermans, J.-N. Tisserant, L. Wang, H. Zhang, R. Hany, *Solar Energy Mater. Solar Cells* **2013**, *117*, 585.

[52] V. Capozzi, G. Casamassima, G. F. Lorusso, A. Minafra, R. Piccolo, T. Trovato, A. Valentini, *Solid State Commun.* **1996**, *98*, 853.

[53] S. Kazaoui, N. Minami, Y. Tanabe, H. J. Byrne, A. Eilmes, P. Petelenz, *Phys. Rev. B* **1998**, *58*, 7689.

[54] C. S. Yannoni, R. D. Johnson, G. Meijer, D. S. Bethune, J. R. Salem, *J. Phys. Chem.* **1991**, *95*, 9.

[55] I. Riedel, J. Parisi, V. Dyakonov, L. Lutsen, D. Vanderzande, J. C. Hummelen, *Adv. Funct. Mater.* **2004**, *14*, 38.

[56] M. T. Lloyd, D. C. Olson, P. Lu, E. Fang, D. L. Moore, M. S. White, M. O. Reese, D. S. Ginley, J. W. P. Hsu, *J. Mater. Chem.* **2009**, *19*, 7638.

[57] R. Steim, F. R. Kogler, C. J. Brabec, *J. Mater. Chem.* **2010**, *20*, 2499.

[58] B. P. Rand, D. P. Burk, S. R. Forrest, *Phys. Rev. B* **2007**, *75*, 115327.

[59] A. Ito, T. Morikawa, T. Takahashi, *Chem. Phys. Lett.* **1993**, *211*, 333.

[60] G. P. Lopinski, J. R. Fox, J. S. Lannin, *Chem. Phys. Lett.* **1995**, *239*, 107.

[61] B. Fan, R. Hany, J.-E. Moser, F. Nüesch, *Org. Electron.* **2008**, 9, 85.

# Supporting Information

**Photochemical Transformations in Fullerene and Molybdenum Oxide Affect the Stability of Bilayer Organic Solar Cells**

*Hui Zhang, Andreas Borgschulte, Fernando A. Castro, Rowena Crockett, Andreas C. Gerecke, Okan Deniz, Jakob Heier, Sandra Jenatsch, Frank Nüesch, Carlos Sanchez-Sanchez, Alina Zoladek-Lemanczyk, Roland Hany\**
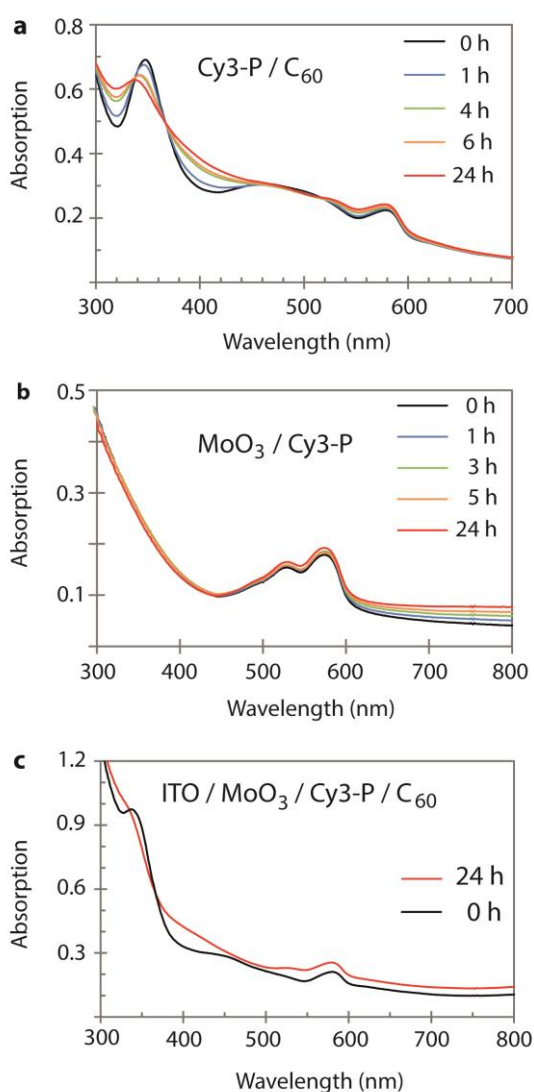


Figure 5S- 1 UV-vis absorption spectra of film stacks on glass upon illumination by a xenon lamp at 1 sun intensity under nitrogen.

(a) 20 nm Cy3-P/40 nm $C_{60}$, (b) 30 nm $MoO_3$/20 nm Cy3-P, (c) ITO/30 nm $MoO_3$/20 nm Cy3-P/40 nm $C_{60}$.
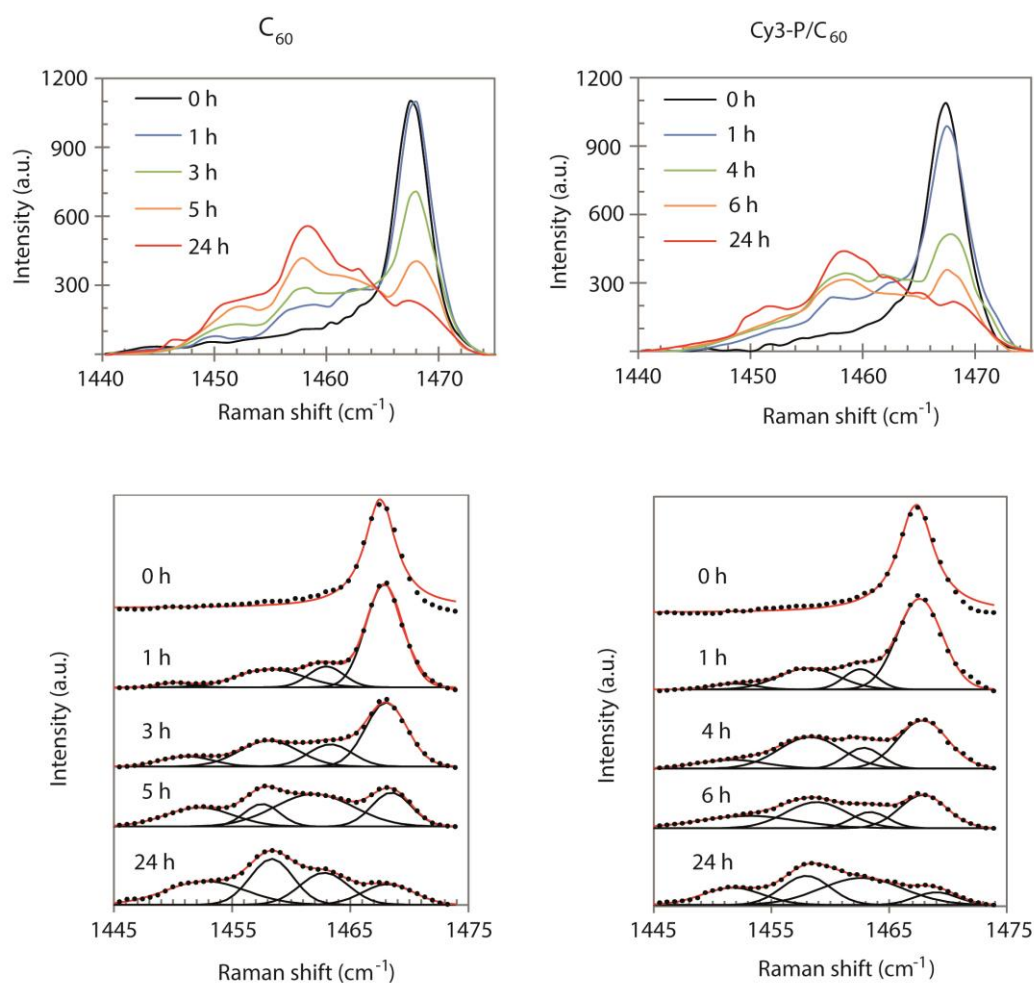
Figure 5S- 2 Raman spectra of a 40 nm $C_{60}$ film (left) and a 20 nm Cy3-P/40 nm $C_{60}$ film (right) upon illumination by a xenon lamp at 1 sun intensity under nitrogen.

Raman measurements were performed in ambient conditions using a Horiba Labram Evolution 800 spectrometer with a resolution of 1.65 cm$^{-1}$. The excitation laser wavelength was 785 nm and the power on the sample was ~200 mW. No visible sample degradation was induced during measurements. Each spectrum is the average of 4 spectra from different points on the sample. The acquisition time for a single spectrum was 10 sec. Raman spectra were baseline corrected and smoothed. Fitting (lower parts) was achieved by Gaussian-Lorentzian peak convolution. Dotted lines indicate the experimental spectra, solid black curves the fitted peaks, the solid red curve is the sum of all fitted curves.

The strongest mode at 1468 cm$^{-1}$ represents the pristine $C_{60}$ molecule. The formation of intermolecular bonds softens this mode and downshifts by ~5 cm$^{-1}$ per additional bond, such that $C_{60}$ dimers are represented by a Raman band at ~1463 cm$^{-1}$, $C_{60}$ linear chains at ~1458 cm$^{-1}$, and branched $C_{60}$ molecules with three bonds at ~1453 cm$^{-1}$.
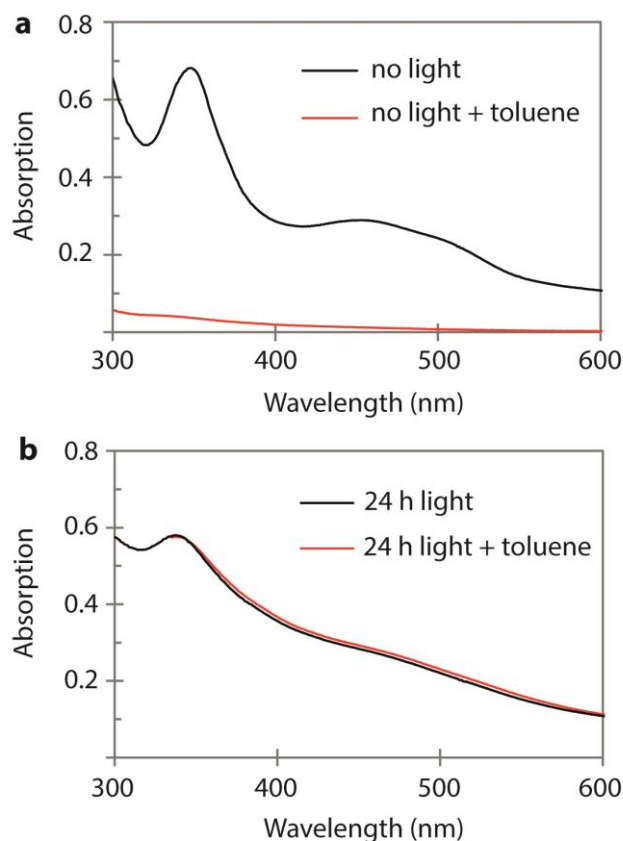
Figure 5S- 3 Solubility of $C_{60}$.

In (a) a 40 nm thick untreated $C_{60}$ film on a 2.5 x 2.5 cm glass substrate was rinsed with 6 mL toluene. This film was almost completely removed. In (b) the $C_{60}$ film was irradiated for 24 h before rinsing with toluene. This film was insoluble in toluene.
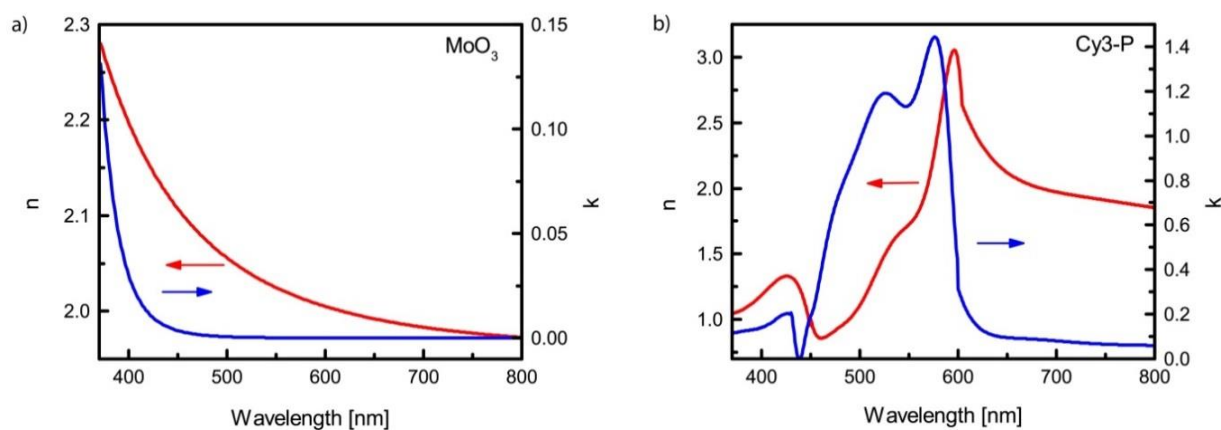


Figure 5S- 4 Refractive indices of $MoO_3$ (a) and Cy3-P (b) measured by ellipsometry.
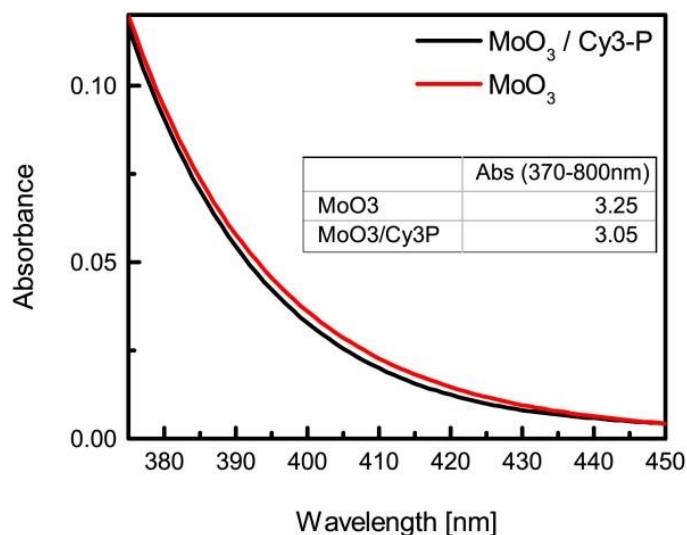
Figure 5S- 5 Simulated layer absorbance of $MoO_3$ in the device structure glass/ $MoO_3$ (30 nm)/Cy3-P (20 nm) (black) and without Cy3-P (red).

The integrated absorbance is shown in the insert table for each device. The layer absorbance was simulated using the optical model implemented in Setfos (www.fluxim.ch). For the sample without Cy3-P layer we observe a higher absorbance in the wavelength range 370 – 450 nm. The integrated absorbance is ~6% higher for the glass/$MoO_3$ sample compared to the one with an additional Cy3-P layer.



Figure 5S- 6 Temporal development of solar cell fill factors upon illumination.

Table 5S- 1 Performance of solar cells upon light irradiation at 1 sun intensity

at t = 0 and after 24 h. Average values from # solar cells are indicated. For cells 1 – 4, individual layers stacks were pre-irradiated for 24 h before completing the device.

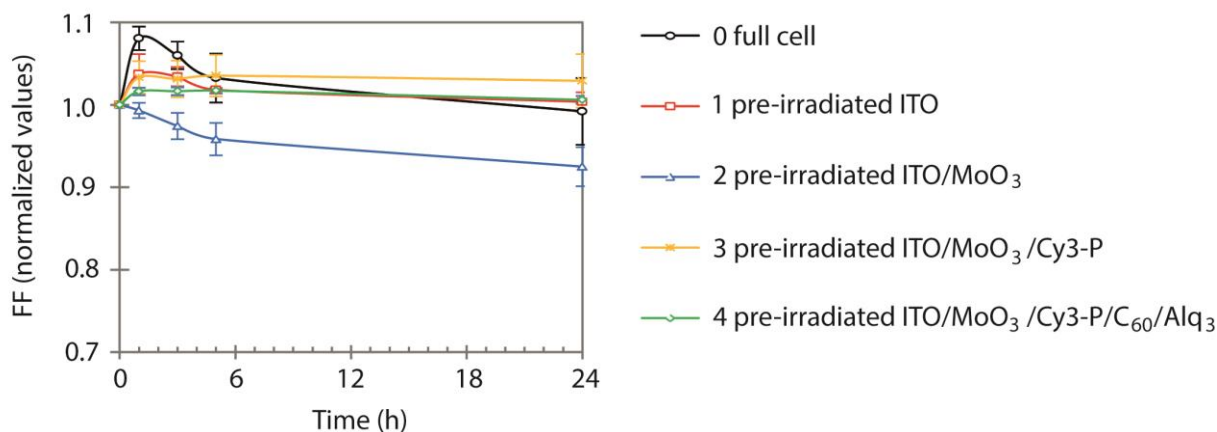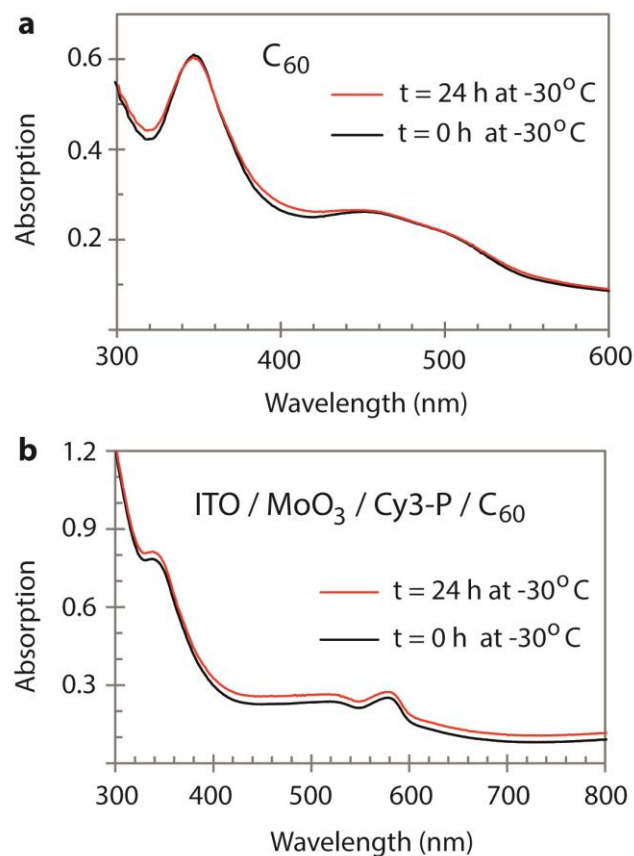| | Device | t = 0 | | | t = 24 h at 1 sun | | |
|---|---|---|---|---|---|---|---|
| | | $V_{oc}$ (V) | $J_{sc}$ (mA cm$^{-2}$) | FF (%) | $V_{oc}$ (V) | $J_{sc}$ (mA cm$^{-2}$) | FF (%) |
| 0 | Full cell (#5) | $0.80 \pm 0.06$ | $4.6 \pm 0.2$ | $67 \pm 2$ | $0.54 \pm 0.03$ | $3.7 \pm 0.2$ | $67 \pm 1$ |
| 1 | ITO (#2) | $0.82 \pm 0.01$ | $4.3 \pm 0.3$ | $69 \pm 1$ | $0.56 \pm 0.03$ | $3.3 \pm 0.4$ | $69 \pm 2$ |
| 2 | ITO/MoO$_3$ (#5) | $0.60 \pm 0.04$ | $4.1 \pm 0.3$ | $75 \pm 3$ | $0.55 \pm 0.04$ | $3.4 \pm 0.2$ | $69 \pm 3$ |
| 3 | ITO/MoO$_3$/Cy3-P (#3) | $0.50 \pm 0.04$ | $4.3 \pm 0.4$ | $68 \pm 2$ | $0.50 \pm 0.04$ | $3.7 \pm 0.3$ | $68 \pm 2$ |
| 4 | ITO/MoO$_3$/Cy3-P/ C$_{60}$/Alq$_3$ (#4) | $0.62 \pm 0.05$ | $3.6 \pm 0.2$ | $66 \pm 3$ | $0.54 \pm 0.03$ | $3.5 \pm 0.2$ | $67 \pm 1$ |



Figure 5S- 7. UV-vis absorption spectra of a (a) 40 nm thick C$_{60}$ film and (b) ITO/30 nm MoO$_3$/20 nm Cy3-P/40 nm C$_{60}$ layer stack upon illumination by a xenon lamp at 1 sun intensity at 243 K.

**Supporting Information 5S-8. ESI-HRMS experiments**

To identify possible transformation processes at the $MoO_3$/Cy3-P interface, samples were irradiated and analyzed by electrospray-high resolution mass spectrometry (ESI-HRMS).

*Sample preparation and irradiation.*

4 samples were prepared:

| | | |
|---|---|---|
| S1 | glass/$MoO_3$ | non-irradiated |
| S2 | glass/$MoO_3$/Cy3-P | non-irradiated |
| S3 | glass/$MoO_3$/Cy3-P | irradiated for 12 h at 1 sun under N2 atmosphere |
| S4 | glass/MoO3/Cy3-P | irradiated for 12 h at 1 sun under ambient air |

Samples were rinsed five times with 0.4 mL acetonitrile in a petri disk. The wash solutions were combined and 0.6 mL was transferred to a separate vial. To this solution, 3 μL of a 1 M solution of acetic acid was spiked. This resulted in a concentration of 5 mM acetic acid. Also, 3 μL of a 1000 ng/μL solution of reserpine were added as an ion abundance reference compound. This resulted in a reserpine concentration of 5 ng/μL.

*ESI-HRMS measurement.*

ESI-HRMS were performed on an Agilent 6530 QTOF mass spectrometer. The samples were directly infused by a syringe pump at a flow rate of 9 μL/min. Ionization was achieved by electrospray in the positive mode. The scan range of the TOF was 50 - 700 m/z at a resolution of 10'000 Δm/m. The relative uncertainty of the accurate mass measurement was 5 ppm.

*Results.*

ESI-HRMS spectra are shown in Figure 5-S8-1 and data evaluation is summarized in Table 5-S8. Irradiation had an effect on the observed mass spectra. The signal of Cy3-P was within experimental uncertainty unaffected by irradiation under nitrogen (sample S3), whereas the signal of Cy3-P decreased in the sample irradiated under air (sample S4). Air-irradiation led to a new signal at m/z 188.144. This mass matches with a possible fragment of Cy3-P (Figure 5-S8-2, compound no. 1 in Table 5-S8). Two signals (compound no. 2 and 3), which were found in all samples containing Cy3-P corresponded to Cy3-P with the loss of one or two methyl groups. As the ratio to Cy3-P was unaffected by irradiation, these structures cannot be linked to irradiation, but rather originate from in-source fragmentation. Compound no. 5 in Table 5-S8 corresponds to the addition of oxygen to Cy3-P. Also this ion appeared in all samples and cannot be clearly linked to irradiation conditions. Other ions (compounds no. 7-24) appeared also in the control sample (S1) and therefore do not originate from Cy3-P.

In summary, air irradiation led to one new ion signal, which matches a possible transformation product. Irradiation under nitrogen did not exhibit clear transformation products and the observed decrease of Cy3-P was within measurement uncertainty.
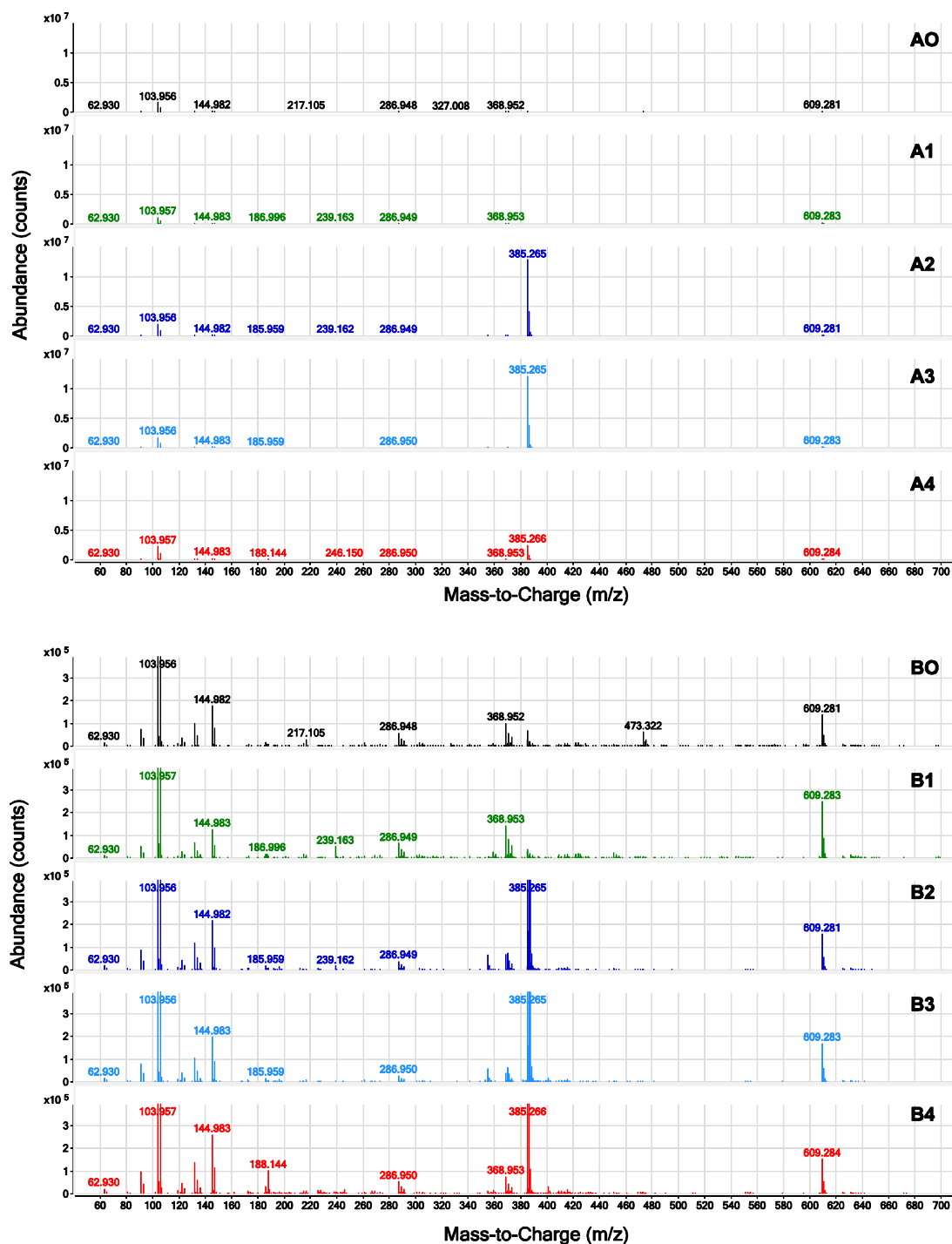


Figure 5S- 8-1 Mass spectra of irradiated Cy3-P and control samples.

In the upper part (A) spectra were scaled to the maximum intensity of all spectra. Lower part (B-spectra): all spectra were scaled to 4 x 105 counts, so that the signal of the reference compound (reserpine at m/z 609.28) is clearly visible. A0 and B0: solvent control; A1 and B1: spectra S1; A2 and B2: spectra S2; A3 and B3: spectra S3; A4 and B4: spectra S4.

**Cy3-P**

$C_{27}H_{33}N_2^+$

m/z: 385.2639

**Fragment 1 of Cy3-P**

$C_{13}H_{18}N_2^+$

m/z: 188.1434

Figure 5S-8-2 Structure of the Cy3-P cation and a possible transformation fragment of Cy3-P (compound no. 1 in Table 5-S8).

Table 5S- 2 Ion abundances and signal ratios of direct infusion ESI-HRMS experiments. Generally only ions with an abundance of larger than 15'000 counts were evaluated. For ions which are probably related to Cy3-P, also signals above 1'000 counts were evaluated. Of each isotope cluster, only the most intense signal is listed.

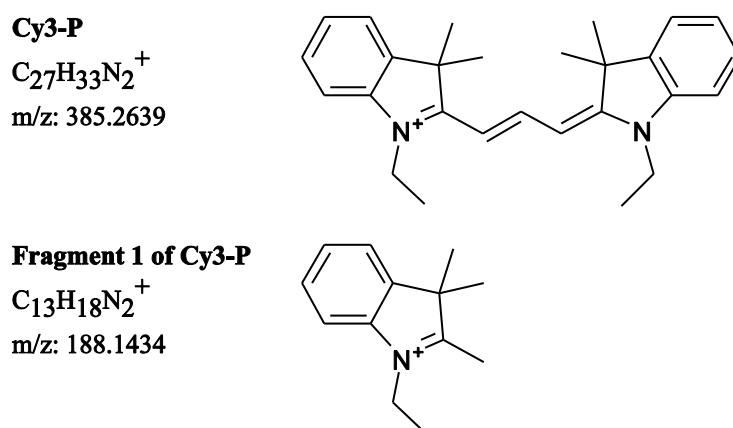| | # | measured mass[a] [Da] | matching mass formulae | interpretation | exact mass [Da] | difference mDa | solvent control | Cy3-P - S1 | Cy3-P - S2 | Cy3-P - S3 | Cy3-P - S4 |
|---|---|---|---|---|---|---|---|---|---|---|---|
| | | | | | | | | | abundance [counts] | | |
| probably related to Cy3-P | 1 | 188.144 | $[C_{13}H_{17}N]^+$ | fragment 1 of Cy3-P$^+$ | 188.1434 | -0.6 | < 1000 | < 1000 | < 1000 | < 1000 | 1.00E+05 |
| | 2 | 355.218 | $[C_{25}H_{27}N_2]^+$ | Cy3-P$^+$ - 2 x (CH$_3$) | 355.2169 | -1.1 | < 1000 | < 1000 | 6.51E+04 | 5.58E+04 | 1.06E+04 |
| | 3 | 370.241 | $[C_{26}H_{30}N_2]^+$ | Cy3-P$^+$ - CH$_3$ | 370.2404 | -0.6 | < 1000 | < 1000 | 7.33E+04 | 6.34E+04 | 1.20E+04 |
| | 4 | 385.266 | $[C_{27}H_{33}N_2]^+$ | Cy3-P$^+$ | 385.2638 | -2.2 | 6.64E+04 | 3.61E+04 | 1.29E+07 | 1.20E+07 | 2.43E+06 |
| | 5 | 401.260 | $[C_{27}H_{33}N_2O]^+$ | Cy3-P$^+$ + O | 401.2587 | -1.3 | 5.90E+03 | 2.80E+03 | 3.20E+03 | 1.81E+04 | 3.00E+04 |
| | 6 | 609.282 | $[C_{33}H_{41}N_2O_9]^+$ | reserpine + H$^+$ | 609.2807 | -1.3 | 1.37E+05 | 2.48E+05 | 1.57E+05 | 1.68E+05 | 1.53E+05 |
| | | | | | | | | | signal ratio to reserpine | | |
| | 1 | | | fragment 1 of Cy3-P | | | < 0.007 | < 0.004 | < 0.007 | <0.01 | 0.66 |
| | 2 | | | Cy3-P - 2 x (CH$_3$) | | | < 0.007 | < 0.004 | 0.42 | 0.33 | 0.07 |
| | 3 | | | Cy3-P - CH$_3$ | | | < 0.007 | < 0.004 | 0.47 | 0.38 | 0.08 |
| | 4 | | | Cy3-P | | | 0.48 | 0.15 | 82.10 | 71.78 | 15.96 |
| | 5 | | | Cy3-P + O | | | 0.04 | 0.01 | 0.02 | 0.11 | 0.20 |
| | | | | | | | | | ratio of reserpine normalized signals to Cy3-P - S2 | | |
| | 1 | | | fragment 1 of Cy3-P | | | - | - | 1.00 | - (at least 66 times lower than ratio of S4) | >94 |
| | 2 | | | Cy3-P - 2 x (CH3) | | | < 0.02 | < 0.01 | 1.00 | 0.80 | 0.17 |
| | 3 | | | Cy3-P - CH3 | | | < 0.01 | < 0.01 | 1.00 | 0.81 | 0.17 |
| | 4 | | | Cy3-P | | | 0.006 | 0.002 | 1.00 | 0.87 | 0.19 |
| | 5 | | | Cy3-P + O | | | 2.11 | 0.55 | 1.00 | 5.28 | 9.64 |
| | | | | | | | | | abundance [counts] | | |
| no known relation to Cy3-P | 7 | 62.930 | $[Cu]^+$ | Cu$^+$ | 62.9291 | -0.9 | < 1.5E+04 | < 1.5E+04 | 1.85E+04 | 1.66E+04 | 2.02E+04 |
| | 8 | 90.936 | $[CuN_2]^+$ | Cu$^+$ + N$_2$ | 90.9352 | -0.8 | 7.41E+04 | 5.14E+04 | 8.83E+04 | 7.88E+04 | 9.62E+04 |
| | 9 | 103.956 | $[CuC_2H_3N]^+$ | Cu$^+$ + ACN | 103.9556 | -0.4 | 1.62E+06 | 1.12E+06 | 1.97E+06 | 1.75E+06 | 2.24E+06 |
| | 10 | 121.967 | $[CuC_2H_5NO]^+$ | Cu$^+$ + ACN + H$_2$O | 121.9662 | -0.8 | 3.72E+04 | 2.83E+04 | 4.09E+04 | 3.85E+04 | 4.63E+04 |
| | 11 | 131.962 | $[CuC_2H_3N_3]^+$ | Cu$^+$ + ACN + N$_2$ | 131.9617 | -0.3 | 9.79E+04 | 6.77E+04 | 1.18E+05 | 1.05E+05 | 1.34E+05 |
| | 12 | 136.113 | ? | ? | - | - | < 1.5E+04 | < 1.5E+04 | 3.05E+04 | < 1.5E+04 | 2.52E+04 |
| | 13 | 144.934 | ? | ? | - | - | < 1.5E+04 | < 1.5E+04 | < 1.5E+04 | < 1.5E+04 | 2.80E+04 |
| | 14 | 144.982 | $[CuC_4H_6N_2]^+$ | Cu$^+$ + 2 * ACN | 144.9822 | 0.2 | 1.78E+05 | < 1.5E+04 | 2.17E+05 | 1.97E+05 | < 1.5E+04 |
| | 15 | 185.960 | $[CuC_6H_9N_3]^+$ | Cu$^+$ + 3 * ACN | 186.0087 | 48.7 | < 1.5E+04 | < 1.5E+04 | < 1.5E+04 | < 1.5E+04 | 3.00E+04 |
| | 16 | 217.105 | ? | ? | - | - | 2.96E+04 | < 1.5E+04 | < 1.5E+04 | < 1.5E+04 | < 1.5E+04 |
| | 17 | 239.163 | ? | ? | - | - | < 1.5E+04 | 5.12E+04 | < 1.5E+04 | < 1.5E+04 | < 1.5E+04 |
| | 18 | 286.949 | ? | ? | - | - | 5.74E+04 | 6.51E+04 | 3.81E+04 | 2.68E+04 | 5.33E+04 |
| | 19 | 358.981 | ? | ? | - | - | < 1.5E+04 | 2.49E+04 | < 1.5E+04 | < 1.5E+04 | < 1.5E+04 |
| | 20 | 368.953 | ? | ? | - | - | 9.94E+04 | 1.42E+05 | 6.73E+04 | 3.80E+04 | 7.44E+04 |
| | 21 | 423.909 | ? | ? | - | - | < 1.5E+04 | 1.84E+04 | < 1.5E+04 | < 1.5E+04 | < 1.5E+04 |
| | 22 | 425.288 | ? | ? | - | - | < 1.5E+04 | 1.81E+04 | < 1.5E+04 | < 1.5E+04 | < 1.5E+04 |
| | 23 | 450.956 | ? | ? | - | - | < 1.5E+04 | 2.29E+04 | < 1.5E+04 | < 1.5E+04 | < 1.5E+04 |
| | 24 | 473.322 | ? | ? | - | - | 6.18E+04 | < 1.5E+04 | < 1.5E+04 | < 1.5E+04 | < 1.5E+04 |

[a] average of measured mass (m/z ratio) in all samples with abundance larger than 15'000 counts. The relative standard deviation was always < 6 ppm.

**Supporting Information 5S-9. Simulated J-V curves during illumination with filtered light**

The opto-electronic simulation tool implemented in Setfos (www.fluxim.ch) was used to model the current-voltage characteristics of the device ITO (140 nm)/MoO$_3$ (30 nm)/Cy3-P (20 nm)/generation layer (1 nm)/C$_{60}$ (40 nm)/Alq$_3$ (2 nm)/Ag (80 nm). The introduction of an artificial generation layer ensures that charges are only generated at the heterojunction interface. Similar to the experimental conditions the illumination spectrum was set to zero below λ = 550 nm. First, the parameters in the active layers and the electrode work functions were adjusted to simulate the experimentally measured J-V curve of an untreated device. In Table 5-S9 we summarize the used parameters to obtain the green solid line (Figure 5-S9-1) which is in good agreement with the experimental J-V characteristics after 0 h of illumination (red squares).

**Table 5S-9** Parameters used for the simulation of the green solid line in Figure 5S-9-1.

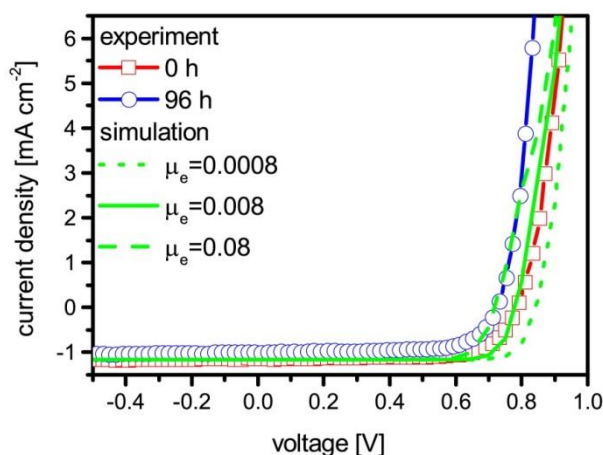| Active layers | $\mu_e$ [cm$^2$ V$^{-1}$ s$^{-1}$] | $\mu_h$ [cm$^2$ V$^{-1}$ s$^{-1}$] | ε | opt. gen. eff. | HOMO [eV] | LUMO [eV] | | Electrodes | Work function [eV] |
|---|---|---|---|---|---|---|---|---|---|
| Cy3-P | 1e-6 | 5e-5 | 4.5 | 0 | 5.68 | 3.9 | | anode | 5.4 |
| Generation layer | 0.008 | 5e-5 | 4.3 | 8.5 | 5.68 | 4.28 | | cathode | 4.55 |
| C$_{60}$ | 0.008 | 1e-6 | 4.1 | 0 | 6.4 | 4.28 | | | |



Figure 5S- 9-1 Experimentally measured cells after 0 h (red squares) and 96 h (blue circles) of illumination, respectively.

For the green solid line the simulation parameters (Table 5-S9) were optimised to model the pristine device (red squares). For the dashed and the dotted green curve the electron mobility in C$_{60}$ was varied according to the legend.

All simulated curves have the same short-circuit currents of 1.16 mA cm$^{-2}$ although we changed the electron mobility by two orders of magnitude. Thus we cannot explain the change in J$_{sc}$ after 96 h of illumination by a decrease of the C$_{60}$ electron mobility. Furthermore, a reduction of $\mu_e$ results in a shift of the open circuit voltage to higher values. This effect is due to the reduced Langevin recombination $R = \eta np(\mu_e + \mu_h)\frac{q}{\varepsilon}$ which is used in our model when the mobility is lowered. An increase in the electron mobility would lower the open circuit voltage as observed in the experiment, but in this case the J-V curve develops a slight S-kink at higher voltages which contradicts the experiment. Therefore we suppose that the experimentally observed change in the J-V characteristics upon illumination is not caused by a change in electron mobility in polymerised C$_{60}$ compared to pristine layers.

A change in short-circuit current can be achieved by varying the optical generation efficiency in the generation layer. Figure 5-S9-2 shows the simulated J-V curve for two different optical generation efficiencies. The short-circuit current for the 96 h illuminated cell was obtained by a reduction of this value by 14% compared to the initial simulation that matches the pristine sample. A decrease of the C$_{60}$ / Cy3-P interface area - induced by a volume decrease of the polymerised C$_{60}$ compared to the fresh one - would probably have a similar effect on charge generation at the heterojunction interface. However, the simulated reduction of charge generation at the interface did not lead to the lowering of the open circuit voltage as experimentally observed.
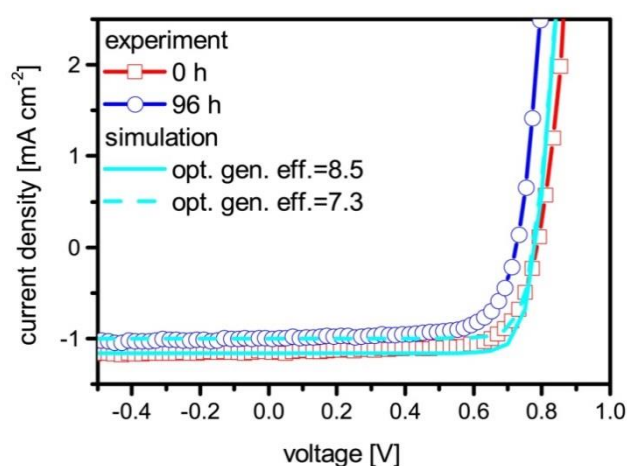


Figure 5S-9-2 Experimentally measured cells after 0 h (red squares) and 96 h (blue circles) of illumination, respectively. For the cyan solid line the simulation parameters (Table 5-S9) were optimised to model the pristine device (red squares). For the dashed cyan curve the optical generation efficiency in the generation layer was lowered by 14%.
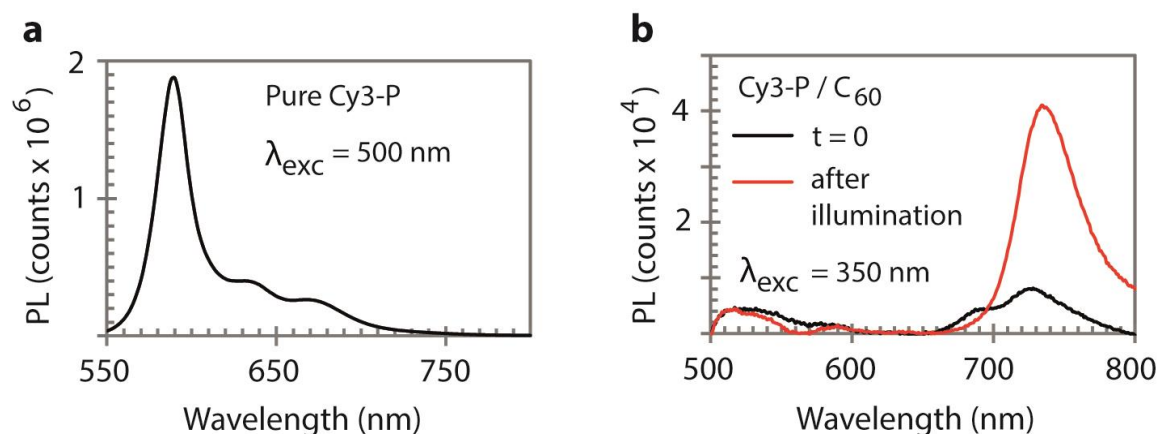
Figure 5S- 10 Fluorescence spectra on glass/MoO$_3$ substrates

of (a) a pure Cy3-P film, and (b) a bilayer film with selective excitation of C$_{60}$. In (b), emission signals are shown for as-prepared films, and after 96 h irradiation with filtered ($\lambda$ > 550 nm) light.
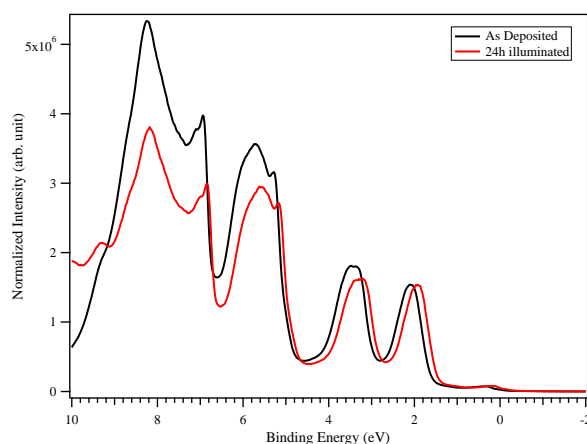


Figure 5S- 11 UPS spectra of as-deposited and illuminated C$_{60}$.

C$_{60}$ (Aldrich, 99.9%) films were grown on an atomically clean Cu(111) single crystal at room temperature. The crystal was cleaned by successive cycles of Ar$^+$ sputtering at 1 keV and 5 mA, followed by annealing at 740 K. The crystal surface cleanness was verified by X-ray photoelectron spectroscopy. C$_{60}$ films with a thickness of ~75 Å were prepared by vapor deposition from a resistively heated quartz crucible in the preparation chamber. Samples were transferred to the analysis chamber without breaking the vacuum.

It has been demonstrated that V$_{oc}$ correlates with the energies of the highest occupied molecular orbital (HOMO) of the donor and the lowest unoccupied molecular orbital (LUMO) of the acceptor material in the case of Ohmic contacts to the electrodes. Therefore, an increase of the C$_{60}$ LUMO level (to more negative values) upon photopolymerization could explain the observed V$_{oc}$ drop during illumination. From the displayed UPS spectra we measure a decrease of ~ 0.1 eV of the HOMO energy during phototransformation. At the same time, we observe a

redshift of the luminescence peak originating from the first excited $C_{60}$ state. It thus appears that polymerization of $C_{60}$ induces a small decrease of the HOMO-LUMO energy gap, but that this change is primarily associated with an energy shift of the HOMO level.
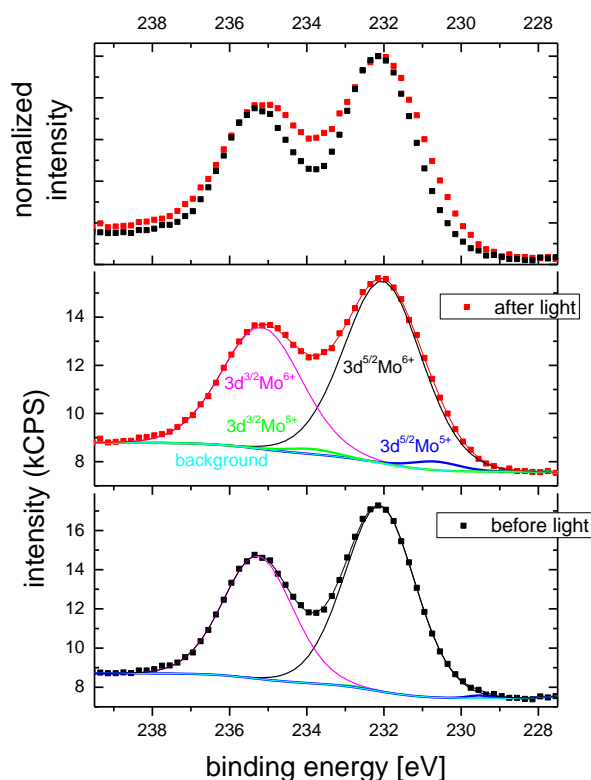


Figure 5S- 12 XPS data of the Mo 3d core level peaks for 30 nm thick molybdenum oxide films on ITO/glass, as-prepared and after 24 h illumination in the glove box.

The samples were inserted via an Ar glove box ($O_2 < 1$ ppm and $H_2O < 0.1$ ppm) directly connected to the spectrometer and transferred without exposure to air. From a fit to $Mo^{6+}$ before illumination, an energy difference of 3.2 eV was found between $Mo^{6+}(3d^{3/2})$ and $Mo^{6+}(3d^{5/2})$, and this value was used as constraint for the fitting of $Mo^{5+}$. As further constraint, the intensities for the $Mo^{5+}$ peaks were fixed to $I(3d^{3/2}) = 0.6 \times (3d^{5/2})$. Before illumination, $Mo^{5+}$ is not detected. $Mo^{5+}$ is formed during illumination, and after 24 h $Mo^{5+}/Mo^{6+} = 0.03$.
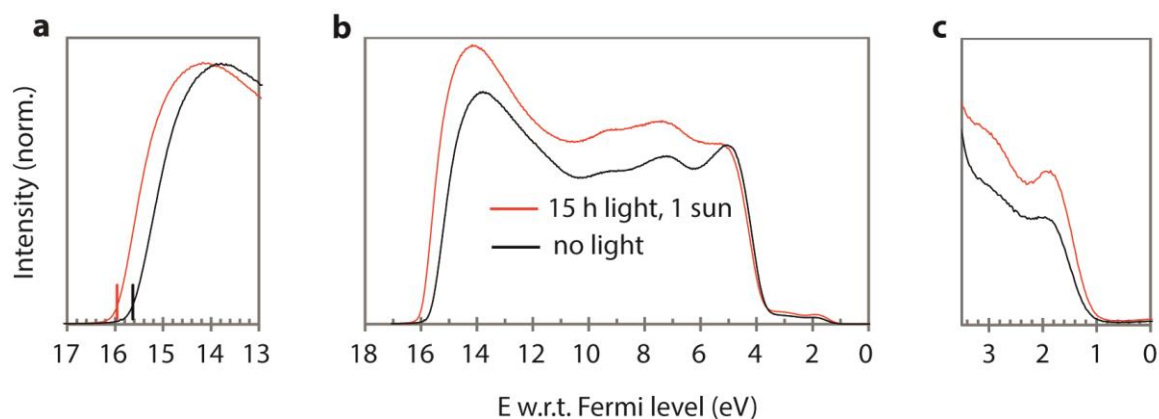
Figure 5S- 13 UPS spectra of as-deposited and illuminated $MoO_3$.

(a) Secondary-electron cut-off, (b) full scan, and (c) magnified spectra of the density of states near the valence band edge.

10 nm thick $MoO_3$ films were deposited on molybdenum substrate holders by thermal evaporation at a pressure of ~4·$10^{-6}$ mbar. Illumination was performed for 15 h under nitrogen using the solar simulator. To minimize exposure to ambient atmosphere, samples were transferred under nitrogen and introduced in a counter flow of nitrogen into the UPS analysis system. Since $MoO_3$ is a photosensitive material, radiation damage due to He I irradiation must be carefully excluded. We observed identical spectra when increasing the measurement time from to 3 to 10 and then to 20 minutes, but the work function was reduced by ~0.2 eV when the sample was irradiated with He I light for 1 hour before measuring the UPS spectra.
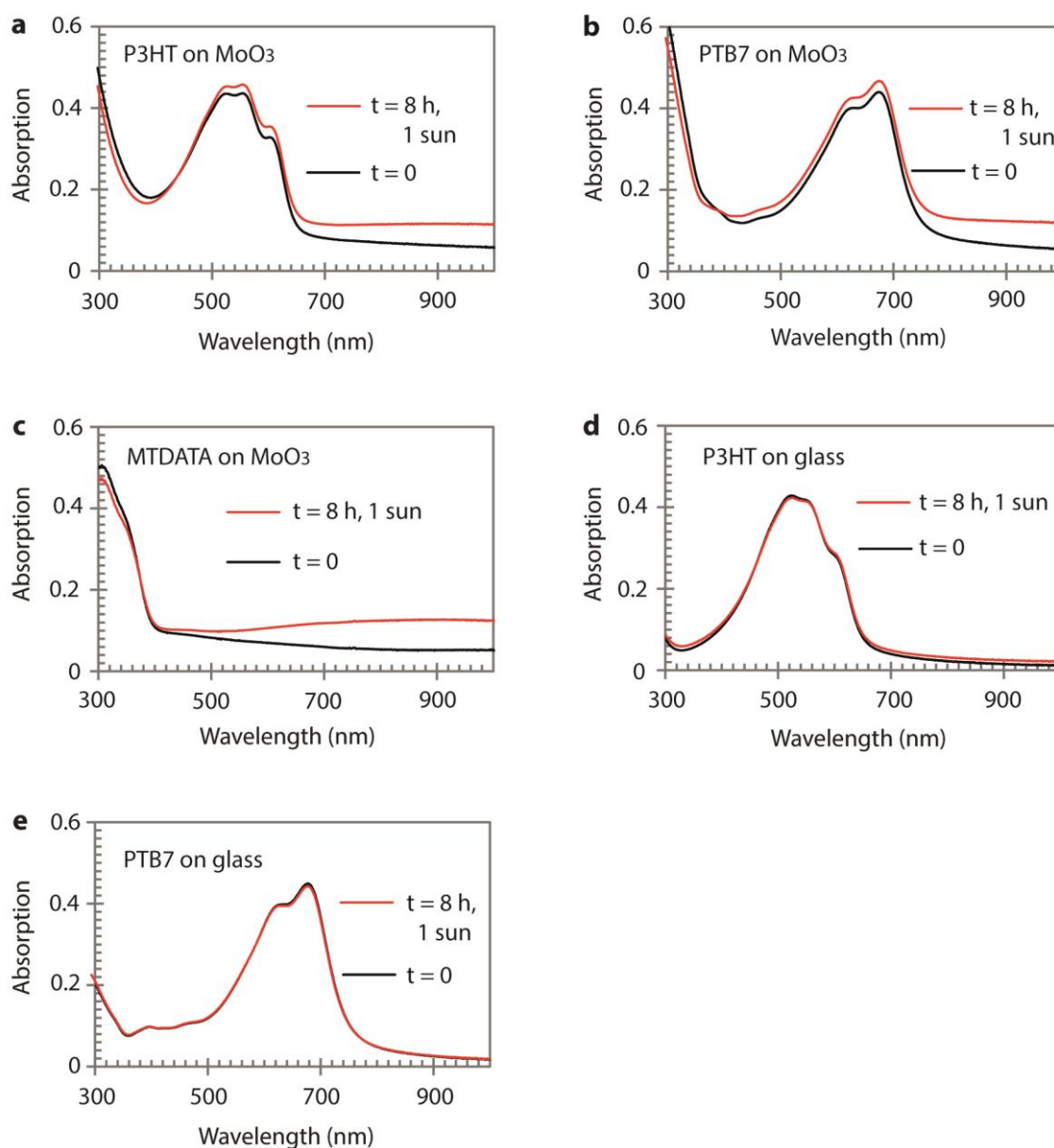
Figure 5S- 14 UV-vis absorption spectra of thin films of organic materials

on glass/30 nm MoO$_3$ (a – c) or glass (d, e). Spectra were measured directly after film deposition and after illumination for 8 h at 1 sun intensity under nitrogen. Spectra (a – c) demonstrate that the photochromism in MoO$_3$ is taking place irrespective of the overlying organic material, spectra (d) and (e) show that P3HT and PTB7 are stable during light processing. P3HT = Poly(3-hexylthiophene), PTB7 = Poly({4,8-bis[2-ethylhexyl)oxy]benzo[1,2-*b*:4,5-b´]dithiophene-2,6-diyl}{3-fluoro-2-[(2-ethylhexyl)carbonyl]thieno[3,4-*b*]thiophenediyl}), MTDATA = 4,4',4''-Tris(N-3methylphenyl-N-phenylamino)triphenylamine.

# Chapter VI. Conclusions and outlook

## *Conclusions*

In this thesis, I showed a way how to produce and optimize visibly transparent organic solar cells and photodetectors using NIR absorbing cyanine dyes. *AVT* of over 65% were achieved, and device performances were on par with reported values for similar, but less transparent, devices. Integration of NIR cyanines into multi-junction structures enhanced the efficiency of solar cells by 34%. I also found that the photostability of cyanines is better than usually assumed. Indeed, during operation in the absence of oxygen and water, degradation processes in other device layers were responsible for the observed limited long term stability.

Transparent photovoltaic cells were fabricated by using a selective NIR absorbing heptamethine cyanine dye (Cy7-P) as electron donor and $C_{60}$ as acceptor, $Alq_3$ as cathode buffer layer and silver/$Alq_3$ as cathode. Devices with an *AVT* of 67% and an efficiency of 0.7% were fabricated. In a second step, the $PF_6^-$ anion was exchanged with the bulky anion trisphate$^-$ (Cy7-T). Thereby, the high *AVT* level could be maintained, but the efficiency increased to 2.2%.

Transparent photodetectors with a high *AVT* value of 68.9% were fabricated by using the same cyanine dye Cy7-T as electron donor and $TiO_2$ as electron acceptor. A broad band gap semiconductor MeO-TPD was introduced as electron blocking layer to reduce the dark current noise, and polymerized $C_{60}$ as $TiO_2$ interface modifier to avoid back recombination of separated carriers. The transparent photodetector further contained a combination of a thin Au film and a $MoO_3$ capping layer as transparent top electrode. The figures of merit of our photodetector at $\lambda = 850$ nm, such as photoconversion efficiencies of 13% - 23% and specific detectivities of $\sim 10^{12}$ cm $Hz^{\frac{1}{2}}$ $W^{-1}$ compared favorably with reported values for organic photodetectors so far.

Tandem solar cells were fabricated by using Cy3-P as a wide band gap donor and Cy7-T as low band gap donor, $C_{60}$ as acceptor for each subcell and a thin $Alq_3$/Au/$MoO_3$ layer as transparent recombination interlayer. Experimental device optimization was based on optical simulations. The maximum current density generated from the two subcells was calculated and adjusted to achieve current matching and to select the proper layer sequence. A maximum efficiency of 4.3% was measured for tandem devices. The $V_{OC}$ of 1.5 V was exactly the sum of the $V_{OC}$s of both individual single cells. Triple-junction devices were fabricated in the same way by introducing an additional, complementary pentamethine cyanine dye (Cy5-P), and efficiencies of 3.6% and a high $V_{OC}$ of 2.1 V were measured. I demonstrated that low mobility

organic semiconductors with extremely high absorption coeeficients can provide decent power coversion efficiencies in multijunction solar cells, even though bilayer heterojunctions were used for the individual subcells.

It is well-known that light exposure induces the formation of intermolecular bonds between $C_{60}$ (photo-polymerization) and color changes in $MoO_3$ (photo-chromism). The influence of these reactions on the long-term stability of organic solar cells, however, has not been addressed so far. We studied the degradation of $ITO/MoO_3/Cy3-P/C_{60}/Alq_3/Ag$ solar cells. We found that the cyanine dye was photostable when illuminated in the absence of oxygen and water. The kinetics of photo-transformations in $C_{60}$ and $MoO_3$ closely followed the trend of the solar cell performance decrease. Irradiations in selective wavelength regions were used to separate the adverse influence of the two photochemical transformations. We found that the major part of the $V_{OC}$ decay was due to transformations in the $MoO_3$ layer, and that changes in $MoO_3$ and $C_{60}$ contributed almost equally to the observed drop in the short-circuit current.

### *Outlook*

For window- and display- integrated applications of transparent organic electronics, *AVT* values above ~75% will be required. To achieve this goal, cyanine dyes with absorption maxima at 1000 nm and beyond could be used in similar devices as proposed here. However, this might be accompanied by a decrease in device performance and stability issues of cyanines with long polymethine chains. A further increase of device *AVT* values could also be achieved by integrating highly transparent and conductive electrodes. The development of such materials is a nascent field of research.

Cyanine dyes possess other interesting properties that can be exploited for organic electronic devices in future work. For example, cyanine dyes can self-assemble into supramolecular aggregates. These aggregates have outstanding opto-electronic properties such as narrow absorption bands with very high extinction coefficients or high charge mobility values. Integration of cyanine aggregates into devices could increase the fundamental processes of charge-generation and transport considerably. The problem encountered so far is the reproducible fabrication of cyanine aggregates from organic solvents. Another issue is the pronounced phase separation between cyanine dyes and fullerene derivatives when coated as a blend thin film from solution. This prevents at the moment the fabrication of high-performing bulk-heterojunction cyanine solar cells.

Multi-junction bilayer structures are one way to circumvent the problem. Further improvements of these devices can be expected by replacing $C_{60}$ with $C_{70}$. This might be accompa-

nied by a positive side-effect on the long-term device stability. Indeed, it is known that the photo-polymerization reaction in $C_{70}$ is substantially suppressed.

# Curriculum Vitae

## Hui Zhang

Date of birth: October 8th, 1984

Place of birth: Hubei, China

Nationality: the People's Republic of China

## Education

11/2011-04/2015, PhD student, in the Group of Prof. Frank Nüesch, Swiss Federal Institute of Technology Lausanne (EPFL) & Swiss Federal Laboratories for Materials Science and Technology (EMPA), Switzerland.

*Thesis topic: NIR sensitive organic dyes for tandem solar cells and transparent photodiodes*

9/2010-10/2011, research assistant in the group of Prof. Massimo Morbidelli in department of chemistry and applied biosciences, Swiss Federal Institute of Technology Zurich (ETH Zurich), Switzerland.

*Research topic: Modification of carbon nanotubes for organic solar cells*

9/2007-7/2010: Master of Chemical Engineering, School of Chemistry and Chemical Engineering, South China University of Technology (SCUT), China.

*Thesis topic: Research on Waterborne polyurethane and polyacrylate adhesive by emulsion polymerization*

9/2003-7/2007: Bachelor of Chemical Engineering, Department of Chemical Engineering and Technology, Wuhan Institute of Technology (WIT), China.

## List of publications

[1] H. Zhang, A. Borgschulte, F. A. Castro, R. Crockett, O. Deniz, J. Heier, S. Jenatsch, F. Nüesch, C. Sanchez, A. Zoladek-Lemanczyk, R. Hany, photochemical transformations in fullerene and molybdenum oxide affect the stability of bilayer organic solar cells, Adv.Energy

Mater., 2015, 5, 1400734.

[2] H. Zhang, S. Jenatsch, J.R. Jonghe, F. Nüesch, R. Steim, A.C. Veron, R. Hany, transparent photodetector using a near infrared absorbing cyanine dye, Sci. Rep., 2015, 5, 9439.

[3] H. Zhang, G. Wicht, C.Gretener, M. Nagel, F. Nüesch, Y. Romanyuk, J.N. Tisserant, R. Hany, semitransparent organic photovoltaics using a near-infrared absorbing cyanine dye, Sol. Energy Mater. Sol. Cells, 2013, 118, 157-164.

[4] H. Zhang, H. Wu, role of surfactant adsorption in controlling morphology of single-walled carbon nanotubes/ polythiophene, Ind. Eng. Chem. Res., 2014, 53, 9088-9093.

[5] H. Zhang, B. Niesen, E. Hack, R. Hany, F. Nüesch, cyanine tandem- and triple- junction solar cells, In preparation, 2015

[6] A.C. Veron, H. Zhang, A. Linden, F. Nüesch, J. Heier, R. Hany, T. Geiger, NIR-absorbing heptamethine dyes with tailor-made counterions for application in light to energy conversion, Org. Lett., 2014, 16, 1044-1047.

[7] L. Wang, C. Hinderling, S. Jenatsch, F. Nüesch, D. Rentsch, R. Steim, H. Zhang, R. Hany, cyanine dye polyelectrolytes for organic bilayer solar cells, Polymer, 2014, 55, 3196-3201.

[8] G. Wicht, S. Bücheler, M. Dietrich, T. Jäger, F. Nüesch, T. Offermans, L. Wang, H. Zhang, R. Hany, stability of bilayer trimethine cyanine dye / fullerene organic solar cells, Sol. Energy Mater. Sol. Cells, 2013, 117, 585-591.

[9] E. Berner, T. Jäger, T. Lanz, F. Nüesch, J.N. Tisserant, G. Wicht, H. Zhang, R. Hany, influence of crystalline titanium oxide layer smoothness on the performance of inverted organic bilayer solar cells, Appl. Phys. Lett., 2013, 102(18), 183903.

[10] H.Q. Fu, L.N. Wang, W.T. Lai, H. Zhang, the film properties of waterborne polyurethane modified by epoxidized soybean oil and styrene, Int. J. Polym. Mater., 2011, 60, 654-664.

[11] H.Q. Fu, H. Huang, Q. Wang, H. Zhang, H.Q. Chen, properties of aqueous polyurethane dispersion modified by epoxide resin and their use as adhesive, J. Disper. Sci. Technol., 2009, 30(5), 634-638.

# List of conferences

H. Zhang, F. Nüesch and R. Hany, oral presentation "Photochemical Transformations in Fullerene and Molybdenum Oxide Affect the Stability of Bilayer Organic Solar Cells" *Solar Fuels and Solar Cells (SFSC 2014)*, Dalian, China, October 21-24, 2014.

H. Zhang, F. Nüesch and R. Hany, oral and poster presentation "Light Induced Degradation Mechanism of Cyanine Dye / Fullerene Organic Solar Cells" *Exploring and Improving Durability of Thin Film Solar Cells*, Winterthur, Switzerland. February 5-6, 2014.

H. Zhang, G. Wicht, F. Nüesch, R. Hany, oral presentation "Near infrared absorbing cyanine dyes for visibly transparent organic solar cells", *Nanotechnology for Next Generation High Efficiency Photovoltaics*, IES Cargèse, Corsica, France, April 1-6, 2013

H. Zhang, G. Wicht, F. Nüesch, R. Hany, oral presentation "Semitransparent organic photovoltaics using a near-infrared absorbing cyanine dye", *Global Organic Photovoltaic Conference (GOPV 2012)*, Suzhou, China, 2012